

TOWARD HYPER-RESOLUTION HYDROLOGIC DATA ASSIMILATION SYSTEMS FOR
IMPROVED PREDICTIONS OF HYDROCLIMATE EXTREMES

by

PEYMAN ABBASZADEH

HAMID MORADKHANI, COMMITTEE CHAIR

GLENN TOOTLE

LEIGH TERRY

DINGWEN TAO

HAMED MOFTAKHARI

A DISSERTATION

Submitted in partial fulfillment of the requirements
for the degree of Doctor of Philosophy in the
Department of Civil, Construction and Environmental Engineering
in the Graduate School of
The University of Alabama

TUSCALOOSA, ALABAMA

2020

Copyright Peyman Abbaszadeh 2020
ALL RIGHTS RESERVED

ABSTRACT

Over the past decades, tropical storms and hurricanes in the Southeast United States have become more frequent and intense, mainly due to the effects of climate change. They often produce torrential rains that may result in catastrophic floods depending on hydrologic, geomorphologic and orographic characteristics of the region. Although hydrological models are widely used to provide estimates of such floods, their predictions most often are not perfect as the models suffer either from inadequate conceptualization of underlying physics or non-uniqueness of model parameters or inaccurate initialization. Data Assimilation (DA) based on Particle Filtering (PF) has been recognized as an effective and reliable mean to integrate the hydrometeorological observations from in-situ stations and remotely sensed sensors into hydrological models for enhancing their prediction skills while accounting for the associated uncertainties. Although recent developments in DA theory and remote sensing technologies have made significant progress in enhancing the performance of the hydrologic models, their usefulness are subject to some inherent limitations that may result in inaccurate and imprecise model predictions, especially in the case of an extreme event such as flooding.

This dissertation is an attempt to identify these limitations and address those by conducting four studies. The first tackles a fundamental problem associated with the utilization of remotely sensed observations in hydrologic data assimilation applications. The two and third are progressive studies that address two conceptual/theoretical problems of using particle filtering approach in hydrologic studies. As a result, the fourth study demonstrates the

effectiveness and usefulness of the developments in all three studies in improving the hyper-resolution hydrologic model predictions over a region in the Southeast Texas where heavy rainfall from Hurricane Harvey caused deadly flooding.

Key Words: Flood prediction, hyper-resolution hydrologic model, Data Assimilation.

DEDICATION

I dedicate this work to my loving and supportive wife, Atieh.

LIST OF ABBREVIATIONS

y_t	Observational data
y'_t	Model prediction
$\text{Cov}_{y_t y'_t}$	Covariance calculated by observational data and model prediction
σ	Standard deviation of observation
σ'	Standard deviation of model prediction
μ	Mean of observation
μ'	Mean of model prediction
T	Total time steps
N	Number of Ensemble
$\overline{y'_{\blacksquare,t}}$	Ensemble mean (model simulation) at time step t

ACKNOWLEDGMENTS

I would like to express my sincerest gratitude and appreciation to my advisor Prof. Hamid Moradkhani for the guidance over the almost four years of research work. I was extremely lucky to have had such a supportive and patient supervisor. He has been a wonderful mentor and friend. He taught me the technical, research and managerial skills to succeed in research. I hope to become a good researcher in order to be able to carry his legacy to the next generation of scientists.

Besides my advisor, I would like to thank my dissertation committee members: Dr. Glenn Tootle, Dr. Leigh Terry, Dr. Dingwen Tao and Dr. Hamed Moftakhari for their time to review my dissertation and their valuable comments and suggestions.

I want to gratefully acknowledge Prof. Dacian Daescu and Dr. Hongxiang Yan who taught me many things that I would have never learned by myself.

I would like to humbly thank my beloved and wonderful wife, Atieh, for being with me in all circumstances, for helping me overcome all difficulties in my life, and for giving me motivation.

Last but not least, my warm acknowledgments to my mother, Mahnaz, and my two dear brothers, Payam and Afshin for all their encouragement and moral support during all these years.

CONTENTS

ABSTRACT.....	ii
DEDICATION.....	iv
LIST OF ABBREVIATIONS.....	v
ACKNOWLEDGMENTS	vi
LIST OF TABLES.....	xii
LIST OF FIGURES	xiii
INTRODUCTION	1
References.....	7
CHAPTER 1 DOWNSCALING SMAP RADIOMETER SOIL MOISTURE OVER THE CONUS USING AN ENSEMBLE LEARNING METHOD	12
Abstract.....	12
Introduction.....	13
Remotely Sensed and Ground-Based Observations	16
SMAP Radiometer Soil Moisture Data.....	16
MODIS Land Surface Temperature (LST) and NDVI	17
National Weather Service (NWS) Precipitation Data.....	18
CONUS-SOIL Data	18
GTOPO30 Topography Data	19
In-situ Soil Moisture Observations	20
The Proposed Satellite Soil moisture Downscaling Approach.....	21

Soil Moisture Downscaling Framework	21
Random Forest (RF)	24
Results and Discussions.....	27
Performance of the Proposed Downscaling Algorithm	28
Downscaled SMAP Soil Moistures versus In-situ Observations.....	31
Validation of Downscaled SMAP Soil Moisture Product	45
Summary and Conclusion.....	51
Acknowledgements.....	52
References.....	54
CHAPTER 2 ENHANCING HYDROLOGIC DATA ASSIMILATION BY EVOLUTIONARY PARTICLE FILTER AND MARKOV CHAIN MONTE CARLO	63
Abstract.....	63
Introduction.....	64
Theory and Methods	67
Sequential Bayesian Estimation.....	67
Particle Filter-Markov Chain Monte Carlo (PF-MCMC).....	69
Evolutionary PF-MCMC (EPFM)	71
Streamflow Prediction Results.....	78
Synthetic Case Study	81
Real Case Study	85
Streamflow Forecasting Results	91
Conclusion	95
Acknowledgement	97
References.....	98

CHAPTER 3 THE QUEST FOR MODEL UNCERTAINTY QUANTIFICATION: A HYBRID ENSEMBLE AND VARIATIONAL DATA ASSIMILATION FRAMEWORK	103
Abstract.....	103
Introduction.....	104
Methodology.....	108
EPFM data assimilation method	109
4DVAR data assimilation method	115
EPFM+4DVAR data assimilation method (HEAVEN)	116
Experimental design	125
HyMOD model	126
SAC-SMA model.....	126
Case studies.....	126
Performance measures	130
Data assimilation setting.....	131
Results and Discussions.....	132
Streamflow prediction results (I): synthetic case study	132
Streamflow prediction results (II): real case studies.....	135
Concluding remarks	147
Acknowledgment	149
References.....	150
CHAPTER 4 MULTIVARIATE REMOTELY SENSED AND IN-SITU DATA ASSIMILATION FOR ENHANCING COMMUNITY WRF-HYDRO MODEL FORECASTING	157
Abstract.....	157
Introduction.....	158

Study Area	163
Datasets.....	164
SMAP Soil Moisture Products.....	164
NLDAS-2 Forcing Data.....	166
USGS Streamflow Gauges.....	167
WRF-Hydro Hydrological Model.....	168
Data Assimilation Approaches	169
Sequential Bayesian Theory	169
Research Framework	173
WRF-Hydro Modeling.....	176
WRF-Hydro Model Setup.....	176
WRF-Hydro Model Calibration.....	179
WRF-Hydro Model Simulation Analysis	186
Assimilation of In-situ and Remotely Sensed Observations	188
Assimilation of Streamflow Observations into the WRF-Hydro Model	188
Assimilation of SMAP Soil Moisture Products into the WRF-Hydro Model	191
Multivariate Assimilation of SMAP Soil Moisture and Streamflow Observations.....	196
Summary and Conclusion.....	197
References.....	199
CONCLUSION.....	209
Supplementary Information	212
Figure 1-S1. Soil texture of top 5 cm soil layer over the CONUS	212

Figure 1-S2. The USCRN and SCAN soil moisture sensors throughout the CONUS and Digital Elevation Map (DEM) showing the variations of elevation.	213
Figure 1-S3. SCAN stations located at (a) Tift, Georgia (b) Whitman, Washington and (c) Fresno, California (https://www.wcc.nrcs.usda.gov/scan/).	214
Figure 3-S1. The comparison of the PF-MCMC and HEAVEN skills for three-day streamflow forecast in the Leaf River Basin during the flood season.	215
Figure 4-S1. Soil texture of top 5 cm soil layer over the CONUS	216
Figure 4-S2. WRF-Hydro simulated streamflow with 95-percentile confidence interval versus USGS observed streamflow for the period of Hurricane Harvey. The blue line and red points are the mean ensemble and observation, respectively. The green line displays the open loop model run.	217
Figure 4-S3. WRF-Hydro simulated streamflow with 95-percentile confidence interval versus USGS observed streamflow for the period of Hurricane Harvey. The blue line and red points are the mean ensemble and observation, respectively. The green line displays the open loop model run.	218
Figure 4-S4. WRF-Hydro simulated streamflow with 95-percentile confidence interval versus USGS observed streamflow for the period of Hurricane Harvey. The blue line and red points are the mean ensemble and observation, respectively. The green line displays the open loop model run.	219
Table 4-S1. Deterministic and probabilistic performance measures for the multivariate assimilation of satellite soil moisture and streamflow observations within the watershed. ...	220
Appendix A.....	221

LIST OF TABLES

Table 1-1 Distribution of in-situ soil moisture sensors over CONUS with respect to the soil texture of top 5 cm soil layer.	23
Table 1-2 Comparison between the downscaled SMAP soil moisture at 1km and in-situ soil moisture measurements within Little Washita River Watershed in 2015 (location information is based on the WGS84 datum).....	46
Table 1-3 Comparison between the downscaled SMAP soil moisture at 1km and in-situ soil moisture measurements within Walnut Gulch Experimental Watershed in 2015 (location information is based on the WGS84 datum).....	50
Table 2-1 Descriptions of parameters for the SAC-SMA model.....	79
Table 2-2 Description of the SAC-SMA model state variables.....	79
Table 2-3 Specifications of four study basins located in the United States.....	86
Table 2-4 Deterministic and probabilistic measures based on an ensemble size of 200 for one-day and five-day ahead streamflow forecasting.	92
Table 4-1 WRF-Hydro model Parameters defined by NCAR	179

LIST OF FIGURES

Figure 1-1 Schematic of the proposed soil moisture downscaling framework.....	27
Figure 1-2 Verification results of the developed Random Forest (RF) models for each group of soil texture over CONUS.....	31
Figure 1-3 Correlation and ubRMSE calculated between in-situ observations (SCAN and USCRN) and downscaled SMAP.	33
Figure 1-4 Comparison of downscaling accuracy between the proposed approach and the uniform disaggregation approach.	34
Figure 1-5 The performance of the proposed downscaling approach under four different input schemes.....	36
Figure 1-6 The accuracy of downscaled SMAP soil moisture versus in-situ soil moisture observations collected from 186 SCAN and 114 USCRN stations for study period 04/01/2015–12/31/2015.....	37
Figure 1-7 Time series, scatter plot and Cumulative Distribution Function (CDF) of original and downscaled SMAP soil moisture data versus in-situ observations at top 5 cm depth.	40
Figure 1-8 (a) Land cover distribution over the western CONUS, (b) original SMAP soil moisture at 36 km spatial resolution, and (c) downscaled SMAP soil moisture at 1km spatial resolution on April 27, 2015.	43
Figure 1-9 Daily in-situ and downscaled SMAP radiometer soil moisture at 1km along with precipitation observation for stations 148, 124, 131, and 149.....	48
Figure 1-10 Comparison between the soil moisture retrieved from CVSs and those downscaled by two downscaling approaches used in this study.....	51
Figure 2-1 Flowchart of the proposed EPFM algorithm.....	72
Figure 2-2 Color coding of the hybrid GA-MCMC process.....	73
Figure 2-3 Synthetic streamflow prediction over four years using (a) PF-MCMC and (b) EPFM.	82
Figure 2-4 The comparison of accuracy, distribution spread, and computational demand for the PF-MCMC and EPFM in the synthetic experiment over four years.....	84

Figure 2-5 The comparison of accuracy, distribution spread, and computational demand for three real case studies over four years of analysis using the PF-MCMC and EPFM.	87
Figure 2-6 Streamflow prediction using the PF-MCMC and EPFM for the Chehalis River Basin in WA over four years.	88
Figure 2-7 The prior and posterior distributions obtained by the PF-MCMC, PF-GA and EPFM for three days..	90
Figure 2-8 The comparison of the PF-MCMC and EPFM skills in one-day ahead streamflow forecast for the synthetic (a and b) and a real case study (c and d).	94
Figure 2-9 The comparison of the PF-MCMC and EPFM skills in five-day ahead streamflow forecast for the synthetic (a and b) and a real case study (c and d).	95
Figure 3-1 Schematic of the proposed HEAVEN method in a reciprocal form..	118
Figure 3-2 Seven study basins located in the western United States.	128
Figure 3-3 Evolution of prior error covariance matrix (B) for six state variables in SAC-SMA model.	134
Figure 3-4 Streamflow prediction using the EPFM and HEAVEN for the Leaf River Basin over one year (left panels)..	137
Figure 3-5 The comparison of accuracy, distribution spread, and computational demand for four assimilation strategies in the real case study over four years.	139
Figure 3-6 The prior and posterior distributions obtained by the EPFM and HEAVEN for four days (183, 213, 225 and 337) where each represents the initial time of an assimilation window.	141
Figure 3-7 The prior and posterior distributions obtained by the EPFM and HEAVEN for the next six days in each assimilation window corresponding to the initial conditions reported in Figure 3-6.	144
Figure 3-8 Taylor diagrams displaying the effectiveness of the two assimilation methods (i.e., EPFM and HEAVEN) for eight real case studies over one year of analysis.....	145
Figure 4-1 Study area located in Southeast Texas along with watershed boundary, WRF- Hydro geogrid domain, lakes, stream networks, major rivers, and USGS streamflow gauges.	164
Figure 4-2. SMAP soil moisture data over the Southwest US.....	166
Figure 4-3 Schematic of the proposed framework.....	175

Figure 4-4 Model calibration, validation and data assimilation configurations used in this study.....	181
Figure 4-5 Model calibration at the USGS 8071280 gauge based on 100 DDS iterations.....	183
Figure 4-6 Evolution of model parameters during the model calibration process over 100 DDS iterations.....	185
Figure 4-7 WRF-Hydro simulated streamflow versus USGS observed streamflow at four gauges within the watershed.	187
Figure 4-8 WRF-Hydro simulated streamflow with 95-percentile confidence interval versus USGS observed streamflow (01/01/2017 to 12/31/2017).....	190
Figure 4-9. The deterministic and probabilistic performance measures of assimilation configurations at four USGS gauges.....	192
Figure 4-10. Upper panel: SMAP soil moisture at 36 km (right) and 1 km (left) spatial resolutions.....	194
Figure 4-11. Univariate assimilation of SMAP soil moisture at 9 km (left) and 36 km (right) spatial resolutions into the WRF-Hydro model.	195

INTRODUCTION

Over the last decade, the development of remote sensing technologies has provided the possibility that the soil moisture data is more accessible than before. Nowadays, remotely sensed satellite products have become the only feasible way to reach an unprecedented amount of soil moisture data at both spatial and temporal scales, which is logistically and economically unachievable from conventional observation networks (Kerr, 2007; Peng et al., 2016). The National Aeronautics and Space Administration (NASA) Soil Moisture Active Passive (SMAP) satellite mission was launched in January 2015 with the aim of acquiring high-resolution soil moisture and freeze-thaw states at a global scale with two to three days revisit frequency. SMAP satellite mission was developed to provide a global map of high-resolution soil moisture by combining L-band (passive) brightness temperatures and high resolution L-band (active) radar backscatter data (Entekhabi et al., 2010). The SMAP provides soil moisture posted on a 36 km Earth-fixed grid using brightness temperature from both ascending (6:00 pm) and descending (6:00 am) passes. After an irrecoverable failure of the SMAP radar in July 2015, the SMAP radiometer became the only operational level 2 (L2_SM_P) soil moisture product providing the coarse-scale (36 km) soil moisture observations. The assessment of SMAP radiometer observations has demonstrated the effectiveness of this procedure against Radio Frequency Interference (RFI) signals (Chan et al., 2016). Over densely vegetated areas where the Soil Moisture and Ocean Salinity (SMOS) satellite is more susceptible to RFI contamination, the SMAP is more capable of retrieving soil moisture. On January 2017, NASA released a product

named the enhanced SMAP radiometer. In this data set, the standard SMAP data gridded at 36 km are interpolated into the global cylindrical EASE-Grid 2.0 projection with 9 km spacing using the Backus-Gilbert optimal interpolation algorithm. Recently, NASA generated a new product, named as the SMAP/Sentinel-1 L2 Radiometer/Radar soil moisture data. In this data set, SMAP L-band brightness temperatures and Copernicus Sentinel-1 C-band backscatter coefficients are used to generate soil moisture data, which is then resampled to an Earth-fixed, cylindrical 3 km Equal-Area Scalable Earth Grid, Version 2.0 (Das et al., 2017). Despite such developments, some land surface applications such as water management, agricultural production and drought monitoring still require soil moisture data at finer resolutions, from a kilometer to sub kilometer scale. Over the last few years, a large number of approaches have been proposed to downscale the coarse resolution of different satellite soil moisture products, such as SMOS (Djamai et al., 2016; Lievens et al., 2016; Molero et al., 2016; Piles et al., 2014), Advanced Microwave Scanning Radiometer - Earth Observing System (AMSR-E) (Choi and Hur, 2012; Sahoo et al., 2013; Song et al., 2014) and SMAP (Knipper et al., 2017; Colliander et al., 2017). In article 1, we developed a new framework based on an ensemble learning method while using atmospheric and geophysical information derived from remote-sensing and ground-based observations to downscale the level 3 daily composite version (L3_SM_P) of SMAP radiometer soil moisture over the Continental United States at 1-km spatial resolution (Abbaszadeh et al., 2018). The results of this study showed that the rescaled soil moisture products using our approach are more accurate compared to that of other conventional downscaling approaches.

Satellite soil moisture data set, even at finer space-time resolutions, suffers from spatial heterogeneity and bias issues (Draper et al., 2012; Yuan et al., 2015). One possible approach to

overcome these difficulties is to improve the accuracy and reliability of soil moisture observations through data assimilation techniques (Mohanty et al., 2017). In addition to this, many researchers (e.g., Lee et al., 2011; Wanders et al., 2014) have concluded that the benefits of satellite soil moisture observations are not fully taken into account unless they are assimilated simultaneously along with streamflow observations. Data assimilation has been recognized as one of the effective methods to improve hydrologic and atmospheric model predictions. The most widely used data assimilation technique in the hydrologic community is the ensemble Kalman filter (EnKF) (Reichle et al., 2002; Crow and Wood, 2003; De Lannoy et al., 2007). The EnKF has been extensively used for assimilation of satellite soil moisture observations during the last decade (Reichle et al., 2008; Hain et al., 2012; Ines et al., 2013). Given the inherent limitations of the EnKF including the Gaussian assumption of errors, linear updating rule and violation of water balance, a more advanced DA approach by means of Particle Filter (PF) was proposed to enhance the assimilation of prognostic variables, such as streamflow and soil moisture, which has garnered attention of Earth system scientists (Moradkhani et al., 2005; Matgen et al., 2010; Moradkhani et al., 2012; Plaza et al., 2012; Yan et al., 2015). The PF approach can relax the Gaussian assumption of error distributions by characterizing multimodal or skewed distribution in state variables and parameters. Therefore, it can provide a thorough representation of the posterior distribution for a given nonlinear and non-Gaussian system. PF has been widely used for assimilation of satellite soil moisture and streamflow observations (Noh et al., 2011; Matgen et al., 2011; Yan et al., 2015; Yan and Moradkhani, 2016; Dong et al., 2017).

While successfully used in numerous applications, PFs may be subject to particle degeneracy and sample impoverishment. Particle degeneracy occurs when a few of the particles

close to the measurement receive significant weights while others are discarded (ensemble collapse to a single point). Although resampling alleviates the degeneracy problem, it may diminish the diversity of particles and increase the number of repeated particles (known as sample impoverishment). To mitigate these issues, researchers have combined PF with several procedures, such as the Markov chain Monte Carlo (MCMC) algorithm (Andrieu et al., 2010; Moradkhani et al., 2012) and metaheuristic techniques (Han et al., 2011; Kwok et al., 2005; Yin et al., 2015). In order to take the advantages of MCMC and metaheuristic algorithms simultaneously, in article 2, we combined these two inside the particle filtering approach to further enhance the assimilation performance (Abbaszadeh et al., 2018). The results of our study confirmed that the developed Evolutionary Particle Filter and Markov Chain Monte Carlo (EPFM) improves both the state and parameter estimation more effectively and reliably as compared with its simpler versions, Particle Filter with Genetic Algorithm (PF-GA, Yin et al., 2015) and Particle Filter with MCMC (PF-MCMC, Moradkhani et al., 2012).

In contrast to the PF that works in a sequential manner, the four-dimensional variational data assimilation (4DVAR) approach operates in a batch-processing manner by using all the observations simultaneously within the assimilation interval. Unlike Bayesian data assimilation, the variational data assimilation most often does not provide estimates of the predictive uncertainty of estimated model states and parameters, which considerably limits the value of the estimated variables in decision-making processes (Abdolghafoorian & Farhadi, 2016; Reichle et al., 2001). Given these concerns, integrating Bayesian and variational assimilation schemes seems a logical step to constrain the deficiencies of each method while benefiting from the strength of each (Hernández & Liang, 2018; Morzfeld et al., 2012; Slivinski et al., 2015; van Leeuwen, 2015; Zhu et al., 2016). For this end, in article 3, we developed a novel approach to

couple a deterministic 4DVAR assimilation method with the PF ensemble data assimilation system, to produce a robust approach for dual-state-parameter estimation (Abbaszadeh et al., 2019). In our proposed method, the Hybrid Ensemble and Variational Data Assimilation framework for Environmental systems (HEAVEN), we characterized the model structural uncertainty in addition to model parameter and input uncertainties.

Streamflow is the main component of the hydrological cycle generated through a combination of land-surface and sub-surfaces processes that incorporates the information of hydrological states and fluxes. Streamflow observations measured by in-situ sensors most often are assimilated into hydrological models to update the model states and/or parameters and hence to improve the estimate of predictive uncertainty (Abbaszadeh et al., 2018; Clark et al., 2008; Moradkhani et al., 2005; Moradkhani et al., 2012). While soil moisture and streamflow are often independently assimilated into the hydrological models, many other studies have shown that their joint assimilation is a more effective approach in improving model predictions and quantifying associated uncertainties (Lee et al., 2011; López López et al., 2017; Yan & Moradkhani, 2016). However, such experiments typically are based on lumped or semi-distributed hydrological models due to their simplicity and low computational requirements. Multivariate (joint) data assimilation refers to the simultaneous assimilation of multiple observation data for different model state variables into a hydrological model. It is therefore of particular interest to examine the benefit of assimilating independently and jointly high-resolution satellite soil moisture data and streamflow observations into a hyper-resolution hydrological model and to understand the extent to which these observations can contribute to improving the model predictions, particularly during the extreme events. As a prototype study, in

article 4, we examined these conjectures by applying our approach over a region in the Southeast Texas where heavy rainfall from Hurricane Harvey caused deadly flooding.

References

- Abbaszadeh, P., Moradkhani, H., & Yan, H. (2018). Enhancing hydrologic data assimilation by evolutionary Particle Filter and Markov Chain Monte Carlo. *Advances in Water Resources*, 111, 192–204. <https://doi.org/10.1016/j.advwatres.2017.11.011>
- Abbaszadeh, P., Moradkhani, H., Zhan, X. (2018). Downscaling SMAP radiometer soil moisture over the CONUS using an ensemble learning method. *Water Resour. Res.* <https://doi.org/10.1029/2018WR023354>
- Abbaszadeh, P., Moradkhani, H., & Daescu, D. N. (2019). The Quest for Model Uncertainty Quantification: A Hybrid Ensemble and Variational Data Assimilation Framework. *Water Resources Research*, 55. <https://doi.org/10.1029/2018WR023629>
- Abdolghafoorian, A., and Farhadi, L. (2016). Uncertainty Quantification in Land Surface Hydrologic Modeling: Toward an Integrated Variational Data Assimilation Framework. *IEEE Journal of Selected Topics in Applied Earth Observations and Remote Sensing*, 9(6), 2628–2637. <https://doi.org/10.1109/JSTARS.2016.2553444>
- Andrieu, C., Doucet, A., Holenstein, R., 2010. Particle Markov chain Monte Carlo methods. *J. R. Stat. Soc. Ser. B. Stat. Methodol.* 72, 269–342. <http://dx.doi.org/10.1111/j.1467-9868.2009.00736.x>.
- Chan, S.K., Bindlish, R., O'Neill, P.E., Njoku, E., Jackson, T., Colliander, A., Chen, F., Burgin, M., Dunbar, S., Piepmeier, J., Yueh, S., Entekhabi, D., Cosh, M.H., Caldwell, T., Walker, J., Wu, X., Berg, A., Rowlandson, T., Pacheco, A., McNairn, H., Thibeault, M., Martinez-Fernandez, J., Gonzalez-Zamora, A., Seyfried, M., Bosch, D., Starks, P., Goodrich, D., Prueger, J., Palecki, M., Small, E.E., Zreda, M., Calvet, J.C., Crow, W.T., Kerr, Y., 2016. Assessment of the SMAP Passive Soil Moisture Product. *IEEE Trans. Geosci. Remote Sens.* 54, 4994–5007. <https://doi.org/10.1109/TGRS.2016.2561938>
- Choi, M., & Hur, Y. (2012). A microwave-optical/infrared disaggregation for improving spatial representation of soil moisture using AMSR-E and MODIS products. *Remote Sensing of Environment*, 124, 259–269. <https://doi.org/10.1016/j.rse.2012.05.009>
- Colliander, A., Jackson, T. J., Bindlish, R., Chan, S., Das, N., Kim, S. B., ... Yueh, S. (2017). Validation of SMAP surface soil moisture products with core validation sites. *Remote Sensing of Environment*, 191, 215–231. <https://doi.org/10.1016/j.rse.2017.01.021>
- Clark, M. P., Rupp, D. E., Woods, R. A., Zheng, X., Ibbitt, R. P., Slater, A. G., ... Uddstrom, M. J. (2008). Hydrological data assimilation with the ensemble Kalman filter: Use of

- streamflow observations to update states in a distributed hydrological model. *Advances in Water Resources*, 31(10), 1309–1324. <https://doi.org/10.1016/j.advwatres.2008.06.005>
- Colliander, A., Member, S., Fisher, J. B., Halverson, G., Merlin, O., Misra, S., ... Passive, A. (2017). Spatial Downscaling of SMAP Soil Moisture Using MODIS Land Surface Temperature and NDVI During SMAPVEX15. *IEEE Geoscience and Remote Sensing Letters*, 14(11), 1–5.
- Das, N., D. Entekhabi, S. Kim, S. Yueh, R. S. Dunbar, and A. Colliander. 2017. SMAP/Sentinel-1 L2 Radiometer/Radar 30-Second Scene 3 km EASE-Grid Soil Moisture, Version 1. [Indicate subset used]. Boulder, Colorado USA. NASA National Snow and Ice Data Center Distributed Active Archive Center. doi: <http://dx.doi.org/10.5067/9UWR1WTHW1WN>.
- Djamai, N., Magagi, R., Goïta, K., Merlin, O., Kerr, Y., & Roy, A. (2016). A combination of DISPATCH downscaling algorithm with CLASS land surface scheme for soil moisture estimation at fine scale during cloudy days. *Remote Sensing of Environment*, 184, 1–14. <https://doi.org/10.1016/j.rse.2016.06.010>
- Dong, J., Steele-Dunne, S. C., Judge, J., & Van De Giesen, N. (2015). A particle batch smoother for soil moisture estimation using soil temperature observations. *Advances in Water Resources*, 83, 111–122. <https://doi.org/10.1016/j.advwatres.2015.05.017>
- Draper, C. S., Reichle, R. H., De Lannoy, G. J. M., & Liu, Q. (2012). Assimilation of passive and active microwave soil moisture retrievals. *Geophysical Research Letters*, 39(4), 1–5. <https://doi.org/10.1029/2011GL050655>
- Entekhabi, D., Njoku, E. G., O'Neill, P. E., Kellogg, K. H., Crow, W. T., Edelstein, W. N., ... Van Zyl, J. (2010). The soil moisture active passive (SMAP) mission. *Proceedings of the IEEE*, 98(5), 704–716. <https://doi.org/10.1109/JPROC.2010.2043918>
- Han, H., Ding, Y.S., Hao, K.R., Liang, X., 2011. An evolutionary particle filter with the immune genetic algorithm for intelligent video target tracking. *Comput. Math. Appl.* 62, 2685–2695. <http://dx.doi.org/10.1016/j.camwa.2011.06.050>.
- Hain, C. R., Crow, W. T., Anderson, M. C., & Mecikalski, J. R. (2012). An ensemble Kalman filter dual assimilation of thermal infrared and microwave satellite observations of soil moisture into the Noah land surface model. *Water Resources Research*, 48(11). <https://doi.org/10.1029/2011WR011268>
- Hernández, F., and Liang, X. (2017). Hybridizing Bayesian and variational data assimilation for robust high-resolution hydrologic forecasting. *Hydrology and Earth System Sciences Discussions*, (August), 1–33. <https://doi.org/10.5194/hess-2017-431>
- Ines, A. V. M., Das, N. N., Hansen, J. W., & Njoku, E. G. (2013). Assimilation of remotely sensed soil moisture and vegetation with a crop simulation model for maize yield prediction. *Remote Sensing of Environment*, 138, 149–164. <https://doi.org/10.1016/j.rse.2013.07.018>

- Kerr, Y. H. (2007). Soil moisture from space: Where are we? *Hydrogeology Journal*, 15(1), 117–120. <https://doi.org/10.1007/s10040-006-0095-3>
- Knipper, K. R., Hogue, T. S., Franz, K. J., & Scott, R. L. (2017). Downscaling SMAP and SMOS soil moisture with moderate-resolution imaging spectroradiometer visible and infrared products over southern Arizona. *Journal of Applied Remote Sensing*, 11(2). <https://doi.org/10.1117/1.JRS.11.026021>
- Kwok, N., Fang, G., Zhou, W., 2005. Evolutionary particle filter: Resampling from the genetic algorithm perspective, in *Proc. Int. Conf. Intell. Robots Syst.*, Shaw Conference Centre, Edmonton, Alberta, Canada, Aug. 2-6, 2935-2940. DOI: 10.1109/IROS.2005.1545119.
- Lee, H., Seo, D. J., & Koren, V. (2011). Assimilation of streamflow and in situ soil moisture data into operational distributed hydrologic models: Effects of uncertainties in the data and initial model soil moisture states. *Advances in Water Resources*, 34(12), 1597–1615. <https://doi.org/10.1016/j.advwatres.2011.08.012>
- Lievens, H., De Lannoy, G. J. M., Al Bitar, A., Drusch, M., Dumedah, G., Hendricks Franssen, H. J., ... Pauwels, V. R. N. (2016). Assimilation of SMOS soil moisture and brightness temperature products into a land surface model. *Remote Sensing of Environment*, 180, 292–304. <https://doi.org/10.1016/j.rse.2015.10.033>
- López López, P., Sutanudjaja, E. H., Schellekens, J., Sterk, G., & Bierkens, M. F. P. (2017). Calibration of a large-scale hydrological model using satellite-based soil moisture and evapotranspiration products. *Hydrology and Earth System Sciences*, 21(6), 3125–3144. <https://doi.org/10.5194/hess-21-3125-2017>
- Matgen, P., Montanari, M., Hostache, R., Pfister, L., Hoffmann, L., Plaza, D., ... Savenije, H. H. G. (2010). Towards the sequential assimilation of SAR-derived water stages into hydraulic models using the Particle Filter: Proof of concept. *Hydrology and Earth System Sciences*, 14(9), 1773–1785. <https://doi.org/10.5194/hess-14-1773-2010>
- Morzfeld, M., X. Tu, E. Atkins, and A.J. Chorin. (2012). A random map implementation of implicit filters. *Journal of Computational Physics*, 231(4), 2049-2066. <http://dx.doi.org/10.1016/j.jcp.2011.11.022>.
- Mohanty, B. P., Cosh, M. H., Lakshmi, V., & Montzka, C. (2017). Soil Moisture Remote Sensing: State-of-the-Science. *Vadose Zone Journal*, 16(1), 0. <https://doi.org/10.2136/vzj2016.10.0105>
- Moradkhani, H., Dechant, C. M., & Sorooshian, S. (2012). Evolution of ensemble data assimilation for uncertainty quantification using the particle filter-Markov chain Monte Carlo method. *Water Resources Research*, 48(12). <https://doi.org/10.1029/2012WR012144>
- Moradkhani, H., Hsu, K.-L., Gupta, H., & Sorooshian, S. (2005). Uncertainty assessment of hydrologic model states and parameters: Sequential data assimilation using the particle filter. *Water Resources Research*, 41(5), 1–17. <https://doi.org/10.1029/2004WR003604>

- Noh, S. J., Tachikawa, Y., Shiiba, M., & Kim, S. (2011). Applying sequential Monte Carlo methods into a distributed hydrologic model: Lagged particle filtering approach with regularization. *Hydrology and Earth System Sciences*, 15(10), 3237–3251. <https://doi.org/10.5194/hess-15-3237-2011>
- Peng, J., Loew, A., Zhang, S., Wang, J., & Niesel, J. (2016). Spatial Downscaling of Satellite Soil Moisture Data Using a Vegetation Temperature Condition Index. *IEEE Transactions on Geoscience and Remote Sensing*, 54(1), 558–566. <https://doi.org/10.1109/TGRS.2015.2462074>
- Piles, M., Sánchez, N., Vall-Llossera, M., Camps, A., Martínez-Fernandez, J., Martínez, J., & Gonzalez-Gambau, V. (2014). A downscaling approach for SMOS land observations: Evaluation of high-resolution soil moisture maps over the Iberian peninsula. *IEEE Journal of Selected Topics in Applied Earth Observations and Remote Sensing*, 7(9), 3845–3857. <https://doi.org/10.1109/JSTARS.2014.2325398>
- Plaza, D. A., De Keyser, R., De Lannoy, G. J. M., Giustarini, L., Matgen, P., & Pauwels, V. R. N. (2012). The importance of parameter resampling for soil moisture data assimilation into hydrologic models using the particle filter. *Hydrology and Earth System Sciences*, 16(2), 375–390. <https://doi.org/10.5194/hess-16-375-2012>
- Reichle, R., McLaughlin, D. B., and Entekhabi, D. (2001). Variational data assimilation of microwave radiobrightness observations for land surface hydrologic applications. *IEEE Transactions on Geoscience and Remote Sensing*, 39(8), 1708–1718.
- Reichle, R., McLaughlin, D. B., & Entekhabi, D. (2002). Hydrologic data assimilation with the ensemble Kalman filter. *Monthly Weather Review*, 130(1), 103–114. [https://doi.org/10.1175/1520-0493\(2002\)130<0103:HDAWTE>2.0.CO;2](https://doi.org/10.1175/1520-0493(2002)130<0103:HDAWTE>2.0.CO;2)
- Sahoo, A. K., De Lannoy, G. J. M., Reichle, R. H., & Houser, P. R. (2013). Assimilation and downscaling of satellite observed soil moisture over the Little River Experimental Watershed in Georgia, USA. *Advances in Water Resources*, 52, 19–33. <https://doi.org/10.1016/j.advwatres.2012.08.007>
- Song, C., Jia, L., & Menenti, M. (2014). Retrieving high-resolution surface soil moisture by downscaling AMSR-E brightness temperature using MODIS LST and NDVI data. *IEEE Journal of Selected Topics in Applied Earth Observations and Remote Sensing*, 7(3), 935–942. <https://doi.org/10.1109/JSTARS.2013.2272053>
- Slivinski, L., Spiller, E., Apte, A., and Sandstede, B. (2015). A hybrid particle–ensemble Kalman filter for Lagrangian data assimilation. *Monthly Weather Review*, 143(1), 195–211.
- Van Leeuwen, P. J. (2015). Nonlinear data assimilation for high-dimensional systems. in *Nonlinear Data Assimilation*, P. J. van Leeuwen, C. Yuan, and S. Reich, Eds. Basel, Switzerland: Springer, ch. 1, pp. 1–73.
- Wanders, N., Karssenber, D., De Roo, A., De Jong, S. M., & Bierkens, M. F. P. (2014). The suitability of remotely sensed soil moisture for improving operational flood forecasting.

Hydrology and Earth System Sciences, 18(6), 2343–2357. <https://doi.org/10.5194/hess-18-2343-2014>

Yin, S., Zhu, X., 2015. Intelligent particle filter and its application to fault detection of nonlinear systems. *IEEE Trans. Ind. Electron.* 62 (6), 3852-3861. DOI:10.1109/TIE.2015.2399396.

Yan, H., DeChant, C. M., & Moradkhani, H. (2015). Improving soil moisture profile prediction with the particle filter-Markov chain Monte Carlo method. *IEEE Transactions on Geoscience and Remote Sensing*, 53(11), 6134–6147. <https://doi.org/10.1109/TGRS.2015.2432067>

Yan, H., & Moradkhani, H. (2016). Combined assimilation of streamflow and satellite soil moisture with the particle filter and geostatistical modeling. *Advances in Water Resources*, 94, 364–378. <https://doi.org/10.1016/j.advwatres.2016.06.002>

Yuan, X., Ma, Z., Pan, M., & Shi, C. (2015). Microwave remote sensing of flash droughts during crop growing seasons, 17, 8196. <https://doi.org/10.1002/2015GL064125>

CHAPTER 1 DOWNSCALING SMAP RADIOMETER SOIL MOISTURE OVER THE CONUS USING AN ENSEMBLE LEARNING METHOD¹

Abstract

Soil moisture plays a critical role in improving the weather and climate forecast, and understanding terrestrial ecosystem processes. It is a key hydrologic variable in agricultural drought monitoring, flood forecasting, and irrigation management as well. Satellite retrievals can provide unprecedented soil moisture information at the global scale, however, the products are generally provided at coarse resolutions (25-50 km²). This often hampers their use in regional or local studies. The National Aeronautics and Space Administration (NASA) Soil Moisture Active Passive (SMAP) satellite mission was launched in January 2015 aiming to acquire soil moisture and freeze-thaw states over the globe with two to three days revisit frequency. This work presents a new framework based on an ensemble learning method while using atmospheric and geophysical information derived from remote-sensing and ground-based observations to downscale the level 3 daily composite version (L3_SM_P) of SMAP radiometer soil moisture over the Continental U.S. (CONUS) at 1km spatial resolution. In the proposed method, a suite of remotely sensed and in-situ data sets are used, including soil texture and topography data among other information. The downscaled product was validated against in-situ soil moisture measurements collected from two high density validation sites and three hundred sparse soil moisture networks throughout the CONUS. On average, the unbiased Root Mean Square Error

¹ Abbaszadeh, P., Moradkhani, H., & Zhan, X. (2018). Downscaling SMAP radiometer soil moisture over the CONUS using an ensemble learning method. *Water Resources Research*, 55, 324–344. <https://doi.org/10.1029/2018wr023354>

(ubRMSE) between the downscaled SMAP soil moisture data and in-situ soil moisture observations adequately met the SMAP soil moisture retrieval accuracy requirement of 0.04 m³/m³. In addition, other statistical measures, i.e., Pearson correlation coefficient and bias, showed satisfactory results.

Keywords: Soil moisture downscaling, SMAP, ensemble learning, CONUS

Introduction

Soil moisture has an important role in the global water and energy balance, affecting hydrological and atmospheric cycles, drought conditions, irrigation management, and so many other processes. Over the last decade, the development of remote sensing technologies has provided the possibility that this environmental variable is more accessible than before.

Nowadays, remotely sensed satellite products have become the only feasible way to reach an unprecedented amount of soil moisture data on both spatial and temporal scales, which is practically unachievable from in-situ observation networks (Kerr, 2007; Njoku & Entekhabi, 1996; Peng et al., 2016).

In the last couple of decades, although prodigious efforts have gone to retrieving soil moisture through various active and passive microwave remote sensing satellites, inevitably they have some limitations. For example, active sensors like the ERS provide observations that are significantly affected by the scattering produced by surface roughness (Verhoest et al., 2008) and vegetation structure (Wagner et al., 2013). Unlike the active sensors, passive microwave radiometers are much less sensitive to scattering, but their products are at coarse resolutions or their sensing depths are shallow (Molero et al., 2016). For instance, the Advanced Microwave Scanning Radiometer-Earth Observing System (AMSR-E) with C-band of 6.9 GHz has footprint

of $74 \times 43 \text{ km}^2$ that provides soil moisture from the 0-1 or 0-2 cm topsoil layer, while with smaller footprints its X-band penetration depth is less than 5 mm (Su et al., 2013). In contrast, through L-band radiometer the Soil Moisture and Ocean Salinity (SMOS) can estimate soil moisture at around 5 cm depth with a repeat cycle of ~ 3 days. This satellite has a coarse spatial resolution ($35\text{--}55 \text{ km}^2$), which makes it inappropriate for local and regional scale applications (Djamai et al., 2016). Recent studies have shown that both the passive and active sensors have to come into play in order to access reliable remotely sensed soil moisture data (Owe et al., 2008; Petropoulos et al., 2015). Launched in 2015, the National Aeronautics and Space Administration (NASA) Soil Moisture Active Passive (SMAP) satellite provides high-resolution soil moisture on a global scale by combining L-band (passive) brightness temperatures and high resolution L-band (active) radar backscatter data (Entekhabi et al., 2010). Unfortunately, due to a malfunction of the SMAP radar instrument on July 2015, since then the radiometer instrument has been the only operational instrument of SMAP satellite and been providing the level 2 soil moisture product (L2_SM_P) (Chan et al., 2016). The assessment of SMAP radiometer observations corroborates the effectiveness of this procedure against Radio Frequency Interference (RFI) signals. Over densely vegetated areas where SMOS is more prone to RFI contamination, SMAP is more capable of retrieving soil moisture (Chan et al., 2016). Using brightness temperature, SMAP satellite provides soil moisture on the 36 km grid cell from both ascending (6:00 pm) and descending (6:00 am) passes.

Although the SMAP soil moisture observation has a decent spatial resolution for global and continental scale applications, it cannot be used directly for regional or local studies, such as agriculture and drought monitoring, unless a fine resolution of this product is available (from 1 to 10 km^2 , Entekhabi et al., 2010). To circumvent this problem, on January 2017, NASA released a

new product named the enhanced SMAP radiometer. In this data set, the standard SMAP data gridded at 36 km are interpolated into 9 km grid spacing using the Backus-Gilbert optimal interpolation algorithm. Despite such progress, some land surface applications such as water resources management, agricultural and crop production still require soil moisture at finer resolutions, from a kilometer to sub kilometer scale.

Over the last few years, a large number of approaches have been developed to downscale the coarse resolution of different satellite soil moisture products, such as SMOS (Djamai et al., 2015, 2016; Lievens et al., 2016; Merlin et al., 2008; Molero et al., 2016; Panciera et al., 2008; Piles et al., 2016; Piles et al., 2014; Piles et al., 2011) and AMSR-E (Choi & Hur, 2012; Sahoo et al., 2013; Song et al., 2014; Zhao & Li, 2013). Among these attempts, Machine Learning (ML) techniques have recently received remarkable attention owing to their superb intelligence capability in downscaling satellite products (Coulibaly et al., 2005; Goyal et al., 2012; Hashmi et al., 2011; Rodriguez-Fernandez et al., 2015; Im et al., 2016; Kaheil et al., 2008; Raje & Mujumdar, 2011; Srivastava et al., 2013; Valverde et al., 2014; Zerenner et al., 2016; Alemohammad et al., 2018; Kolassa et al., 2018). ML is a class of data analysis methods that allows computers to find the hidden pattern of a phenomenon through learning from data in an intelligent way.

More investigations have shown that Random Forest (RF) algorithm in comparison with other ML approaches is more suitable for downscaling the satellite products (He et al., 2016; Hutengs & Vohland, 2016; Im et al., 2016; Jing et al., 2016; Ke et al., 2016; Park et al., 2017; Pelletier et al., 2016). This is due to the fact that RF model is much more flexible through randomization, and adopts an ensemble approach. In this paper, we use the RF model in order to downscale the standard SMAP soil moisture radiometer product gridded at 36 km to 1 km

resolution over the Continental U.S. (CONUS) for the year 2015 (April to December). In this study, we develop multiple RF models based on soil properties of topsoil (0-5 cm) and use them collectively to better estimate the soil moisture not only at a finer spatial resolution, but also over a very large region with different climate and land surface characteristics.

The rest of this paper is organized as follows. Section 2 summarizes both satellite and ground-based observations used in this research and describes concisely the study area. Section 3 elaborates on the developed soil moisture downscaling approach. The results and discussions are included in Section 4. The conclusions of this paper and recommendations for future works are in the final section of the paper.

Remotely Sensed and Ground-Based Observations

SMAP Radiometer Soil Moisture Data

SMAP satellite with a sensing depth of 5 cm provides soil moisture on a global scale. Over the CONUS, SMAP was calibrated and validated against in-situ measurements collected from several Core Validation Sites (CVSs) with the aim of reducing the unbiased Root Mean Square Error (ubRMSE) below $0.04 \text{ m}^3/\text{m}^3$ (Colliander et al., 2017; Jackson et al., 2016). In this study, we propose a soil moisture downscaling framework to downscale the SMAP descending overpass (L3_SM_P) over the CONUS. The L3_SM_P is a daily composite of L2_SM_P product. This soil moisture data can be assessed from the NASA Distributed Active Archive Center (DAAC) at the National Snow and Ice Data Center (NSIDC). We use the soil moisture product entitled “SMAP L3 Radiometer Global Daily 36 km EASE-Grid Soil Moisture, Version 3 (SPL3SMP)”, which is available at <https://nsidc.org/data/smap/smap-data.html>.

MODIS Land Surface Temperature (LST) and NDVI

Over the past few years, vegetation index and surface temperature have been widely used for downscaling satellite soil moisture data (Fang & Lakshmi, 2014; Im et al., 2016; Merlin et al., 2008, 2015; Peng et al., 2015; Piles et al., 2011; Song et al., 2014; Srivastava et al., 2013). These land surface parameters are available from Moderate Resolution Imaging Spectroradiometer (MODIS) instrument. The common use of this geostationary satellite is due to its high temporal resolution that provides more cloud-free observations.

The MODIS is a key instrument of the NASA Earth Observing System (EOS) Terra and Aqua platforms for monitoring the seasonality of global terrestrial vegetation. MODIS is a multi-spectral sensor. Its spectral bands range from visible, near infrared, to thermal infrared, making it ubiquitous in many land, ocean, and atmospheric research studies. The equatorial crossing time for Terra and Aqua satellites are 10:30 am (descending) and 1:30 pm (ascending), respectively. In this study, in order to be consistent with the SMAP data, the daytime overpass for Terra in the descending node is used to collect MODIS LST and NDVI data. The MODIS products are the version-5 MODIS-Terra 1 km resolution daily LST data and the version-5 MODIS-Terra 1 km resolution 16-day NDVI data (data sets MOD11A1 and MOD13A2, respectively). MOD11A1 is comprised of daytime and nighttime land surface temperatures. MOD13A2 is atmospherically corrected data set. The MODIS products are retrieved from the NASA Land Processes Distributed Active Archive Center (LPDAAC) at the USGS Earth Resources Observation and Science (EROS) Center (<http://e4ftl01.cr.usgs.gov/MOLT/>).

National Weather Service (NWS) Precipitation Data

The most obvious way the atmosphere affects soil moisture is through precipitation (Crow et al., 2012). The soil moisture spatial and temporal variations are strongly correlated with the precipitation patterns. The teleconnection of precipitation regimes on the soil moisture variability has been corroborated by many studies at regional and global scales (Jones & Brunzell, 2009; Seneviratne et al., 2010). In this study, NWS precipitation data along with other atmospheric and geophysical information are used to investigate the usefulness of these climate variables in estimating soil moisture at finer resolution.

The NWS operations at the River Forecast Centers (RFCs) provide quality controlled and multi-sensor precipitation data with a spatial resolution of roughly 4 km² over the CONUS, Puerto Rico, and Alaska. The data is presented at 24 hourly accumulation that is the end of the “hydrologic day”, a standard for river modeling. This product is primarily used to simulate streamflow across the CONUS (<http://water.weather.gov/precip/>).

CONUS-SOIL Data

Soil texture is defined as the proportion of small (clay), medium (silt), and large (sand) particles in a specific soil mass. This property of soil significantly affects the soil moisture profile, since it influences water infiltration rate, permeability, and water storage. Soil texture heterogeneity dominates the soil moisture spatial structure (Mattikalli et al., 1998). Many studies corroborated the utilization of soil texture data as an important source of information for downscaling soil moisture maps (Chakrabarti et al., 2016; Mascaro et al., 2011; Ranney et al., 2015; Reichle et al., 2001; Shin & Mohanty, 2013).

In this study, we use soil texture information from the CONUS-SOIL data set. CONUS-SOIL data set is specifically used for regional climate and hydrologic modeling over the CONUS (Miller & White, 1998). This product is available at 1 km, which generates a spatial representation of soil texture and other properties of soil surface for a wide range of land surface models. CONUS-SOIL discretizes each soil property in 11 depth layers (up to 250 cm) where each layer is classified by 12 standard soil texture classes. Since SMAP provides soil moisture at the top 5 cm of the soil column, we only use the first layer of soil with depth of 5 cm to extract the soil texture information. Figure 1-S1 (in supplementary file) illustrates the soil texture of top 5 cm soil layer over the CONUS. CONUS-SOIL is available in both gridded and vector formats, and can be retrieved via <http://www.soilinfo.psu.edu/>.

GTOPO30 Topography Data

Topographic data such as slope, aspect, curvature and elevation significantly affect the distribution of soil moisture, specifically in the topsoil layer, at different scales (Crow et al., 2012). Elevation is known as one of the most effective topographic features in many studies to downscale coarse-scale soil moisture maps (Busch et al., 2012; Coleman & Niemann, 2013; Mascaro et al., 2011; Pellenq et al., 2003; Ranney et al., 2015; Wilson et al., 2005). Hence, we use this variable in our proposed approach to downscale the SMAP soil moisture data.

GTOPO30 is a global Digital Elevation Model (DEM) developed by USGS EROS Data Center in late 1996. This data set has an approximately 1 km spatial resolution. Figure 1-S2 (in supplementary file) shows the DEM with colors representing the variation of elevation from 0 to 4587 meters above sea level. More information along with the data set can be found at <https://lta.cr.usgs.gov/GTOPO30>. In this study, we used this data set, although there are other

topography data products available, such as Shuttle Radar Topography Mission (SRTM) and National Elevation Dataset (NED), which alternatively could be used.

In-situ Soil Moisture Observations

The U.S. Climate Reference Network (USCRN) sensors provide the soil information, such as soil moisture and soil temperature, at five different depths (5, 10, 20, 50, and 100 cm). Figure 1-S2 (in supplementary file) demonstrates the USCRN stations located at 114 sites across the CONUS. The grid spacing of these sensors was determined so as to competently represent the US annual temperature and precipitation variance. The soil moisture and soil temperature for each station are obtained from three independent samples of soil located in a 5-meter radius around the main instrument tower. This leads not only to an accurate measurement of such quantities, but also yields a more realistic representation of soil properties in a specified location. The USCRN records the soil moisture profile at 5-minute intervals, and transmits them as hourly data for satellite calibration/validation purposes.

The Soil Climate Analysis Network (SCAN) sensors monitor soil moisture content at five different depths (5, 10, 20, 50, and 100 cm approximately), air temperature, relative humidity, and some other climate variables mainly over the agricultural areas. In this study, we use 186 SCAN sensors that have been in operation for the period of the study. The SCAN sensors measure the soil moisture values hourly to aid different applications such as drought assessment/monitoring and satellite soil moisture validation. Both USCRN and SCAN sensors report the soil moisture in the volumetric unit (m^3/m^3). Figure 1-S2 (in supplementary file) shows a map of SCAN soil moisture sensors located at 186 sites throughout the CONUS. USCRN instruments are scattered uniformly across the US, while SCAN stations are installed in

certain areas to accommodate specific research needs (Coopersmith et al., 2015). These two soil moisture networks have also been used for the validation of SMAP product (Jackson et al., 2016; Pan et al., 2016; Velpuri et al., 2015).

The Proposed Satellite Soil moisture Downscaling Approach

This section elaborates the developed methodology in two separate subsections. In Section 3.1, we present the theoretical basis of the proposed downscaling framework. Section 3.2 explains the ensemble learning algorithm used in Section 3.1.

Soil Moisture Downscaling Framework

To downscale SMAP radiometer soil moisture, we use those high-resolution data sets that are known to be strongly associated with the soil moisture spatial and dynamical heterogeneities. As discussed in the previous section, the covariates including NDVI, surface temperature, precipitation, elevation, and soil texture are available at the appropriate resolutions and expected to have reasonable explanatory power on the soil moisture profile at different scales. Atmospheric covariates (i.e., precipitation and surface temperature) are used to maintain the temporal dynamics of the downscaled soil moisture. Geophysical covariates (i.e., soil texture and elevation) are included to capture the spatial patterns and variability of the downscaled soil moisture. Auxiliary covariates, such as NDVI (as a measure of greenness), are also included to account for the influence of vegetation dynamics on the downscaled soil moisture spatial and temporal patterns.

In this study, we use RF as an ensemble learning approach to formulate the downscaling framework. The basis of this technique and its implementation will be explained in detail later in

Section 3.2. The main contribution of this research is to introduce a new way to incorporate the aforementioned atmospheric and geophysical variables into the RF model, leading to improved estimates of soil moisture at finer resolutions. The following steps summarize the structure of the proposed soil moisture downscaling scheme.

1) Classify the in-situ soil moisture stations (i.e., SCAN and USCRN) according to their soil texture properties. The results are shown in Table 1-1. As mentioned in Section 2.4, only the soil texture of the top 5 cm soil layer is used in this study in order to be consistent with the SMAP's sensing depth. Further investigation indicates that SCAN and USCRN in-situ stations are distributed proportionally to be representative of different climate conditions and soil texture classes over CONUS. The study area is mostly dominated by loamy (24.5%), silty loam (24.3%), and sandy loam (22.6%) surface soil layers. These land surfaces encompass more than 200 stations for the soil moisture monitoring. Sandy clay loam, silty and sandy clay soil types altogether cover less than 0.5% of the CONUS area. Only one station was found from the entire installed instruments throughout the CONUS that monitors the soil moisture for these rare land surfaces. As shown in Table 1-1, sandy loam with 22.6% surface soil coverage comprises 72 stations across CONUS, while, clay loam with 4.2% encompasses 12 instruments. The same analogy can be applied to those regions characterized by sandy and loamy sand soil textures. This implies a relatively fair distribution of soil moisture instruments over the CONUS. It should be noted that some of the land surface layers are not considered in the proposed downscaling model since they either do not incorporate soil moisture stations (e.g., silty and sandy clay) or they include non-soil layers (e.g., bedrock and water). Overall, these land surfaces cover a negligible (less than 0.5%) portion of the CONUS area.

Table 1-1 Distribution of in-situ soil moisture sensors over CONUS with respect to the soil texture of top 5 cm soil layer.

Soil Texture	Soil Texture Acronym	Soil Moisture Stations		Total Stations	% of CONUS
		USCRN	SCAN		
Bedrock	BR	-	-	-	0.001
Clay	C	3	6	9	3.384
Clay Loam	CL	4	8	12	4.210
Loam	L	28	41	69	24.552
Loamy Sand	LS	5	8	13	3.670
Other	O	1	0	1	1.545
Organic Materials	OM	2	0	2	1.176
Sand	S	13	11	42	6.977
Sandy Clay Loam	SCL	0	1	1	0.382
Silt	SI	0	0	0	0.004
Sandy Clay	SC	0	0	0	0
Silty Clay	SIC	1	1	2	1.506
Silty Clay Loam	SICL	7	14	21	4.395
Silty Loam	SIL	29	45	74	24.329
Sandy Loam	SL	21	51	72	22.603
Water	W	-	-	-	1.259
	Total	114	186	300	

As shown in Table 1-1, there are nine stations installed throughout the CONUS whose prevailing soil type is clay. It is important to know that these stations are not necessarily located on clay soil layer. Indeed, these stations are situated in the regions whose dominant soil type within a 1 km grid cell is clay.

2) Using those classified in-situ stations in the first step, we develop twelve distinct RF models. Each of these will downscale the SMAP radiometer soil moisture over a specific land surface layer. For example, for the clay soil type, nine stations provide a data collection with 2448 rows and 6 columns. 2448 is calculated by 9×272 , where 272 refers to the period of study (04/01/2015 until 12/31/2015). Six columns indicate five input covariates (including NDVI,

surface temperature, precipitation, elevation, and SMAP soil moisture data), and one output variable (in-situ soil moisture data). The dimension of this data set may decrease if it contains missing values. It is important to note that the input data are extracted from those points (latitudes and longitudes) where the in-situ stations are located. In this study, we randomly separate 80% of the data collection to train the model, and the rest of the data (20%) is used to verify the model. By trial and error, we found that this set of model calibration and verification data set (80/20), although not significant, results in better model performance as compared to other combinations. The random splitting of the data set ensures that the developed model is able to generalize well to unseen data and to avoid over-training. Thus, the developed RF model can be well suited for the soil moisture prediction at different geographical locations with different land-atmosphere characteristics.

3) The CONUS area is divided into different sub-regions based on the soil texture of the top 5 cm soil layer. The results in percentage of CONUS was reported in Table 1-1. The SMAP soil moisture over each of these regions is downscaled to 1 km spatial resolution using the corresponding calibrated RF model in Step 2.

Random Forest (RF)

The principle of the proposed downscaling approach is to build a function that maps the input covariates to the output variable using the following equations:

$$SM_d = f(C) + \varepsilon \quad (1)$$

$$C = (c_1, c_2, c_3, \dots, c_N) \in \mathbb{R}^N \quad (2)$$

where SM_d is the downscaled soil moisture data (response), C is an input vector, c_i represents the input covariates (i.e., precipitation, surface temperature, elevation, original SMAP, and NDVI),

and N is the input vector dimension (in this study N is equal to 5). In this formulation, depending on the relationship between response variables and input covariates, f can be a non-linear or a linear function.

Although implementation of such regression-based model is easy, one drawback of this model is that it generally provides a single estimate and does not represent the uncertainty associated with the estimates. The approach taken in this study to characterize the uncertainty in our downscaling is the ensemble learning approach, such as Random Forest (RF). The idea of searching over random subset of decision rules while splitting nodes was first initiated by Amit and Geman (1996), later on, Breiman (2001) developed this idea and introduced the RF. RF is a machine learning technique, which is most appropriate for regression and classification problems. The adaptive, randomized and de-correlated features of decision rules involved in RF make it more suitable approach when the relationship between the predictors and the response variable is complex and highly nonlinear. For a regression problem, first a number of decision trees are built during the training phase, and then the mean prediction of these trees is calculated as the output of this approach. RF divides the input feature space into many regression trees, known as forest, where each tree is generated using a bootstrap sample. A bootstrap sample contains about two-thirds of the training input data, and the left samples (one-third) are used for the validation of each tree. This is one of the key features of RF algorithm (also known as out-of-bag (OOB) samples) to estimate the model generalization error. This approach is based on the bagging (bootstrap aggregation) method that combines the results of many decision trees to reduce the chance of overfitting and improve the generalization. RF can be easily implemented in a parallel computing platform, which makes it more advantageous for large scale problems (Breiman, 2001).

As previously mentioned, we randomly split the data set into two groups (using the 80% of data) to train and (using the 20% of data) to verify the RF model. The random splitting of the data set for model calibration and verification ensures the generalizability of the developed downscaling approach. In Step 1, a bootstrap method is used to sample M subsets from the training data sets. In Step 2, M independent regression trees are built to train the model using the bootstrapped samples. In Step 3, the predicted value is obtained over M replications. In Step 4, the final result is taken as the average of the individual tree outputs. This model selects a random subset of predictors in each decision tree to inject randomness in the RF model, which in turn alleviates the redundancy of predictors and diversifies the forecast decision trees (He et al., 2016).

The ensemble posterior is calculated by averaging M posteriors as follows: $p_t(SM_d|C)$ specifies the conditional distribution of the downscaled soil moisture (SM_d) given the bootstrapped samples from the training input covariate vector (C).

$$p(SM_d|C) = \frac{1}{M} \sum_{t=1}^M p_t(SM_d|C) \quad (3)$$

In this study, we used MATLAB TreeBagger built-in function to implement the RF algorithm. In the developed downscaling framework, each of the 12 RF models has been set to have 100 decision trees. This value was obtained using trial and error method, such that any value more than this does not improve the downscaling accuracy. This issue will be further discussed in the next section. Up to this point, we developed multiple RF models to map input covariates to a target variable. The next step is to implement the calibrated models on the test data sets to evaluate the model robustness and generalizability. Figure 1-1 depicts a schematic of the proposed soil moisture downscaling framework.

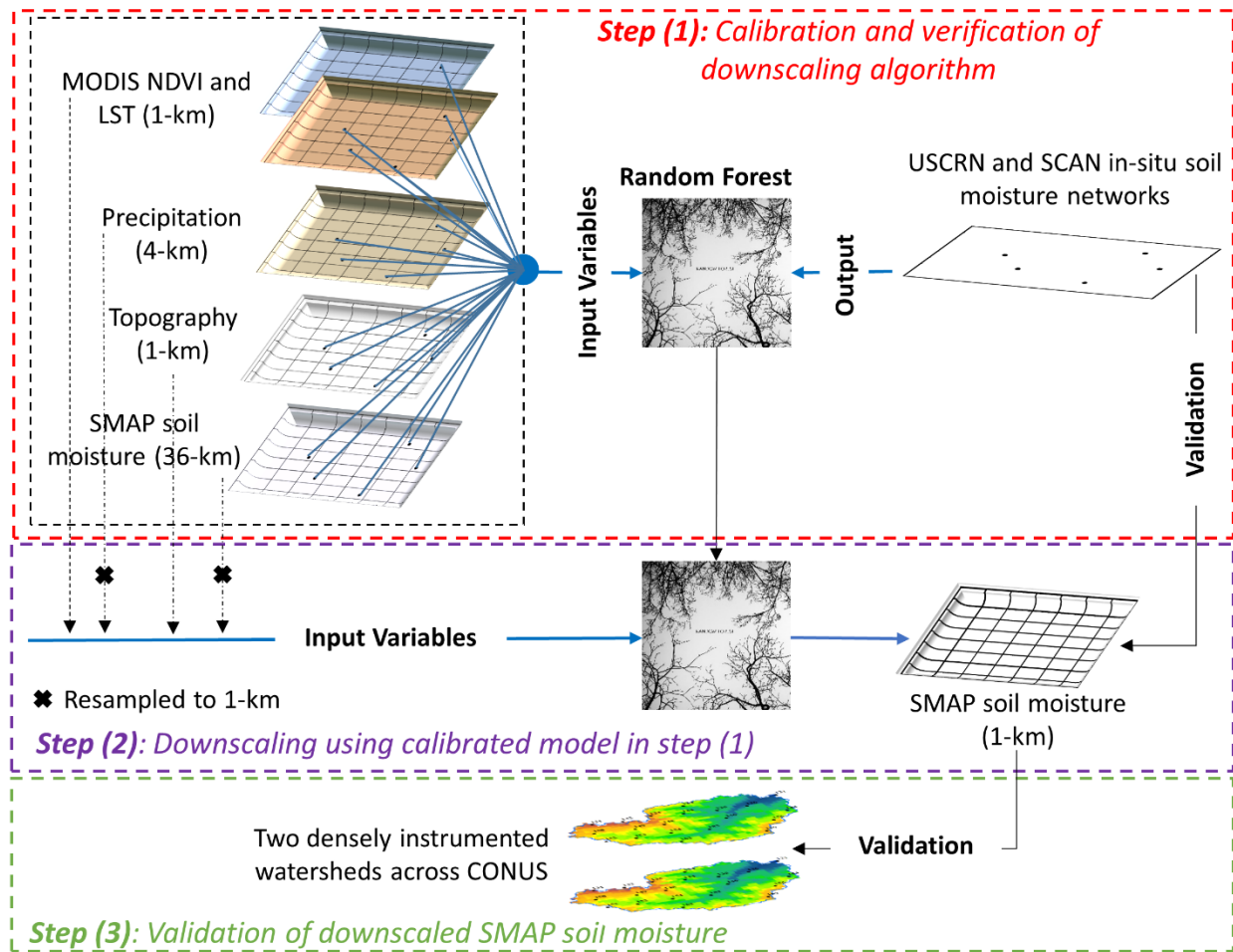


Figure 1-1 Schematic of the proposed soil moisture downscaling framework.

Results and Discussions

In this study, we discuss the results in three parts. Section 4.1 reports the performance of the developed RF models. Section 4.2 presents the comparison of the downscaled SMAP soil moisture products versus three hundred sparse soil moisture networks throughout the CONUS. In Section 4.3, the downscaled SMAP soil moisture data is validated against in-situ soil moisture measurements collected from two CVSs.

Performance of the Proposed Downscaling Algorithm

In this study, we used the Pearson correlation coefficient 'R' (Gan et al., 2014), unbiased Root Mean Square Error 'ubRMSE' (Entekhabi et al., 2010), and bias to measure the performance of the proposed downscaling algorithm. 'R' is a common index to measure the strength of a linear association between two quantitative variables. The Pearson correlation coefficient is calculated at a 95% confidence level and ranges between -1 to 1. The bias measures the average tendency of overestimation (positive value) or underestimation (negative value) of the simulated data. The ideal value of bias is 0, showing a more accurate model simulation. The standard 'RMSE' is very sensitive to biases in either the mean or the amplitude of variations. This bias can easily be removed by using the 'ubRMSE'. The 'ubRMSE' is a metric that SMAP uses to report the product accuracy. For soil moisture retrievals, the aforementioned metrics provide a more comprehensive description of product quality compared to other measures (Jackson et al., 2012). The SMAP mission requirement for soil moisture product accuracy is $\text{ubRMSE}=0.040 \text{ m}^3/\text{m}^3$ (Chan et al., 2016).

As mentioned earlier, the first step in developing the proposed downscaling scheme in this study is to calibrate and verify the RF models using the atmospheric and geophysical data sampled from locations where in-situ observations are available. The distribution pattern of in-situ soil moisture sensors over CONUS according to their soil texture properties makes it possible to develop twelve RF models to downscale soil moisture over more than 98% of the CONUS area. Figure 1-2 illustrates the performance of the developed soil moisture downscaling algorithm. Here we reported only the results of the verification step, which implies the ability of the calibrated models to generalize to unseen data. The statistical performance measures shown in this figure indicate that there is a very good agreement between the simulated and observed

soil moisture values over different soil texture classes with different land-atmosphere couplings. In this study, we noticed that using only a single RF model would have generated a significant bias in model prediction and led to a worse model fit, however, as results indicate, multiple RF models classified based on the stations' soil texture properties simultaneously minimize the bias throughout the simulation process and enhance the model performance. The developed models based on those regions with abundant soil moisture stations (i.e., loamy, silty loam, and sandy loam) would be more reliable to predict the soil moisture and less prone to uncertainty than those areas with limited soil moisture sensors (i.e., silty clay and sandy clay loam). We also realized that although increasing the number of decision trees from 10 to 100 in random forest algorithm does not show significant improvement in model calibration and validation steps, it does so in downscaling step and generating the downscaled soil moisture data with higher accuracy. Also, it should be mentioned that using more than 100 decision trees does not enhance the downscaling accuracy and instead only makes the proposed approach computationally more intensive. In this study, we used the Pearson correlation coefficient 'R' (Gan et al., 2014), unbiased Root Mean Square Error 'ubRMSE' (Entekhabi et al., 2010), and bias to measure the performance of the proposed downscaling algorithm. 'R' is a common index to measure the strength of a linear association between two quantitative variables. The Pearson correlation coefficient is calculated at a 95% confidence level and ranges between -1 to 1. The bias measures the average tendency of overestimation (positive value) or underestimation (negative value) of the simulated data. The ideal value of bias is 0, showing a more accurate model simulation. The standard 'RMSE' is very sensitive to biases in either the mean or the amplitude of variations. This bias can easily be removed by using the 'ubRMSE'. The 'ubRMSE' is a metric that SMAP uses to report the product accuracy. For soil moisture retrievals, the aforementioned metrics provide a more

comprehensive description of product quality compared to other measures (Jackson et al., 2012). The SMAP mission requirement for soil moisture product accuracy is $ubRMSE=0.040 \text{ m}^3/\text{m}^3$ (Chan et al., 2016).

As mentioned earlier, the first step in developing the proposed downscaling scheme in this study is to calibrate and verify the RF models using the atmospheric and geophysical data sampled from locations where in-situ observations are available. The distribution pattern of in-situ soil moisture sensors over CONUS according to their soil texture properties makes it possible to develop twelve RF models to downscale soil moisture over more than 98% of the CONUS area. Figure 1-2 illustrates the performance of the developed soil moisture downscaling algorithm. Here we reported only the results of the verification step, which implies the ability of the calibrated models to generalize to unseen data. The statistical performance measures shown in this figure indicate that there is a very good agreement between the simulated and observed soil moisture values over different soil texture classes with different land-atmosphere couplings. In this study, we noticed that using only a single RF model would have generated a significant bias in model prediction and led to a worse model fit, however, as results indicate, multiple RF models classified based on the stations' soil texture properties simultaneously minimize the bias throughout the simulation process and enhance the model performance. The developed models based on those regions with abundant soil moisture stations (i.e., loamy, silty loam, and sandy loam) would be more reliable to predict the soil moisture and less prone to uncertainty than those areas with limited soil moisture sensors (i.e., silty clay and sandy clay loam). We also realized that although increasing the number of decision trees from 10 to 100 in random forest algorithm does not show significant improvement in model calibration and validation steps, it does so in downscaling step and generating the downscaled soil moisture data with higher accuracy. Also, it

should be mentioned that using more than 100 decision trees does not enhance the downscaling accuracy and instead only makes the proposed approach computationally more intensive.

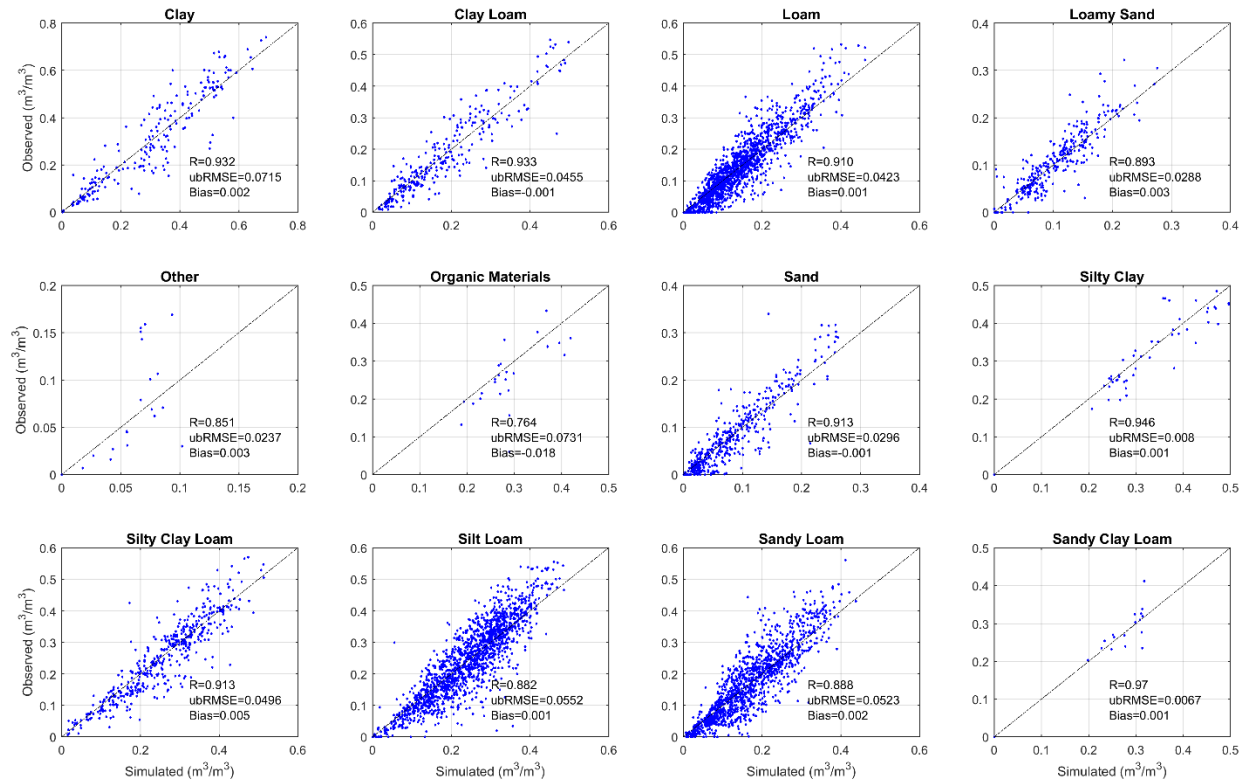


Figure 1-2 Verification results of the developed Random Forest (RF) models for each group of soil texture over CONUS.

In the next step, these calibrated and verified models will be used to downscale the SMAP radiometer soil moisture from 36 km to 1 km spatial resolution over CONUS for the period of 04/01/2015 to 12/31/2015.

Downscaled SMAP Soil Moistures versus In-situ Observations

In this section, we compare the downscaled SMAP soil moistures at 1km spatial resolution with those SCAN and USCRN in-situ soil moisture observations scattered throughout the CONUS. Figure 1-3 reports the results indicating a consistently high correlation between the downscaled SMAP and in-situ soil moistures almost everywhere across the CONUS except for a

few isolated points with slightly low correlation in the Rocky Mountains. The same analogy and pattern is discernible for ubRMSE. The CONUS average correlation and ubRMSE values are highlighted in each subplot in Figure 1-3. The average correlations between downscaled SMAP and in-situ data are 0.65 (SCAN) and 0.70 (CRN). The average ubRMSE is reported as 0.047 m^3/m^3 and 0.040 m^3/m^3 respectively for SCAN and USCRN networks. More investigation also reveals a negligible amount of bias between the downscaled SMAP product and in-situ observations. Such that the average bias is reported at 0.004 m^3/m^3 and 0.002 m^3/m^3 respectively for SCAN and USCRN networks (not illustrated in Figure 1-3). These results are encouraging compared with those obtained from original SMAP soil moisture products as they show overestimation over arid regions with bare soils and underestimation over cold vegetated areas (Ma et al., 2017).

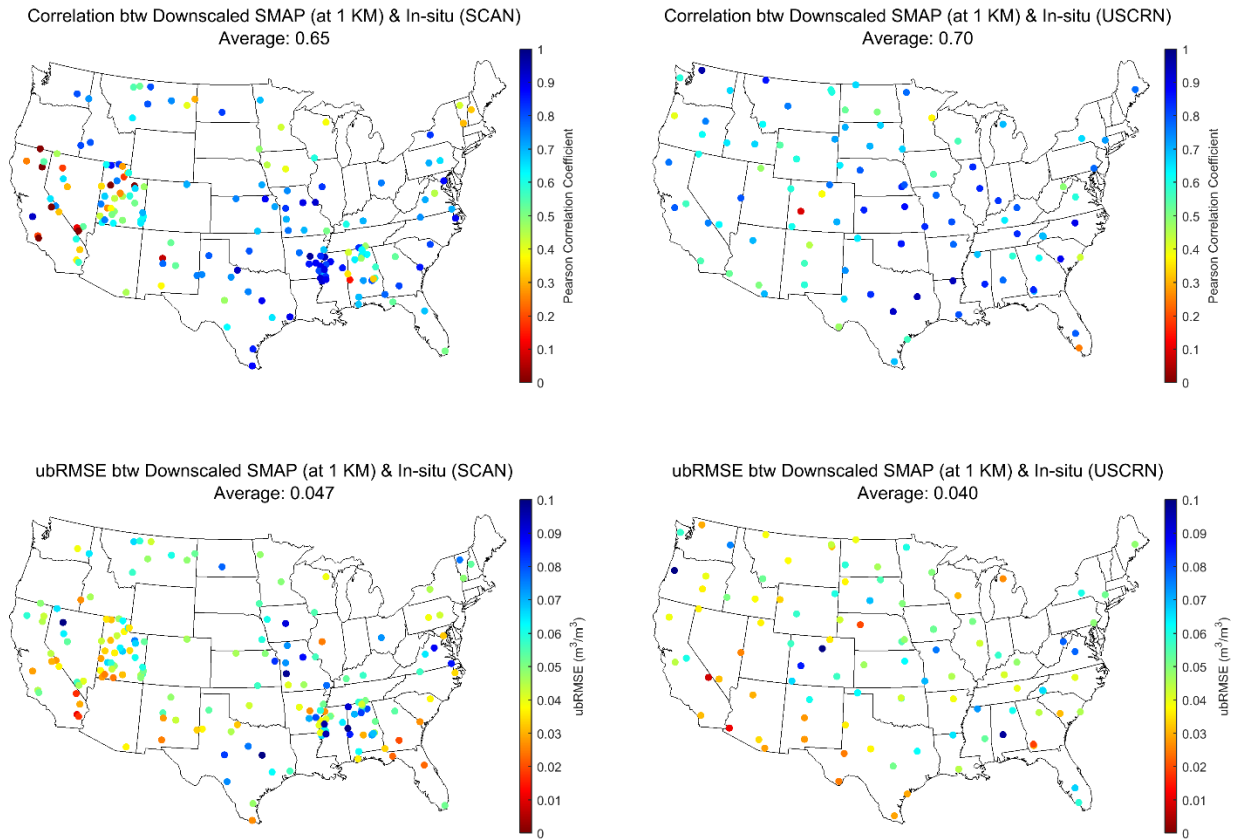


Figure 1-3 Correlation and ubRMSE calculated between in-situ observations (SCAN and USCRN) and downscaled SMAP.

For a few instruments on the East and West coasts, the model failed to meet the SMAP accuracy requirement (8 stations out of 300, not shown in Figure 1-3). The reason behind this may be attributed either to RFI signals that would contaminate the soil moisture retrievals over the stations located in densely vegetated areas or to the spatial mismatch of the SMAP footprint. Each of these cases may create an obstacle to retrieving the SMAP soil moisture data. For example, ‘CA Bodega 6 WSW’ is one of those eight stations, which is located on the Pacific West Coast at Bodega Bay, California. This station is occupied by sandy soil. The SMAP pixel over this region may have been more susceptible either to the attenuation of microwave signal by the vegetation or to flooding due to heavy rainfall throughout the year. Hence, the SMAP pixel for this region is most often missing or discarded by the SMAP data quality flag, which leads to

a worse downscaling result over corresponding in-situ stations. Despite such limitation, the downscaled SMAP soil moistures correlate well with in-situ observation networks over almost entire CONUS, including those mountainous and forested areas in the Eastern and Southeastern U.S. These areas are generally challenging for retrieving soil moisture due to the attenuation of microwave signal by the vegetation. Figure 1-3 also implies the better performance of downscaled SMAP soil moisture over bare soils in comparison with vegetated soils.

Although the reported results are promising, they may not be fully indicative of the effectiveness of the proposed downscaling algorithm, therefore, we compare the results from the proposed approach with those obtained from a uniform disaggregation approach, where the value of fine-resolution grid cell is set to be the same value as its correspondent coarse-resolution grid cell. Figure 1-4 illustrates this comparison and shows that the proposed downscaling approach significantly outperforms the uniform disaggregation approach.

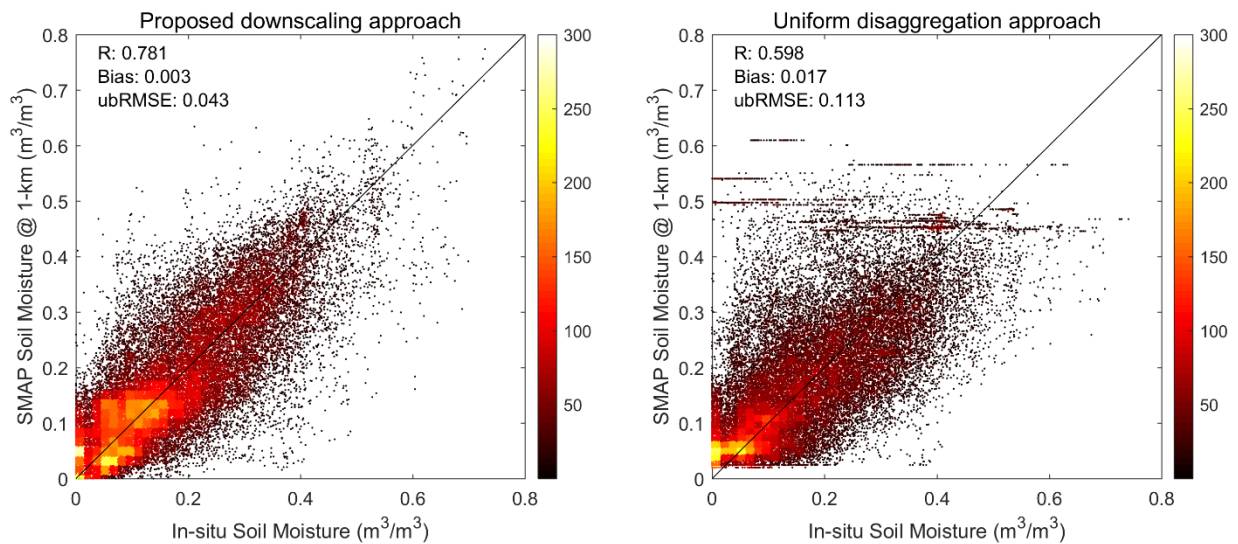


Figure 1-4 Comparison of downscaling accuracy between the proposed approach and the uniform disaggregation approach. Both SCAN and USCRN in-situ observations were used in this analysis.

To analyze the importance of each input variable, i.e., NDVI, surface temperature, precipitation and topography, on the downscaling accuracy, we performed a leave-one-out

approach where one input variable was removed and the downscaling was implemented.

Therefore, the proposed downscaling algorithm is run under four different input schemes as follows:

Scheme 1: {NDVI, surface temperature, precipitation} +SMAP

Scheme 2: {NDVI, surface temperature, topography} +SMAP

Scheme 3: {surface temperature, precipitation, topography} +SMAP

Scheme 4: {NDVI, precipitation, topography} +SMAP

Figure 1-5 reports the results in four subplots. All three performance measures are also shown in this figure. The results confirmed that NDVI, surface temperature and precipitation have almost similar influence on the downscaling accuracy, however, topography shows to be less influential than other variables on the results. By comparing the results in Figure 1-4 (where all input variables were taken into account) with those in this figure, it is seen that the inclusion of all input variables in the downscaling framework is essential for achieving the best downscaling accuracy. It is important to note that since the objective of this study is to downscale SMAP product, SMAP data must be included in all four input schemes.

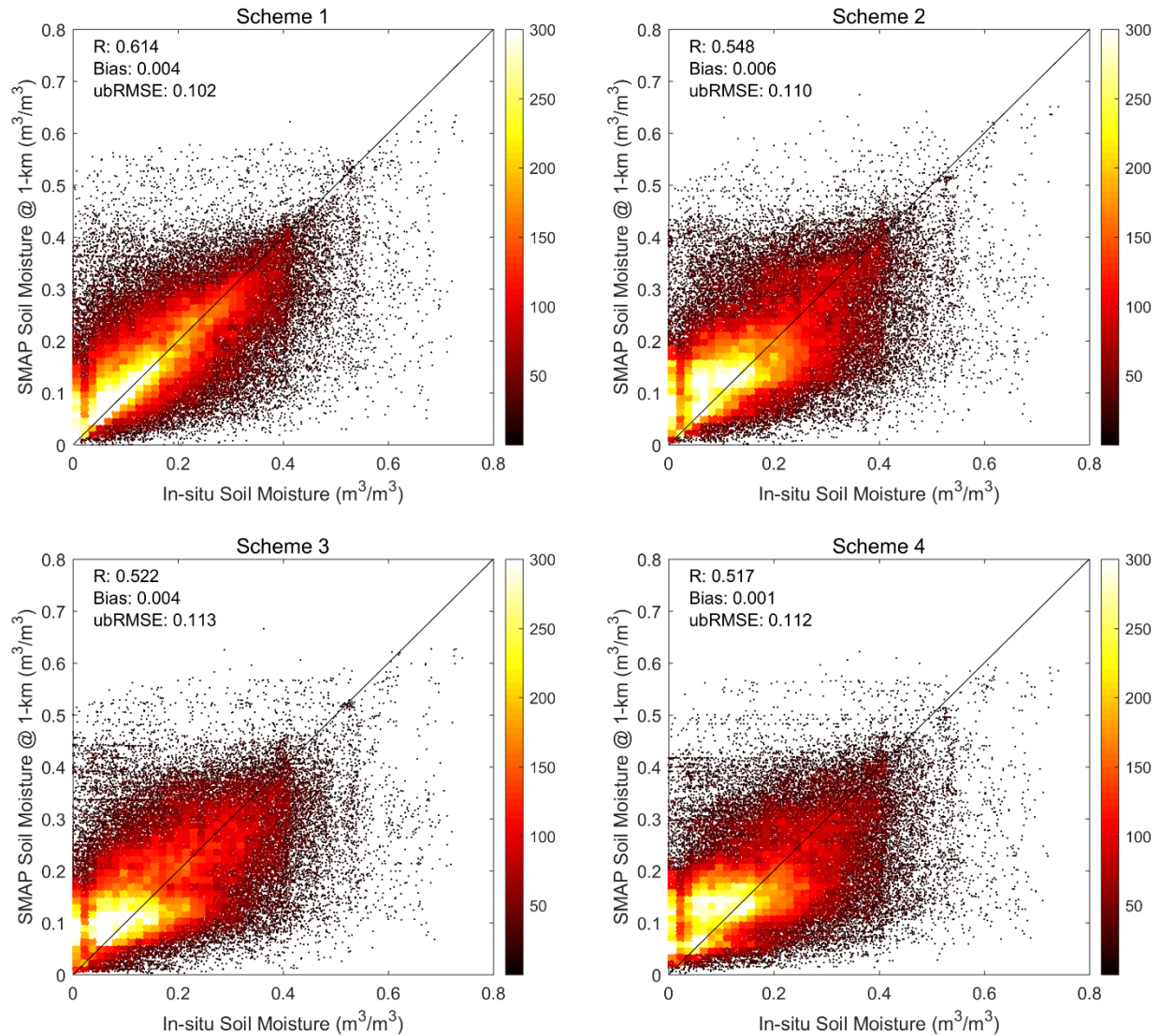


Figure 1-5 The performance of the proposed downscaling approach under four different input schemes. Both SCAN and USCRN in-situ observations were used in this analysis.

In Figure 1-6, we use the Taylor diagram (Taylor, 2001) to provide a conclusive comparison between the performance of the downscaled SMAP by the proposed approach and the in-situ soil moisture measurements at daily time scale collected from 186 SCAN and 114 USCRN stations scattered across the CONUS. The Taylor diagram graphically summarizes several important statistical indices to compare the similarity/dissimilarity between two patterns. This figure can be generated using three statistical metrics. RMSD is extensively used to assess

the performance of satellite soil moisture products versus in-situ measurements (Merlin et al., 2015). This metric integrates the three main components, namely, time series correlation, mean bias, and bias in the variance to evaluate the quality of data. The standard deviation ratio between the downscaled and in-situ soil moisture is on the radial distance and their correlation is on the angle of the polar plot. The black point shown in Figure 1-6 is named as the reference point, where all the metrics are considered optimal. The distance to this point indicates the centered normalized RMSD between the downscaled soil moisture and in-situ soil moisture patterns.

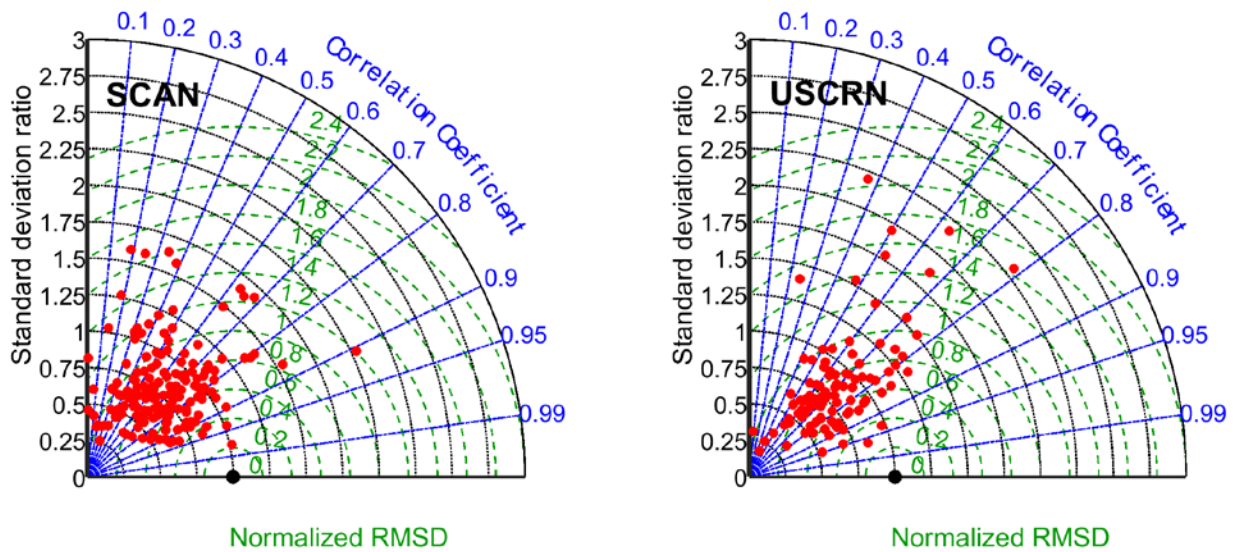


Figure 1-6 The accuracy of downscaled SMAP soil moisture versus in-situ soil moisture observations collected from 186 SCAN and 114 USCRN stations for study period 04/01/2015–12/31/2015. RMSD is represented by green dashed line while correlation coefficient is displayed by blue dotted line.

The Taylor diagrams are showing most of the correlations above 0.7 for both SCAN and USCRN networks. It is also evident that most of the standard deviation ratios are less than 1 (black dashed line in Figure 1-6), indicating the higher variability of in-situ data compared to the downscaled data across almost all the stations in CONUS. It is, however, noted that a few stations end up inflating the standard deviation ratio. Further investigation revealed that the SMAP satellite has had poor performance over those sites due to the severe spatial heterogeneity

(e.g., climate, topography, soil texture, vegetation, and land cover) that dominates the corresponding satellite's footprint.

Downscaled Soil Moisture Temporal Dynamic

The most reliable soil moisture downscaling technique should be able to satisfy two important criteria: first, the downscaled soil moisture estimates must capture the temporal dynamics of in-situ soil moisture observations (Mishra et al., 2017; Peng et al., 2015; Piles et al., 2014), and second, the spatial pattern of the downscaled soil moisture data must follow that of the original soil moisture map (Kaheil et al., 2008; Kim & Barros, 2002; Piles et al., 2011; Sanchez et al., 2012). To investigate whether the downscaled soil moisture product would meet the temporal variability criterion, in this section, we evaluate the performance of the downscaled SMAP soil moisture by the proposed approach at three different SCAN in-situ soil moisture stations located in different climate regimes. Figure 1-S3 (in supplementary file) depicts these stations and their adjacent environment. The vegetation condition and climate regime of these three locations are summarized here to explain the downscaled soil moisture performance analysis. As mentioned earlier, and is seen from Figure 1-S3, although these in-situ measurements do not represent the soil moisture heterogeneity within the SMAP footprint, they do represent the surrounding vegetation and land cover types. Station 2027 (Figure 1-S3.a) is instrumented in the Little River Experimental Watershed (LREW) in Tift County, Georgia where the prevailing climate is humid subtropical providing abundant rainfall throughout the year. The land use is a mixture of forest, crops, and pasture. Station 2198 (Figure 1-S3.b) is located in Whitman County, Washington. This region is mostly dominated by grassland and pasture, and experiences a mild and temperate climate. October through April are the wettest months (often in

the form of snow), while August is the driest month. Station 2217 (Figure 1-S3.c) is located in the semi-arid Monocline Ridge area in Fresno County, California where the climate is mostly characterized by hot and dry summers and mild and moist winters. In this area, the majority of precipitation falls during winter. Monocline Ridge is an uninhabited and unvegetated region.

Temporal variations of soil moisture from the downscaled SMAP (at 1km), original SMAP (at 36 km), and in-situ observations are illustrated along with precipitation (daily mean) in Figure 1-7, and their performance is evaluated using three statistical metrics, i.e., R, ubRMSE (m^3/m^3), and bias (m^3/m^3). The detail information of each instrument including the station ID, soil texture type, and the location name are displayed in this figure. The black dotted line, purple and blue points are indicating respectively the in-situ soil moisture at 5 cm, the original SMAP soil moisture at top 5 cm and the downscaled SMAP soil moisture time series. Although both SMAP products closely follow the precipitation patterns, their consistency against the in-situ soil moisture observation differs based on the land-atmosphere characteristics. For example, in Tift County, Georgia, both original and downscaled SMAP data could well track the dynamics of the drying and wetting of soil moisture caused by precipitation. While, the original SMAP soil moisture noticed a significant amount of bias (Bias= $0.077 \text{ m}^3/\text{m}^3$) compared to the downscaled one (Bias= $-0.008 \text{ m}^3/\text{m}^3$). This may be due to the station's location where the dominant soil type is relatively well-drained loamy sand causing rapid soil drying after the precipitation event. The downscaled SMAP could capture this pattern properly, while the original SMAP failed to do so. The same analogy can be seen in Whitman County, Washington. In this station, the original SMAP underestimated the soil moisture almost throughout the whole period of study. This problem was mitigated by the downscaled SMAP soil moisture.

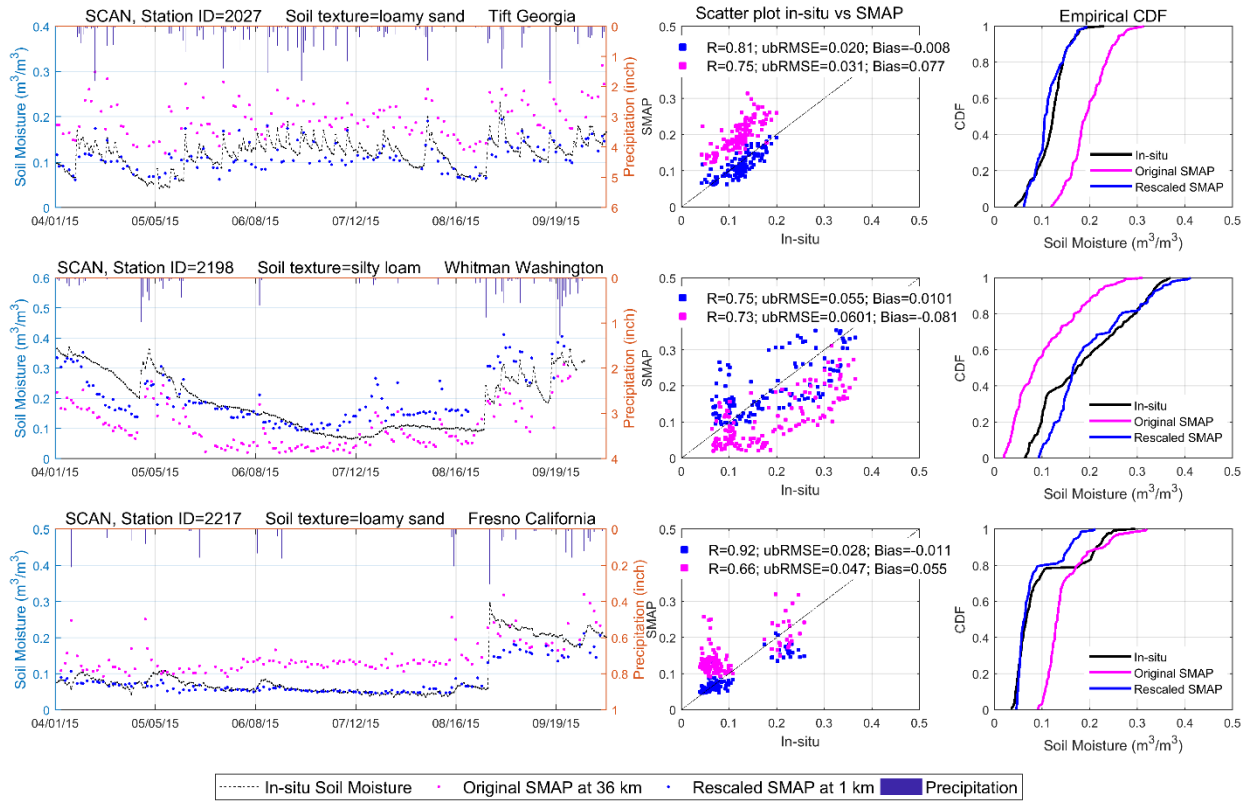


Figure 1-7 Time series, scatter plot and Cumulative Distribution Function (CDF) of original and downscaled SMAP soil moisture data versus in-situ observations at top 5 cm depth.

As mentioned above, although both SMAP products are reasonably able to reproduce the in-situ soil moisture temporal dynamics, the original SMAP product may severely bias the soil moisture estimates. This issue was more clearly observed in the station 2217, which is located in Fresno County, California where the original SMAP overestimated the soil moisture almost all days over the study period. This is mainly because fine and coarser resolution soil moisture observations often ignore the role of spatial scale differences in explaining differences between in-situ and satellite soil moisture. In particular, the soil moisture dynamic range decreases by moving from small to large scale. The proposed downscaling algorithm is able to remove the systematic bias from the SMAP soil moisture when rescaling it to a finer resolution. For all three stations investigated here, the Cumulative Distribution Function (CDF) in Figure 1-7 shows that

the CDF of the downscaled SMAP perfectly matches with that of the in-situ measurements. This further supports the effectiveness of the proposed algorithm in rescaling the coarse resolution SMAP soil moisture, while reducing the mismatch between that and in-situ observations. The statistical measures that are reported in this figure indicate that great improvement was made by the downscaled soil moisture data. It is worth mentioning that although the original SMAP soil moisture retrievals are validated using those stations that are not within the USCRN and SCAN soil moisture networks (at the time of study), they are in good agreement with these sparse in-situ stations (Zhang et al., 2017). In Figure 1-7, the correlation coefficient and ubRMSE calculated between the original SMAP and in-situ observations imply this link between the two.

Downscaled Soil Moisture Spatial heterogeneity

Up to this point, we discussed how the downscaled soil moistures could capture the mean and amplitude of variations of in-situ observations over different geographical locations with different land-atmosphere regimes. The ensuing task is to investigate the spatial consistency between the coarse and fine resolution soil moisture maps. The soil moisture spatial pattern is dependent on the heterogeneity of soil parameters (e.g., soil texture, vegetation, and topography) that are generally not distributed homogeneously in the area. This results in an uncertainty in the soil moisture retrievals, which consequently affects the downscaled soil moisture accuracy (Piles et al., 2011). Here, we try to assess the extent to which the downscaled soil moisture map could fill this gap, and contribute to decreasing the discrepancy between the spatial variability of soil parameters and soil moistures. Figure 1-8 demonstrates an example of the original SMAP soil moisture data and the downscaled soil moisture on April 27, 2015, over the western CONUS. This figure also illustrates the land cover distribution. Figure 1-8 indicates that the spatial pattern

of downscaled SMAP soil moisture (Figure 1-8.c) closely follows the spatial heterogeneity of soil parameters such as vegetation cover (Figure 1-8.a) and topography (previously shown in Figure 1-S2, in supplementary file). Likewise, the downscaled soil moisture data (Figure 1-8.c) closely matches the spatial pattern of the original soil moisture data (Figure 1-8.b) across almost the entire western CONUS. Discrepancies between the original and downscaled data mostly occur in densely vegetated areas (i.e., evergreen and deciduous forests) where the SMAP soil moisture is prone to underestimation due to the attenuation of microwave signal by vegetation.

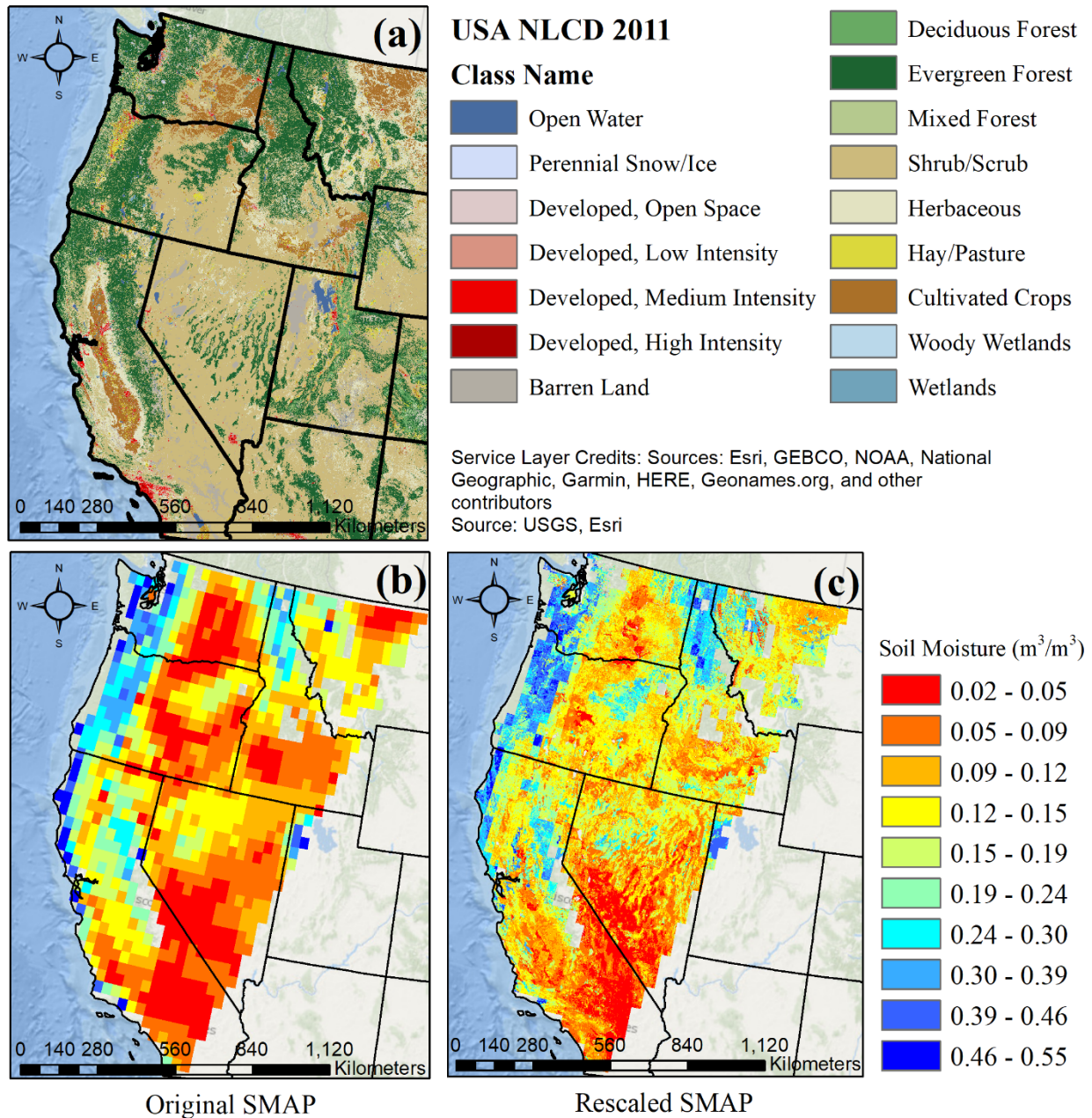


Figure 1-8 (a) Land cover distribution over the western CONUS, (b) original SMAP soil moisture at 36 km spatial resolution, and (c) downscaled SMAP soil moisture at 1km spatial resolution on April 27, 2015.

According to Figure 1-8, the downscaled SMAP soil moisture shows comparatively more water content in the topsoil layer than original SMAP. This is because the downscaled soil moisture at 1km is obtained based on the soil moisture at point scale. Therefore, the fine-resolution SMAP product will lead to a lower soil moisture, similar to the one observed by

SMAP satellite, if it is averaged to a coarser spatial scale. Another plausible reason behind this, is the fact that SMAP is measuring a large-scale average, and the averaging process dissipates anomalies more rapidly compared to the point (in-situ) scale, leading to a faster drydown time scale (Shellito et al., 2016; Shellito & Small, 2017). Here the downscaled SMAP soil moistures are obtained using the model that is calibrated by in-situ observations. It was found that the downscaled soil moistures are slightly wetter than the original SMAP product following rainfall events while correlating well with the in-situ observations. Chen et al. (2017) showed that although SMAP retrievals underestimate soil moisture, they capture its dynamics well. Therefore, our conclusion is consistent with that of Chen et al., (2017). The downscaled SMAP soil moistures generated in this study are shown to track the dynamics of in-situ observations well, and clearly capture the spatial heterogeneity of soil parameters with high spatial correspondence to the original SMAP soil moisture data.

The accuracy of downscaled soil moisture product in this study appears to be very good as compared to, for example, Mishra et al. (2018), who reported the CONUS average correlation between the thermal-infrared (TIR) downscaled SMAP (passive) and SCAN is around 0.54, while in this study, the correlation between the downscaled SMAP product and SCAN networks is 0.65. However, it is noted that the successful use of a downscaling approach may be restricted to its certain characteristics and needs of a user, knowing that each method may have certain strengths and weaknesses (Colliander et al., 2018; Chakrabarti, 2015, 2016, 2018). For example, in the work by Colliander et al. (2018), the authors proposed a disaggregation approach to downscale the SMAP soil moisture over a small domain (including three 36-km SMAP pixels), where the surface temperature is controlled by soil evaporation, the topographical variation is relatively moderate, and the vegetation density is relatively low.

Validation of Downscaled SMAP Soil Moisture Product

In these subsections, we evaluate the accuracy of downscaled SMAP soil moisture against two densely instrumented watersheds located in two different geographical zones in CONUS. In addition, in order to fully assess the performance of the proposed downscaling algorithm, similar to Section 4.2, the results are also compared with those obtained from the uniform disaggregation approach.

Study Area (1): Little Washita River Watershed

The Little Washita River Watershed (LWRW) is located in southwest Oklahoma in the Great Plains region of the U.S. and comprises an area of 610 km². A wide range of textures covers the watershed's surface layer, of which, sandy clay loam (SCL) is the most dominant. There is a network of twenty in-situ soil moisture stations distributed evenly over the entire watershed. This is called the Agricultural Research Service's (ARS) Micronet. These stations are equipped with capacitance probes that record the soil moisture at a depth of approximately 3cm to 7cm with an hourly measurement interval. Many of these sensors also provide surface temperature measurements. In this study, the data set were collected daily for the period of 04/01/2015 to 12/31/2015 in order to be consistent with the period of available SMAP satellite data.

Validation Results Based on LWRW

The results reported in Table 1-2 indicate that the downscaled SMAP soil moisture product matches well with the in-situ observations for the majority of stations, except for a few

stations (121 and 136) that are located along the mainstream of the watershed at low altitudes, hence more prone to accumulation of soil moisture storage. Despite this concern, the majority of stations located within the watershed are showing satisfactory results (Table 1-2) which further validate the effectiveness of the RF approach. For the proposed downscaling method, the average values of ubRMSE, bias, and R across all stations are reported $0.035 \text{ m}^3/\text{m}^3$, $-0.009 \text{ m}^3/\text{m}^3$ and 0.824, respectively, which are better than those from the uniform disaggregation approach. As seen in Table 1-2, the ubRMSE value for all soil types are less than the SMAP mission accuracy target of $0.04 \text{ m}^3/\text{m}^3$ (Jackson et al., 2016). However, for the uniform disaggregation approach, this value slightly exceeds the SMAP accuracy requirement.

Table 1-2 Comparison between the downscaled SMAP soil moisture at 1km and in-situ soil moisture measurements within Little Washita River Watershed in 2015 (location information is based on the WGS84 datum).

Station ID	Soil texture	Latitude	Longitude	Proposed downscaling approach			Uniform Disaggregation approach		
				ubRMSE (m^3/m^3)	Bias (m^3/m^3)	R	ubRMSE (m^3/m^3)	Bias (m^3/m^3)	R
121	L	34.9586	-97.8986	-	-	-	-	-	-
124	SL	34.9728	-98.0581	0.036	0.008	0.802	0.048	0.016	0.759
131	SIL	34.9503	-98.2336	0.04	-0.004	0.872	0.036	-0.028	0.804
132	S	34.9428	-98.1819	0.034	0.027	0.861	0.051	0.114	0.588
133	S	34.9492	-98.1281	0.04	-0.02	0.741	0.042	0.08	0.719
136	L	34.9278	-97.9656	-	-	-	-	-	-
146	L	34.8853	-98.0231	0.048	-0.079	0.787	0.05	-0.025	0.604
148	SIL	34.8992	-98.1281	0.036	-0.001	0.825	0.047	-0.038	0.766
152	L	34.8611	-98.2511	0.039	-0.032	0.749	0.048	-0.008	0.719
154	L	34.8553	-98.1369	0.063	-0.032	0.874	0.046	-0.01	0.802
159	SL	34.7967	-97.9933	0.03	0.038	0.85	0.031	0.058	0.781
134	SL	34.92745	-98.075452	0.026	-0.012	0.913	0.044	0.039	0.773
135	L	34.93346	-98.018777	0.02	-0.015	0.847	0.046	0.113	0.763
144	L	34.86071	-97.91114	0.03	-0.051	0.841	0.043	-0.039	0.594
149	SIL	34.89139	-98.181246	0.038	-0.008	0.787	0.049	-0.042	0.872

150	SIL	34.90525	-98.25106	0.021	-0.005	0.773	0.046	0.01	0.866
153	L	34.85872	-98.199458	0.029	-0.069	0.815	0.057	-0.044	0.718
156	SL	34.83896	-97.962534	0.033	0.06	0.857	0.051	0.068	0.828
162	SL	34.79735	-98.126933	0.048	-0.011	0.857	0.035	-0.095	0.67
182	SL	34.84504	-98.073473	0.02	0.045	0.777	0.042	0.083	0.74
Average				0.035	-0.009	0.824	0.045	0.014	0.742

The results affirm that the downscaled SMAP soil moisture not only captures the spatial distribution of soil moisture (as shown in Table 1-2), but also adequately monitors its temporal dynamics. The time series of downscaled SMAP soil moistures versus in-situ observations at twenty Micronet stations were examined. The results showed that the downscaled soil moistures across all twenty stations closely follow the dynamics of in-situ observations and precipitation pattern, such as dry-down and wet-up periods. For example, Figure 1-9 illustrates time-series comparisons between the downscaled SMAP soil moistures and in-situ observations from a few selected stations (i.e., station 148, 124, 131 and 149) between 04/01/2015 and 12/31/2015.

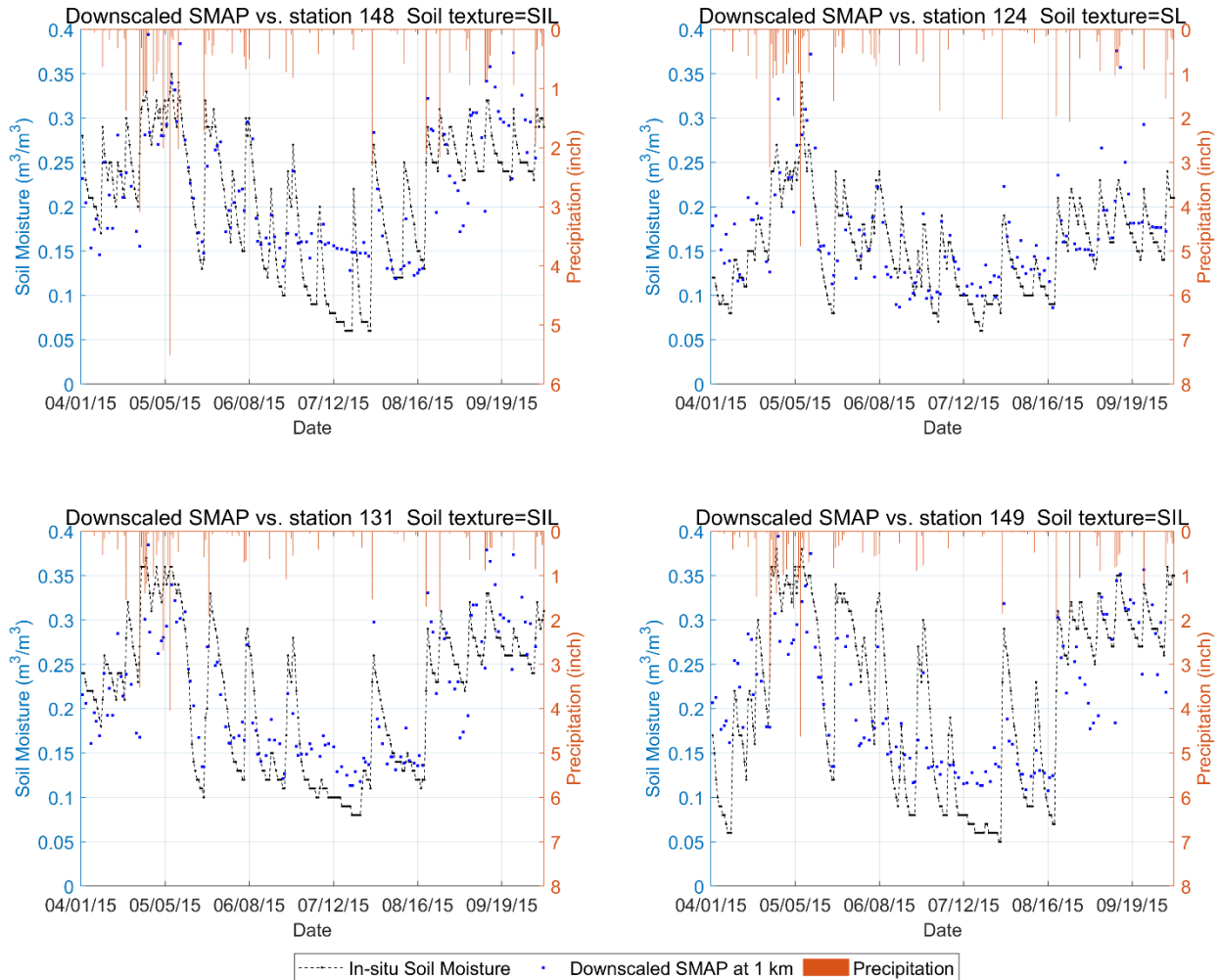


Figure 1-9 Daily in-situ and downscaled SMAP radiometer soil moisture at 1km along with precipitation observation for stations 148, 124, 131, and 149.

Study Area (2): Walnut Gulch Experimental Watershed

The Walnut Gulch Experimental Watershed (WGEW) is one of two ARS experimental watersheds on western rangelands located in the southeastern Arizona with an area of 149 km². The predominant soil surface over this watershed is loamy. There are nineteen soil moisture stations (identified as RG##) uniformly situated inside the watershed monitoring soil moisture every 30 minutes at a depth of approximately 3cm to 7cm. These sensors also measure soil

temperature and precipitation. In this paper, the data set are collected daily (hourly averaged) from 04/01/2015 to 12/31/2015, so as to be consistent with the time period of the current study.

Validation Results Based on WGEW

The results reported in Table 1-3 imply a satisfactory performance of the downscaled SMAP soil moisture product versus in-situ observations for the majority of stations, except for a couple of stations (e.g., station RG076 and RG092) situated close to the outlet of the watershed. The reason behind this may be attributed to the locations of these stations which were determined to accommodate the hydrologic research objectives of the watershed, not to validate the satellite soil moisture data products (Colliander et al., 2017). In the proposed downscaling method, the average values of ubRMSE, bias, and R across all stations ($0.029 \text{ m}^3/\text{m}^3$, $0.008 \text{ m}^3/\text{m}^3$ and 0.637) are found to be more accurate than those from the uniform disaggregation approach ($0.039 \text{ m}^3/\text{m}^3$, $-0.002 \text{ m}^3/\text{m}^3$ and 0.517). More importantly, on average, the ubRMSE value for this watershed ($0.029 \text{ m}^3/\text{m}^3$) is much lower than the SMAP mission accuracy target of $0.04 \text{ m}^3/\text{m}^3$. This indicates a successful application of the proposed algorithm for downscaling satellite soil moisture data. We examined the temporal variation of downscaled soil moisture data set and found that they are able to capture the dynamics of in-situ observations well. Further investigation also revealed that discrepancies between downscaled and in-situ soil moistures mostly occur during the North American Monsoon season when the spatial distribution of soil moisture over WGEW is more heterogeneous.

Table 1-3 Comparison between the downscaled SMAP soil moisture at 1km and in-situ soil moisture measurements within Walnut Gulch Experimental Watershed in 2015 (location information is based on the WGS84 datum).

Station ID	Soil texture	Latitude	Longitude	Proposed downscaling approach			Uniform Disaggregation approach		
				ubRMSE (m ³ /m ³)	Bias (m ³ /m ³)	R	ubRMSE (m ³ /m ³)	Bias (m ³ /m ³)	R
RG003	L	31.72044	-110.14294	0.039	0.001	0.58	0.051	0.016	0.207
RG013	L	31.7238	-110.0911	0.031	-0.002	0.644	0.043	-0.057	0.472
RG014	L	31.69683	-110.09869	0.026	-0.041	0.691	0.033	0.011	0.594
RG018	L	31.70487	-110.08492	0.032	-0.037	0.435	0.039	0.007	0.39
RG020	L	31.6761	-110.07712	0.025	0.027	0.729	0.037	-0.002	0.471
RG028	L	31.72201	-110.0434	0.03	0.013	0.637	0.029	-0.005	0.709
RG034	L	31.69886	-110.0403	0.031	0.042	0.477	0.033	0.012	0.603
RG037	L	31.68613	-110.01556	0.028	0.064	0.448	0.045	0.054	0.149
RG040	L	31.72429	-110.01431	0.023	0.019	0.783	0.03	-0.006	0.662
RG046	L	31.70931	-109.99436	0.065	0.011	0.677	0.057	-0.03	0.634
RG057	L	31.72842	-109.98571	0.028	0.001	0.853	0.032	-0.026	0.681
RG069	L	31.76997	-109.9026	0.021	0.005	0.607	0.053	-0.062	0.706
RG070	L	31.75861	-109.89881	0.024	0.084	0.583	0.027	0.023	0.75
RG076	L	31.71956	-110.12815	-	-	-	-	-	-
RG082	L	31.73618	-109.94271	0.032	-0.014	0.631	0.037	-0.032	0.586
RG083	L	31.74377	-110.05292	0.015	-0.058	0.719	0.031	0.045	0.671
RG089	L	31.75682	-109.98308	0.02	-0.032	0.673	0.06	-0.028	-0.126
RG092	L	31.7386	-110.13545	-	-	-	-	-	-
RG100	L	31.67398	-110.01608	0.026	0.06	0.641	0.031	0.03	0.645
Average				0.029	0.008	0.637	0.039	-0.002	0.517

Using two CVSs, we summarize the accuracy of both downscaling approaches in Figure 1-10. It is observed that the proposed downscaling approach outperforms the uniform disaggregation approach for all performance measures used. It is also noted that when the downscaled SMAP soil moisture (or the original SMAP) is compared with in-situ observation for validation purposes, an unavoidable significant discrepancy between these two sets of data exacerbates the analysis. This is due to inherent properties of each observation. SMAP measures

a large-scale average of soil moisture, while in-situ station measures soil moisture at specific point. Even if all CVS in-situ observations within the downscaled or original SMAP grid cells are averaged to represent the soil moisture, significant differences are still to be expected.

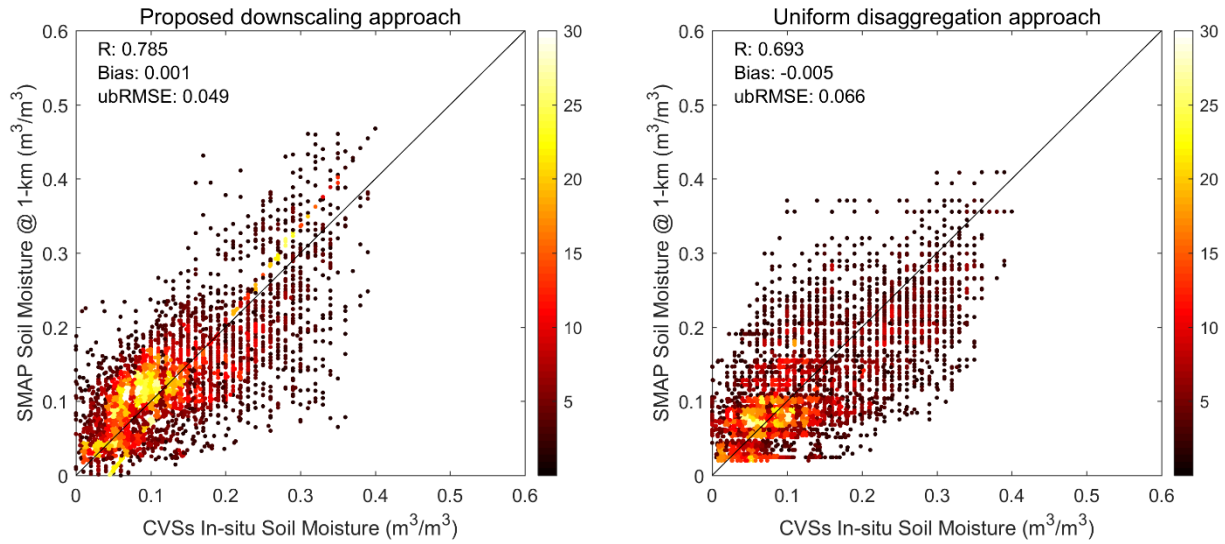


Figure 1-10 Comparison between the soil moisture retrieved from CVSs and those downscaled by two downscaling approaches used in this study.

Summary and Conclusion

This paper presents a new framework based on an ensemble learning algorithm to downscale SMAP radiometer soil moisture from its native resolution of 36 km to a finer resolution of 1km while using atmospheric and geophysical information acquired from high-resolution remote-sensing data and ground-based observations. The data sets used in the proposed model have been widely utilized in many studies for rescaling satellite soil moisture data, and are similar to those ancillary data used in SMAP Level 2 Enhanced Passive Soil Moisture Product (L2_SM_P_E) and standard L2_SM_P (Chan et al., 2017). This study was performed for the period of nine months (04/01/2015 to 12/31/2015) over the CONUS. The validation results based on in-situ soil moisture measurements collected from two CVSs and

three hundred sparse soil moisture networks confirmed that the downscaled SMAP soil moistures would adequately meet the SMAP soil moisture retrieval accuracy requirement ($ubRMSE=0.040\text{ m}^3/\text{m}^3$), and capture the spatial heterogeneity of soil parameters and dynamics of in-situ soil moisture observations. The downscaled soil moisture data obtained from the proposed downscaling approach is also compared with those from the uniform disaggregation approach over both CVSs and three hundred soil moisture networks, and in all cases, the proposed approach outperformed the uniform disaggregation approach. The results of this study also revealed that the inclusion of all input variables would result in best downscaling accuracy, however, the topography data was found to affect the results less than other input variables. The other merit of the proposed methodology is that it is not restricted to boundary conditions such as semiarid or humid regions, and it can be applied over a large area with different climatological patterns and soil characteristics.

The proposed rescaling model was calibrated using three hundred sparse in-situ soil moisture sensors evenly distributed over the CONUS. Future works may consider using other in-situ observations from different operational networks, such as COSMOS (Zreda et al., 2012) and GPS (Larson et al., 2010), and some others available from the International Soil Moisture Network (ISMN) (Kim et al., 2017) for model calibration and validation purposes.

Acknowledgements

We appreciate all who have provided high-quality in-situ soil moisture data for Little Washita River Watershed (<http://ars.mesonet.org/>), Walnut Gulch Experimental Watershed (<https://www.tucson.ars.ag.gov/dap/>), USCRN (<https://www.ncdc.noaa.gov/crn/uscrn/>) and

SCAN (<https://www.wcc.nrcs.usda.gov/scan/>) soil moisture networks. We also greatly thank two anonymous reviewers for constructive comments that improved the earlier version of this article.

References

- Alemohammad, S. H., Kolassa, J., Prigent, C., Aires, F., & Gentine, P. (2018). Global Downscaling of Remotely-Sensed Soil Moisture using Neural Networks. *Hydrology and Earth System Sciences Discussions*, 1–19. <https://doi.org/10.5194/hess-2017-680>
- Amit, Y., & Geman, D. (1997). Shape Quantization and Recognition with Randomized Trees. *Neural Computation*, 9(7), 1545–1588. <https://doi.org/10.1162/neco.1997.9.7.1545>
- Breiman, L. (2001). Random forests. *Machine Learning*, 45(1), 5–32. <https://doi.org/10.1023/A:1010933404324>
- Busch, F. A., Niemann, J. D., & Coleman, M. (2012). Evaluation of an empirical orthogonal function-based method to downscale soil moisture patterns based on topographical attributes. *Hydrological Processes*, 26(18), 2696–2709. <https://doi.org/10.1002/hyp.8363>
- Chakrabarti, S., Bongiovanni, T., Judge, J., Rangarajan, A., & Ranka, S. (2016). Disaggregation of SMAP L3 Brightness Temperatures to 9km using Kernel Machines. *IEEE Geoscience and Remote Sensing Letters*. arXiv:1601.05350v2
- Chakrabarti, S., Bongiovanni, T., Judge, J., Nagarajan, K., & Principe, J. C. (2015). Downscaling satellite-based soil moisture in heterogeneous regions using high-resolution remote sensing products and information theory: A synthetic study. *IEEE Transactions on Geoscience and Remote Sensing*, 53(1), 85–101. <https://doi.org/10.1109/TGRS.2014.2318699>
- Chakrabarti, S., Judge, J., Bongiovanni, T., Rangarajan, A., & Ranka, S. (2016). Disaggregation of Remotely Sensed Soil Moisture in Heterogeneous Landscapes Using Holistic Structure-Based Models. *IEEE Transactions on Geoscience and Remote Sensing*, 54(8), 4629–4641. <https://doi.org/10.1109/TGRS.2016.2547389>
- Chakrabarti, S., Judge, J., Bongiovanni, T., Rangarajan, A., & Ranka, S. (2018). Spatial Scaling Using Temporal Correlations and Ensemble Learning to Obtain High-Resolution Soil Moisture. *IEEE Transactions on Geoscience and Remote Sensing*, 56(3), 1238–1250. <https://doi.org/10.1109/TGRS.2017.2722236>
- Chan, S. K., Bindlish, R., O'Neill, P. E., Njoku, E., Jackson, T., Colliander, A., ... Kerr, Y. (2016). Assessment of the SMAP Passive Soil Moisture Product. *IEEE Transactions on Geoscience and Remote Sensing*, 54(8), 4994–5007. <https://doi.org/10.1109/TGRS.2016.2561938>
- Chan, S. K., Bindlish, R., O'Neill, P., Jackson, T., Njoku, E., Dunbar, S., ... Kerr, Y. (2017). Development and assessment of the SMAP enhanced passive soil moisture product. *Remote*

Sensing of Environment, 931-914. <https://doi.org/10.1016/j.rse.2017.08.025>

Chen, Y., Yang, K., Qin, J., Cui, Q., Lu, H., La, Z., ... Tang, W. (2017). Evaluation of SMAP, SMOS, and AMSR2 soil moisture retrievals against observations from two networks on the Tibetan Plateau. *Journal of Geophysical Research: Atmospheres*, 122(11), 5780–5792. <https://doi.org/10.1002/2016JD026388>

Choi, M., & Hur, Y. (2012). A microwave-optical/infrared disaggregation for improving spatial representation of soil moisture using AMSR-E and MODIS products. *Remote Sensing of Environment*, 124, 259–269. <https://doi.org/10.1016/j.rse.2012.05.009>

Coleman, M. L., & Niemann, J. D. (2013). Controls on topographic dependence and temporal instability in catchment-scale soil moisture patterns. *Water Resources Research*, 49(3), 1625–1642. <https://doi.org/10.1002/wrcr.20159>

Colliander, A., Jackson, T. J., Bindlish, R., Chan, S., Das, N., Kim, S. B., ... Yueh, S. (2017). Validation of SMAP surface soil moisture products with core validation sites. *Remote Sensing of Environment*, 191, 215–231. <https://doi.org/10.1016/j.rse.2017.01.021>

Colliander, A., Cosh, M. H., Misra, S., Jackson, T. J., Crow, W. T., Chan, S., ... Yueh, S. H. (2017). Validation and scaling of soil moisture in a semi-arid environment: SMAP validation experiment 2015 (SMAPVEX15). *Remote Sensing of Environment*, 196, 101–112. <https://doi.org/10.1016/j.rse.2017.04.022>

Colliander, A., Fisher, J. B., Halverson, G., Merlin, O., Misra, S., Bindlish, R., ... Yueh, S. (2017). Spatial Downscaling of SMAP Soil Moisture Using MODIS Land Surface Temperature and NDVI During SMAPVEX15. *IEEE Geoscience and Remote Sensing Letters*, 14(11), 2107–2111. <https://doi.org/10.1109/LGRS.2017.2753203>

Coopersmith, E. J., Bell, J. E., & Cosh, M. H. (2015). Extending the soil moisture data record of the U.S. Climate Reference Network (USCRN) and Soil Climate Analysis Network (SCAN). *Advances in Water Resources*, 79, 80–90. <https://doi.org/10.1016/j.advwatres.2015.02.006>

Coulibaly, P., Dibike, Y. B., & Anctil, F. (2005). Downscaling Precipitation and Temperature with Temporal Neural Networks. *Journal of Hydrometeorology*, 6(4), 483–496. <https://doi.org/10.1175/JHM409.1>

Crow, W. T., Berg, A. A., Cosh, M. H., Loew, A., Mohanty, B. P., Panciera, R., ... Walker, J. P. (2012). Upscaling Sparse Ground-Based Soil Moisture Observations for the Validation of Coarse-Resolution Satellite Soil Moisture Products, *Reviews of Geophysics*, 50(2). <https://doi.org/10.1029/2011RG000372>

Djamai, N., Magagi, R., Goïta, K., Merlin, O., Kerr, Y., & Roy, A. (2016). A combination of DISPATCH downscaling algorithm with CLASS land surface scheme for soil moisture estimation at fine scale during cloudy days. *Remote Sensing of Environment*, 184, 1–14. <https://doi.org/10.1016/j.rse.2016.06.010>

- Djamai, N., Magagi, R., Goita, K., Merlin, O., Kerr, Y., & Walker, A. (2015). Disaggregation of SMOS soil moisture over the Canadian Prairies. *Remote Sensing of Environment*, *170*, 255–268. <https://doi.org/10.1016/j.rse.2015.09.013>
- Entekhabi, B. D., Njoku, E. G., Neill, P. E. O., Kellogg, K. H., Crow, W. T., Edelstein, W. N., ... Zyl, J. Van. (2010). The Soil Moisture Active Passive (SMAP) Mission. *Proceedings of the IEEE*, *98(5)*, 704–716. <https://dspace.mit.edu/handle/1721.1/60043>
- Entekhabi, D., Reichle, R. H., Koster, R. D., & Crow, W. T. (2010). Performance Metrics for Soil Moisture Retrievals and Application Requirements. *Journal of Hydrometeorology*, *11(3)*, 832–840. <https://doi.org/10.1175/2010JHM1223.1>
- Fang, B., & Lakshmi, V. (2014). Soil moisture at watershed scale: Remote sensing techniques. *Journal of Hydrology*, *516*, 258–272. <https://doi.org/10.1016/j.jhydrol.2013.12.008>
- Gan, Y., Duan, Q., Gong, W., Tong, C., Sun, Y., Chu, W., ... Di, Z. (2014). A comprehensive evaluation of various sensitivity analysis methods: A case study with a hydrological model. *Environmental Modelling and Software*, *51*, 269–285. <https://doi.org/10.1016/j.envsoft.2013.09.031>
- Goyal, M. K., Burn, D. H., & Ojha, C. S. P. (2012). Evaluation of machine learning tools as a statistical downscaling tool: Temperatures projections for multi-stations for Thames River Basin, Canada. *Theoretical and Applied Climatology*, *108(3–4)*, 519–534. <https://doi.org/10.1007/s00704-011-0546-1>
- Hashmi, M. Z., Shamseldin, A. Y., & Melville, B. W. (2011). Statistical downscaling of watershed precipitation using Gene Expression Programming (GEP). *Environmental Modelling & Software*, *26(12)*, 1639–1646. <https://doi.org/10.1016/j.envsoft.2011.07.007>
- He, X., Chaney, N. W., Schleiss, M., & Sheffield, J. (2016). Spatial downscaling of precipitation using adaptable random forests. *Water Resources Research*, *52(10)*, 8217–8237. <https://doi.org/10.1002/2016WR019034>
- Hutengs, C., & Vohland, M. (2016). Downscaling land surface temperatures at regional scales with random forest regression. *Remote Sensing of Environment*, *178*, 127–141. <https://doi.org/10.1016/j.rse.2016.03.006>
- Im, J., Park, S., Rhee, J., Baik, J., & Choi, M. (2016). Downscaling of AMSR-E soil moisture with MODIS products using machine learning approaches. *Environmental Earth Sciences*, *75(15)*, 1–19. <https://doi.org/10.1007/s12665-016-5917-6>
- Jackson, T. J., O'Neill, P., Njoku, E., Chan, S., Bindlish, R., Colliander, A., ... Entekhabi, D. (2016). Calibration and Validation for the L2/3_SM_P Version 3 Data Products.
- Jackson, T. J., O'Neill, P., Njoku, E., Chan, S., Bindlish, R., Colliander, A., ... Entekhabi, D. (2016). Soil Moisture Active Passive (SMAP) Project Calibration and Validation for the L2/3_SM_P Version 3 Data Products, (SMAP Project), JPL D-93720, Jet Propulsion Laboratory, Pasadena,.

- Jackson, T., Colliander, A., Kimball, J., Reichle, R., Crow, W., Entekhabi, D., & Neill, P. O. (2012). Science Data Calibration and Validation Plan.
- Jing, W., Yang, Y., Yue, X., & Zhao, X. (2016). A spatial downscaling algorithm for satellite-based precipitation over the Tibetan plateau based on NDVI, DEM, and land surface temperature. *Remote Sensing*, 8(8). <https://doi.org/10.3390/rs8080655>
- Jones, A. R., & Brunsell, N. A. (2009). A scaling analysis of soil moisture-precipitation interactions in a regional climate model. *Theoretical and Applied Climatology*, 98(3–4), 221–235. <https://doi.org/10.1007/s00704-009-0109-x>
- Kaheil, Y. H., Gill, M. K., Mckee, M., Bastidas, L. A., & Rosero, E. (2008). Downscaling and Assimilation of Surface Soil Moisture Using Ground Truth Measurements. *IEEE Transactions on Geoscience and Remote Sensing*, 46(5), 1375–1384.
- Ke, Y., Im, J., Park, S., & Gong, H. (2016). Downscaling of MODIS One kilometer evapotranspiration using Landsat-8 data and machine learning approaches. *Remote Sensing*, 8(3), 1–26. <https://doi.org/10.3390/rs8030215>
- Kerr, Y. H. (2007). Soil moisture from space: Where are we? *Hydrogeology Journal*, 15(1), 117–120. <https://doi.org/10.1007/s10040-006-0095-3>
- Kim, G., & Barros, A. P. (2002). Downscaling of remotely sensed soil moisture with a modified fractal interpolation method using contraction mapping and ancillary data. *Remote Sensing of Environment*, 83(3), 400–413. [https://doi.org/10.1016/S0034-4257\(02\)00044-5](https://doi.org/10.1016/S0034-4257(02)00044-5)
- Kim, H., Parinussa, R., Konings, A. G., Wagner, W., Cosh, M. H., Lakshmi, V., ... Choi, M. (2017). Global-scale assessment and combination of SMAP with ASCAT (active) and AMSR2 (passive) soil moisture products. *Remote Sensing of Environment*, 260–275. <https://doi.org/10.1016/j.rse.2017.10.026>
- Kolassa, J., Reichle, R. H., Liu, Q., Alemohammad, S. H., Gentine, P., Aida, K., ... Walker, J. P. (2018). Estimating surface soil moisture from SMAP observations using a Neural Network technique. *Remote Sensing of Environment*, 204, 43–59. <https://doi.org/10.1016/j.rse.2017.10.045>
- Larson, K. M., Braun, J. J., Small, E. E., Zavorotny, V. U., Gutmann, E. D., & Bilich, A. L. (2010). GPS Multipath and Its Relation to Near-Surface Soil Moisture Content. *IEEE Journal of Selected Topics in Applied Earth Observations and Remote Sensing*, 3(1), 91–99. <https://doi.org/10.1109/JSTARS.2009.2033612>
- Lievens, H., De Lannoy, G. J. M., Al Bitar, A., Drusch, M., Dumedah, G., Hendricks Franssen, H. J., ... Pauwels, V. R. N. (2016). Assimilation of SMOS soil moisture and brightness temperature products into a land surface model. *Remote Sensing of Environment*, 180, 292–304. <https://doi.org/10.1016/j.rse.2015.10.033>
- Ma, C., Li, X., Wei, L., & Wang, W. (2017). Multi-scale validation of SMAP soil moisture products over cold and arid regions in Northwestern China using distributed ground

- observation data. *Remote Sensing*, 9(4). <https://doi.org/10.3390/rs9040327>
- Mascaro, G., Vivoni, E. R., & Deidda, R. (2011). Soil moisture downscaling across climate regions and its emergent properties. *Journal of Geophysical Research*, 116, 1–19. <https://doi.org/10.1029/2011JD016231>
- Mattikalli, N. M., Engman, E. T., Jackson, T. J., & Ahuja, L. R. (1998). Microwave remote sensing of temporal variations of brightness temperature and near-surface soil water content during a watershed-scale field experiment, and its application to the estimation of soil physical properties. *Water Resources Research*, 34(9), 2289–2299. <https://doi.org/10.1029/98WR00553>
- Merlin, O., Malbêteau, Y., Notfi, Y., Bacon, S., Er-Raki, S., Khabba, S., & Jarlan, L. (2015). Performance metrics for soil moisture downscaling methods: Application to DISPATCH data in central Morocco. *Remote Sensing*, 7(4), 3783–3807. <https://doi.org/10.3390/rs70403783>
- Merlin, O., Walker, J. P., Chehbouni, A., & Kerr, Y. (2008). Towards deterministic downscaling of SMOS soil moisture using MODIS derived soil evaporative efficiency. *Remote Sensing of Environment*, 112(10), 3935–3946. <https://doi.org/10.1016/j.rse.2008.06.012>
- Miller, D. A., & White, R. A. (1998). A Conterminous United States Multilayer Soil Characteristics Dataset for Regional Climate and Hydrology Modeling. *Earth Interactions*, 2(2), 1–26.
- Mishra, V., Ellenburg, W. L., Griffin, R. E., Mecikalski, J. R., Cruise, J. F., Hain, C. R., & Anderson, M. C. (2018). An initial assessment of a SMAP soil moisture disaggregation scheme using TIR surface evaporation data over the continental United States. *International Journal of Applied Earth Observation and Geoinformation*, 68, 92–104. <https://doi.org/10.1016/j.jag.2018.02.005>
- Mishra, A., Vu, T., Veettil, A. V., & Entekhabi, D. (2017). Drought monitoring with soil moisture active passive (SMAP) measurements. *Journal of Hydrology*, 552, 620–632. <https://doi.org/10.1016/j.jhydrol.2017.07.033>
- Molero, B., Merlin, O., Malbêteau, Y., Al Bitar, A., Cabot, F., Stefan, V., ... Jackson, T. J. (2016). SMOS disaggregated soil moisture product at 1 km resolution: Processor overview and first validation results. *Remote Sensing of Environment*, 180, 361–376. <https://doi.org/10.1016/j.rse.2016.02.045>
- Njoku, E. G., & Entekhabi, D. (1996). Passive microwave remote sensing of soil moisture. *Journal of Hydrology*, 184(1–2), 101–129. [https://doi.org/10.1016/0022-1694\(95\)02970-2](https://doi.org/10.1016/0022-1694(95)02970-2)
- Owe, M., de Jeu, R., & Holmes, T. (2008). Multisensor historical climatology of satellite-derived global land surface moisture. *Journal of Geophysical Research: Earth Surface*, 113(1), 1–17. <https://doi.org/10.1029/2007JF000769>
- Pan, M., Cai, X., Chaney, N., Entekhabi, D., & Wood, E. F. (2016). An Initial Assessment of

- SMAP Soil Moisture Retrievals Using High Resolution Model Simulations and In-situ Observations. *Geophysical Research Letters*, 9662–9668. <https://doi.org/10.1002/2016GL069964>
- Panciera, R., Walker, J. P., Kalma, J. D., Kim, E. J., Member, S., Hacker, J. M., ... Experiment, F. (2008). The NAFE ' 05 / CoSMOS Data Set : Toward SMOS Soil Moisture Retrieval , Downscaling , and Assimilation. *Cosmos*, 46(3), 1–10. <https://doi.org/10.1109/TGRS.2007.915403>
- Park, S., Park, S., Im, J., Rhee, J., Shin, J., & Park, J. (2017). Downscaling GLDAS Soil Moisture Data in East Asia through Fusion of Multi-Sensors by Optimizing Modified Regression Trees. *Water*, 9(5), 332. <https://doi.org/10.3390/w9050332>
- Pellenq, J., Kalma, J., Boulet, G., Saulnier, G. M., Wooldridge, S., Kerr, Y., & Chehbouni, A. (2003). A disaggregation scheme for soil moisture based on topography and soil depth. *Journal of Hydrology*, 276(1–4), 112–127. [https://doi.org/10.1016/S0022-1694\(03\)00066-0](https://doi.org/10.1016/S0022-1694(03)00066-0)
- Pelletier, C., Valero, S., Inglada, J., Champion, N., & Dedieu, G. (2016). Assessing the robustness of Random Forests to map land cover with high resolution satellite image time series over large areas. *Remote Sensing of Environment*, 187, 156–168. <https://doi.org/10.1016/j.rse.2016.10.010>
- Peng, J., Niesel, J., & Loew, A. (2015). Evaluation of soil moisture downscaling using a simple thermal-based proxy-the REMEDHUS network (Spain) example. *Hydrology and Earth System Sciences*, 19(12), 4765–4782. <https://doi.org/10.5194/hess-19-4765-2015>
- Peng, J., Loew, A., Zhang, S., & Wang, J. (2016). Spatial downscaling of global satellite soil moisture data using temperature vegetation dryness index. *IEEE Transactions on Geoscience and Remote Sensing*, 1(54), 558–566.
- Petropoulos, G. P., Ireland, G., & Barrett, B. (2015). Surface soil moisture retrievals from remote sensing: Current status, products & future trends. *Physics and Chemistry of the Earth*, 83–84, 36–56. <https://doi.org/10.1016/j.pce.2015.02.009>
- Piles, M., Sánchez, N., Vall-Llossera, M., Camps, A., Martínez-Fernandez, J., Martínez, J., & Gonzalez-Gambau, V. (2014). A downscaling approach for SMOS land observations: Evaluation of high-resolution soil moisture maps over the Iberian peninsula. *IEEE Journal of Selected Topics in Applied Earth Observations and Remote Sensing*, 7(9), 3845–3857. <https://doi.org/10.1109/JSTARS.2014.2325398>
- Piles, M., Petropoulos, G. P., Sanchez, N., Gonzalez-Zamora, angel, & Ireland, G. (2016). Towards improved spatio-temporal resolution soil moisture retrievals from the synergy of SMOS and MSG SEVIRI spaceborne observations. *Remote Sensing of Environment*, 180, 403–417. <https://doi.org/10.1016/j.rse.2016.02.048>
- Piles, M., Camps, A., Vall-Llossera, M., Corbella, I., Panciera, R., Rudiger, C., ... Walker, J. (2011). Downscaling SMOS-derived soil moisture using MODIS visible/infrared data. *IEEE Transactions on Geoscience and Remote Sensing*, 49(9), 3156–3166.

<https://doi.org/10.1109/TGRS.2011.2120615>

- Raje, D., & Mujumdar, P. P. (2011). A comparison of three methods for downscaling daily precipitation in the Punjab region. *Hydrological Processes*, 25(23), 3575–3589. <https://doi.org/10.1002/hyp.8083>
- Ranney, K. J., Niemann, J. D., Lehman, B. M., Green, T. R., & Jones, A. S. (2015). A method to downscale soil moisture to fine resolutions using topographic, vegetation, and soil data. *Advances in Water Resources*, 76, 81–96. <https://doi.org/10.1016/j.advwatres.2014.12.003>
- Reichle, R. H., Entekhabi, D., & McLaughlin, D. B. (2001). Downscaling of radio brightness measurements for soil moisture estimation: A four-dimensional variational data assimilation approach. *Water Resources Research*, 37(9), 2353–2364. <https://doi.org/10.1029/2001WR000475>
- Rodriguez-Fernandez, N. J., Aires, F., Richaume, P., Kerr, Y. H., Prigent, C., Kolassa, J., ... Drusch, M. (2015). Soil Moisture Retrieval Using Neural Networks: Application to SMOS. *IEEE Transactions on Geoscience and Remote Sensing*, 53(11), 5991–6007. <https://doi.org/10.1109/TGRS.2015.2430845>
- Sahoo, A. K., De Lannoy, G. J. M., Reichle, R. H., & Houser, P. R. (2013). Assimilation and downscaling of satellite observed soil moisture over the Little River Experimental Watershed in Georgia, USA. *Advances in Water Resources*, 52, 19–33. <https://doi.org/10.1016/j.advwatres.2012.08.007>
- Sanchez, N., Piles, M., Scaini, A., Martinez-Fernandez, J., Camps, A., & Vall-Llossera, M. (2012). Spatial patterns of SMOS downscaled soil moisture maps over the remedhus network (Spain). *International Geoscience and Remote Sensing Symposium (IGARSS)*, 714–717. <https://doi.org/10.1109/IGARSS.2012.6351465>
- Seneviratne, S. I., Corti, T., Davin, E. L., Hirschi, M., Jaeger, E. B., Lehner, I., ... Teuling, A. J. (2010). Investigating soil moisture-climate interactions in a changing climate: A review. *Earth-Science Reviews*, 99(3–4), 125–161. <https://doi.org/10.1016/j.earscirev.2010.02.004>
- Shellito, P. J., & Small, E. E. (2017). Controls on surface soil drying rates observed by SMAP and simulated by the Noah land surface model. *Hydrology and Earth System Sciences Discussions*, 22, 1649–1663. <https://doi.org/10.5194/hess-2017-338>
- Shellito, P. J., Small, E. E., Colliander, A., Bindlish, R., Cosh, M. H., Berg, A. A., ... Walker, J. P. (2016). SMAP soil moisture drying more rapid than observed in situ following rainfall events. *Geophysical Research Letters*, 43, 8068–8075. <https://doi.org/10.1002/2016GL069946>
- Shin, Y., & Mohanty, B. P. (2013). Development of a deterministic downscaling algorithm for remote sensing soil moisture footprint using soil and vegetation classifications. *Water Resources Research*, 49(10), 6208–6228. <https://doi.org/10.1002/wrcr.20495>
- Song, C., Jia, L., & Menenti, M. (2014). Retrieving high-resolution surface soil moisture by

- downscaling AMSR-E brightness temperature using MODIS LST and NDVI data. *IEEE Journal of Selected Topics in Applied Earth Observations and Remote Sensing*, 7(3), 935–942. <https://doi.org/10.1109/JSTARS.2013.2272053>
- Srivastava, P. K., Han, D., Ramirez, M. R., & Islam, T. (2013). Machine Learning Techniques for Downscaling SMOS Satellite Soil Moisture Using MODIS Land Surface Temperature for Hydrological Application. *Water Resources Management*, 27(8), 3127–3144. <https://doi.org/10.1007/s11269-013-0337-9>
- Su, C. H., Ryu, D., Young, R. I., Western, A. W., & Wagner, W. (2013). Inter-comparison of microwave satellite soil moisture retrievals over the Murrumbidgee Basin, southeast Australia. *Remote Sensing of Environment*, 134(2013), 1–11. <https://doi.org/10.1016/j.rse.2013.02.016>
- Taylor, K. E. (2001). Summarizing multiple aspects of model performance in a single diagram. *Journal of Geophysical Research: Atmospheres*, 106(D7), 7183–7192. <https://doi.org/10.1029/2000JD900719>
- Valverde, M. C., Araujo, E., & Campos Velho, H. (2014). Neural network and fuzzy logic statistical downscaling of atmospheric circulation-type specific weather pattern for rainfall forecasting. *Applied Soft Computing Journal*, 22, 681–694. <https://doi.org/10.1016/j.asoc.2014.02.025>
- Velpuri, N. M., Senay, G. B., & Morissette, J. T. (2015). Evaluating New SMAP Soil Moisture for Drought Monitoring in the Rangelands of the US High Plains. *Rangelands*, 38(4), 183–190. <https://doi.org/10.1016/j.rala.2016.06.002>
- Verhoest, N. E. C., Lievens, H., Wagner, W., Alvarez-Mozos, J., Moran, M. S., & Mattia, F. (2008). On the soil roughness parameterization problem in soil moisture retrieval of bare surfaces from synthetic aperture radar. *Sensors*, 8(7), 4213–4248. <https://doi.org/10.3390/s8074213>
- Wagner, W., Hahn, S., Kidd, R., Melzer, T., Bartalis, Z., Hasenauer, S., ... Rubel, F. (2013). The ASCAT soil moisture product: A review of its specifications, validation results, and emerging applications. *Meteorologische Zeitschrift*, 22(1), 5–33. <https://doi.org/10.1127/0941-2948/2013/0399>
- Wilson, D. J., Western, A. W., & Grayson, R. B. (2005). A terrain and data-based method for generating the spatial distribution of soil moisture. *Advances in Water Resources*, 28(1), 43–54. <https://doi.org/10.1016/j.advwatres.2004.09.007>
- Zerenner, T., Venema, V., Friederichs, P., & Simmer, C. (2016). Downscaling near-surface atmospheric fields with multi-objective Genetic Programming. *Environmental Modelling and Software*, 84, 85–98. <https://doi.org/10.1016/j.envsoft.2016.06.009>
- Zhang, X., Zhang, T., Zhou, P., Shao, Y., & Gao, S. (2017). Validation analysis of SMAP and AMSR2 soil moisture products over the United States using ground-based measurements. *Remote Sensing*, 9(2). <https://doi.org/10.3390/rs9020104>

Zhao, W., & Li, A. (2013). A downscaling method for improving the spatial resolution of AMSR-E derived soil moisture product based on MSG-SEVIRI data. *Remote Sensing*, 5(12), 6790–6811. <https://doi.org/10.3390/rs5126790>

Zreda, M., Shuttleworth, W. J., Zeng, X., Zweck, C., Desilets, D., Franz, T., & Rosolem, R. (2012). COSMOS: The cosmic-ray soil moisture observing system. *Hydrology and Earth System Sciences*, 16(11), 4079–4099. <https://doi.org/10.5194/hess-16-4079-2012>

CHAPTER 2 ENHANCING HYDROLOGIC DATA ASSIMILATION BY EVOLUTIONARY PARTICLE FILTER AND MARKOV CHAIN MONTE CARLO²

Abstract

Particle Filters (PFs) have received increasing attention by researchers from different disciplines including the hydro-geosciences, as an effective tool to improve model predictions in nonlinear and non-Gaussian dynamical systems. The implication of dual state and parameter estimation using the PFs in hydrology has evolved since 2005 from the PF-SIR (sampling importance resampling) to PF-MCMC (Markov Chain Monte Carlo), and now to the most effective and robust framework through evolutionary PF approach based on Genetic Algorithm (GA) and MCMC, the so-called EPFM. In this framework, the prior distribution undergoes an evolutionary process based on the designed mutation and crossover operators of GA. The merit of this approach is that the particles move to an appropriate position by using the GA optimization and then the number of effective particles is increased by means of MCMC, whereby the particle degeneracy is avoided and the particle diversity is improved. In this study, the usefulness and effectiveness of the proposed EPFM is investigated by applying the technique on a conceptual and highly nonlinear hydrologic model over four river basins located in different climate and geographical regions of the United States. Both synthetic and real case studies

² Abbaszadeh, P., Moradkhani, H., Yan, H., 2018. Enhancing hydrologic data assimilation by evolutionary Particle Filter and Markov Chain Monte Carlo. *Adv. Water Resour.* 111, 192–204.
<https://doi.org/10.1016/j.advwatres.2017.11.011>

demonstrate that the EPFM improves both the state and parameter estimation more effectively and reliably as compared with the PF-MCMC.

Keywords: Particle Filters; Markov Chain Monte Carlo; Genetic Algorithm; Hydrologic Prediction

Introduction

Accurate and reliable estimation of prognostic variables, such as streamflow and soil moisture, has always been one of the main challenges for hydrologists. Although hydrologic modeling can provide estimates of these quantities, the simulation results are potentially biased or erroneous given the following uncertainties: 1) forcing data uncertainty due to the limitation of measurements and spatio-temporal representativeness of the data; 2) parameter uncertainty due to conceptualization of the model and non-uniqueness of parameters; 3) model structural uncertainty due to the imperfect representation of a real system; 4) initial and boundary condition uncertainty. Therefore, hydrologic predictions are better generated within a probabilistic framework, providing a mechanism to estimate the uncertainties involved in all layers of hydrologic predictions (Moradkhani et al., 2012). Most often, this is performed through Bayesian inference. Bayesian methods have been well acknowledged and used in numerous efforts to estimate the uncertainties in hydrologic model predictions (e.g., Kuczera and Parent, 1998; Marshal et al., 2004; Moradkhani et al., 2005; DeChant and Moradkhani, 2014; Yan et al., 2015; Pathiraja et al., 2016; Pathiraja et al., 2016).

Data Assimilation (DA) has been recognized as one of the effective methods to improve hydrologic prediction. Currently, the most widely used DA technique in the hydrologic community is the ensemble Kalman filter (EnKF) (Reichle et al., 2002; Crow and Wood, 2003; Moradkhani et al., 2005; De Lannoy et al., 2007). Although the successful application of the

EnKF and its variants has been reported in hydrologic literature, this technique has some inherent features resulting in sub-optimal performance. These include the Gaussian assumption of errors, linear updating rule within the EnKF and violation of water balance that limit its superiority (Moradkhani et al., 2005; Matgen et al., 2010; Noh et al., 2011; Plaza et al., 2012; DeChant and Moradkhani, 2012; Yan and Moradkhani, 2016). Given these concerns, data assimilation by means of Particle Filter (PF) as a viable alternative to the EnKF has garnered increasing attention in literature (e.g., Noh et al., 2011; Liu et al., 2012; Moradkhani et al., 2012; Montzka et al., 2013; Dong et al., 2015; Yan et al., 2017). The PF approach can relax the Gaussian assumption of error distributions by potentially characterizing multimodal or skewed distribution in state variables and parameters. Therefore, it can provide a thorough representation of the posterior distribution for a given nonlinear and non-Gaussian system. DeChant and Moradkhani (2012) presented a detailed performance assessment between the EnKF and PF, and found more robust and effective performance of the PF with respect to the EnKF verified by both deterministic and probabilistic measures. Van Leeuwen (2009) provided a comprehensive review of the PF and its applications in geophysical systems.

Despite the success of the PF, one potential limitation has been the particle degeneracy. Particle degeneracy occurs when most of the particles have negligible weight, such that the variance of importance weights increases over time and the particles lose their ability to correctly approximate the posterior distribution (Moradkhani et al., 2005). In order to mitigate the particle degeneracy problem, several procedures have been proposed. Noh et al. (2011) proposed the lagged filtering approach to preserve the sample diversity. Andrieu et al. (2010) proposed the MCMC technique within the PF to reduce weight degeneracy. Moradkhani et al. (2012) re-designed the PF-MCMC by integrating the variable variance multiplier (VVM) (Leisenring and

Moradkhani, 2012) for the appropriate and objective perturbation of observation and parameters, and then conducted the combined state parameter estimation using the PF-MCMC.

On the other hand, intelligent search and optimization methods categorized as Metaheuristic Algorithms (MAs) in computer science literature have also been used to mitigate the degeneracy problem. This includes Genetic Algorithm (GA) (Higuchi, 1997; Kwok et al., 2005; Park et al., 2009), Evolution Strategy (ES) (Uosaki et al., 2003; Uosaki et al., 2004), Particle Swarm Optimization (PSO) (Wang et al., 2006; Li et al., 2013), Ant Colony Optimization (ACO) (Xu et al., 2009; Park et al., 2010; Zhu et al., 2010), Immune Genetic Algorithm (IGA) (Han et al., 2011), and Inverse Weed Optimization (IWO) (Ahmadi et al., 2012). Among these attempts, GA has received more attention and is known as a more effective method to combine with the PF to prevent the particle degeneracy. Kwok et al. (2005) proposed an evolutionary PF where the genetic operators were performed on the prior particles. However, the procedure only included the crossover operator. Heris and Khaloozadeh (2014) incorporated the Non-dominated Sorting GA II (NSGA-II) within the PF framework to improve the estimation performance. This strategy is only feasible for simple models due to large computational burden, since an optimization problem should be solved in every iteration. Literature suggests that instead of formulating PF into a GA optimization problem, incorporating only the evolutionary concept of this approach within the PF has more potential to improve its performance, while making it computationally less intensive. For example, Yin and Zhu (2015) used GA operators, i.e., crossover and mutation, within the PF to modify the small-weight particles and they concluded that GA could be an appropriate choice to combine with PF in order to obtain better posterior distributions.

More specifically, in the entire hybrid GA and PF models developed by far, the researchers have proposed different formulations to set up GA parameters (crossover and mutation). Although these approaches could enhance the effectiveness of the PFs in different applications, the methods appear too subjective in terms of GA parameter selection. This means an inappropriate selection of these parameters may degrade the assimilation performance. In addition, although GA regulates the particle weights properly, it may lead to sub-optimal performance since it is possible that the shuffled particles after the GA operators move outside the posterior distribution. To cope with these deficiencies, in this study we combine MCMC with GA algorithm (hereafter referred to as GA-MCMC) and use it within the importance sampling step of the PF-MCMC model (Moradkhani et al. 2012). The presented algorithm is named the Evolutionary Particle Filter with MCMC (EPFM). The developed method not only reduces the subjectivity of GA with respect to its parameter selection, but also enables the user to further tackle the particle degeneracy and sample impoverishment problems to improve the hydrologic predictions.

The rest of the paper is organized as follows. In section 2, the theory and details of the proposed EPFM are described. In section 3, the synthetic and real case studies are presented and the results are discussed. Finally, the conclusion of this paper is provided in section 4.

Theory and Methods

Sequential Bayesian Estimation

Following previous work by Moradkhani (2008), the differential equations that describe the generic nonlinear dynamic system are described as follows:

$$x_t = f(x_{t-1}, u_t, \theta) + \omega_t \quad (1)$$

$$y_t = h(x_t) + v_t \quad (2)$$

where $x_t \in \mathbb{R}^n$ is a vector of the uncertain state variables at time t , u_t is the uncertain forcing data, $\theta \in \mathbb{R}^d$ is a vector of model parameters, $y_t \in \mathbb{R}^m$ is a vector of observation data, ω_t represents the model error, and v_t is the measurement error. In most cases, ω_t and v_t are assumed as white noises with mean zero and covariance Q_t and R_t , respectively. Furthermore, the two noises ω_t and v_t are assumed to be independent. Since Moradkhani et al. (2005) provided a detailed literature on the sequential Bayesian filtering formalism, in this paper only a concise introduction is presented. Based on the Bayes' Law, the posterior distribution of the state variables at time t is as follows:

$$p(x_t|y_{1:t}) = p(x_t|y_{1:t-1}, y_t) = \frac{p(y_t|x_t)p(x_t|y_{1:t-1})}{p(y_t|y_{1:t-1})} = \frac{p(y_t|x_t)p(x_t|y_{1:t-1})}{\int p(y_t|x_t)p(x_t|y_{1:t-1})dx_t} \quad (3)$$

$$p(x_t|y_{1:t-1}) = \int p(x_t, x_{t-1}|y_{1:t-1})dx_{t-1} = \int p(x_t|x_{t-1})p(x_{t-1}|y_{1:t-1})dx_{t-1} \quad (4)$$

where $p(y_t|x_t)$ is the likelihood for time step t , $p(x_t|y_{1:t-1})$ is the prior distribution, and $p(y_t|y_{1:t-1})$ is the normalization factor. The marginal likelihood function $p(y_{1:t})$ can be computed as:

$$p(y_{1:t}) = p(y_1) \prod_{t=1}^t p(y_t|y_{1:t-1}) \quad (5)$$

where the normalization factor $p(y_t|y_{1:t-1})$ is calculated as follows:

$$p(y_t|y_{1:t-1}) = \int p(y_t, x_t|y_{1:t-1})dx_t = \int p(y_t|x_t)p(x_t|y_{1:t-1})dx_t \quad (6)$$

The multi-dimensional integration and analytical solution of (3) is only feasible for special cases, such as the linear systems with Gaussian noise. Therefore, for practical reasons the posterior distribution is approximated using a set of random replicates with associated weights.

Particle Filter-Markov Chain Monte Carlo (PF-MCMC)

The PF-MCMC (Moradkhani et al., 2012) is an extension of the PF-SIR (sampling importance resampling) (Moradkhani et al., 2005). The application of MCMC to the PF leads to a more complete estimation of posteriors and reduces the risk of parameter impoverishment. The PF-MCMC consists of two steps: 1) generating ensemble model state predictions and parameters; and 2) updating predictions and parameters when new observations become available. This leads to the posterior in (3), which is approximated as:

$$p(x_t|y_{1:t}) \approx \sum_{i=1}^N w^{i+} \delta(x_t - x_t^i) \quad (7)$$

where w^{i+} is the posterior weight of the i -th particle, δ is the Dirac delta function, and N is the number of particles. The normalized weights are calculated using:

$$w^{i+} = \frac{w^{i-} \cdot p(y_t|x_t^i, \theta_t^i)}{\sum_{i=1}^N w^{i-} \cdot p(y_t|x_t^i, \theta_t^i)} \quad (8)$$

where w^{i-} is the prior particle weights, and the $p(y_t|x_t^i, \theta_t^i)$ can be computed from the likelihood $L(y_t|x_t^i, \theta_t^i)$. For simplicity, a Gaussian likelihood can be used to estimate $L(y_t|x_t^i, \theta_t^i)$:

$$L(y_t|x_t^i, \theta_t^i) = \frac{1}{\sqrt{(2\pi)^m |R_t|}} \exp \left[-\frac{1}{2} (y_t - h(x_t^i))^T R_t^{-1} (y_t - h(x_t^i)) \right] \quad (9)$$

To obtain approximate samples from $p(x_t|y_{1:t})$, a resampling operation is necessary. The SIR algorithm is suggested to resample the particles with a probability greater than the uniform probability. This algorithm eliminates the particles with lower weights, while retaining the particles with higher weights. After application of the SIR algorithm, all the particle weights are set to $1/N$. Because particles with large weights are likely to be drawn multiple times during resampling, this may result in a loss of diversity among particles, the problem known as sample

impoverishment. To avoid the sample impoverishment, a perturbation of the resampled parameters is recommended. Then, a proposal distribution is formed to generate proposed parameters $\theta_t^{i,p}$:

$$\theta_t^{i,p} = \theta_t^{i+} + \varepsilon_t^i \quad \varepsilon_t^i \sim N[0, s_t \text{Var}(\theta_t^{i-})] \quad (10)$$

where θ_t^{i+} is the parameters after SIR, $\text{Var}(\theta_t^{i-})$ is the variance of the prior parameters at the current time step, and s_t is a small tuning time-variant parameter. To reject the parameter samples $\theta_t^{i,p}$ that move outside the filtering posterior distribution, a metropolis acceptance ratio α is used to determine whether to accept the proposed parameters:

$$\alpha = \min\left(1, \frac{p(x_t^{i,p}, \theta_t^{i,p} | y_{1:t})}{p(x_t^{i+}, \theta_t^{i+} | y_{1:t})}\right) \quad (11)$$

where $p(x_t^{i,p}, \theta_t^{i,p} | y_{1:t})$ is the proposed joint probability distribution:

$$p(x_t^{i,p}, \theta_t^{i,p} | y_{1:t}) \propto p(y_{1:t} | x_t^{i,p}, \theta_t^{i,p}) \cdot p(x_t^{i,p} | \theta_t^{i,p}, y_{1:t-1}) \cdot p(\theta_t^{i,p} | y_{1:t-1}) \quad (12)$$

$$x_t^{i,p} = f(x_{t-1}^{i+}, u_t^{i+}, \theta_t^{i,p}) \quad (13)$$

where $x_t^{i,p}$ is a sample from the proposal state distribution at time step t and u_t^{i+} is the perturbed forcing data associated with the i th particle. It is noted that we perturb the forcing data by N times prior to generating the proposal distribution. Therefore, it is necessary to use the same perturbed forcing data u_t^{i+} to calculate the proposed state $x_t^{i,p}$. Unlike the variants of the Kalman filters, this algorithm does not adjust the state variables, and therefore preserves the water balance.

Since the optimal tuning factor s_t is unknown in a sequential framework, it is beneficial to treat variables s_t as a time-variant quantity and estimate it automatically. Moradkhani et al.

(2012) modified the variable variance multiplier (VVM) method (Leisenring and Moradkhani, 2012), to automatically obtain the most fitting tuning factor s_t in (11).

Evolutionary PF-MCMC (EPFM)

Here, we propose an approach relying on hybrid GA and MCMC techniques to pre-process the ensemble members within the PF-MCMC method (Moradkhani et al., 2012). The developed methodology integrates the MCMC algorithm with the evolutionary concept of GA to enhance the performance of particle filtering. The proposed algorithm is illustrated in Figure 2-1. The main idea behind this method is to construct a more informative prior, which leads to a more reliable posterior distribution. It is important to mention that in this framework, the MCMC technique is used twice, once during the importance sampling step, when it is combined with the GA to obtain the desirable proposal state distribution (proposed GA-MCMC framework which will be discussed in section 2.3.1, green dashed line shown in Figure 2-1), and later in the resampling step for parameter updating, as discussed in section 2.2. In fact, what distinguishes the EPFM from the PF-MCMC is the utilization of GA-MCMC in the importance sampling step of the PF-MCMC approach. Here, the hybrid GA-MCMC technique and how it is used within the PF-MCMC model are explained in detail.

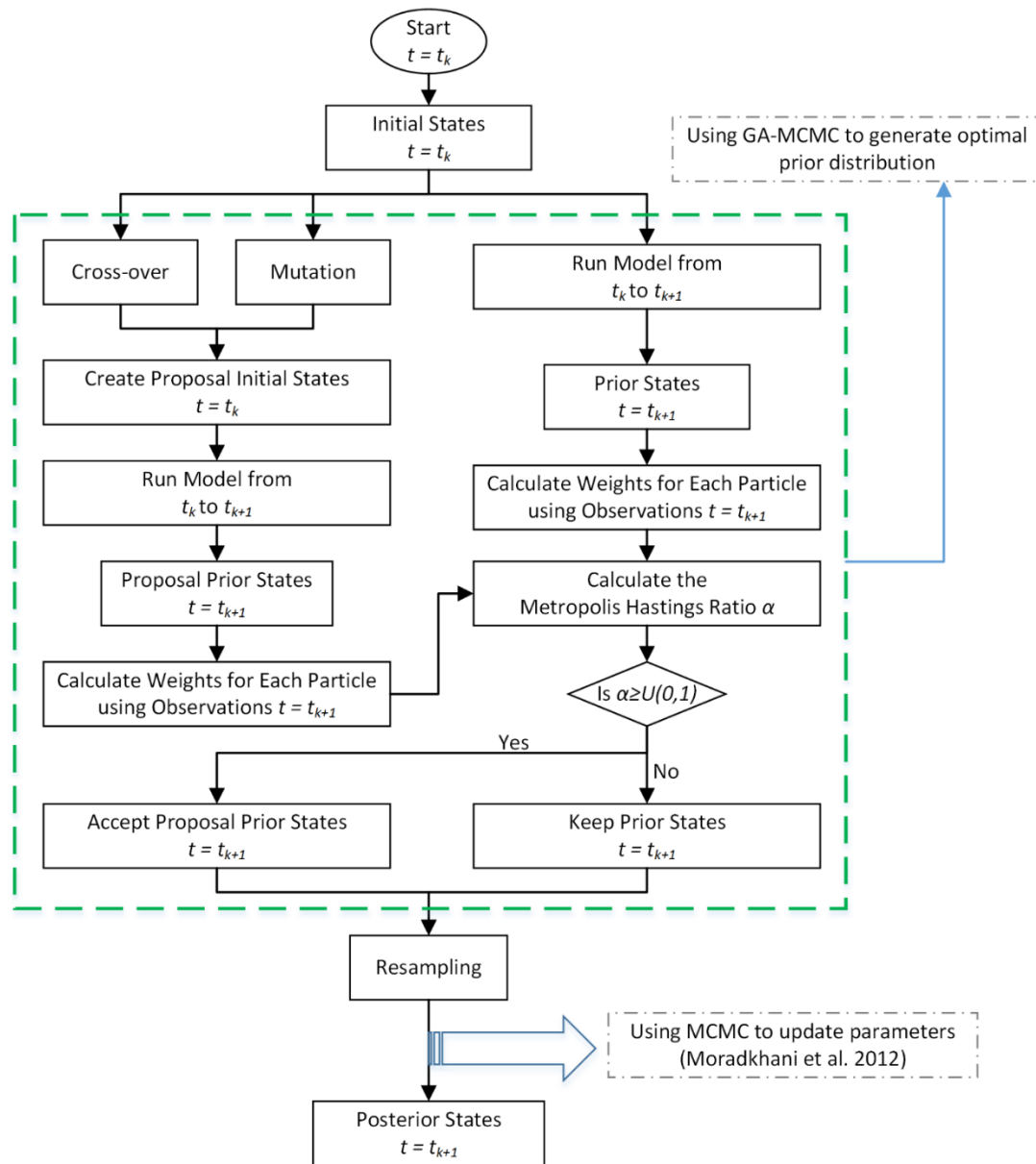


Figure 2-1 Flowchart of the proposed EPFM algorithm. In this study, the MCMC is used twice: before resampling step in order to accept or reject the new generated particle (state variable) leading to an appropriate state prior distribution, and after the resampling step during the update of the model parameters.

Hybrid GA-MCMC

The GA-MCMC is a new strategy that can be applied to PF to simultaneously mitigate the particle degeneration by increasing the particle diversity and enhance the accuracy and reliability of data assimilation. The GAs are adaptive heuristic search methods based on principles of natural evolution and genetics. The GA encodes the decision variables of a problem into finite-length strings of alphabets (Holland, 1975). The strings, also referred to as chromosomes, are the candidate solutions to the search problem. A chromosome is composed of a sequence of genes from a certain alphabet. An alphabet could consist of continuous values, binary digits, integers, symbols, matrices, etc. The representation of chromosomes depends on how the problem is structured in the GA. Figure 2-2 demonstrates a color coding of the proposed GA-MCMC process.

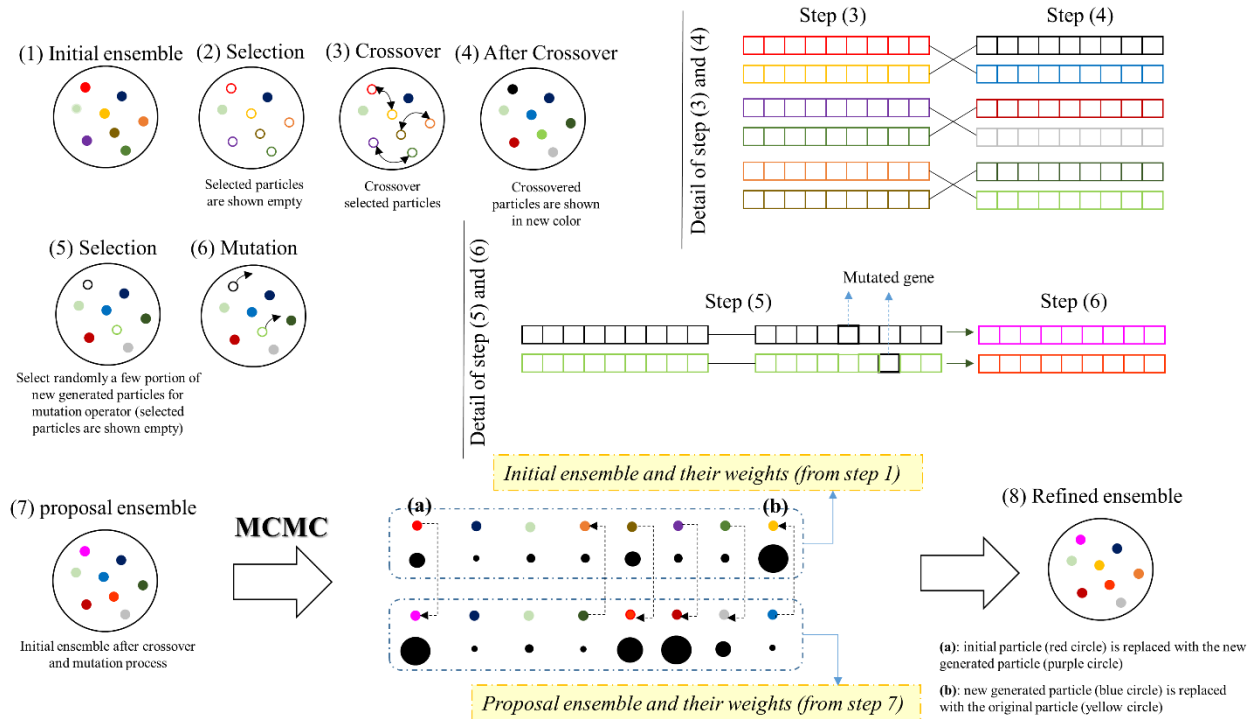


Figure 2-2 Color coding of the hybrid GA-MCMC process. The upper panel shows the details of crossover and mutation process. Each particle is looked upon as a string of chromosome (for example, see the detail of step 3 and step 4). The lower panel shows the MCMC process. The

GA generates the proposal particles and the MCMC decides to accept or reject the proposal particles.

As it is seen from Figures 2-1 and 2-2, we use two basic operators of GA, crossover and mutation, to combine particles with each other. It is worth mentioning that each particle ($x_t \in \mathbb{R}^n$) in EPFM algorithm is looked upon as a chromosome. In GA terminology, each chromosome is comprised of number of genes or in similar term each particle is made of number of state variables. To do the crossover, the chromosomes should be selected from the ensemble. Based on Darwin's evolution theory, the best chromosomes should survive and produce new offspring. There are many approaches to select the best chromosomes, for instance, roulette wheel selection, tournament selection, rank selection, Boltzman selection, and some others. In the current research, the roulette wheel selection as a simple selection method is chosen and briefly described here. Since parent chromosomes are selected according to their fitness values, we need to assign a fitness value for each chromosome. Therefore, those chromosomes that have significant fitness values will be more likely to be selected as the parent chromosomes.

The value of weights, as an appropriate indication of ensemble member quality, can be directly used as the fitness value. Hence, the particle weight is defined as the fitness value as shown in eq. 14:

$$f_t^i = w_t^{i+} \quad (14)$$

It is necessary for the chromosomes to be arranged in the descending order of their fitness values. Then a roulette wheel selection should be implemented to select parent chromosomes. This selection method assumes that the probability of a selection is proportional to the fitness of a chromosome. In this study, each chromosome is characterized by its fitness value f_t^i ($i = 1, 2, \dots, N$). Thus, the selection probability of the i -th chromosome is given as:

$$P_t^i = \frac{f_t^i}{\sum f_t^i} \quad (15)$$

This method is analogous to a roulette wheel in which each slice is proportional in size to the fitness value (f_t^i) of each chromosome. The selection of a chromosome is equivalent to randomly choosing a point on the wheel and locating the corresponding sector. In this method, a line segment of length $\sum_{i=1}^N f_t^i$ out of consecutive sectors of length $f_t^i (i = 1, 2, \dots, N)$ is constructed, and using a random number r ($0 < r < \sum_{i=1}^N f_t^i$) the corresponding sector is identified, resulting in the respective chromosome (Lipowski and Lipowska, 2012). Hence, the chromosomes with larger weights will have higher chance to generate new offspring chromosomes, while the chromosomes with smaller weights will have less chance to do so. This inspires to reduce the number of particles with small weights and find more particles with large weights. This property of GA not only intensifies the diversity of population to prevent the particle degeneracy, but also improves the reliability and accuracy of model estimation by providing a more realistic form of posterior distribution.

Up to this point, the proposed methodology allows us to know how to select the parent particles for the crossover operation (step 2 shown in Figure 2-2). There are numerous methods in genetic algorithm to do a crossover. There are one-point and two-point crossovers for binary encoding situation, and arithmetic and discrete crossover for float encoding situation (Janikow and Michalewicz, 1991; Magalhaes-Mendes, 2013). Generally, the application of genetic operators depends on the problem defined. In this study, the arithmetic crossover, which is widely used in the context of evolutionary PF, is adopted for the crossover operation (Park et al., 2009; Yin and Zhu, 2015). In the arithmetic crossover, a pair of new particles (offspring) is generated by a linear combination of a pair of parent particles. It is noted that the roulette wheel selection is implemented based on a crossover probability (ρ_c), such that it specifies how many

particles are to be nominated for the crossover operation (step 2 shown in Figure 2-2). The formulation of the arithmetic crossover operator can be expressed as:

$$x_{t-1}^{i'} = \xi \cdot x_{t-1}^i + (1 - \xi) \cdot x_{t-1}^j \quad (16)$$

$$x_{t-1}^{j'} = (1 - \xi) \cdot x_{t-1}^i + \xi \cdot x_{t-1}^j \quad (17)$$

where x_{t-1}^i and x_{t-1}^j are the parent particles (the red and yellow particles shown in step 3 of Figure 2-2), $x_{t-1}^{i'}$ and $x_{t-1}^{j'}$ are the pair of new offspring particle (the black and blue particles in step 4 of Figure 2-2), and ξ is a uniform random value in the range of $[0,1]$. This parameter plays a pivotal role in transferring information from the parent particle to offspring particle. It should be noted that if $\xi = 1$ the crossover will not occur, however, if $\xi = 0$ more information will be transferred from x_{t-1}^j to $x_{t-1}^{i'}$ (x_{t-1}^i to $x_{t-1}^{j'}$).

To further promote diversity of the particles, a mutation strategy is designed. This process alters each chromosome (particle) through changing its gene (details of step 5 in Figure 2-2). It is realized by the equation 18 that x_{t-1}^k and $x_{t-1}^{k'}$ are the particles before and after mutation process, respectively (the black and purple particles in step 5 and 6 of Figure 2-2). The mutation operation is executed with the appropriate mutation probability (ρ_m). For instance, if $\rho_m = 0.1$, this means that 10% of the newly generated offspring (crossed over particles) are randomly selected to do the mutation operation (step 5 shown in Figure 2-2). It should be noted that the mutated gene is chosen randomly along the chromosomes (see detail of step 5 in Figure 2-2).

$$x_{t-1}^{k'} = x_{t-1}^k + \eta \quad x_{t-1}^k \in \{x_{t-1}^{i'}, x_{t-1}^{j'}\} \quad \eta \sim N\left(0, \psi \text{Var}(x_{t-1}^{k-})\right) \quad (18)$$

where $N(0, \psi \text{Var}(x_{t-1}^{k-}))$ represents a random sample from the Gaussian distribution with mean zero and variance $\psi \text{Var}(x_{t-1}^{k-})$, where $\text{Var}(x_{t-1}^{k-})$ is the variance of the prior states at the time $t - 1$, and ψ is a small tuning parameter. Here, we use Gaussian mutation process, in which ψ

should be tuned according to different systems. In this study, it is preferred to use 0.01 as the value of the tuning parameter. Therefore, the new proposal state $x_{t-1}^{i,p}$ is generated through the aforementioned crossover and mutation process. The number of proposal states is the same as the initial ensemble (N). This is highlighted in Figure 2-2, illustrating eight particles in both the initial ensemble and the refined ensemble. In the EPFM, the proposal states can be viewed as a new generation of offspring.

The ensuing task is to come up with an approach to accept or reject the proposal particles. This study uses the MCMC algorithm as an effective technique to decide which offspring should survive or be eliminated.

The MCMC move is illustrated in Figure 2-2, and the PDF of the proposed joint state parameters

$p(x_t^{i,p}, \theta_t^{i-} | y_{1:t})$ is estimated as:

$$x_t^{i,p} = f(x_{t-1}^{i,p}, u_t^i, \theta_t^{i-}) \quad (19)$$

$$p(x_t^{i,p}, \theta_t^{i-} | y_{1:t}) \propto p(y_t | x_t^{i,p}, \theta_t^{i-}) \cdot p(x_t^{i,p} | \theta_t^{i-}, y_{1:t-1}) \cdot p(\theta_t^{i-} | y_{1:t-1}) \quad (20)$$

Where $p(y_t | x_t^{i,p}, \theta_t^{i-})$ is calculated based on the same likelihood function used in equation (9).

To calculate the proposal state PDF $p(x_t^{i,p} | \theta_t^{i-}, y_{1:t-1})$, an assumption is made that the proposal states are assumed to fit marginal Gaussian distributions with a mean of μ_t and a variance of σ_t^2 .

Although a joint distribution would be preferred in this scenario, the marginal priors are selected because the states have nonlinear relationships, and thus have a joint distribution that is difficult to fit. To calculate the proposal PDF based on the Gaussian distribution, weighted mean and variance of the filtering posterior must be calculated as follows:

$$x_t^{i-} = f(x_{t-1}^{i+}, u_t^i, \theta_t^{i-}) \quad (21)$$

$$\mu_t = \sum w_{t-1}^{i+} x_t^{i-} \quad (22)$$

$$\sigma_t^2 = \sum w_{t-1}^{i+} (x_t^{i-} - \mu_t)^2 \quad (23)$$

The joint PDF of the proposal and prior states are then compared via the metropolis acceptance ratio α to determine the acceptance probability in (24).

$$\alpha = \min \left(1, \frac{p(x_t^{i,p}, \theta_t^{i-} | y_{1:t})}{p(x_t^{i-}, \theta_t^{i-} | y_{1:t})} \right) = \min \left(1, \frac{p(y_{1:t} | x_t^{i,p}, \theta_t^{i-}) \cdot p(x_t^{i,p} | \theta_t^{i-}, y_{1:t-1})}{p(y_{1:t} | x_t^{i-}, \theta_t^{i-}) \cdot p(x_t^{i-} | \theta_t^{i-}, y_{1:t-1})} \right) \quad (24)$$

The acceptance and rejection of the new states is shown in Figure 2-2. This acceptance/rejection process ensures that in each time step an appropriate prior state distribution is constructed, leading to a better estimation of the posterior distribution. This concept is the core part of this proposed EPFM technique, which is formulated using the GA-MCMC algorithm.

Streamflow Prediction Results

In this study, synthetic and three real data experiments are performed to compare the effectiveness and robustness of the proposed EPFM with those of the PF-MCMC. The Sacramento Soil Moisture Accounting Model (SAC-SMA) is used here to simulate the streamflow at four different basins. The SAC-SMA model, which was first introduced by Burnash (1974), is referred to as the spatially-lumped continuous soil moisture model, and represents each basin vertically by two soil zones: an upper zone and a lower zone. The upper zone models the short-term storage capacity while the lower zone accounts for long-term groundwater storage. This model is used to generate daily streamflow from daily potential evapotranspiration (PET) and precipitation data. Model parameters are tabulated in Table 2-1 and the model state variables are summarized in Table 2-2.

Table 2-1 Descriptions of parameters for the SAC-SMA model.

Parameters	Description	Units	Range
Capacity parameters			
UZWWM	Upper zone tension water maximum	mm	1.0-150
UZFWM	Upper zone free water maximum	mm	1.0-150
LZWWM	Lower zone tension water maximum	mm	1.0-500
LZFPM	Lower zone free primary maximum	mm	1.0-1000
LZFSM	Lower zone free secondary maximum	mm	1.0-1000
ADIMP	Additional impervious area	-	0.0-0.4
Recession parameters			
UZK	Upper zone depletion parameter	1/day	0.1-0.5
LZPK	Lower zone primary depletion parameter	1/day	0.0001-0.025
LZSK	Lower zone secondary depletion parameter	1/day	0.01-0.25
Percolation and other			
ZPERC	Maximum percolation rate	-	1.0-250
REXP	Percolation equation exponent	-	0.0-0.5
PCTIM	Impervious area of watershed	-	0.0-0.1
PFREE	Free water percolation from upper to lower zone	-	0.0-0.1
Routing parameter			
Kq	Nash-Cascade Routing Parameter	1/day	0.01-0.99
Not estimated			
RIVA	Riparian vegetated area	-	0.0
SIDE	Deep recharge to channel base flow	-	0.0
RSERV	Lower zone free water not transferable to tension water	-	0.3

Table 2-2 Description of the SAC-SMA model state variables.

State Variables	Description	Units
UZTWC	Upper zone temperature water content	mm
UZFWC	Upper zone free water content	mm
LZTWC	Lower zone tension water content	mm
LZFPC	Lower zone free primary water content	mm
LZFSC	Lower zone free secondary water content	mm
ADIMC	Additional impervious area water content	mm

In the DA setting, precipitation and PET are assumed to have lognormal and normal error distributions with a relative error of 25%, respectively. Using these values, it is presumed that meteorological observations errors, stemming from spatial heterogeneity inherent in these variables and sensor errors, can be accounted for (DeChant and Moradkhani, 2012). Also, the streamflow observation errors are assumed to be normally distributed with a 15% relative error. For a synthetic study, the model is assumed perfect with no structural error. While for a real case study, the model error is assumed to follow a normal distribution with a relative error of 25%. This study assumes that all errors are uncorrelated, and applies them with the same magnitude in both the PF-MCMC and EPFM.

In order to provide an assessment of the EPFM performance, both deterministic and probabilistic measures are used in this study, including the Nash-Sutcliffe Efficiency (NSE), Kling-Gupta Efficiency (KGE), Mean Absolute Bias (MAB), Reliability (R), and 95% exceedance ratio (ER95). Since these measures have been described by a large and sufficient body of literature, only a brief definition of each is provided here.

NSE has been widely used for calibration and evaluation of hydrological models since it was developed in 1970. This measure determines the relative magnitude of residual variance (“noise”) compared to the observed data variance (“information”). NSE can range from $-\infty$ to 1 with NSE=1 as perfect fit between observation and simulation. A successor of this metric, called KGE developed by Gupta et al. (2009), has also been recently used as a robust measure in analyzing the accuracy of hydrological simulations. This metric measures the Euclidean distance in a three-dimensional space between the ideal point (1, 1, 1) and the Pearson product-moment correlation coefficient, relative variability (standard deviation), and ratio of the average

observation and simulation over the analysis period. Similar to NSE, KGE varies from $-\infty$ to 1, with KGE=1 being a perfect fit between the observed and simulated values.

Mean Absolute Bias (MAB) is the magnitude of the bias for a given estimate. The perfect value of this metric is zero, meaning that no bias is observed between the simulated and observed data. The Exceedance Ratio at 95 percentile (ER95) is an indicator by which the spread of the ensemble is evaluated (DeChant and Moradkhani, 2012). It is noted that the ideal value for ER95 is 5%. An ER95 greater than 5% indicates the predictive distribution is too narrow, while less than 5% indicates the predictive distribution is too wide. The R value represents the reliability with zero as the worst and 1 as the best value. This value is associated with the predictive quantile-quantile plot (Q-Q plot), which reflects its proximity to uniform distribution (DeChant and Moradkhani, 2012).

Synthetic Case Study

We first conduct a synthetic case study to demonstrate the usefulness and applicability of the EPFM for streamflow prediction. With the refined prior distributions, it is hypothesized that the EPFM could lead to a more accurate and reliable streamflow prediction. In this paper, Leaf River Basin located in the southern Mississippi was considered for a synthetic study. This basin has an area of 743 square miles, with the prevailing climate of humid subtropical, characterized by mild, temperate winters and dry summers, and precipitation that is fairly well distributed throughout the year.

Synthetic streamflow observations were generated by adding Gaussian noise (15% relative error) to streamflow simulations. The synthetic streamflow data represent noisy measurements that are sequentially assimilated into the SAC-SMA model. The initial state

variables and parameter sets were generated by Latin Hypercube Sampling (LHS) method resulting in a more uniform ensemble spread over all possible parameter permutations and therefore reducing the sampling variance.

Streamflow prediction over four years of analysis using both filters is shown in Figure 2-3. Note that this figure is reported based on an ensemble size of 100. The assimilation results are also numerically shown in this figure indicating that the EPFM outperforms the PF-MCMC according to both deterministic and probabilistic measures.

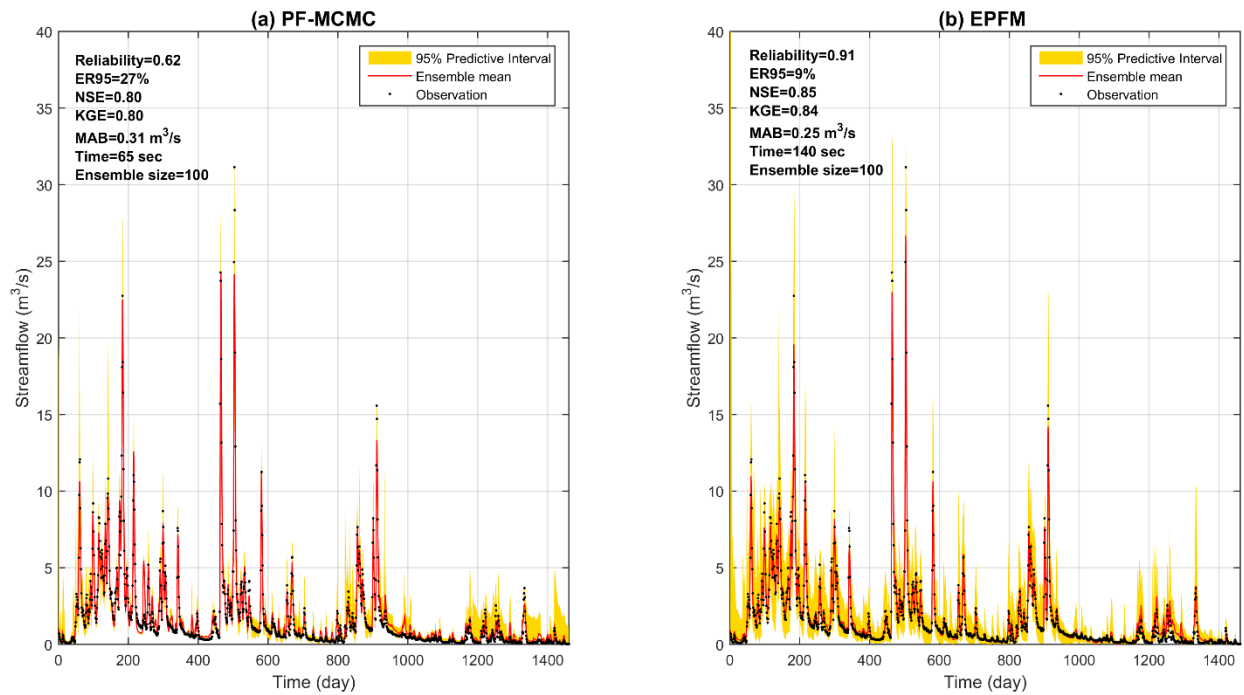


Figure 2-3 Synthetic streamflow prediction over four years using (a) PF-MCMC and (b) EPFM.

It is observed that the EPFM outperforms the PF-MCMC based on both deterministic and probabilistic measures. These results suggest that the proposed EPFM produces a more accurate expected value than the PF-MCMC according to deterministic measures. The probabilistic measures also show the improved performance of EPFM in streamflow prediction. For example, the reliability (R) increases from 0.62 for the PF-MCMC to 0.91 for the EPFM, indicating a

more reliable ensemble prediction by the EPFM. To analyze the spread of the ensemble prediction, the ER95 is used. The ER95 will be 5% for an ideal distribution. ER95 greater than 5% suggests that the distribution is too narrow (meaning that the observations are falling outside the ensemble range at 95 percentile and ER95 less than 5% suggests that the distribution is too wide. The ER95 of PF-MCMC is 27% indicating that the PF-MCMC remains overconfident due to particle degeneracy. However, the ER95 of EPFM at 9% is closer to the optimal value suggesting a more accurate characterization of the uncertainty.

In order to further investigate the ability of proposed EPFM method to estimate the posterior distribution and explore the scalability of EPFM (i.e., ability to consistently outperform PF-MCMC across ensemble sizes), the analysis was further performed over five different ensemble sizes of 50, 100, 200, 500 and 1000. Figure 2-4 depicts the results for both deterministic and probabilistic performance measures based on the five different ensemble sizes for the synthetic experiment. Over the six subplots in Figure 2-4, similar trends can be observed. First, it is noted that with increasing the ensemble size, the DA performances improve for both approaches. For example, in the EPFM, the KGE increases from 0.83 to 0.95 and the reliability (R) increases from 0.77 to 0.96, as the ensemble size increase from 50 to 1000. These results are in accordance with previous studies whereas large ensemble size leads to better estimation of the posterior and reduction of weight degeneracy (DeChant and Moradkhani, 2012; Yan et al., 2015). Secondly, compared with the PF-MCMC, the proposed EPFM produces smaller mean absolute bias and greater NSE/KGE/R values regardless of the ensemble size. These results suggest that the EPFM produces a more accurate expected value and a more reliable ensemble prediction than the PF-MCMC at all ensemble sizes. It is also noted that the ER95 of PF-MCMC is greater than 5% at all ensemble sizes meaning slightly overconfident prediction. Figure 2-4

summarizes the computational demand (seconds) of both algorithms. Although the EPFM is more accurate than the PF-MCMC, the computational complexity is larger for the same ensemble size. However, EPFM can provide the same level of accuracy in prediction for much smaller ensemble size (e.g., 100) as compared to the PF-MCMC with the ensemble size of 1000, meaning that with less computational demand it can provide comparable performance with the PF-MCMC. This issue further highlights that by using GA-MCMC technique in the importance sampling step of the PF, we can effectively improve the assimilation results without a need to increase the ensemble size. Therefore, the developed method is suitable for assimilation of high-dimensional problems where large ensemble sizes would have been needed in former versions of particle filtering. This promising result is also in accordance with literature suggesting that the improvements of importance sampling in PFs might provide the potential for data assimilation application in large-scale systems (Van Leeuwen, 2009).

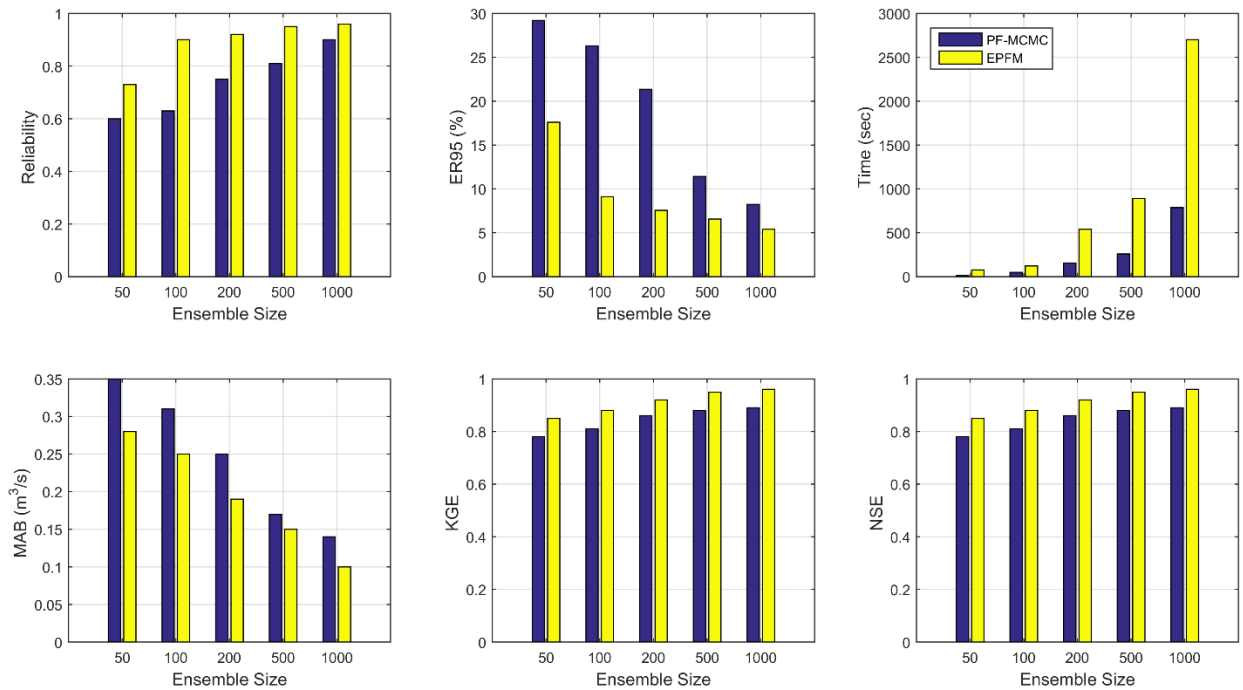


Figure 2-4 The comparison of accuracy, distribution spread, and computational demand for the PF-MCMC and EPFM in the synthetic experiment over four years.

In a summary, in terms of both deterministic and probabilistic measures, the proposed EPFM outperforms PF-MCMC regardless of the ensemble size. This finding comes at no surprise since the EPFM is formulated in an intelligent framework, where the GA can shuffle and increase diversity of the particles during the filtering process. The MCMC move is then used to reject the shuffled particles that move outside the posterior distribution, ensuring that shuffled particles contribute to improved performance.

Real Case Study

In addition to the synthetic study, three real data experiments are also performed in three basins located in different climate and geographical conditions, to fully examine the performance of the proposed EPFM. The daily precipitation, potential evapotranspiration, and streamflow data for the following three river basins are acquired from the Model Parameter Estimation Experiment (MOPEX) project (Duan et al., 2006):

1) The Chehalis River Basin with an area of 895 square miles is the second largest basin in Washington State. This region has a mostly oceanic climate, with wet winters, autumns and springs, and relatively dry summers, such that it receives more than 4100 mm precipitation annually, making it the wettest area in Washington State. Average temperatures over much of this region in January range from -7°C to 9°C and in July vary from 7°C to 27°C .

2) The Indian Creek Watershed is located in the Klamath National Forest, and drains into the Klamath River in California State. This watershed encompasses the area of 739 square miles, and is located predominantly in California with a small northern portion extending into Oregon State. Indian Creek watershed with mean annual precipitation of 762 mm is dominated by semi-

arid climate conditions, with summer temperatures of 24 °C to 41 °C, while in the winter, it can drop as low as -9 °C.

3) The Carson River Watershed originates from the Alpine County in California with an area of nearly 3,966 square miles, 85% of which lies in Nevada State. The prevalent climate of this basin is arid and hot, with sparsely distributed precipitation throughout the year. This watershed has an annual precipitation of 127 mm, while annual evaporation exceeds 1524 mm. More hydro-climatic information about the aforementioned three basins is provided in Table 2-3.

Table 2-3 Specifications of four study basins located in the United States. P, PE and \bar{p} stand for precipitation, potential evaporation, and daily average precipitation, respectively.

Basin #	USGS ID	Area (mi ²)	Station Name	Lon (°)	Lat (°)	P/PE	\bar{p} (mm)
1	12027500	895	Chehalis River near Grand Mound, WA	123°02'04"	46°46'34"	2.05	3.34
2	11401500	739	Indian Creek NR Crescent Mills Calif, CA	120°55'37"	40°04'41"	0.60 1	1.90
3	10312000	3360	Carson RV NR Fort Churchill, NV	119°18'40"	39°17'30"	0.39 3	1.23
4	02472000	743	Leaf River NR Collins, MS	89°24'25"	31°42'25"	1.35	1.0

Figure 2-5 summarizes both deterministic (KGE, NSE, and MAB) and probabilistic (Reliability and ER95) measures for five different ensemble sizes for the three basins. Also, in this figure, the computational demand of both algorithms is provided. Expectedly the use of MCMC twice in the EPFM method demands more computation, however, as seen in both deterministic and probabilistic measures, the EPFM provides more accurate and reliable predictions than PF-MCMC for all basins regardless of the ensemble size.

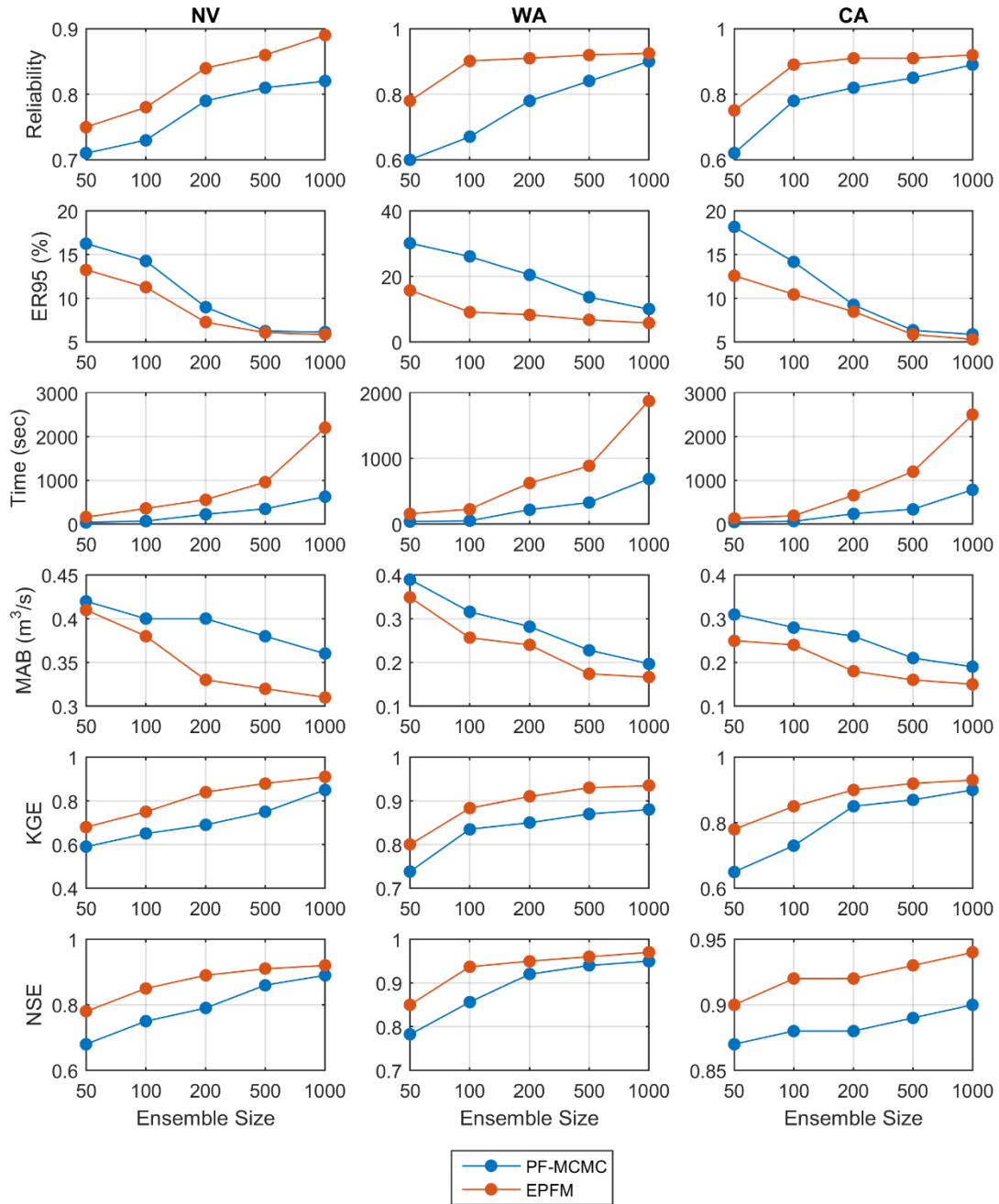


Figure 2-5 The comparison of accuracy, distribution spread, and computational demand for three real case studies over four years of analysis using the PF-MCMC and EPFM.

Further support for these results is provided in Figure 2-6 where the streamflow prediction and its uncertainty interval is shown for the Chehalis River Basin as an example.

Similar to the synthetic study, the EPFM improves the PF-MCMC performance by 7% and 6% in

terms of NSE and KGE, respectively. For the probabilistic measurement, the reliability is improved from 0.67 of PF-MCMC to 0.90 of EPFM, with an increase of about 15%.

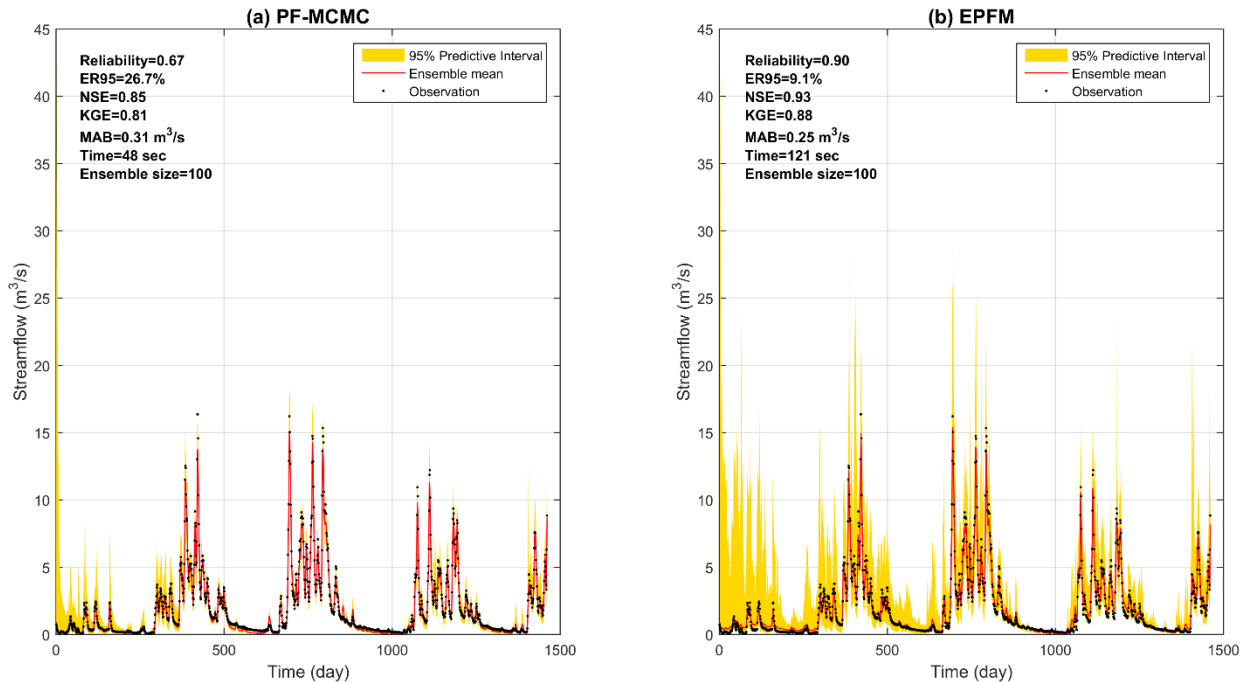


Figure 2-6 Streamflow prediction using the PF-MCMC and EPFM for the Chehalis River Basin in WA over four years.

To further interpret the GA-MCMC step within the EPFM, the comparisons of both EPFM priors and posteriors seem necessary. Figure 2-7 presents the prior and posterior distributions at three daily time steps ($t = 50, 431, \text{ and } 761$) for the Chehalis River Basin in WA. Two subplots are included for each time step: the first subplot (a1, b1, and c1) consists of the likelihood function, the prior PDF before the GA-MCMC, and the EPFM refined prior PDF after the GA-MCMC. This subplot also illustrates the prior PDF for the PF-GA model, the model for which we used only GA algorithm (without MCMC) in the importance sampling step. This analysis was performed to further investigate why the filtering benefits from the combination of MCMC with GA. The second subplot (a2, b2, and c2) compares the estimated posteriors using

the priors with and without the GA-MCMC step. This subplot also represents the posterior distributions based on the PF-GA model only. In cases of a and c, it is observed that in the PF prior PDFs, a large percentage of particles end up far from the observations and they possess negligible weights. As a result, after the resampling, the posteriors provide low skill predictions. Instead, the EPFM can provide more informative priors whereas the shuffled particles are drawn in the vicinity of the observations using the GA-MCMC step. It is noted that many more particles now end up close to the observations by implementing this framework, resulting in posteriors with higher accuracy and reliability. More specifically, the GA-MCMC provides the possibility of eliminating most of the small-weight particles and replacing them with the new particles with larger weights, which are effectively used in generating the posterior distribution. This procedure also enhances the diversity of particles when the assimilation is implemented, and consequently the degeneracy problem can be mitigated. Moreover, this figure indicates that although using the GA in the PF-GA could improve the diversity of particles, it does not necessarily guarantee that the shuffled particles are properly representing the prior distribution. For instance, in Figure 2-7-b1, PF-GA prior PDF is even not as good as PF-MCMC prior PDF, indicating that single GA algorithm could not enhance the prior distribution and consequently resulted in an inaccurate posterior distribution. Similarly, other subplots show no evidence of promising results when PF-GA model is implemented.

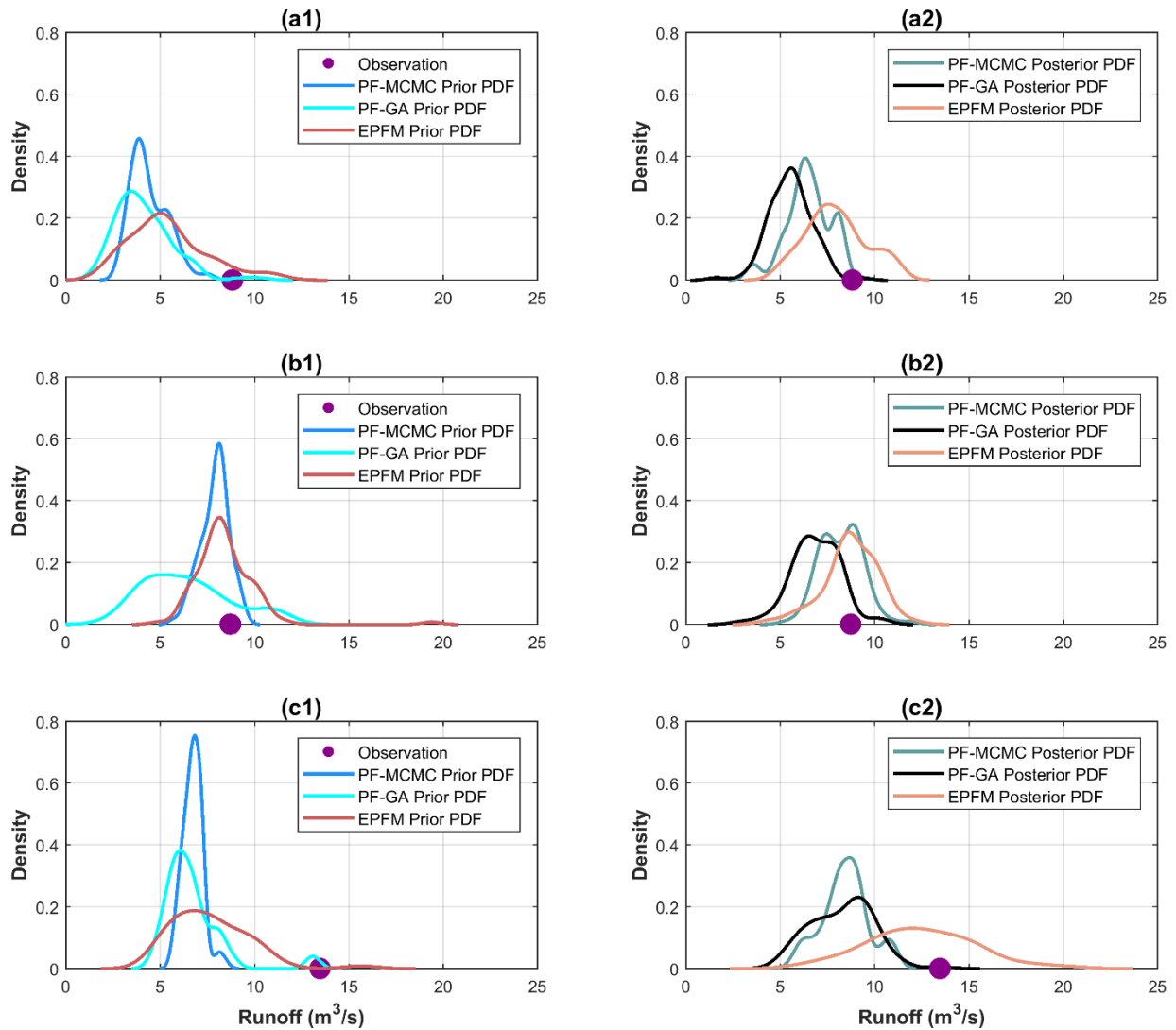


Figure 2-7 The prior and posterior distributions obtained by the PF-MCMC, PF-GA and EPFM for three days: (a) day = 50, (b) day = 431, (c) day = 761. These results are reported for the Chehalis River Basin in WA.

The two parameters of crossover and mutation probability need to be tuned when GA is implemented. The choice of these parameters depends on the specific problem, and this choice may affect the efficiency of GA. This issue plays an important role in many applications where GA is combined with the PF. The researchers have proposed different formulations to define the aforementioned probabilities in their studies (Park et al., 2007; Han et al., 2011). However, those

approaches could not be considered as a universal method to determine the GA parameters since they were designed for a specific application and case study, hence it cannot be generalized. This issue was also corroborated in the current study where different sets of GA parameters were investigated in implementing the PF-GA. In this paper, by using GA-MCMC algorithm within the importance sampling step of the PF-MCMC, not only can the subjective choice of GA parameters be overcome, but also the effectiveness of the PF-MCMC method is improved. Therefore, the crossover and mutation probabilities can take any values, that is, changing these parameters does not exacerbate the results, and the EPFM always outperforms its counterparts, i.e., PF-GA and PF-MCMC.

In summary, the motivation of this study was to overcome the particle degeneracy and sample impoverishment problems that the earlier versions of PF have been more susceptible to. The focus of the EPFM is on increasing the particle diversity which is achieved through GA, however, if some particles move far away from the background states, the MCMC will capture those and discard from the pool of particles.

Streamflow Forecasting Results

Data assimilation plays a very important role in both weather forecasting and hydrologic forecasting by improving model initial conditions. In addition to the streamflow prediction analysis, the applicability and usefulness of the proposed EPFM algorithm against PF-MCMC algorithm for one-day and five-day ahead streamflow forecasting was also investigated in the current research for both synthetic and real case studies. At each time step, we used the posterior distributions updated by the EPFM and PF-MCMC to generate the streamflow forecasts, forcing with the perfect meteorological data.

Table 2-4 summarizes the EPFM and PF-MCMC model performance statistics for one-day and five-day ahead forecasting experiments over all case studies used in this paper. We found that for both lead times, the proposed EPFM data assimilation method provided more accurate and reliable results than the PF-MCMC method. This result suggests the superiority of EPFM to its ascendant, PF-MCMC and the potential for operational streamflow forecasting. As seen the forecasting skills of both methods decrease from one-day to five-day lead time. This is mainly due to the effect of initial condition on forecasting skill (Li et al., 2009; DeChant and Moradkhani, 2011; Yuan et al., 2016).

Table 2-4 Deterministic and probabilistic measures based on an ensemble size of 200 for one-day and five-day ahead streamflow forecasting.

Case studies	ER95 (%)	Reliability	NSE	KGE	MAB (m ³ /s)	ER95 (%)	Reliability	NSE	KGE	MAB (m ³ /s)
One-day ahead forecasting (EPFM)					One-day ahead forecasting (PF-MCMC)					
NV	13.24	0.71	0.85	0.80	0.45	19.21	0.65	0.80	0.78	0.53
WA	15.21	0.66	0.79	0.65	0.61	25.41	0.57	0.74	0.62	0.75
CA	16.55	0.77	0.71	0.69	0.51	22.29	0.61	0.65	0.63	0.58
Synthetic	2.25	0.86	0.95	0.92	0.26	16.41	0.83	0.91	0.90	0.34
Five-day ahead forecasting (EPFM)					Five-day ahead forecasting (PF-MCMC)					
NV	22.16	0.65	0.69	0.67	0.51	25.11	0.61	0.60	0.59	0.58
WA	21.02	0.58	0.70	0.68	0.63	27.89	0.55	0.65	0.63	0.77
CA	20.22	0.69	0.62	0.60	0.55	27.64	0.60	0.59	0.58	0.62
Synthetic	8.5	0.77	0.74	0.72	0.30	19.09	0.71	0.70	0.65	0.39

Since flood events are main concern for emergency managers, here, we further analyze this issue. To this end we compared the EPFM and PF-MCMC for one-day ahead streamflow forecasting skill during the flood season for a synthetic (days=200 to 400) and for a real case study (days=300 to 600). The real case study considered here is Chehalis River Basin in WA. The majority of precipitation in this basin falls as snow during winter season due to the strong atmospheric river, and peak flood often occurs in spring due to snowmelt. When temperature

rises and snow starts to melt, the soil can become nearly saturated over weeks leading to clustered flood events (Figure 2-8). From this figure, it is seen that the EPFM provides better ensemble forecasts than the PF-MCMC. According to deterministic measures, the ensemble mean of EPFM (NSE=0.95, MAB=0.26) shows higher skill than the PF-MCMC (NSE=0.91, MAB=0.34) and offers a better ability to forecast extreme events (e.g., day=345). According to probabilistic measures, the ER95 of EPFM (2.25%) is closer to the ideal value 5% than the PF-MCMC (16.41%). The higher ER95 value of PF-MCMC indicates that the ensemble forecast distribution is too narrow and over-confident. This result can also be observed in Figure 2-8 since the ensemble from PF-MCMC fails to forecast peak events (e.g., Day=260 and 345), while the 95% predictive interval of the EPFM can capture these peak events. After the assimilation of a peak flood, the EPFM leads to better forecast as it can create a better initial condition that is closer to the real condition (i.e., saturated soil moisture). According to Figure 2-8 (a and b), during the flood recession period (Day=220 to 240; Day=350 to 380), the PF-MCMC leads to under-forecast while the EPFM ensemble forecast accurately presents the uncertainty and the ensemble mean closely follows the observation. Similar results can also be observed in Figure 2-8 (c and d) for a real case study. In summary, the EPFM outperforms PF-MCMC and generates more skillful streamflow forecasts. To further support this claim, we compared the EPFM and PF-MCMC for five-day ahead streamflow forecasting skill during the flood season for the synthetic (days=50 to 350) and the same real case study (days=650 to 850) (Figure 2-9). Similar to one-day ahead streamflow forecasting results, both deterministic and probabilistic measures demonstrated the superiority of the EPFM. These results are also consistent with those reported in Table 2-4.

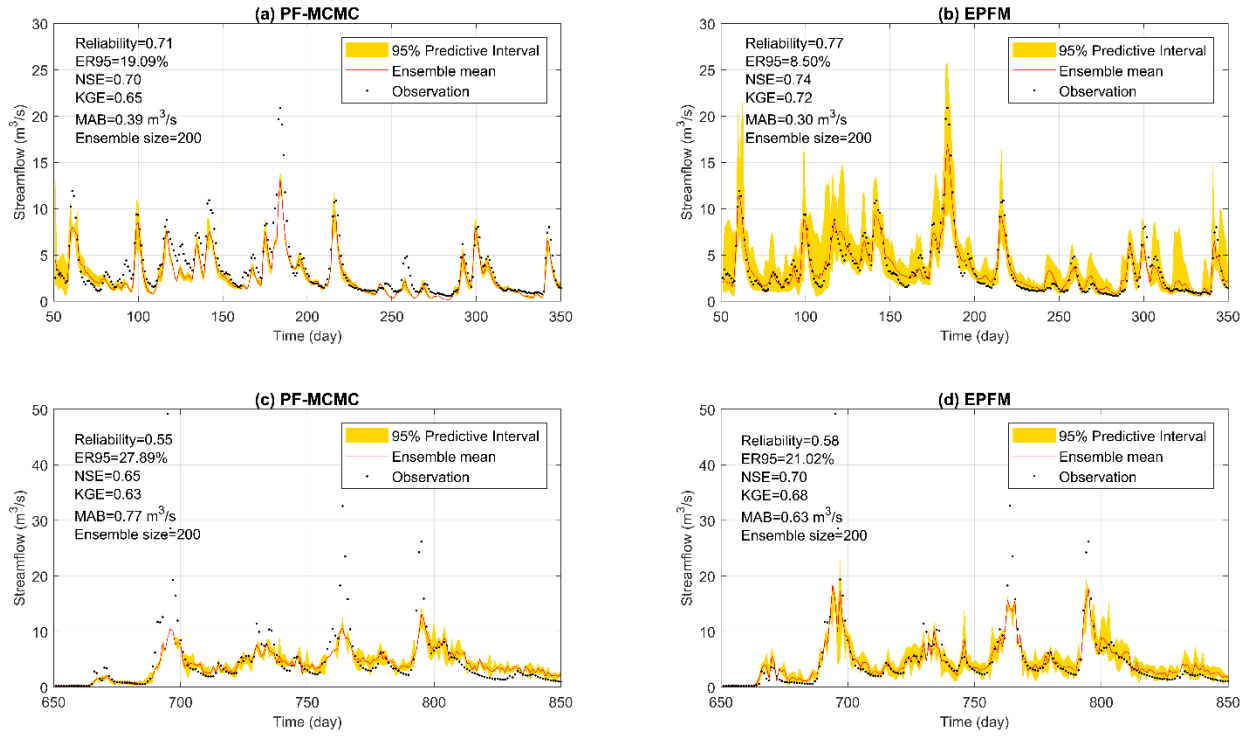


Figure 2-8 The comparison of the PF-MCMC and EPFM skills in one-day ahead streamflow forecast for the synthetic (a and b) and a real case study (c and d), Chehalis River Basin in WA, during the flood season.

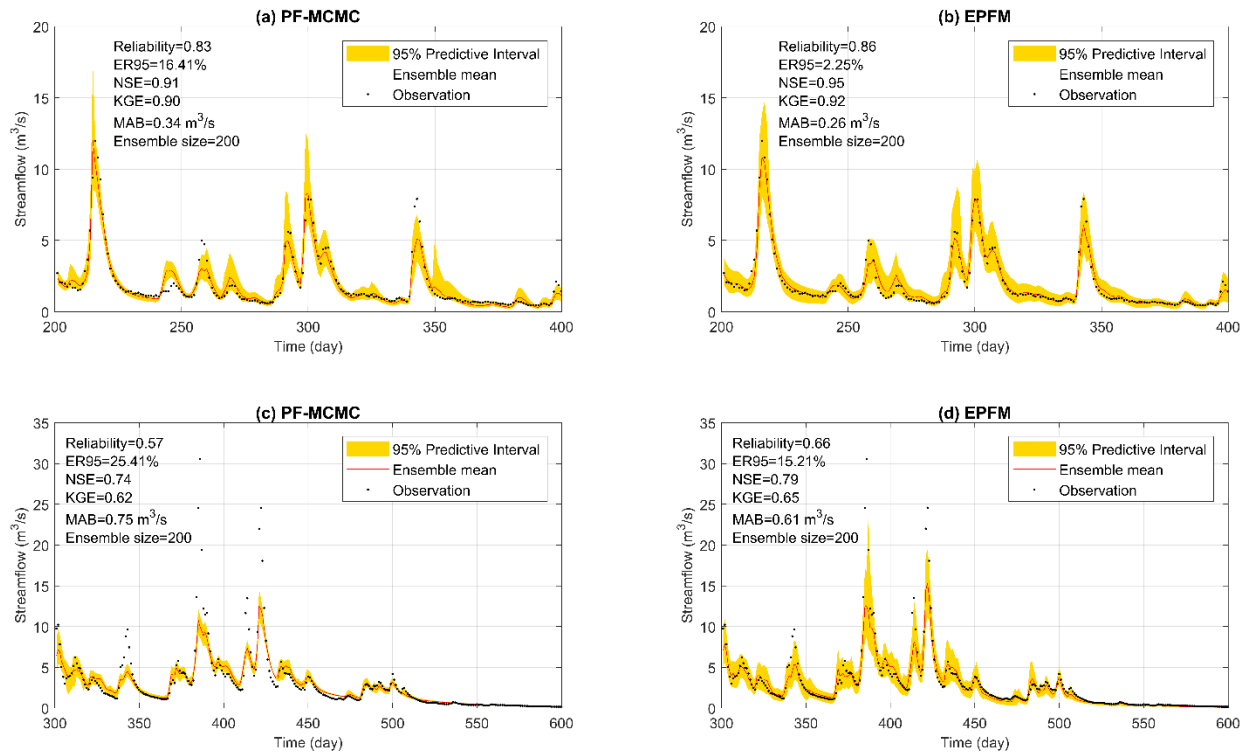


Figure 2-9 The comparison of the PF-MCMC and EPFM skills in five-day ahead streamflow forecast for the synthetic (a and b) and a real case study (c and d), Chehalis River Basin in WA, during the flood season.

Conclusion

A new data assimilation technique, the EPFM was proposed in this paper to characterize a more accurate and reliable posterior distribution for state variables of interest in data assimilation applications.

What distinguishes the proposed EPFM model from the recently developed PF-MCMC model (Moradkhani et al. 2012) is the utilization of GA-MCMC technique in the importance sampling step of the PF-MCMC model. The success and applicability of EPFM was evaluated through both deterministic and probabilistic measures. The EPFM provides a comprehensive approach for both state (using GA-MCMC within the importance sampling step) and parameter

updating (using MCMC within the resampling step), such that the user can select and update either state, parameter, or both given their needs in research.

This study suggests using the GA-MCMC technique within the particle filtering given the following features:

1. It provides the possibility of generating more informative prior leading to better estimation of the posterior distribution. In fact, the GA-MCMC expands the search space by implementing the crossover and mutation steps in the GA, and subsequently the search space is refined via the MCMC technique resulting in more desirable prior distribution.
2. It significantly minimizes the particle degeneracy and sample impoverishment problems that have been the main concerns in using particle filtering.
3. It alleviates the need for large ensemble size which had made it traditionally a limiting factor in using widespread application of particle filters.
4. In the standard PF-GA algorithm, which was recently emerged in the DA community, the usefulness of the model is more subjective in terms of GA operator (i.e., crossover and mutation) selection. This problem can be significantly alleviated with the proposed GA-MCMC approach embedded in the algorithm.
5. Using the GA-MCMC, a small ensemble size suffices to set up the DA. This is particularly a beneficial feature of this algorithm making it more attractive for large-scale systems where increasing the ensemble size and model runs would be a concern.
6. This approach enhances the usefulness and effectiveness of the particle filtering as demonstrated through deterministic and probabilistic measures.

It is noted that a lumped hydrologic model was used in this study for the proof of concept through a comparative analysis with currently the most advanced data assimilation method (PF-

MCMC) for hydrologic applications. However, to address the heterogeneity in forcing and landscape characteristics, further examination of the EPFM scalability to distributed models is desired that should follow the current study.

Acknowledgement

Partial financial support for this project was provided by the National Science Foundation Cyber- Innovation for Sustainability Science and Engineering (CyberSEES), Grant No. CCF-1539605.

References

- Ahmadi, M., Mojallali, H., Izadi-Zamanabadi, R., 2012. State estimation of nonlinear stochastic systems using a novel meta-heuristic particle filter. *Swarm. Evol. Comput.* 4 (6), 44–53. <http://dx.doi.org/10.1016/j.swevo.2011.11.004>.
- Andrieu, C., Doucet, A., Holenstein, R., 2010. Particle Markov chain Monte Carlo methods. *J. R. Stat. Soc. Ser. B. Stat. Methodol.* 72, 269–342. <http://dx.doi.org/10.1111/j.1467-9868.2009.00736.x>.
- Burnash, R.J.C., Ferral, R.L., 1974. A generalized streamflow simulation system, *Mathematical Models in Hydrology*, 2.
- Crow, W.T., Wood, E.F., 2003. The assimilation of remotely sensed soil brightness temperature imagery into a land surface model using ensemble Kalman filter- ing: A case study based on ESTAR measurements during SGP97. *Adv. Water Resour.* 26 (2), 137–149. [http://dx.doi.org/10.1016/S0309-1708\(02\)00088-X](http://dx.doi.org/10.1016/S0309-1708(02)00088-X).
- DeChant CM, Moradkhani H., 2011. Improving the characterization of initial condition for ensemble streamflow prediction using data assimilation. *Hydrol. Earth Syst. Sci.* 15, 3399–410. <https://doi.org/10.5194/hess-15-3399-2011>.
- DeChant, C.M., Moradkhani, H., 2012. Examining the effectiveness and robustness of sequential data assimilation methods for quantification of uncertainty in hydrologic forecasting. *Water Resour. Res.* 48, 1–15. <http://dx.doi.org/10.1029/2011WR011011>.
- DeChant, C.M., Moradkhani, H., 2014. Toward a reliable prediction of seasonal forecast uncertainty: Addressing model and initial condition uncertainty with ensemble data assimilation and sequential Bayesian combination. *J. Hydrol.* 519, 2967–2977. <http://dx.doi.org/10.1016/j.jhydrol.2014.05.045>.
- De Lannoy, G.J.M., Reichle, R.H., Houser, P.R., Pauwels, V.R.N., Verhoest, N.E.C., 2007. Correcting for forecast bias in soil moisture assimilation with the ensemble Kalman filter. *Water Resour. Res.* 43, W09410, doi:10.1029/2006WR005449.
- Dong, J., Steele-Dunne, S.C., Judge, J., van de Giesen, N., 2015. A particle batch smoother for soil moisture estimation using soil temperature observations. *Adv. Water Resour.* 83, 111–122. <http://dx.doi.org/10.1016/j.advwatres.2015.05.017>.
- Duan, Q., Schaake, J., Andréassian, V., Franks, S., Goteti, G., Gupta, H.V., et al., 2006. Model parameter estimation experiment (MOPEX): an overview of science strategy and major results from the second and third workshops. *J. Hydrol.* 320, 3–17. <http://dx.doi.org/10.1016/j.jhydrol.2005.07.031>.
- Gupta, H.V., Kling, H., Yilmaz, K.K., Martinez, G.F., 2009. Decomposition of the mean squared error and nse performance criteria: implications for improving hydro- logical modelling. *J. Hydrol.* 377 (1), 80–91.

- Han, H., Ding, Y.S., Hao, K.R., Liang, X., 2011. An evolutionary particle filter with the immune genetic algorithm for intelligent video target tracking. *Comput. Math. Appl.* 62, 2685–2695. <http://dx.doi.org/10.1016/j.camwa.2011.06.050>.
- Heris, S.M.K., Khaloozadeh, H., 2014. Non-dominated sorting genetic filter a multi-objective evolutionary particle filter. in *Proc. Iran. Conf. Intell. Syst.* 1-6. DOI:10.1109/IranianCIS.2014.6802580.
- Higuchi, T., 1997. Monte carlo filter using the genetic algorithm operators. *Journal of Sstist. Comput. Simul.* 59, 1–23. <http://dx.doi.org/10.1080/00949659708811843>.
- Holland, H., 1975. *Adaption in Natural and Artificial Systems*. The University of Michigan Press, Ann Arbor, MI.
- Janikow, C.Z., Michalewicz, Z., 1991. An experimental comparison of binary and floating point representation in genetic algorithms, in: *Proceedings of the International Conference on Genetic Algorithms*, San Diego, CA, USA. 31–36.
- Kuczera, G., Parent, E., 1998. Monte Carlo assessment of parameter uncertainty in conceptual catchment models: The Metropolis algorithm. *J. Hydrol.* 211 (1-4), 69-85. [http://dx.doi.org/10.1016/S0022-1694\(98\)00198-X](http://dx.doi.org/10.1016/S0022-1694(98)00198-X).
- Kwok, N., Fang, G., Zhou, W., 2005. Evolutionary particle filter: Resampling from the genetic algorithm perspective, in *Proc. Int. Conf. Intell. Robots Syst., Shaw Conference Centre, Edmonton, Alberta, Canada, Aug. 2-6, 2935-2940*. DOI: 10.1109/IROS.2005.1545119.
- Laio, F., and S. Tamea (2007), Verification tools for probabilistic forecasts of continuous hydrological variables, *Hydrol. Earth Syst. Sci.*, 11(4), 1267–1277, doi:10.5194/hess-11-1267-2007.
- Leisenring, M., Moradkhani, H., 2012. Analyzing the uncertainty of suspended sediment load prediction using sequential data assimilation. *J. Hydrol.* 468-469, 268–282. <http://dx.doi.org/10.1016/j.jhydrol.2012.08.049>.
- Li, H., Luo, L., Wood, E.F., Schaake, J., 2009. The role of initial conditions and forcing uncertainties in seasonal hydrologic forecasting. *Journal of Geophysical Research: Atmospheres.* 114(D4).
- Li, M., Pang, B., He, Y., Nian, F., 2013. Particle Filter Improved by Genetic Algorithm and Particle Swarm Optimization Algorithm. *J. Software.* 8 (3), 666–672. doi:10.4304/jsw.8.3.666-672.
- Lipowski, A., Lipowska, D., 2012. Roulette-wheel selection via stochastic acceptance. *Physica A.* 391, 2193–2196. <http://dx.doi.org/10.1016/j.physa.2011.12.004>.
- Liu, Y., Weerts a, H., Clark, M., Hendricks Franssen, H.J., Kumar, S., Moradkhani, H., et al., 2012. Advancing data assimilation in operational hydrologic forecasting: Progresses, challenges, and emerging opportunities. *Hydrol. Earth Syst. Sci.* 16, 3863–3887.

<http://dx.doi.org/10.5194/hess-16-3863-2012>.

- Magalhaes-Mendes, J., 2013. A comparative study of crossover operators for genetic algorithms to solve the job shop scheduling problem. *WSEAS Trans. Comput.* 12, 164–173.
- Marshall, L., Nott, D., Sharma, A., 2004. A comparative study of Markov chain Monte Carlo methods for conceptual rainfall-runoff modeling. *Water Resour. Res.* 40, W02501, doi:10.1029/2003WR002378.
- Matgen, P., M. Montanari, R. Hostache, L. Pfister, L. Hoffmann, D. Plaza, V. R. N. Pauwels, G. J. M. De Lannoy, R. De Keyser, and H. H. G. Savenije (2010), Towards the sequential assimilation of SAR-derived water stages into hydraulic models using the Particle Filter: Proof of concept, *Hydrology and Earth System Science*, 14, 1773–1785.
- Matgen, P., Montanari, M., Hostache, R., Pfister, L., Hoffmann, L., Plaza, D., Pauwels, V.R.N., De Lannoy, G.J.M., De Keyser, R., Savenije, H., 2010. Towards the sequential assimilation of SAR-derived water stages into hydraulic models using the particle filter: proof of concept. *Hydrol. Earth Syst. Sci.* 14 (9), 1773–1785. <http://dx.doi.org/10.5194/hess-14-1773-2010>.
- Montzka, C., Grant, J.P., Moradkhani, H., Franssen, H-J.H., Weihermüller, L., Drusch, M., et al., 2013. Estimation of radiative transfer parameters from L-band passive microwave brightness temperatures using advanced data assimilation. *Vadose Zo J* 12, 1–17. <http://dx.doi.org/10.2136/vzj2012.0040>.
- Moradkhani, H., Hsu, K.-L., Gupta, H., Sorooshian, S., 2005. Uncertainty assessment of hydrologic model states and parameters: sequential data assimilation using the particle filter. *Water Resour. Res.* 41, W05012. <http://dx.doi.org/10.1029/2004WR003604>.
- Moradkhani, H., Sorooshian, S., Gupta, H.V., Houser, P.R., 2005. Dual state-parameter estimation of hydrological models using ensemble Kalman filter. *Adv. Water Resour.* 28, 135–147. <http://dx.doi.org/10.1016/j.advwatres.2004.09.002>.
- Moradkhani, H., 2008. Hydrologic remote sensing and land surface data assimilation. *Sensors* 8, 2986–3004. <http://dx.doi.org/10.3390/s8052986>.
- Moradkhani, H., DeChant, C.M., Sorooshian, S., 2012. Evolution of ensemble data assimilation for uncertainty quantification using the particle filter-Markov chain Monte Carlo method. *Water Resour. Res.* 48, W12520. <http://dx.doi.org/10.1029/2012WR012144>.
- Noh, S.J., Tachikawa, Y., Shiiba, M., Kim, S., 2011. Applying sequential Monte Carlo methods into a distributed hydrologic model: lagged particle filtering approach with regularization. *Hydrol. Earth Syst. Sci.* 15 (10), 3237–3251. <http://dx.doi.org/10.5194/hess-15-3237-2011>.
- Park, S., Hwang, J., Rou, K., Kim, E., 2007. A new particle filter inspired by biological evolution: Genetic filter. *World Academy of Science, Engineering and Technology*, 33.
- Park, S., Hwang, J.P., Kim, E., Kang, H., 2009. A New Evolutionary Particle Filter for the

- Prevention of Sample Impoverishment. *IEEE Trans. Signal Process.* 13 (4), 801-809.
- Park, S., Kim, Y., Lim, M., 2010. Novel Adaptive Particle Filter Using Adjusted Variance and Its Application. *Int. J. Control Autom. Syst.* 4 (8), 801-807. doi:10.1007/s12555-010-0412-4.
- Pathiraja, S., Marshall, L., Sharma, A., Moradkhani, H., 2016. Hydrologic modeling in dynamic catchments: a data assimilation approach. *Water Resour. Res.* <http://dx.doi.org/10.1002/2015WR017192>.
- Pathiraja, S., Marshall, L., Sharma, A., Moradkhani, H., 2016. Detecting non-stationary hydrologic model parameters in a paired catchment system using data assimilation. *Adv. Water Resour.* 94, 103–119. <http://dx.doi.org/10.1016/j.advwatres.2016.04.021>.
- Plaza, D.A., De Keyser, R., De Lannoy, G.J.M., Giustarini, L., Matgen, P., Pauwels, V.R.N., 2012. The importance of parameter resampling for soil moisture data assimilation into hydrologic models using the particle filter. *Hydrol. Earth Syst. Sci.* 16, 375–390. <http://dx.doi.org/10.5194/hess-16-375-2012s>.
- Reichle, R., McLaughlin, D.B., Entekhabi, D., 2002. Hydrologic data assimilation with the ensemble Kalman filter. *Mon. Weather. Rev.* 130, 103–114. [http://dx.doi.org/10.1175/1520-0493\(2002\)130<0103:HDAWTE>2.0.CO;2](http://dx.doi.org/10.1175/1520-0493(2002)130<0103:HDAWTE>2.0.CO;2).
- Uosaki, K., Kimura, Y., Hatanaka, T., 2003. Nonlinear state estimation by evolution strategies based particle filters. In: *The 2003 Congress on Evolutionary Computation, 2003 (CEC '03)*. 3, 2102–2109.
- Uosaki, K., Kimura, Y., Hatanaka, T., 2004. Evolution strategies based particle filters for state and parameter estimation on nonlinear models. In: *Congress on Evolutionary Computation, 2004 (CEC2004)*. 1, 884–890.
- Van Leeuwen, P., 2009. Particle filtering in geophysical systems. *Mon. Weather Rev.* 137 (12), 4089-114. <https://doi.org/10.1175/2009MWR2835.1>.
- Wang, Q., Xie, L., Liu, J., Xiang, Z., 2006. Enhancing Particle Swarm Optimization Based Particle Filter Tracker. In: Huang DS., Li K., Irwin G.W. (eds) *Computational Intelligence. ICIC 2006. Lecture Notes in Computer Science*, vol 4114. Springer, Berlin, Heidelberg. DOI: 10.1007/978-3-540-37275-2_151.
- Xu, B., Chen, Q., Wang, X., Zhu, J., 2009. A novel estimator with moving ants. *Simul. Model Pract. Theory.* 17 (10), 1663–1677. <http://dx.doi.org/10.1016/j.simpat.2009.07.006>.
- Yan, H., DeChant, C.M., Moradkhani, H., 2015. Improving soil moisture profile prediction with the particle filter-Markov chain Monte Carlo method. *IEEE Trans. Geosci. Remote Sens.* 53, 6134–6147. <http://dx.doi.org/10.1109/TGRS.2015.2432067>.
- Yan, H., Moradkhani, H., 2016. Combined assimilation of streamflow and satellite soil moisture with the particle filter and geostatistical modeling. *Adv. Water Resour.* 94, 364-378.

<http://dx.doi.org/10.1016/j.advwatres.2016.06.002>.

Yan, H., Moradkhani, H., Zarekarizi, M., 2017. A probabilistic drought forecasting framework: A combined dynamical and statistical approach. *J. Hydrol.* 548, 291-304.

<http://dx.doi.org/10.1016/j.jhydrol.2017.03.004>.

Yin, S., Zhu, X., 2015. Intelligent particle filter and its application to fault detection of nonlinear systems. *IEEE Trans. Ind. Electron.* 62 (6), 3852-3861. DOI:10.1109/TIE.2015.2399396.

Yuan, X., Ma, F., Wang, L., Zheng, Z., Ma, Z., Ye, A., Peng, S., 2016. An experimental seasonal hydrological forecasting system over the Yellow River basin–Part 1: Understanding the role of initial hydrological conditions. *Hydrol. Earth Syst. Sci.* 20(6), 2437-2451.

Zhu, J., Xu, B., Wang, F., Wang, Z., 2010. A Real-Time Moving Ant Estimator for Bearings-Only Tracking. In: Tan Y., Shi Y., Tan K.C. (eds) *Advances in Swarm Intelligence. ICSI 2010. Lecture Notes in Computer Science*, vol 6145. Springer, Berlin, Heidelberg. DOI: 10.1007/978-3-642-13495-1_34.

CHAPTER 3 THE QUEST FOR MODEL UNCERTAINTY QUANTIFICATION: A HYBRID ENSEMBLE AND VARIATIONAL DATA ASSIMILATION FRAMEWORK³

Abstract

This article presents a novel approach to couple a deterministic four-dimensional variational (4DVAR) assimilation method with the particle filter (PF) ensemble data assimilation system, to produce a robust approach for dual-state-parameter estimation. In the proposed methodology, we characterize the model structural uncertainty in addition to model parameter and input uncertainties. The sequential PF is formulated within the 4DVAR system to design a computationally efficient feedback mechanism throughout the assimilation period. In this framework, the 4DVAR optimization produces the maximum a-posteriori (MAP) estimate of state variables at the beginning of the assimilation window without the need to develop the adjoint of the forecast model. The 4DVAR solution is then perturbed by a newly defined prior error covariance matrix to generate an initial condition ensemble for the PF system to provide more accurate and reliable posterior distributions within the same assimilation window. The prior error covariance matrix is updated from one cycle to another over the main assimilation period to account for model structural uncertainty resulting in an improved estimation of posterior distribution. The premise of the presented approach is that it: (1) accounts for all sources of uncertainties involved in hydrologic predictions, (2) uses a small ensemble size, and (3) precludes the particle degeneracy and sample impoverishment. The proposed method is

³ Abbaszadeh, P., Moradkhani, H., Daescu, D.N., (2019). The Quest for model uncertainty quantification: a hybrid ensemble and variational data assimilation framework. *Water Resources. Research.* 55(3), 2407–2431. <https://doi.org/10.1029/2018WR023629>

applied on a nonlinear hydrologic model and the effectiveness, robustness, and reliability of the method is demonstrated for several river basins across the United States.

Keywords: four-dimensional variational system, particle filter, hydrologic data assimilation

Introduction

Soil moisture and streamflow are among those key environmental variables that greatly affect flood forecasting, drought monitoring, and agricultural production that all collectively control the land and atmospheric system. Although, theoretically, these quantities can be estimated through hydrologic modeling, in practice they are often biased or erroneous due to the presence of uncertainties in all layers of hydrologic predictions. Data assimilation (DA) has been well-received in the hydrologic community as one of the most effective methods in characterizing the aforementioned uncertainties while estimating parameters, prognostic, and diagnostic variables (Clark et al., 2008; Liu et al., 2012; Moradkhani et al., 2005b; Pathiraja et al., 2016; Abbaszadeh et al., 2018; Moradkhani et al., 2018; Vrugt et al., 2006).

Generally, DA is defined as the application of Bayes' theorem to probabilistically condition the states of a dynamical model on observations (Moradkhani et al., 2018). A plethora of techniques is available to assimilate observations into a model for better initialization of the system and quantification of model parameter uncertainties. They all have some overlapping features making it difficult to define a clear-cut classification. Bayesian data assimilation seeks probabilistic estimates of state variables of interest in order to characterize their uncertainties. These probability distributions are sequentially adjusted according to the Bayes' theorem to better match the observations. In the hydrologic community, the best known and ubiquitous Bayesian approach is the ensemble Kalman filter (EnKF) (Crow and Wood, 2003; De Lannoy et

al., 2007; Moradkhani et al., 2005a; Reichle et al., 2002). Despite the widespread use of the EnKF and its different variants in numerous hydrologic applications, it is subject to some inherent limitations that result in suboptimal performance of this technique. These include (1) the linear updating rule, (2) Gaussian assumption of errors in observations, and (3) violation of water balance (e.g., DeChant and Moradkhani, 2012; Matgen et al., 2010; Noh et al., 2011; Plaza et al., 2012). PF as an effective alternative to EnKF has emerged for applications in nonlinear and non-Gaussian systems (Dong et al., 2015; Moradkhani et al., 2012; Yan and Moradkhani, 2015; Yan et al., 2017, Abbaszadeh et al., 2018; Pathiraja et al., 2018a). While successfully used in numerous applications, PFs may be subject to particle degeneracy and sample impoverishment. Particle degeneracy occurs when a few of particles close to the measurement receive significant weights while others are discarded (ensemble collapse to a single point). Although resampling alleviates the degeneracy problem, it may diminish the diversity of particles and increase the number of repeated particles (known as sample impoverishment). To mitigate these issues, researchers have combined PF with several procedures, such as the Markov Chain Monte Carlo (MCMC) algorithm (Andrieu et al., 2010; Moradkhani et al., 2012), metaheuristic techniques (Han et al., 2011; Kwok et al., 2005; Yin et al., 2015), and a combination of these two (Liang et al., 2001; Abbaszadeh et al., 2018; Zhu et al., 2018). The successful application of Bayesian data assimilation techniques owes to their stochastic nature as they enable the uncertainty quantification in forecasting systems (Verkade and Werner, 2011; Zhu et al., 2002).

However, variational data assimilation approaches are more similar to traditional and standard calibration procedures that primarily rely on nonlinear least squares optimization (Efstratiadis and Koutsoyiannis, 2010). Variational data assimilation can be considered as a Bayesian method (in the case of a quadratic cost function resulting from Gaussian statistics),

which seeks to minimize a cost function defined as the departures of the simulated values from the observations within an assimilation window (Reichle et al., 2001). This class of data assimilation includes different variants, such as three-dimensional variational data assimilation (3DVAR), which estimates the state of a system at a particular time using the information at that time only, and 4DVAR, where information is propagated both forward and backwards across a specified window, known as the assimilation window, to best estimate the initial conditions at the beginning of that time period. By linearizing the model's dynamics, 4DVAR efficiently finds the optimum solution in the convex search space by the use of gradient descent methods. While this component has made 4DVAR the most far-reaching approach in meteorological science, it has been less popular in hydrology due to difficulties in linearizing the hydrologic model (Liu and Gupta, 2007). In addition to this problem, in variational data assimilation, the adjoint models require increased software development efforts and are often difficult to maintain given the increased complexity incorporated in hydrologic models. Despite these obstacles, some research efforts have gone to the 4DVAR assimilation of hydrologic variables, such as soil moisture, into the land surface models (Jones et al., 2004; Lee et al., 2011; Seo et al., 2009; Tian et al., 2009).

In contrast to the PF that works in a sequential manner, the 4DVAR approach operates in a batch-processing manner by using all the observations simultaneously within the assimilation interval. Unlike Bayesian data assimilation, the variational data assimilation most often does not provide estimates of the predictive uncertainty of estimated model states and parameters, which considerably limits the value of the estimated variables in decision-making processes (Abdolghafoorian and Farhadi, 2016; Reichle et al., 2001). Given these concerns, integrating Bayesian and variational assimilation schemes seems a logical step to constrain the deficiencies of each method while benefiting from the strength of each (Chorin and Tu, 2009; Chorin et al.,

2010; Morzfeld et al., 2012; van Leeuwen, 2015; Slivinski et al., 2015; Atkins et al., 2013; Zhu et al., 2016; Hernández and Liang, 2017). Bannister (2017) presented a holistic review of these hybrid techniques and explained thoroughly their necessities in the data assimilation area.

In this paper, we present an approach to integrate the PF and 4DVAR data assimilation methods to leverage the best advantages of both in a single framework. More specifically, we seek to address the following questions that have been the main concerns in many hydrologic data assimilation studies: (1) In data assimilation, mischaracterization of errors leads to suboptimal model performance, and in the worst case, to degraded estimates, even compared to the open loop model run (Pathiraja et al., 2018a; Salamon and Feyen, 2009). While many efforts have gone to characterizing the model parameter and forcing uncertainties, less attention has been given to account for the model structural uncertainty in hydrologic studies. Ignoring model structural uncertainty leads to an inaccurate and biased simulation of the hydrologic processes (Parrish et al., 2012; Pathiraja et al., 2018a). Therefore, the first question is how we can benefit from the advantage of the 4DVAR method to better account for the model structural uncertainty when particle filtering is in operation. (2) Under a perfect model assumption, the observation error covariance R is the only matrix to be estimated. However, for imperfect model scenarios, the prior (background) state error covariance B should also be prescribed (Zhu et al., 2017). In standard particle filtering, this matrix does not play a role during the updating process except for initialization of state variables. To reduce the uncertainty in initial conditions, in many geoscience applications the prior state error covariance B is inflated. This is done through either deterministic additive means with an inflation factor (Anderson and Anderson, 1999) or multiplicative inflation of the B matrix (Anderson, 2001). Therefore, the second objective of this research is to introduce a new approach to dynamically estimate and update this error covariance

matrix throughout the assimilation process, and thus, generate more accurate and reliable posterior distributions. It is noted that the idea of using dynamic B matrix has been previously discussed in several studies (e.g., Wang et al., 2008; Wu et al., 2013; Lorenc et al., 2014; Lorenc, 2017).

The remainder of this paper is organized as follows: Section 2 briefly describes the PF and 4DVAR data assimilation approaches. In this section, we elaborate on the formulation of our proposed approach, which integrates both methods. Section 3 presents the experimental design, including the study areas, multiple performance measures used in this study, and DA settings for both synthetic and real case studies. Sections 4 and 5 discuss the performance of the proposed hybrid approach respectively over a synthetic experiment and several real case studies. Section 6 concludes the results and presents some recommendations and suggestions for future work.

Methodology

In this study, instead of using standard PF, we use the enhanced version of this method, the evolutionary particle filter with MCMC (EPFM), recently developed by the authors of this paper (Abbaszadeh et al., 2018). EPFM is a data assimilation technique that uses the evolutionary concept of the Genetic Algorithm (GA) combined with MCMC technique to effectively shuffle the particles before the resampling step of the filtering to produce a more complete representation of the posterior distribution for both state variables and parameters. EPFM significantly mitigates the particle degeneracy and sample impoverishment, the issues that mainly result in the suboptimal performance of the particle filtering and even sometimes the failure of this approach. The proposed method is a combination of the EPFM and 4DVAR methods. It should be noted that although we use EPFM approach as a sequential data

assimilation method in this study to introduce our hybrid approach, any variant of PF can be used as well. Section 2.2 presents a comprehensive description of 4DVAR data assimilation approach. Linearizing the observation operator h and forecast model operator \mathcal{M} often are not achievable or feasible for hydrologic models. To circumvent this issue, we formulate our hybrid model in such a way that relaxes the linearization constraints of 4DVAR method in hydrologic applications. This issue will be further discussed in section 2.3, where we explain the proposed HEAVEN method.

The following two equations describe the generic nonlinear dynamic system.

$$x_t = \mathcal{M}(x_{t-1}, u_t, \theta) + \omega_t \quad \omega_t \sim N(0, Q_t) \quad (1)$$

$$y_t = h(x_t) + v_t \quad v_t \sim N(0, R_t) \quad (2)$$

where $x_t \in \mathbb{R}^n$ and $\theta \in \mathbb{R}^d$ are vectors of uncertain state variables and model parameters, respectively. u_t represents the uncertain forcing data, $y_t \in \mathbb{R}^m$ indicates a vector of observation data, ω_t and v_t are the model and measurement errors, respectively. More often, ω_t and v_t are assumed to be independent and follow white noises with mean zero and covariance Q_t and R_t respectively (Gaussian distribution). Based on these definitions, the EPFM, 4DVAR and HEAVEN approaches are formulated respectively in the following subsections.

EPFM data assimilation method

The EPFM is a sequential data assimilation approach built based on recently developed PF-MCMC method (Moradkhani et al., 2012) and GA-MCMC approach (Abbaszadeh et al., 2018). GA-MCMC is an evolutionary Monte Carlo approach that can be used within any particle filtering algorithm to preprocess the ensemble members towards enhancing the assimilation results. Such an operation simultaneously alleviates the particle degeneration phenomenon by

intensifying the particles' diversity and generating more accurate and reliable estimation of posterior distributions. In this method, we use the following formulas which are based on Bayes theorem to calculate the posterior distribution of the state variables at time t .

$$p(x_t|y_{1:t}) = p(x_t|y_{1:t-1}, y_t) = \frac{p(y_t|x_t)p(x_t|y_{1:t-1})}{p(y_t|y_{1:t-1})} = \frac{p(y_t|x_t)p(x_t|y_{1:t-1})}{\int p(y_t|x_t)p(x_t|y_{1:t-1})dx_t} \quad (3)$$

$$p(x_t|y_{1:t-1}) = \int p(x_t, x_{t-1}|y_{1:t-1})dx_{t-1} = \int p(x_t|x_{t-1})p(x_{t-1}|y_{1:t-1})dx_{t-1} \quad (4)$$

where $p(y_t|x_t)$ is the likelihood for time step t , $p(x_t|y_{1:t-1})$ is the prior distribution, and $p(y_t|y_{1:t-1})$ is the normalization factor. The marginal likelihood function $p(y_{1:t})$ can be computed as:

$$p(y_{1:t}) = p(y_1) \prod_{t=2}^t p(y_t|y_{1:t-1}) \quad (5)$$

where the normalization factor $p(y_t|y_{1:t-1})$ is calculated as follows:

$$p(y_t|y_{1:t-1}) = \int p(y_t, x_t|y_{1:t-1})dx_t = \int p(y_t|x_t)p(x_t|y_{1:t-1})dx_t \quad (6)$$

Since only in special cases the analytical solution of equation (3) is available, such as those with linear systems and white Gaussian noise, for practical reasons, the posterior distribution is not calculated directly by this equation and instead it is approximated using a set of particles with associated weights.

$$p(x_t|y_{1:t}) \approx \sum_{i=1}^N w^{i+} \delta(x_t - x_t^i) \quad (7)$$

where w^{i+} , δ and N denote the posterior weight of the i -th particle, Dirac delta function and the ensemble size, respectively. The posterior weight is normalized as follows:

$$w^{i+} = \frac{w^{i-} \cdot p(y_t|x_t^i, \theta_t^i)}{\sum_{i=1}^N w^{i-} \cdot p(y_t|x_t^i, \theta_t^i)} \quad (8)$$

where w^{i-} is the prior particle weights, and the $p(y_t|x_t^i, \theta_t^i)$ can be computed from the likelihood $L(y_t|x_t^i, \theta_t^i)$. To calculate this, for simplicity, a Gaussian likelihood is used as follows:

$$L(y_t|x_t^i, \theta_t^i) = \frac{1}{\sqrt{(2\pi)^m |R_t|}} \exp \left[-\frac{1}{2} (y_t - h(x_t^i))^T R_t^{-1} (y_t - h(x_t^i)) \right] \quad (9)$$

It is noted that the EPFM benefits from MCMC technique twice, before resampling step, when it is combined with GA (earlier called as GA-MCMC) to shuffle the particles and generate more appropriate proposal state distribution, and after resampling step for parameter updating. This feature of EPFM method improves the assimilation results while avoids the particle degeneracy and sample impoverishment problems with no need to increase the ensemble size.

Here the implementation of GA-MCMC method, as an effective tool to shuffle the particles in importance sampling step of the filtering, is explained. Weights of the particles are considered as the fitness value f_t^i .

$$f_t^i = w_t^{i+} \quad (10)$$

Next, the particles are sorted in descending order of their fitness values to implement the roulette wheel selection method. This approach is applied based on a crossover probability (ρ_c) to select a portion of particles for crossover operation. Basically, ρ_c specifies how many particles are to be selected in this step. Each pair of these selected particles undergoes an arithmetic crossover operator to generate a new pair of particles. This is formulated by the following relationships:

$$x_{t-1}^{i',j'} = \xi \cdot x_{t-1}^{i,j'} + (1 - \xi) \cdot x_{t-1}^{i,j''} \quad j' \neq j'' \quad (11)$$

$$x_{t-1}^{i',j''} = (1 - \xi) \cdot x_{t-1}^{i,j'} + \xi \cdot x_{t-1}^{i,j''} \quad j' \neq j'' \quad (12)$$

where $x_{t-1}^{i,j'}$ and $x_{t-1}^{i,j''}$ are the selected particles from the main ensemble $\{x_{t-1}^i\}$ by the roulette wheel selection method before resampling step at time $t - 1$, $x_{t-1}^{i',j'}$ and $x_{t-1}^{i',j''}$ are a new pair of

particles at the same time, and ξ is a uniform random number which varies between 0 and 1. i and i' refer to the ensemble pool before and after crossover operator. j' and j'' indicate two particles. To further increase the diversity of the particles, a mutation strategy is also designed. The mutation operation is executed with the appropriate mutation probability (ρ_m). It is important to note that the performance of the EPFM approach is not sensitive to the choice of ρ_c and ρ_m (see Abbaszadeh et al. (2018) for more information). ρ_m specifies how many of the crossoverd particles are selected for mutation operation. One of the state variables of the selected particle is then randomly altered by the following equation:

$$x_{t-1}^{i',k} = x_{t-1}^{i,k} + \eta \quad x_{t-1}^{i,k} \in \{x_{t-1}^{i',j'}, x_{t-1}^{i',j''}\} \quad \eta \sim N(0, \psi \text{Var}(x_{t-1}^i)) \quad (13)$$

where $N(0, \psi \text{Var}(x_{t-1}^i))$ denotes a random sample drawn from a Gaussian distribution with mean zero and variance of $\psi \text{Var}(x_{t-1}^i)$, where $\text{Var}(x_{t-1}^i)$ is the variance of the states at time $t - 1$, and ψ is a small tuning parameter, which was set to 0.01 in this approach through ad hoc process. Therefore, the new proposal state $x_{t-1}^{i,p}$ is generated through the crossover and mutation operators. The MCMC approach is then used to decide which new particles from $x_{t-1}^{i,p}$ should remain or be replaced with the old corresponding particle. This acceptance/rejection step is necessary as it ensures an appropriate prior state distribution is constructed in each time step, and thus, a more desirable posterior distribution is estimated. To know whether to accept or reject the proposed states, the metropolis acceptance ratio α is calculated as follows:

$$\alpha = \min\left(1, \frac{p(x_t^{i,p}, \theta_t^{i-} | y_{1:t})}{p(x_t^{i-}, \theta_t^{i-} | y_{1:t})}\right) = \min\left(1, \frac{p(y_{1:t} | x_t^{i,p}, \theta_t^{i-}) \cdot p(x_t^{i,p} | \theta_t^{i-}, y_{1:t-1})}{p(y_{1:t} | x_t^{i-}, \theta_t^{i-}) \cdot p(x_t^{i-} | \theta_t^{i-}, y_{1:t-1})}\right) \quad (14)$$

where $p(x_t^{i,p}, \theta_t^{i-} | y_{1:t})$ is the proposed joint probability distribution.

$$p(x_t^{i,p}, \theta_t^{i-} | y_{1:t}) \propto p(y_t | x_t^{i,p}, \theta_t^{i-}) \cdot p(x_t^{i,p} | \theta_t^{i-}, y_{1:t-1}) \cdot p(\theta_t^{i-} | y_{1:t-1}) \quad (15)$$

$$x_t^{i,p} = \mathcal{M}(x_{t-1}^{i,p}, u_t^i, \theta_t^{i-}) \quad (16)$$

where $p(y_t | x_t^{i,p}, \theta_t^{i-})$ is computed similar to the equation (9) and the proposal state PDF $p(x_t^{i,p} | \theta_t^{i-}, y_{1:t-1})$ is calculated based on an assumption that the proposal states follow the marginal Gaussian distributions with mean μ_t (Eq. 18) and variance σ_t^2 (Eq. 19). Although, a joint distribution is perfect match to this scenario, we prefer to select the marginal priors due to the nonlinear nature of state variables that makes fitting a joint distribution difficult. To calculate the proposal PDF, weighted mean and variance of the Gaussian distribution are calculated as follows:

$$x_t^{i-} = \mathcal{M}(x_{t-1}^{i+}, u_t^i, \theta_t^{i-}) \quad (17)$$

$$\mu_t = \sum w_{t-1}^{i+} x_t^{i-} \quad (18)$$

$$\sigma_t^2 = \sum w_{t-1}^{i+} (x_t^{i-} - \mu_t)^2 \quad (19)$$

Up to this point, we obtained the appropriate prior state variables $\{x_{t-1}^{i'}\}$. The next step is to use this updated ensemble to recalculate the posterior weights (w^{i+}) using equation (8). For this, we use those posterior particle weights computed before GA operator implementation as prior particle weights (w^{i-}). It is important to note that in the EPFM approach we draw samples from a proposal distribution $q(x|y)$, which is generated using the GA and MCMC steps, not from the original prior as traditionally done in particle filtering applications. For more detailed information about proposal distributions, we refer the readers to Doucet and Johansen (2009) who provided a thorough description of particle filtering and its different variants. Those particles were also used for assigning fitness values (f^i) in GA operation. After this, we will do resampling to generate posterior state variables.

To do resampling, the sampling importance resampling (SIR) algorithm is suggested. In this method, we resample those particles whose probabilities are greater than the uniform probability. This approach discards the particles with smaller weights, while retain those whose weights are larger. At the end of each time step, the particle weights are again set to $1/N$. Apparently, the particles with larger weights are more likely to be drawn multiple times during the resampling step, leading to a loss of diversity in particles known as sample impoverishment. To avoid this, the resampled parameters are perturbed and new proposal distribution is formed as follows:

$$\theta_t^{i,p} = \theta_t^{i+} + \varepsilon_t^i \quad \varepsilon_t^i \sim N\left(0, s_t \text{Var}(\theta_t^{i-})\right) \quad (20)$$

where θ_t^{i+} shows the parameter after resampling at time t , $\text{Var}(\theta_t^{i-})$ is the variance of the prior parameters at time t , and s_t is a small time-variant tuning parameter. To accept or reject the proposal parameters $\theta_t^{i,p}$ we calculate the metropolis acceptance ratio α as follows:

$$\alpha = \min\left(1, \frac{p\left(x_t^{i,p'}, \theta_t^{i,p} \mid y_{1:t}\right)}{p\left(x_t^{i+}, \theta_t^{i+} \mid y_{1:t}\right)}\right) \quad (21)$$

$$p\left(x_t^{i,p'}, \theta_t^{i,p} \mid y_{1:t}\right) \propto p\left(y_{1:t} \mid x_t^{i,p'}, \theta_t^{i,p}\right) \cdot p\left(x_t^{i,p'} \mid \theta_t^{i,p}, y_{1:t-1}\right) \cdot p\left(\theta_t^{i,p} \mid y_{1:t-1}\right) \quad (22)$$

$$x_t^{i,p'} = \mathcal{M}\left(x_{t-1}^{i+}, u_t^{i+}, \theta_t^{i,p}\right) \quad (23)$$

where $p\left(x_t^{i,p'}, \theta_t^{i,p} \mid y_{1:t}\right)$ is the proposed joint probability distribution, $x_t^{i,p'}$ is a sample drawn from the proposal state distribution at time step t , u_t^{i+} is the perturbed forcing data associated with the i -th particle and x_{t-1}^{i+} is the posterior of state variables generated from $\{x_{t-1}^{i'}\}$ in the resampling step. It should be noted that to calculate the proposed state $x_t^{i,p'}$ we use the perturbed forcing data u_t^{i+} . The optimal tuning parameter s_t in equation (20) is unknown and needs to be estimated automatically as a time-variant quantity. If the s is too small, the posterior distribution

is overconfident. On the contrary, if the s is too large, the resampled parameters poorly characterize the posterior. To overcome this issue and calculate the s parameter, we used the variable variance multiplier (VVM) method developed by Leisenring and Moradkhani (2012) and further modified by Moradkhani et al. (2012).

Up to this point, we explained the particle filtering approach used in this study. However, we should note that the implementation of PF relies on the assumption of Gaussian likelihood function given unavailability of information on the type of likelihood function. In addition, in the calculation of the metropolis acceptance ratio in the MCMC step, it is assumed that the proposal state follows the marginal Gaussian distribution. These may imply an approximation to the full Bayesian solution, which is unavoidable in hydrology for practical reasons. For future studies, one may want to explore the feasibility of space-time particle filter that characterizes the transition proposal density in the MCMC step to avoid the need to approximate the actual PDF.

4DVAR data assimilation method

The 4DVAR approach provides an estimate (analysis) to a time-distributed sequence of state variables by minimizing a cost function defined as:

$$\begin{aligned}
 J(x_0, \dots, x_K) &= J^b + J^o + J^q \\
 &= \frac{1}{2} (x_0 - x_{0,b})^T B^{-1} (x_0 - x_{0,b}) + \frac{1}{2} \sum_{k=0}^K (y_k - h_k(x_k))^T R_k^{-1} (y_k - h_k(x_k)) \\
 &\quad + \frac{1}{2} \sum_{k=1}^K (x_k - \mathcal{M}_{k-1 \rightarrow k}(x_{k-1}))^T Q_k^{-1} (x_k - \mathcal{M}_{k-1 \rightarrow k}(x_{k-1})) \quad (24)
 \end{aligned}$$

where $x_{0,b} \in \mathbb{R}^n$, $y_k \in \mathbb{R}^m$, $B \in \mathbb{R}^{n \times n}$, $R_k \in \mathbb{R}^{m \times m}$, $Q_k \in \mathbb{R}^{n \times n}$. Error covariance matrices are the same as those defined in section 2.1. The optimal solution is the joint maximum likelihood estimate of the state variables in the interval $[t_0, t_K]$ given the observations.

The computational cost may be reduced by neglecting the model error (perfect model scenario). By imposing the model equations as strong constraint,

$$x_k = \mathcal{M}_{k-1 \rightarrow k}(x_{k-1}) \quad k = 1:K \quad (25)$$

where $\mathcal{M}_{k-1 \rightarrow k}$ denotes the nonlinear forecast model from t_{k-1} to t_k , the state at time t_k is expressed as:

$$x_k = \mathcal{M}_{0 \rightarrow k}(x_0) \quad k = 1:K \quad (26)$$

In this context, the cost functional is expressed in terms of the in initial state x_0 as:

$$\begin{aligned} J(x_0) &= J^b + J^o \\ &= \frac{1}{2} (x_0 - x_{0,b})^T B^{-1} (x_0 - x_{0,b}) \\ &\quad + \frac{1}{2} \sum_{k=0}^K (y_k - h_k(x_k))^T R_k^{-1} (y_k - h_k(x_k)) \end{aligned} \quad (27)$$

The optimal solution (analysis) is obtained through an iterative method that, typically, relies on linearized versions of the model and observational operator to obtain a quadratic approximation to the cost J (outer iteration) and adjoint modeling for gradient information. We refer the interested readers to these publications (Talagrand and Courtier, 1987; Tremolet, 2006; Zupanski, 1997), which provide more detailed information of fundamentals of the 4DVAR methods.

EPFM+4DVAR data assimilation method (HEAVEN)

Here, we develop the integration of EPFM and 4DVAR data assimilation methods to create an improved methodology for which all sources of uncertainties involved in the

hydrologic predictions are accounted. The main idea behind the HEAVEN method is that it provides the possibility that both sequential and variational assimilation approaches can effectively feed each other in a single framework in order to generate a more comprehensive representation of posterior distributions. HEAVEN is a framework that enables the particle filter to account for the hydrologic model structural uncertainty by using 4DVAR approach without a need to linearize the model and observation operators. In this approach, we operate the EPFM filter within the assimilation window for which the best initial condition is estimated by 4DVAR method. In doing so, the question arises as how to use the deterministic (single) initial condition achieved by 4DVAR method to initialize the EPFM filter, which is an ensemble-based approach. To cope with this problem, we define a prior error covariance B , which involves two components: dynamic (B_d) and static (B_s) prior error covariances, to perturb the deterministic solution of 4DVAR approach and generate best initial condition for the EPFM filter. This error covariance matrix is updated and propagated from cycle-to-cycle during the whole assimilation period. Dynamic error covariance matrix B_d is calculated within the EPFM framework while static error covariance matrix B_s comes from the 4DVAR approach. In this study, we calculate B_d using the equation presented by Shaw and Daescu (2016), who developed the formula to derive the model error ensemble for the weak-constraint 4DVAR method. In the remainder of this section, we first present a schematic of the HEAVEN in Figure 3-1, then elaborate on the approach for better understanding and implementation. It is worth mentioning that both 4DVAR and PF (steps 1 and 4 shown in Figure 3-1) components of HEAVEN follow the Bayes' theorem. Steps 5 and 6 are based on the statistical principles described by Shaw and Daescu (2016), while step 2 is an ad hoc procedure. Step 3 is not considered as an individual operation as it represents a transition phase from step 2 to 4.

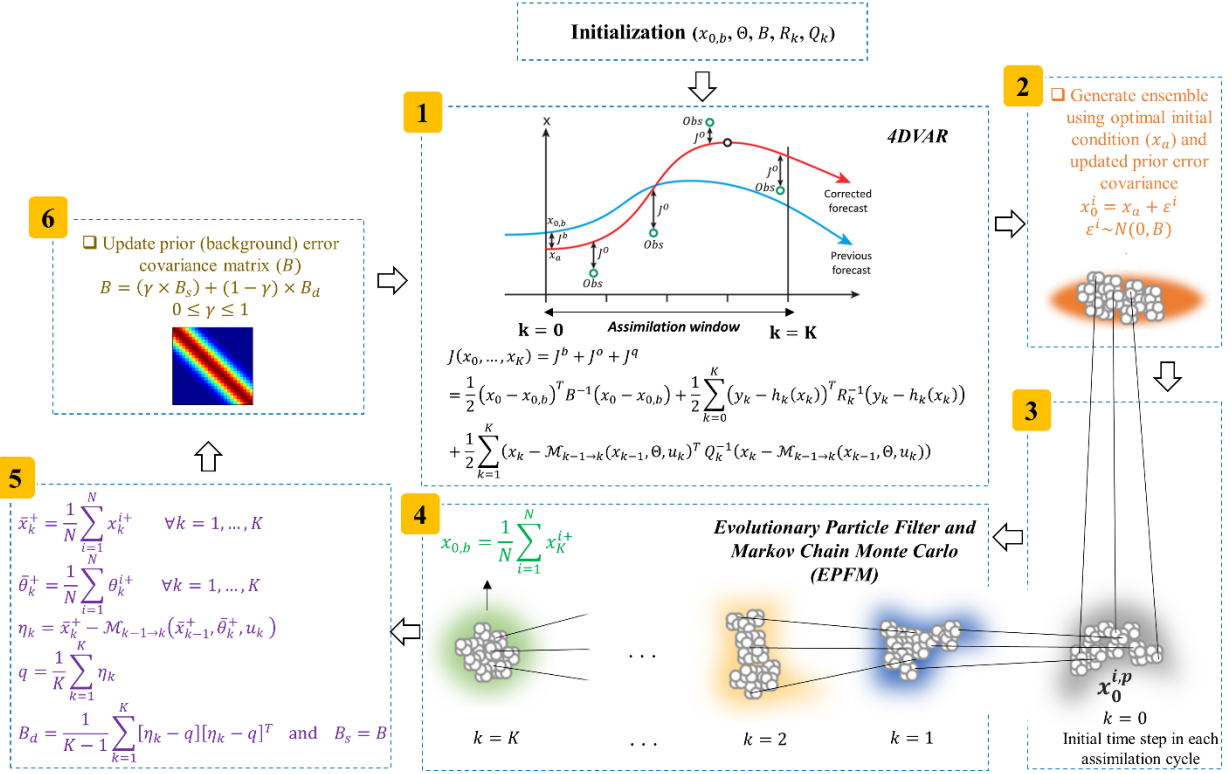


Figure 3-1 Schematic of the proposed HEAVEN method in a reciprocal form. B_s and B_d are respectively the static and dynamic prior error covariance matrices. Steps 1 through 6 indicate the procedure for one assimilation cycle. k, K, N, i show time step in each assimilation window, assimilation window size, ensemble size, and particle index respectively. B, R_k, Q_k specify prior, observation, and model error covariance matrices respectively. Initial deterministic guess for state variables and parameters are also respectively represented by $x_{0,b}$ and Θ .

For the time period of T and assimilation window size K ($[t_0, t_{k=K}]$), the number of assimilation cycles in the HEAVEN becomes T/K . For example, for a one year analysis period of $T = 365$ days, with the assumption of $K = 5$ days, 73 assimilation cycles or windows are defined. In each assimilation cycle, k ranges between 0 to K , where $k = 0$ indicates the initial time step.

Initialization: Three error covariance matrices, B, R_k, Q_k should be prescribed.

Observation error covariance matrix R_k at each time step can be specified as:

$$R_k = [\max\{(\lambda \times Obs_k), 1\}]^2 \quad (28)$$

where λ is the error percentage in observations and Obs_k is observation at time k . Prior error covariance matrix B can be specified as:

$$B = \text{diag} \left([\Omega \times x_{0,b}]^2 \right) \quad (29)$$

where Ω is the error percentage in initial state variables and $x_{0,b}$ is the deterministic initial guess for state variables. Similarly, the model error covariance can be calculated by the following formula:

$$Q_k = \Gamma \times \text{diag} \left([\pi \times x_{0,b}]^2 \right) \quad (30)$$

where π is the error percentage in model structure and Γ is the model error covariance inflation ($\Gamma \geq 1$) or deflation factor ($\Gamma \leq 1$). It should be noted that in this study we use the model error covariance matrix in a static form, which means it is once defined in the initialization step and used for the entire assimilation cycles. Therefore, in our formulation Q_k becomes Q . Since in this study, a dual state–parameter estimation of hydrologic model is presented, it is necessary to assign a deterministic initial guess for the model parameters Θ . Using Latin hypercube sampling (LHS), the initial ensemble of parameters θ^i for the assimilation cycle τ is generated. Since 4DVAR cost function is executed deterministically, we use the ensemble mean of θ^i as follows:

$$\Theta = \frac{1}{N} \sum_{i=1}^N \theta^i \quad (31)$$

Step 1: 4DVAR finds an initial condition by which the model forecasts best fit the observations within the assimilation interval. We specify the model parameters Θ at each time step within the assimilation interval. We then find the best initial state variables (also known as analysis) x_a by minimizing the 4DVAR cost function. For each of the perfect and imperfect model scenarios, we respectively use strong- and weak-constraint 4DVAR methods in order to

be consistent with their inherent definitions. Figure 3-1 demonstrates weak-constraint 4DVAR cost function, but as mentioned earlier, it can be simplified to strong-constraint 4DVAR as well. In either formulation, the best initial condition (analysis) x_a can be computed through the minimization of the cost function. Therefore, we use cost functions (32) and (33) for real and synthetic case studies respectively. To run both weak-constraint and strong-constraint 4DVAR, forecast state variables within the assimilation interval are required. This can be achieved by the model forward run.

$$\begin{aligned}
J(x_0, \dots, x_K) &= J^b + J^o + J^q \\
&= \frac{1}{2} (x_0 - x_{0,b})^T B^{-1} (x_0 - x_{0,b}) + \frac{1}{2} \sum_{k=0}^K (y_k - h_k(x_k))^T R_k^{-1} (y_k - h_k(x_k)) \\
&\quad + \frac{1}{2} \sum_{k=1}^K (x_k - \mathcal{M}_{k-1 \rightarrow k}(x_{k-1}, \Theta, u_k))^T Q^{-1} (x_k - \mathcal{M}_{k-1 \rightarrow k}(x_{k-1}, \Theta, u_k)) \quad (32)
\end{aligned}$$

$$\begin{aligned}
J(x_0) &= J^b + J^o \\
&= \frac{1}{2} (x_0 - x_{0,b})^T B^{-1} (x_0 - x_{0,b}) \\
&\quad + \frac{1}{2} \sum_{k=0}^K (y_k - h_k(x_k))^T R_k^{-1} (y_k - h_k(x_k)) \quad (33)
\end{aligned}$$

As briefly discussed before, variational data assimilation methods require linearization of observation h and model \mathcal{M} operators. This significantly hampers their utilization in hydrological applications where such linearizations are not often achievable. To circumvent this problem, we use a derivative-free optimization method to minimize the 4DVAR cost function. Derivative-free optimization methods are those in mathematical optimization discipline that do not use derivatives and finite differences in the classical sense to find optimal solutions (Rios & Sahinidis, 2013). In this paper, we use Nelder-Mead algorithm to find the optimal solution x_a of the 4DVAR cost functions. This method requires no derivatives to be computed and the

objective function does not need to be smooth. Nelder-Mead algorithm is very fast, simple and effective for the problems with small dimensions (Gao & Han, 2012). For higher dimensional problems, there are other techniques, such as Metaheuristic Algorithms (MAs), however, their implementations are computationally intensive and therefore, their use may require high performance computing approach. In this study, we used *fminsearch* in MATLAB to use Nelder-Mead algorithm and find the optimal solution of the 4DVAR cost function. The algorithm first makes a simplex around the initial guess $(x_{0,b})$ and then updates the simplex repeatedly to minimize the objective functions (Eqs. 32 and 33). The ideal scenario for implementing the proposed HEAVEN approach is to use forecast model adjoint for the minimization of 4DVAR cost function. This, however, may not be practical in hydrologic applications, and therefore we employed the Nelder-Mead algorithm, which was sufficient for the model used in this study. If the model adjoint is not achievable, we encourage the readers to select the most appropriate optimization technique depending on their used model.

Step 2: In this step, we generate initial state ensemble x_0^i for particle filtering from the deterministic solution of 4DVAR approach x_a . This can be done by equation (34). It should be reminded that the prior error covariance matrix B is the one used in the 4DVAR cost function in step 1. It should be mentioned that here we used background error covariance matrix to generate the ensemble around the 4DVAR solution (x_a) knowing that the analysis error covariance matrix is not available.

$$x_0^i = x_a + \varepsilon^i \quad \varepsilon^i \sim N(0, B) \quad (34)$$

Step 3: To ensure that an appropriate initial condition x_0^i is replicated for cycle τ , which later results in better estimation of the posterior distributions in that window interval, we run the forward model for cycle τ using two initial ensemble scenarios: (1) x_0^i and (2) state posterior

distribution obtained in the last time step ($k = K$) of assimilation cycle $\tau - 1$ (x_K^i) (particles depicted with the green glow color in Figure 3-1). Under these two initial conditions, we calculate y_k^i for ensemble members within the assimilation interval $[t_0, t_K]$, and based on their discrepancies from the observations Obs_k , one can decide to preserve the particles x_0^i or replace them with those already available from the previous cycle $\tau - 1$. Here, we present a pseudo-code to further clarify the implementation of step 3 in the HEAVEN framework.

```

Step 3
 $x_0^i = x_a + \varepsilon^i$    and    $x_0^i = x_K^i$                                 ▷ initialization
for  $i = 1:N$  do                                                    ▷ for each ensemble member
  for  $k = 1:K$  do                                                  ▷ within the assimilation interval
     $x_k^i = \mathcal{M}_{k-1 \rightarrow k}(x_{k-1}^i, u_k, \theta^i) + \omega_k$        $\omega_k \sim N(0, Q_k)$                 ▷ run model
     $y_k^i = h_k(x_k^i) + v_k$                                         $v_k \sim N(0, R_k)$ 
     $E_k^i = |y_k^i - Obs_k|$                                           ▷ absolute error
  end for
   $e^i = \sum_{k=1}^K \frac{E_k^i}{\sqrt{R_k}}$                                 ▷ discrepancy of each
end for
ensemble
end for
 $\{e_1^i\}$                                                             ▷ initialized with  $x_a + \varepsilon^i$ 
 $\{e_2^i\}$                                                             ▷ initialized with  $x_K^i$ 
for  $i = 1:N$  do                                                  ▷ for each ensemble member
  if  $e_1^i < e_2^i$  then
     $x_0^{i,p} = x_a^i$ 
  else
     $x_0^{i,p} = x_K^i$ 
  end if
end for

```

Step 4: In this step, we run the EPFM filter with the initial proposal states $x_0^{i,p}$ and ensemble members θ^i to create state and parameter posterior distributions in the window interval $[t_0, t_K]$ and assimilation cycle τ . Then, we calculate the mean of state posterior distribution at $k = K$ in order to initialize the 4DVAR approach for the next assimilation cycle $\tau + 1$. This

means that the prior knowledge for 4DVAR cost function at cycle τ is derived from the information of EPFM posterior at the last time step of cycle $\tau - 1$. This indicates how 4DVAR and EPFM feed each other from cycle-to-cycle. x_k^{i+} is the state posterior distribution obtained by EPFM at time k ($1 \leq k \leq K$).

$$x_{0,b} = \frac{1}{N} \sum_{i=1}^N x_{k=K}^{i+} \quad (35)$$

Step 5: In this paper, EPFM as an ensemble-based sequential data assimilation method is combined with a 4DVAR approach to capture the model structural uncertainty and dynamically update the prior error covariance matrix B . B incorporates two components, B_d and B_s . The dynamic error covariance matrix B_d is calculated using the ensemble estimates of model error within the assimilation cycle τ , while static error covariance matrix B_s is obtained from the previous assimilation cycle $\tau - 1$. The best estimates of the state variables and parameters are obtained as the expected values from their posterior distributions at each time within the assimilation window. θ_k^{i+} is the parameter posterior distribution obtained by the EPFM at time k ($1 \leq k \leq K$).

$$\bar{x}_k^+ = \frac{1}{N} \sum_{i=1}^N x_k^{i+} \quad \text{and} \quad \bar{\theta}_k^+ = \frac{1}{N} \sum_{i=1}^N \theta_k^{i+} \quad \forall k = 1, \dots, K \quad (36)$$

$$\eta_k = \bar{x}_k^+ - \mathcal{M}_{k-1 \rightarrow k}(\bar{x}_{k-1}^+, \bar{\theta}_k^+, u_k) \quad (37)$$

η_k is the estimate of model error at each time within the assimilation window.

$$q = \frac{1}{K} \sum_{k=1}^K \eta_k \quad (38)$$

q is the model error bias within the assimilation window.

$$B_d = \frac{1}{K-1} \sum_{k=1}^K [\eta_k - q][\eta_k - q]^T \quad (39)$$

B_d dynamic prior error covariance matrix in the assimilation cycle τ .

$$B_s = B \quad (40)$$

B is the prior error covariance matrix from the previous assimilation cycle $\tau - 1$. B_s is the static prior error covariance matrix at assimilation cycle τ .

Step 6: In this step, we update prior error covariance matrix B using the following formula. γ is a tuning factor.

$$B = (\gamma \times B_s) + (1 - \gamma) \times B_d \quad 0 \leq \gamma \leq 1 \quad (41)$$

In this formalism, if γ is zero, the prior error covariance B is updated only using the model error calculated within the EPFM framework at assimilation cycle τ . If $\gamma = 1$, the B matrix is the one used in the previous assimilation cycle $\tau - 1$ within the 4DVAR cost function, meaning that no update is made from cycle $\tau - 1$ to τ . The updated matrix B in the assimilation cycle τ will be used as prior error covariance for the 4DVAR cost function in the next assimilation cycle $\tau + 1$. This completes one assimilation cycle of the HEAVEN (Figure 3-1). As shown in Algorithm 1, it is reminded that the model evolution errors (η_k) are used to update only the B matrix, while the Q matrix remains unchanged throughout the assimilation cycles. It is also important to note that in higher dimensional problems, regularization of B_d , such as localization, might be necessary (see Bannister, 2017).

Algorithm 1: HEAVEN $\{x_{0,b}, \Theta, B, Q, R_k\}$

▷ initialization (Eqs. 28,29,30,31)

for $\tau = 1: \frac{T}{K}$ **do**

▷ assimilation cycle

 $t_{k=0} = t_{(\tau \times K)} - K \quad t_{k=K} = t_{(\tau \times K)}$ $[t_{k=0}, t_{k=K}] \quad \forall k = 0, 1, 2, \dots, K$

▷ assimilation interval

Step 1**if** Synthetic case **then** $x_a = \text{Minimize } (J^b + J^o)$

▷ Eq. 33

end if**if** Real case **then** $x_a = \text{Minimize } (J^b + J^o + J^q)$

▷ Eq. 32

end if**Step 2** x_0^i

▷ Eq. 34

Step 3 $x_0^{i,p}$ **Step 4**Run EPFM filter $\{x_0^{i,p}, \theta^i\}$ $\{x_k^{i+}, \theta_k^{i+}\}$

▷ posterior distributions

 $\{x_{0,b}\}$

▷ Eqs. 35 and 36

Step 5 $\{B_d\}$ and $B_s = B$

▷ Eqs. 37,38,39

Step 6

Update B matrix

▷ Eq. 41

Create θ^i using LHS

$$\Theta = \frac{1}{N} \sum_{i=1}^N \theta^i$$

 $\{x_{0,b}, \Theta, B, Q, R_k\}$

▷ available for the next cycle

end for

Experimental design

In this study, a synthetic and several real data experiments are performed to evaluate the effectiveness, usefulness and robustness of the HEAVEN in estimating the states and parameters with better characterization of their posteriors. All the experiments are conducted with the HyMOD and Sacramento Soil Moisture Accounting (SAC-SMA) models.

HyMOD model

The HyMOD model (Boyle, 2001) is a conceptual and parsimonious-lumped hydrologic model containing five parameters and five state variables. Using these parameters, the model move the water through a series of quick-flow and slow-flow tanks, to route the runoff to the outlet. For more information about this model, we refer the readers to Moradkhani et al. (2005b).

SAC-SMA model

The SAC-SMA model, initially introduced by Burnash et al. (1973), is a spatially-lumped continuous soil moisture model used operationally at the National Weather Service River Forecast System (NWSRFS) to generate daily streamflow from mean areal precipitation (MAP) and daily potential evapotranspiration (PET) data. In this model, each basin is represented vertically by two soil zones: an upper zone, which models the short-term moisture storage, and a lower zone, which accounts for long-term groundwater storage. In SAC-SMA model, the precipitation over the impervious area contributes directly to generating direct runoff. The model has 14 parameters and 9 state variables. The SAC-SMA is the model used by the NWS for operational river and flash flood forecasting throughout the United States.

Case studies

Synthetic case study

In this paper, we use Leaf River Basin, located in southern Mississippi (MS), for a synthetic analysis. Leaf River Basin with an area of 1944 km² is the main tributary of the Pascagoula River, which drains into the Gulf of Mexico. The prevailing climate of this region is humid subtropical with mild winters and dry summers and well distributed precipitation

throughout the year. Data for the synthetic case study was collected from the NWS Hydrology Laboratory. This basin has been extensively used as a synthetic case study in several hydrologic data assimilation studies (e.g., Bulygina and Gupta, 2011; Dechant and Moradkhani, 2012; Parrish et al., 2012; Vrugt et al., 2006).

Real case studies

For the real data experiments, we use seven basins located in different climate regimes and geographical conditions in the western United States (Figure 3-2) to better examine the robustness and performance of the proposed method. These river basins are among those test basins included in the Model Parameter Estimation Experiment (MOPEX) project (Duan et al., 2006) where the water management effects can be ignored. In the following, we briefly describe these watersheds and their hydroclimate characteristics.

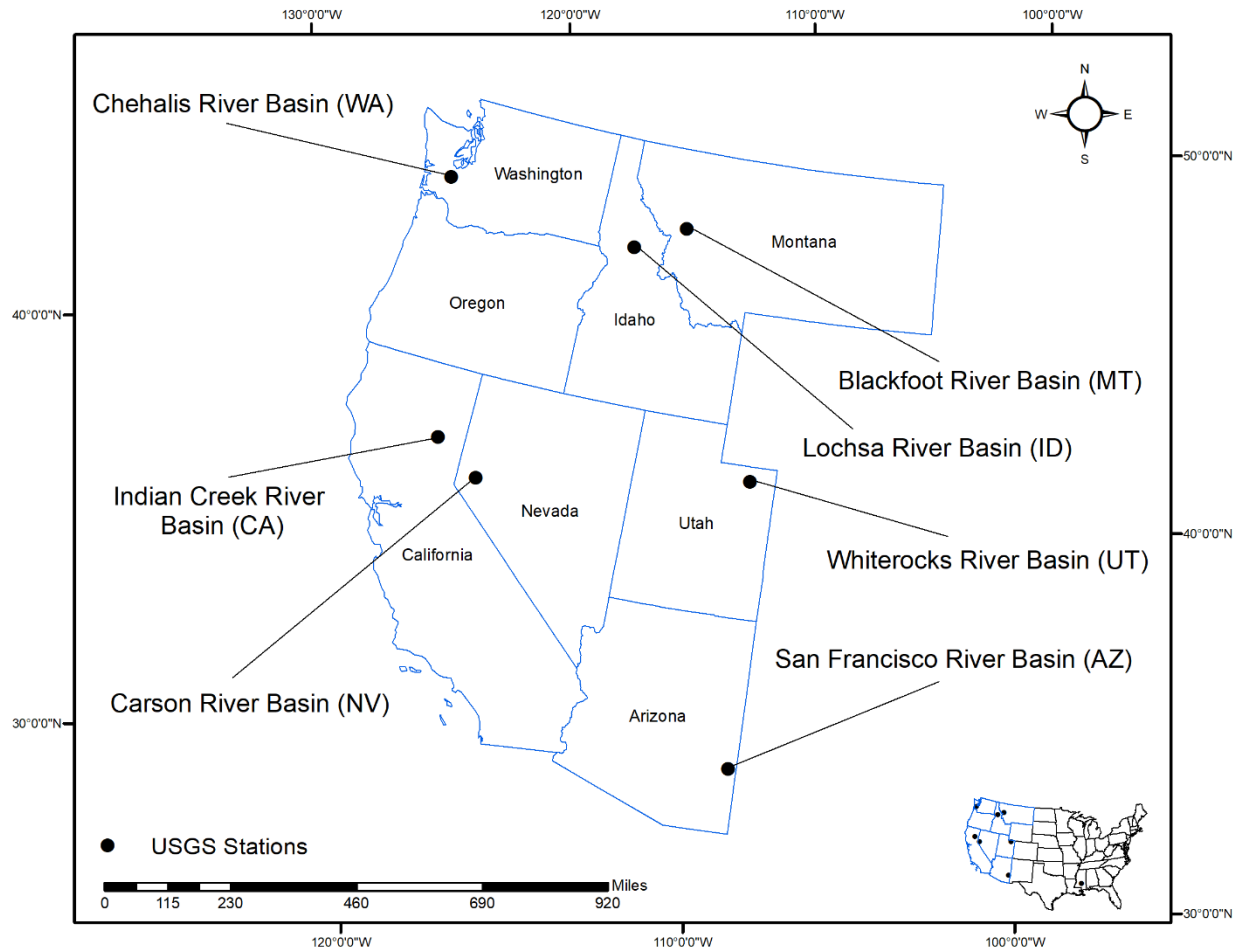


Figure 3-2 Seven study basins located in the western United States.

(1) The Chehalis River Basin (area=2318 km²) is one of the largest basins in Washington dominated mostly by oceanic climate. This region is generally wet throughout the year, except the summer, which is relatively dry. With more than 1,400 mm precipitation annually, this watershed is the wettest area in the state. This basin is mainly fed by rainfall precipitation, although a small portion of mountainous regions accumulates snow during the winter. (2) The Indian Creek Basin (area=1914 km²) lies in the Klamath National Forest in California, which drains into the Klamath River. This basin, with mean annual precipitation of 762 mm, is characterized by semiarid to subhumid climate conditions. (3) The Carson River Basin

(area=3372 km²) is an endorheic basin, which starts at the Alpine County in California and ends at the Nevada state. This region is mostly dominated by arid and hot climate with varying precipitation throughout the year. The annual precipitation in this basin reaches to 127 mm, while annual evaporation exceeds 1,524 mm. Therefore, ground water becomes the primary source for municipal and industrial water use in this watershed. (4) The Blackfoot River Basin (area=5923 km²), the snow-fed and spring-fed river, lies in west-central Montana. This basin encompasses a diverse range of ecosystems from high-elevation glaciated peaks, montane forests, and foothills to semiarid prairie pothole regions. A dry and cold climate dominates the watershed, with an average annual rainfall of 430 mm and an average annual snowfall of 2,000 mm. (5) The Lochsa River Basin (area=3051 km²) is located in the mountains of north-central Idaho. This basin is in the temperate climate zone where the precipitation generally occurs as rain in the summer and snow in the winter. (6) The Whiterocks River Basin (area=282 km²) is located in the semiarid region of northeastern Utah. In the mountainous regions of the watershed, more often precipitation falls as rain from April through September and as snow in winter months. This basin typically experiences hot, dry summers and cold winters with average annual precipitation of around 250 mm. (7) The San Francisco River Basin (area=7163 km²) is the largest tributary to the upper Gila River, which is located in southeastern Arizona and southwestern New Mexico. This basin is characterized by semiarid to humid climatic conditions with extreme seasonal precipitation events. The location of these watersheds are depicted in Figure 3-2.

Performance measures

In order to provide a robust analysis of each assimilation run, it is necessary to assess the model performance through multiple deterministic and probabilistic measures. These are described below.

$$\text{Nash – Sutcliffe efficiency (NSE)} = 1 - \frac{\sum_{t=1}^T (y_t - y'_t)^2}{\sum_{t=1}^T (y_t - \bar{y}_t)^2} \quad (42)$$

$$\text{Reliability} = 1 - \frac{2}{T} \sum_{t=1}^T \left| \frac{z_t}{T} - U_t \right| \quad (43)$$

$$\text{95\% Exceedance Ratio (ER95)} = \frac{1}{T} \sum_{t=1}^T (y'_{97.5\%,t} < y_t \text{ or } y'_{2.5\%,t} > y_t) \times 100\% \quad (44)$$

$$\begin{aligned} \text{Kling – Gupta Efficiency (KGE)} \\ = 1 - \sqrt{\left(\left(\frac{\text{Cov}_{y_t, y'_t}}{\sigma \sigma'} \right) - 1 \right)^2 + \left(\left(\frac{\sigma'}{\sigma} \right) - 1 \right)^2 + \left(\left(\frac{\mu'}{\mu} \right) - 1 \right)^2} \end{aligned} \quad (45)$$

$$\text{Mean Absolute Bias (MAB)} = \frac{1}{T} \sum_{t=1}^T |y_t - y'_t| \quad (46)$$

$$\text{Correlation Coefficient} = \frac{\text{Cov}_{y_t, y'_t}}{\sigma \sigma'} \quad (47)$$

$$\begin{aligned} \text{centered Root Mean Square Difference (RMSD)} \\ = \sqrt{\frac{1}{T} \sum_{t=1}^T \left((y'_t - \bar{y}'_t) - (y_t - \bar{y}_t) \right)^2} \end{aligned} \quad (48)$$

Nash-Sutcliffe efficiency (NSE) (Nash and Sutcliffe, 1970) is widely used to assess the goodness of fit of hydrologic models. NSE varies between 0 (worse prediction skill) to 1 (perfect prediction skill). y_t and y'_t are the observed and simulated streamflow values, respectively.

Reliability (Renard et al., 2010) is a measure of the fit of the Q-Q quantile plot to uniform.

Similar to NSE, this measure also varies between 0 (farthest possibility from uniform) to 1

(exactly uniform). For the description of the z_t and U_t calculation, we refer the readers to Renard

et al. (2010). The 95% Exceedance Ratio (ER95) (Moradkhani et al., 2006) is an indicator to evaluate the spread of the ensemble. A perfect ensemble has a 5% exceedance of the 95% predictive bounds. A value greater than 5% (too narrow predictive distribution) indicates an overconfident forecast, while a value less than 5% (too wide predictive distribution) indicates an underconfident forecast. Similar to NSE, the Kling–Gupta Efficiency (KGE) varies from $-\infty$ to 1, such that a value of 1 indicates a perfect fit between observed and simulated streamflow values. The pairs of (μ, σ) and (μ', σ') represent the first two statistical moments (means and standard deviations) of y_t and y'_t , respectively. Mean absolute bias (MAB) is a metric that indicates the magnitude of the bias for a given estimate. A perfect prediction has a MAB value of 0 indicating no bias between the observed and simulated streamflow data. The correlation coefficient indicates the strength and direction of a linear relationship between two variables. The centered root mean square difference (RMSD) is similar to the RMSD, but both observed and simulated data are centered before the differences are calculated. This performance measure has a range between 0 (perfect analogs) and ∞ (total dissimilarity). RMSD along with correlation coefficient provide complementary statistical information of pattern similarity between two series (Taylor, 2001).

Data assimilation setting

This section describes the data assimilation setting for both synthetic and real data experiments. In this study, for all data assimilation runs, we assume a lognormal and a normal error distribution with a relative error of 25% for precipitation and PET, respectively. Therefore, using these values, we assume that all meteorological observation errors, including sensor errors and those associated with spatial heterogeneity are taken into account. In addition, streamflow

observation errors are assumed to be normally distributed with a 15% relative error. For real case studies, the model error is assumed to follow a normal distribution with a relative error of 25%.

Results and Discussions

In this section, first we examine the applicability and usefulness of the proposed method on the synthetic case (section 4.1), and later several real case studies (section 4.2) are discussed to indicate the effectiveness of this method in streamflow prediction and uncertainty quantification.

Streamflow prediction results (I): synthetic case study

The first task in synthetic case study is to define two parameters of K and γ at which the proposed data assimilation approach operates. K is the assimilation window size, and γ specifies the portion of dynamic (B_d) and static (B_s) prior error covariances that participate in evolving prior error covariance (B) in each cycle throughout the assimilation period. The performance of HEAVEN can be optimized by tuning both K and γ parameters. By running the HEAVEN model for different K and γ , we obtained the most appropriate values of these two parameters. Here, we considered that K changes between one to 30 days and knowing that γ varies from 0 to 1, we considered a step size of $\Delta\gamma=0.01$ for fine tuning of this parameter. For $\gamma=0$, only dynamic error covariance is propagated throughout the assimilation process, while for $\gamma=1$, the initial guess for B matrix ($B = B_s$) is linearly augmented along the assimilation cycles.

In addition to the SAC-SMA model, we used the HyMOD model, a more parsimonious hydrologic model, to further investigate the influence of these two parameters on the model performance. The tuning factor γ versus model performance for both SAC-SMA and HyMOD

hydrologic models showed that the covariance matrix corresponding to $\gamma = 0.75$ and $k=7$ days provides better results in all performance measures.

Further analysis revealed that the model performance is more dependent on the assimilation window size than the parameter γ . Thus, the assimilation window size should be appropriately chosen, as a small window size (~ 2 days) may unnecessarily increase the computational time and decrease the model performance, while a large window size (> 20 days), irrespective of the potential for improving the model performance, may lead to local optima of the cost function. Here, a range of k values under different model scenarios, i.e., using different ensemble sizes (50, 100, 200, and 500), and γ values were examined and concluded that for both hydrologic models a time interval of seven days results in more reliable and accurate streamflow prediction. Also, we investigated the evolution of prior error covariance matrix B throughout the entire assimilation period, and detected that it directly correlates with the streamflow observation which enables the HEAVEN to properly capture the high and low flows over four years of analysis in the Leaf River Basin. In general, when streamflow rises, the covariance matrix inflates, and when streamflow declines, the covariance matrix shrinks. For clarity, we illustrate this evidence for one year in Figure 3-3. Both deterministic and probabilistic measures shown in this figure indicates the superiority of HEAVEN in streamflow prediction. Note that this figure is reported based on an ensemble size of 50, although improved results are achievable by using larger ensembles.

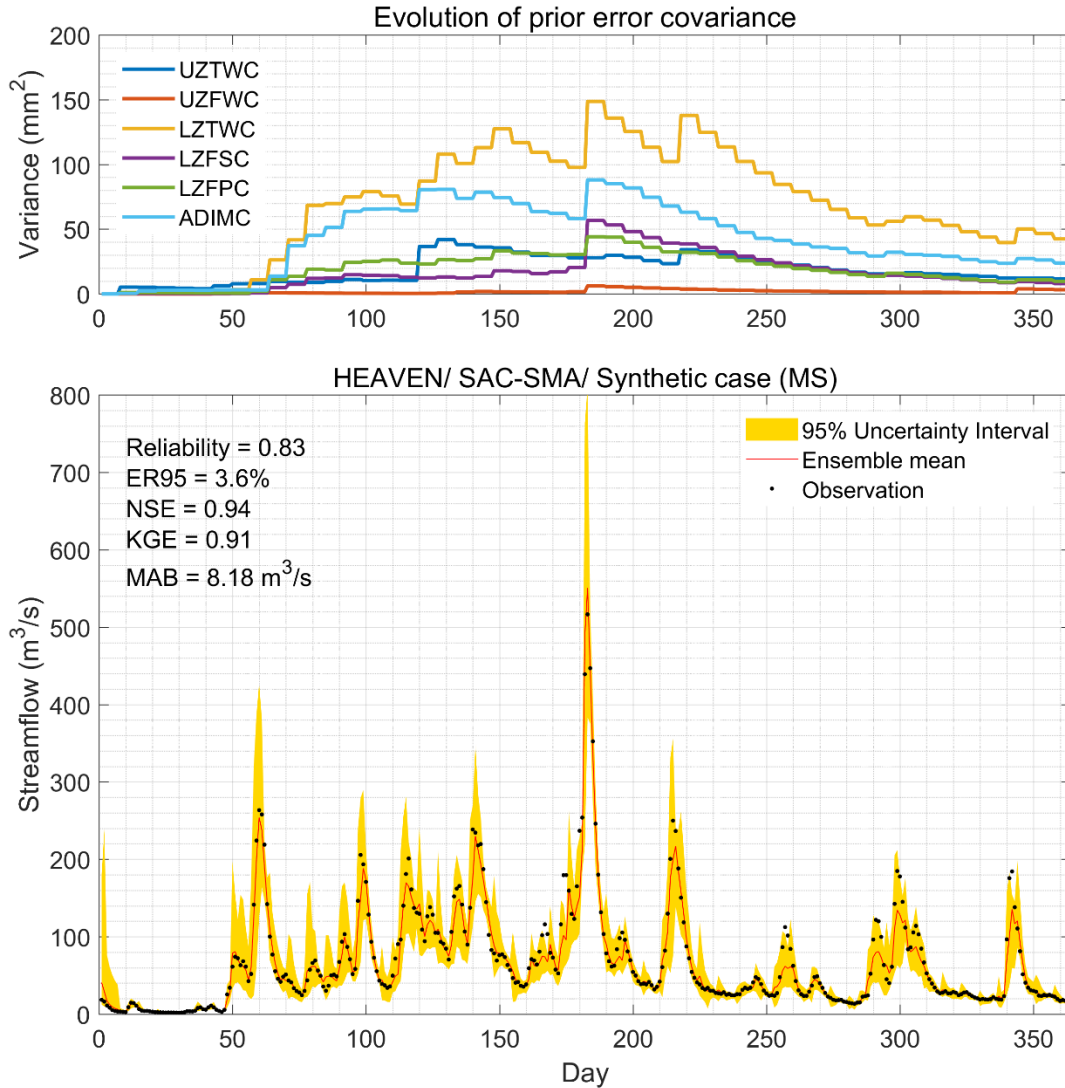


Figure 3-3 Evolution of prior error covariance matrix (B) for six state variables in SAC-SMA model. Synthetic streamflow prediction by the HEAVEN for SAC-SMA experiment over one year based on an ensemble size of 50.

In the synthetic experiment, we initialize B ($B=B_S$) with a zero matrix. Since this is a singular matrix at time zero, we initialize the B matrix with a very small value. This is apparent from the first panel of Figure 3-3, which demonstrates almost zero variance for all state variables in the first assimilation window (from $t=0$ to $t=7$). For different ensemble sizes, the HEAVEN outperforms the EPFM according to both deterministic and probabilistic measures. For instance,

for the ensemble size of 50, the reliability increases from 0.71 for the EPFM to 0.83 for the HEAVEN. To analyze the ensemble spread, the ER95 is calculated. The ER95 of HEAVEN at 3.6% is closer to the optimal value (5%), indicating an accurate uncertainty characterization. Deterministic measures also indicated that the proposed HEAVEN (KGE=0.91 and MAB=8.18 m³/s) produces an ensemble mean very close to the observation than the EPFM (KGE=0.78 and MAB=11.09 m³/s). Although the proposed method requires additional steps as compared to the EPFM, both filters show almost the same computational demand for a given ensemble size. It is worth noting that the performance of HEAVEN even using much smaller ensemble sizes (e.g., 50) is similar to that of EPFM with the ensemble size of 200, meaning that HEAVEN with less computational demand is able to provide the same level of accuracy and precision as EPFM. This can be attributed to the derivative-free optimization algorithm used in the HEAVEN, which operates fast and does not increase the computing complexity. The results also reveal that the proposed filter does not suffer from the particle degeneracy and sample impoverishment problems even when a small ensemble size is used. In fact, the GA combined with MCMC in the EPFM (Abbaszadeh et al., 2018) considerably alleviates the weight degeneracy and sample impoverishment problems. Also, the formulation used in regenerating the replicates of state variables and parameters from one cycle to another throughout the assimilation period helps reduce the ensemble size without compromising the accuracy during the assimilation.

Streamflow prediction results (II): real case studies

In addition to the synthetic study, several real data experiments are conducted in the basins located in different environmental settings (i.e., climate zones and hydrological properties) to fully examine the effectiveness and usefulness of the proposed method. One of

these experiments is based on the real data for the same basin used in the synthetic case. Figure 3-4 demonstrates streamflow prediction along with its uncertainty estimate for the Leaf River Basin using the EPFM and HEAVEN over one year. This result is based on an ensemble size of 100. Both deterministic (KGE, NSE, and MAB) and probabilistic (Reliability and ER95) measures are summarized in this figure, and they all indicate that the HEAVEN provides more accurate and reliable predictions than the EPFM approach. For example, the HEAVEN improves the EPFM performance by 12% and 36% in terms of Reliability and MAB, respectively. Further analysis revealed that although the EPFM performs well, it remains slightly biased for low flows as compared to the HEAVEN unless a large ensemble size is employed. As seen in Figure 3-4, the EPFM shows a relatively low performance in predicting low flows during dry periods. These results are further supported in the right panel of Figure 3-4, where the *S*-shape predictive QQ plots show that the HEAVEN is better able to characterize high and low flows compared to the EPFM. Also, we noticed a large contrast between these two filters when data assimilation is performed on the real data set. This explains the importance of accounting for model error using the HEAVEN method. Unlike the synthetic case where B and R are the only error covariance matrices, here in the real case data assimilation scenario, the model error covariance matrix Q plays a crucial role. Conventionally, in the hydrologic data assimilation, one may account for model structural error by simple perturbation of the model predictions y_t . This is because the model (\mathcal{M}) and observation (h) operators are not explicitly distinguishable in hydrologic systems. Therefore, matrix Q is not basically formed and fully taken into account within the EPFM filter.

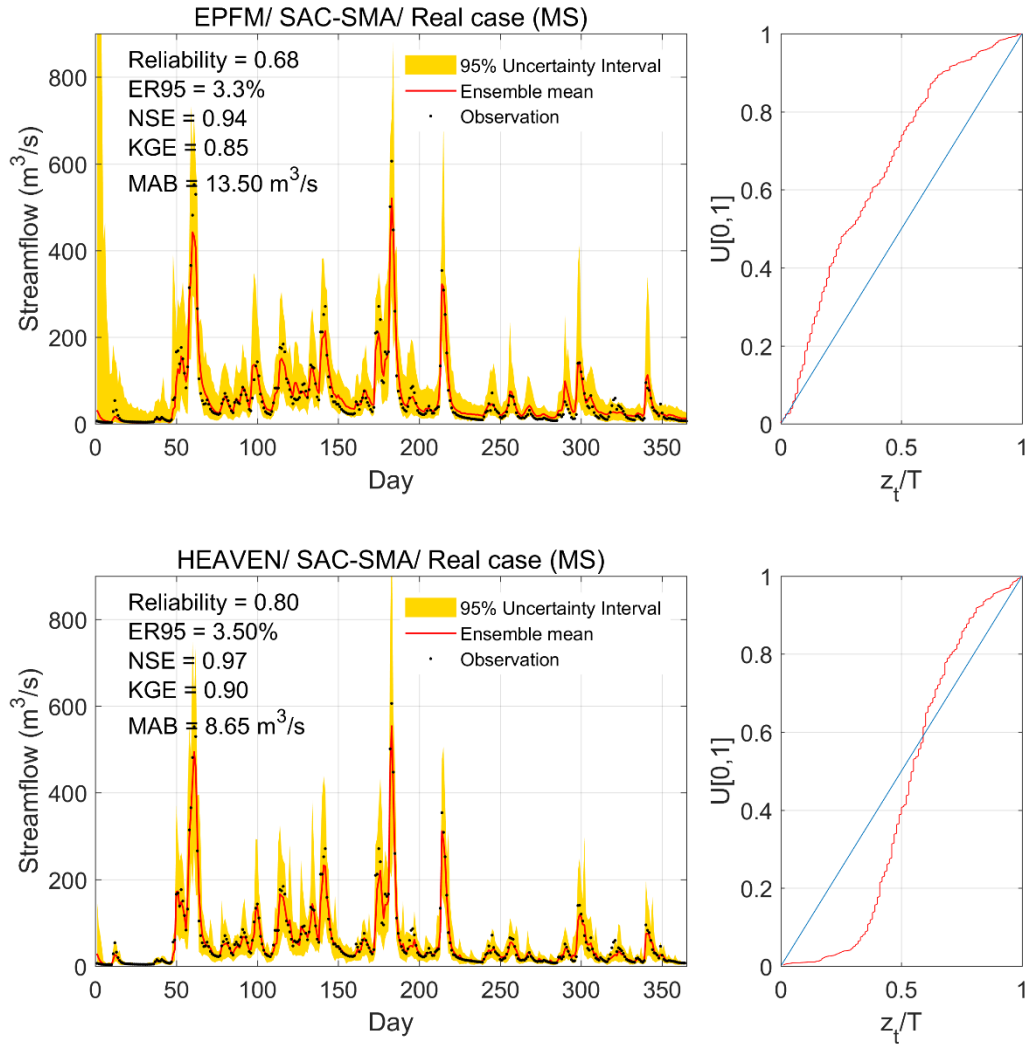


Figure 3-4 Streamflow prediction using the EPFM and HEAVEN for the Leaf River Basin over one year (left panels). Predictive QQ plots (right panels).

The proposed HEAVEN filter is able to fully account for model structural error, as it uses weak-constraint 4DVAR approach to explicitly characterize the Q matrix, and consequently provides a more accurate and reliable posterior distribution. It should be noted that in this study the model error covariance is neither inflated nor deflated ($\lambda = 1$). However, depending on the case study, tuning of this parameter may improve the assimilation results. Unlike the synthetic case in which the B matrix was initialized with zero matrix, in the real case study, this matrix is

initialized according to equation 29. As seen in the upper panel of Figure 3-3, although the prior error covariance matrix B automatically inflates or deflates over time, it is always greater than the initialized B_s matrix. The Q matrix is initialized similar to the B_s matrix (see equations 29 and 30) and used in a static form throughout the assimilation period. This means that the magnitude of prior error covariance matrix B is always greater than the Q matrix, unless the Q matrix is inflated. The B and Q matrices collectively capture the model structural error and contribute to generating more reliable and accurate posterior distributions.

In summary, the proposed algorithm, regardless of the ensemble size, outperforms the original EPFM according to both deterministic and probabilistic measures. This finding indicates that integrating the sequential and variational data assimilation approaches (EPFM and 4DVAR) provides the possibility to fully account for all sources of uncertainties involved in the hydrologic predictions. It is important to mention that by applying the proposed framework on both hydrologic models, we were able to achieve better performance in forecasting. This was validated by comparing the current approach with the variants of the particle filter. Figure S1 (in supplemental file) shows the PF-MCMC and HEAVEN skills for 3-day streamflow forecast in Leaf River Basin in Mississippi, during the flood season. To reduce the possibility of sample impoverishment in the particle filter, Moradkhani et al., (2012) combined the PF with MCMC algorithm. In addition, in Figure 3-5, we summarized multiple deterministic (i.e., KGE, NSE and MAB) and probabilistic (i.e., ER95 and Reliability) measures along with model runtime for four different assimilation strategies, i.e., HEAVEN, EPFM, PF-MCMC and PF-SIR. This comparison was made for the real case study, Leaf River Basin, over four years. This figure indicates that even using small ensemble size (e.g., 50), HEAVEN outperforms the benchmark approach, PF-SIR, with much larger ensemble size (e.g., 1000). This means that HEAVEN

approach with a smaller ensemble size has less model runtime and better model performance than the PF-SIR at a larger ensemble size. This further highlights the superiority of the proposed HEAVEN approach to its simpler versions (PF-SIR, PF-MCMC and EPFM).

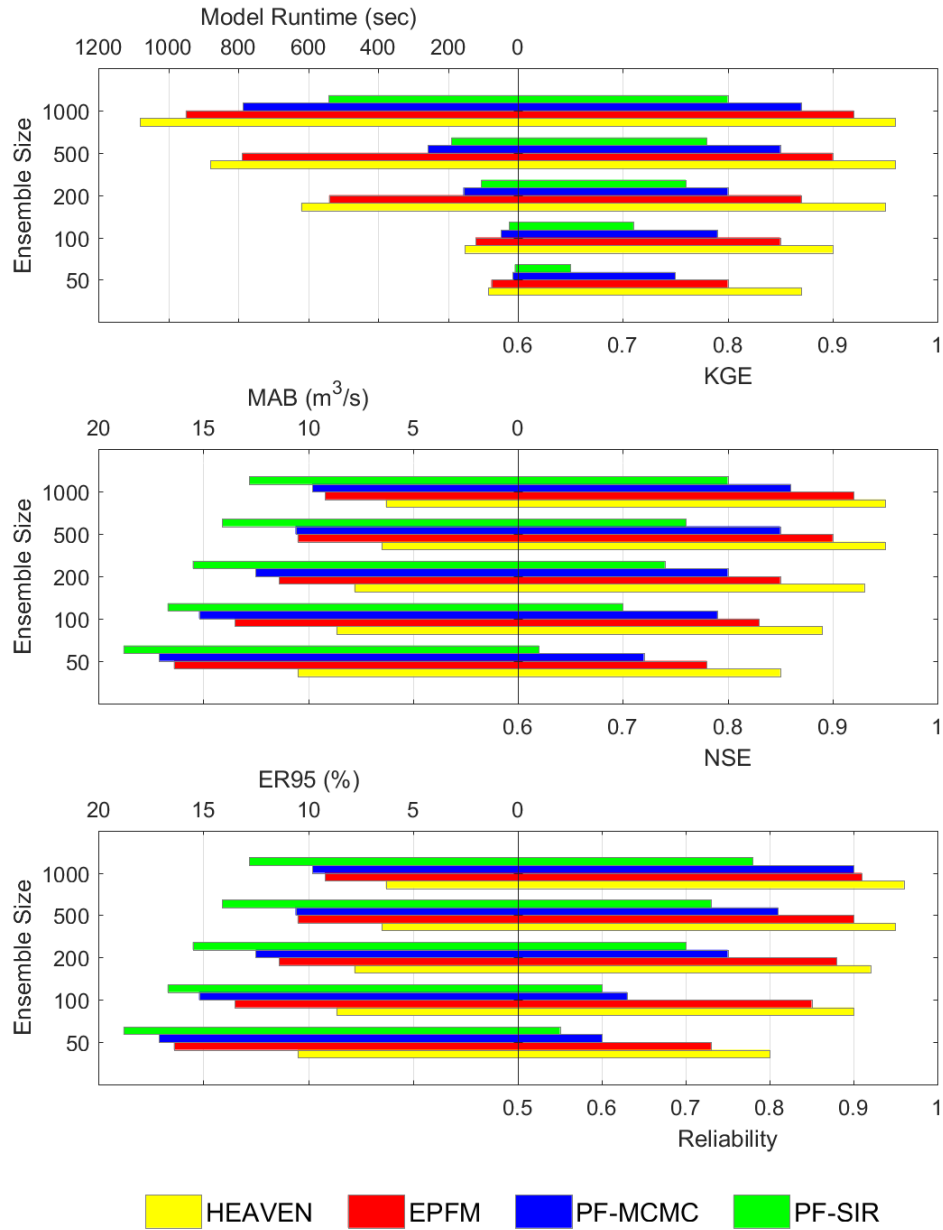


Figure 3-5 The comparison of accuracy, distribution spread, and computational demand for four assimilation strategies in the real case study over four years.

Up to this point, we compared the efficacy of HEAVEN and EPFM approaches over the Leaf River Basin for both synthetic and real case scenarios. To further interpret how 4DVAR cost function provides a more reliable and accurate initial condition for particle filtering in each assimilation cycle, we examine the prior and posterior distributions at four daily time steps ($t = 183, 213, 225$ and 337 days) for the Leaf River Basin using the HEAVEN method. These four days represent the initial time of four different assimilation cycles, which were chosen according to different streamflow regimes. For example, Figure 3-6a ($t=183$) displays a peak flow (with streamflow observation of $605.9 \text{ m}^3/\text{s}$), while Figure 3-6c ($t=225$) indicates a low flow (with streamflow observation of $17.8 \text{ m}^3/\text{s}$). The black points in Figure 3-6 illustrate such extreme events. We recall that the results being discussed here for these four days were actually obtained from the real case data assimilation performed by HEAVEN, which was previously reported in Figure 3-4 for one-year assimilation period. To interpret the results presented in Figure 3-6, we first explain the keywords included in the figure legend. In Figure 3-6a ($t=183$), 4DVAR prior (shown with a red point) is a deterministic streamflow value based on a priori model state ($x_{0,b}$). $x_{0,b}$ is available from the mean of model state ensemble at time $t=182$ (or the last time step of the previous assimilation cycle as seen in step 4 of Figure 3-1). 4DVAR analysis (green point) is a deterministic streamflow value based on an optimal initial state (x_a). x_a is obtained by minimization of the 4DVAR cost function (step 2 in Figure 3-1). HEAVEN prior PDF (shown with a blue curve) is a kernel probability distribution fitted to the streamflow values based on the simulations obtained from the prior ensemble model states ($x_0^{i,p}$, step 3 in Figure 3-1). HEAVEN posterior PDF (brown curve) is a kernel probability distribution fitted to the streamflow values based on the simulations obtained from the posterior ensemble model states ($x_{k=0}^{i,+}$). EPFM prior and posterior PDFs are also shown in magenta and cyan colors, respectively. To avoid confusion,

it should be noted that all 4DVAR products in this study (such as those shown in Figure 3-6) are obtained from the variational portion of the HEAVEN model, and not related to any single 4DVAR data assimilation run.

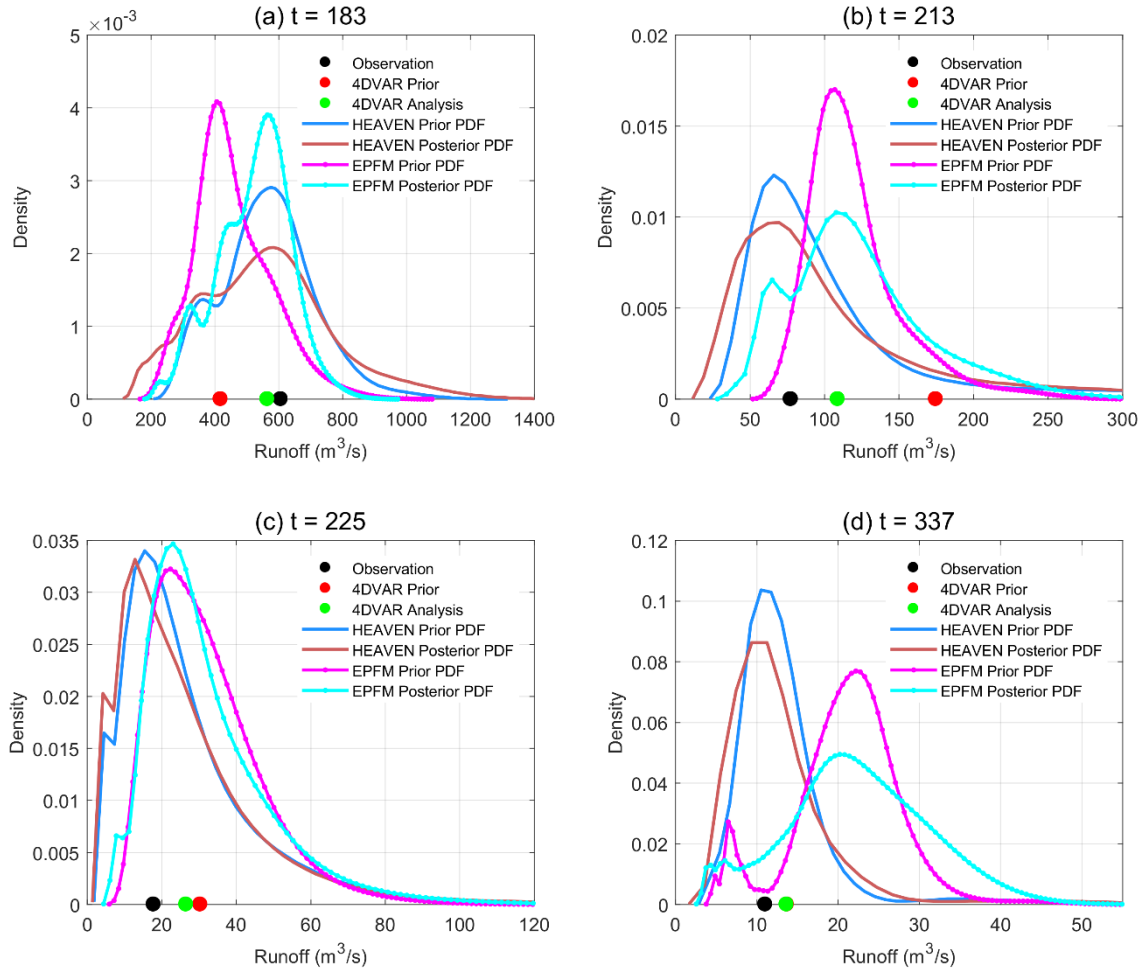


Figure 3-6 The prior and posterior distributions obtained by the EPFM and HEAVEN for four days (183, 213, 225 and 337) where each represents the initial time of an assimilation window.

The HEAVEN approach seeks to find an optimal prior distribution at the beginning of each assimilation window by minimization of the 4DVAR cost function that measures the distance between prior state estimates and observations over the time interval $[t_{k=0}, t_{k=K}]$. For instance, in Figure 3-6.a, $t_{k=0} = 183$ and $t_{k=K}=189$ (here, the assimilation interval $K=7$ days, as

discussed before in section 4.1). As Figure 3-6 illustrates, the 4DVAR approach moves a deterministic background initial condition (shown with a red point) towards an optimal location (known as 4DVAR analysis and shown with a green point) close to the observation (shown with a black point). In Figure 3-6.a, this improvement was made by 88% (from 412 m³/s to 583 m³/s), showing a great success for this approach to capture the high flows. A similar interpretation can be drawn from Figure 3-6.c, showing the applicability of this method in predicting low flows. Once the optimal deterministic initial state (x_a) is obtained, we perturb it by ε , where ε is assumed to follow normal distribution with mean zero and variance $B^{1/2}$. B has already been propagated through both static (B_s) and dynamic (B_d) prior error covariance matrices. The result of this step, x^i , undergoes an acceptance/rejection process in Step 3 to generate an appropriate prior distribution ($x_0^{i,p}$). This results in prior streamflow distribution, shown with a blue curve in Figure 3-6. In step 4, we initialize the particle filtering (here EPFM) component of the HEAVEN with $x_0^{i,p}$ and obtain the posterior distributions for the time interval $[t_{k=0}, t_{k=K}]$. As an example, the posterior distribution at $t_{k=0}=183$ is depicted with a brown curve in Figure 3-6.a. The premise of this methodology is that the improved estimation of posterior distribution while accounting for model error within the HEAVEN, results in more accurate and reliable streamflow predictions within the assimilation window. This is reported for all four time intervals in Figure 3-7 while compared with those obtained by the EPFM model when no account of model error exists. For instance, for the assimilation window initialized at $t_{k=0}=183$, the next six days show a flood recession period for streamflow, as it declines from 447.4 m³/s to 45.30 m³/s. In this case, it is observed that the HEAVEN provides more accurate and reliable streamflow predictions due to better estimation of both prior and posterior distributions. As we discussed in our recent publication (Abbaszadeh et al. 2018), the EPFM is a robust evolutionary

ensemble-based data assimilation approach to predict the streamflow owing to its unique features. However, the added feature in the HEAVEN that is mainly the characterization of model error make this new approach more suitable when model error is a serious concern. Further analysis reveals that the SAC-SMA model with improved initial condition from the HEAVEN at $t=189$ is able to forecast streamflow up to seven days with a better degree of accuracy and reliability. The second row in Figure 3-7 indicates that streamflow increased from $75.4 \text{ m}^3/\text{s}$ to $353.9 \text{ m}^3/\text{s}$ in one day (between $t=213$ and $t=214$) followed by a slow decay for the next five days. The results demonstrate how both prior and posterior distributions characterized by the HEAVEN accurately and precisely track streamflow changes as compared to the EPFM. The third row in Figure 3-7 illustrates the capability of both filters in predicting low flows. It indicates that a small shift for both prior and posterior distributions at the beginning of the assimilation window (see Figure 3-6.c) results in more accurate and reliable streamflow predictions in low flow events. Likewise, in the fourth row for Figure 3-7, the HEAVEN outperforms the EPFM, specifically on days $t=338$ and $t=339$ where the EPFM particles located far from the observations.

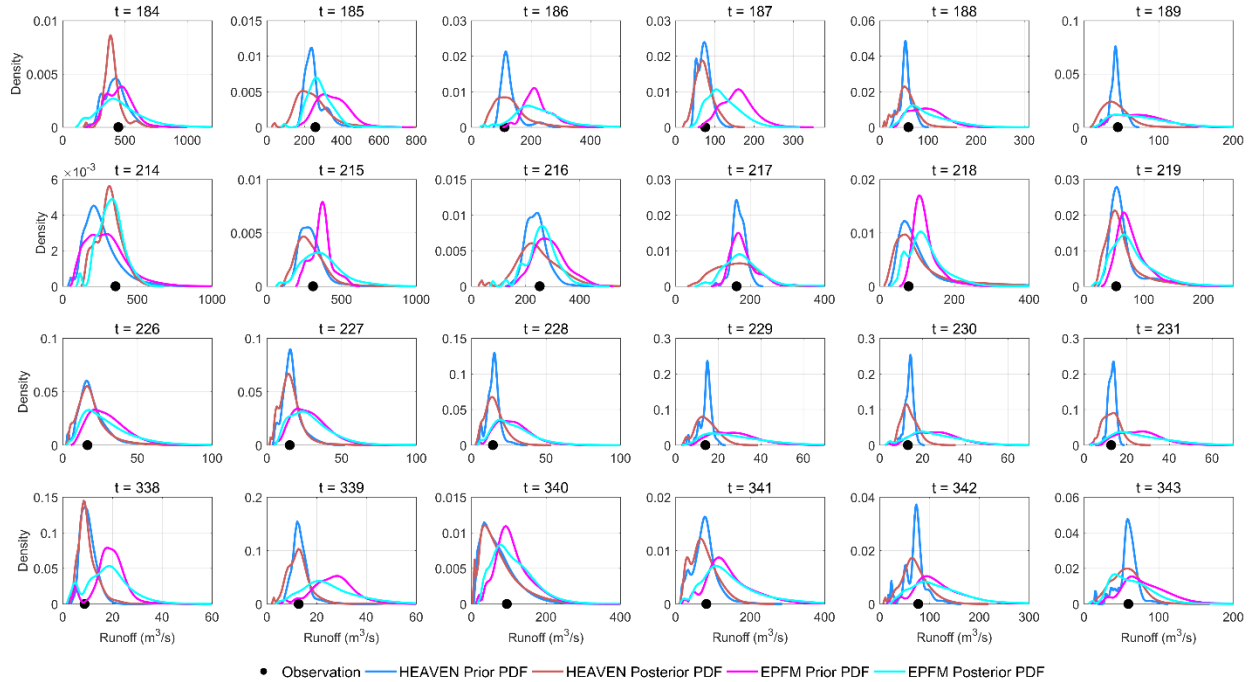


Figure 3-7 The prior and posterior distributions obtained by the EPFM and HEAVEN for the next six days in each assimilation window corresponding to the initial conditions reported in Figure 3-6.

Up to this point, using synthetic and real case experiments, we examined how HEAVEN is capable of properly characterizing the posterior distribution with higher accuracy and reliability for different streamflow regimes. The ensuing task is to further investigate the robustness and scalability of the proposed HEAVEN method compared to its original EPFM version. To accomplish this, we applied both filters on seven real case experiments introduced in section 3.2.2 and analyzed their performances over four different ensemble sizes of 50, 100, 200, and 500. In order to summarize the obtained results, we used the Taylor diagram that displays the comparative assessment of different techniques by using three performance measures, that is, normalized standard deviation, correlation coefficient and normalized centered RMSD. Figure 3-8 presents two Taylor diagrams summarizing the statistics of the comparison between the

ensemble mean, obtained by both HEAVEN and EPFM filters, and observations for seven real case experiments plus Leaf River Basin used in this study.

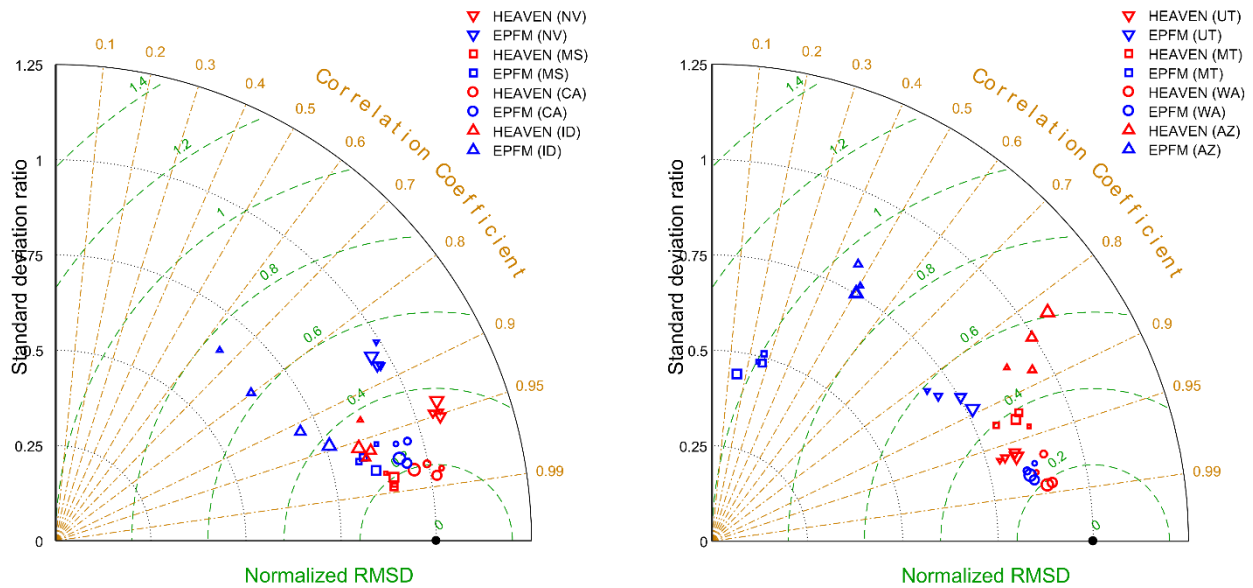


Figure 3-8 Taylor diagrams displaying the effectiveness of the two assimilation methods (i.e., EPFM and HEAVEN) for eight real case studies over one year of analysis. The symbols indicate different case studies in each panel. The size of each symbol represent the ensemble size (50, 100, 200, and 500) schematically. Normalized RMSD is represented by green dashed line while correlation coefficient is displayed by brown dotted line. Normalized standard deviation and correlation coefficient are on the radial axis and angular axis, respectively. The observation is shown with a black point on the horizontal axis.

The symbol below/above the standard deviation of 1 represents the ensemble mean wherein the variability is smaller/larger than that of the streamflow observation. The black point (observation) shown on the horizontal axis represents the normalized RMSD equal to 0, and both the ratio of standard deviations and the correlation coefficient are equal to 1. In all cases, it is seen that the ratios of standard deviation for the HEAVEN ensemble mean are closer to 1 than the EPFM ensemble means. These diagrams also show that there is a good range of correlation obtained by the HEAVEN, with most values above 0.90. In addition to these two measures, the normalized centered RMSD indicates that the HEAVEN outperforms the EPFM regardless of the

ensemble size. For all eight real case experiments, it is seen that the HEAVEN with a small ensemble size (e.g., 50) yields more accurate streamflow predictions as compared to the EPFM even with an ensemble size of 500. As shown in Figure 3-8, for two watersheds located in Arizona and Montana, there is a considerable difference between the performances of the two filters. A more plausible reason for this may be attributed to the hydroclimate conditions of these two regions. The Blackfoot River Basin in Montana is a snow-dominated basin due to the strong atmospheric river in winter, and floods often happen due to peak spring melt. However, the San Francisco River Basin in Arizona is a rain-fed basin with extreme rainfall events that are followed by dry periods. The results from the EPFM imply that this model does not properly capture the streamflow fluctuations resulting from either evapotranspiration (AZ) or snowmelt (MT). However, the HEAVEN better represents the streamflow variations and detects extreme events. Furthermore, the HEAVEN robustness can be explained by how it characterizes the model structural error by taking into account both B and Q error covariance matrices in the 4DVAR cost function. However, EPFM does not account for the model structural error. Therefore, the ensemble mean obtained by the HEAVEN shows higher skill than the EPFM for all real case experiments. We also compared the probabilistic performance measures (i.e., ER95 and Reliability) between these two filters and found that the HEAVEN always outperforms the EPFM regardless of the ensemble size. For example, for the Chehalis River Basin (WA) with an ensemble size of 50, although both filters deterministically show similar performance in predicting streamflow, the probabilistic measures show that the HEAVEN provides more reliable posterior distribution than the EPFM. The ER95 of the HEAVEN (3.9%) is closer to the ideal value of 5% than the EPFM with ER95=10.21%. The higher ER95 value of the EPFM is because the ensemble distribution is too narrow, which indicates an overconfident streamflow prediction.

The Reliability increases from 0.72 for the EPFM to 0.85 for the HEAVEN, indicating a more reliable ensemble prediction by the HEAVEN. Therefore, we conclude that the proposed HEAVEN approach, by characterizing the model structural uncertainty, along with the model parameter and input data uncertainties, provides a more accurate and reliable posterior distribution as compared with the EPFM method. The superiority of the HEAVEN is further confirmed when we assess the capability of both approaches in predicting high flow events. This corroborates with the findings of others (Pathiraja et al., 2018a and 2018b; Shoaib et al., 2016), who demonstrated that accounting for the model structural uncertainty is particularly important in predicting high flow events.

It should be noted that, although techniques to combine the hybrid particle filter and 4DVAR have been previously explored (Chorin and Tu, 2009; Chorin et al., 2010; Morzfeld et al., 2012; van Leeuwen, 2015; Slivinski et al., 2015; Atkins et al., 2013; Zhu et al., 2016), the objective, formulation and implementation of the proposed approach is fundamentally different from other methods. HEAVEN is a framework in which any variant of particle filtering can be used to account for and quantify the hydrologic model structural uncertainty, along with other sources of uncertainties involved in model predictions, without a need to calculate the adjoint and tangent linear of forecast model, which is most often not practical in hydrologic studies.

Concluding remarks

This paper proposes a new hybrid ensemble and variational data assimilation method that effectively combines both sequential (EPFM) and variational (4DVAR) assimilation approaches to account for all sources of uncertainties involved in hydrologic predictions, and thus leads to more accurate and reliable posterior distributions for both state variables and parameters in data

assimilation applications. The effectiveness and usefulness of this technique was evaluated by both deterministic and probabilistic measures, and the robustness and superiority of this filter was examined through eight real case studies located in different geographical and climate zones across the United States. This study suggests using the HEAVEN approach for the following features:

- (1) It operates simultaneously on both batch-processing and sequential manners, leading to a more complete estimation of posteriors for any streamflow regimes, including low and high flows.
- (2) It characterizes model structural uncertainty by incorporating an explicit form of model error covariance matrix (Q) in the 4DVAR cost function.
- (3) It propagates the prior error covariance matrix (B), which consists of a linear combination of static (B_s) and dynamic (B_d) error covariance matrices, from one cycle to another cycle over the entire assimilation period to fully account for a wide range of uncertainties in model predictions, and thus lead to more accurate and reliable posterior distributions.
- (4) It precludes the particle degeneracy and sample impoverishment.

In this study, we used a lumped hydrologic model as a proof of concept for the proposed joint Bayesian and variational data assimilation approach, although implementation and analysis with a distributed hydrologic model would be the next step to further analyze the improved performance and investigate the HEAVEN scalability. These aspects will be included in our upcoming research paper. One attractive feature of HEAVEN is that it needs neither tangent linear nor adjoint versions of forecast model, making it more suitable in hydrologic applications. However, for those models in which such linearization of model and observation operators are

accessible, it is expected that the results and the computational efficiency of the implementation may be further improved. This conjecture will be investigated in future research.

Acknowledgment

Partial financial support for this project was provided by the National Science Foundation Cyber- Innovation for Sustainability Science and Engineering (CyberSEES), Grant No. CCF-1539605. The data sets used in this study were acquired from Model Parameter Estimation Experiment (MOPEX) located at http://www.nws.noaa.gov/ohd/mopex/mo_datasets.htm.

References

- Abbaszadeh, P., Moradkhani, H., and Yan, H. (2018). Enhancing hydrologic data assimilation by evolutionary Particle Filter and Markov Chain Monte Carlo. *Advances in Water Resources*, 111. <https://doi.org/10.1016/j.advwatres.2017.11.011>
- Abdolghafoorian, A., and Farhadi, L. (2016). Uncertainty Quantification in Land Surface Hydrologic Modeling: Toward an Integrated Variational Data Assimilation Framework. *IEEE Journal of Selected Topics in Applied Earth Observations and Remote Sensing*, 9(6), 2628–2637. <https://doi.org/10.1109/JSTARS.2016.2553444>
- Anderson, J. L. (2001). An Ensemble Adjustment Kalman Filter for Data Assimilation. *Monthly Weather Review*, 129(12), 2884–2903. [https://doi.org/10.1175/1520-0493\(2001\)129<2884:AEAKFF>2.0.CO;2](https://doi.org/10.1175/1520-0493(2001)129<2884:AEAKFF>2.0.CO;2)
- Anderson, J. L., and Anderson, S. L. (1999). A Monte Carlo Implementation of the Nonlinear Filtering Problem to Produce Ensemble Assimilations and Forecasts. *Monthly Weather Review*, 127(12), 2741–2758. [https://doi.org/10.1175/1520-0493\(1999\)127<2741:AMCIOT>2.0.CO;2](https://doi.org/10.1175/1520-0493(1999)127<2741:AMCIOT>2.0.CO;2)
- Andrieu, C., Doucet, A., and Holenstein, R. (2010). Particle Markov chain Monte Carlo methods. *Journal of the Royal Statistical Society Series B-Statistical Methodology*, 72(3), 269–342. <https://doi.org/10.1111/j.1467-9868.2009.00736.x>
- Atkins, E., Morzfeld, M., Chorin., A. J. (2013). Implicit particle methods and their connection with variational data assimilation. *Monthly Weather Review*, 141(6), 1786–1803.
- Bannister, R. N. (2017). A review of operational methods of variational and ensemble-variational data assimilation. *Quarterly Journal of the Royal Meteorological Society*, 143(703), 607–633. <https://doi.org/10.1002/qj.2982>
- Boyle, D. (2001), Multicriteria calibration of hydrological models, Ph.D.dissertation, Univ. of Ariz., Tucson.
- Bulygina, N., and Gupta, H. (2011). Correcting the mathematical structure of a hydrological model via Bayesian data assimilation. *Water Resources Research*, 47(5). <https://doi.org/10.1029/2010WR009614>
- Burnash, R. J., R. L. Ferral, and R. A. McGuire (1973). A generalized streamflow simulation system conceptual modeling for digital computers, report, U. S. Dep. of Commer. Natl. Weather Serv. and State of Calif. Dep. of Water Resour.
- Chorin, A. J., and Tu, X. (2009). Implicit sampling for particle filters. *Proceedings of the*

National Academy of Sciences, 106(41), 17249–17254.

- Chorin, A. J., Morzfeld, M., Tu, X. (2010). Implicit filters for data assimilation. *Communications in Applied Mathematics and Computational Science*, 5, 221–240.
- Clark, M. P., Rupp, D. E., Woods, R. A., Zheng, X., Ibbitt, R. P., Slater, A. G., ... Uddstrom, M. J. (2008). Hydrological data assimilation with the ensemble Kalman filter: Use of streamflow observations to update states in a distributed hydrological model. *Advances in Water Resources*, 31(10), 1309–1324. <https://doi.org/10.1016/j.advwatres.2008.06.005>
- Crow, W. T., and Wood, E. F. (2003). The assimilation of remotely sensed soil brightness temperature imagery into a land surface model using Ensemble Kalman filtering: A case study based on ESTAR measurements during SGP97. *Advances in Water Resources*, 26(2), 137–149. [https://doi.org/10.1016/S0309-1708\(02\)00088-X](https://doi.org/10.1016/S0309-1708(02)00088-X)
- DeChant, C. M., and Moradkhani, H. (2011). Improving the characterization of initial condition for ensemble streamflow prediction using data assimilation. *Hydrology and Earth System Sciences*, 15(11), 3399–3410. <https://doi.org/10.5194/hess-15-3399-2011>
- DeChant, C. M., and Moradkhani, H. (2012). Examining the effectiveness and robustness of sequential data assimilation methods for quantification of uncertainty in hydrologic forecasting. *Water Resources Research*, 48(4), 1–15. <https://doi.org/10.1029/2011WR011011>
- Dong, J., Steele-Dunne, S. C., Judge, J., and Van De Giesen, N. (2015). A particle batch smoother for soil moisture estimation using soil temperature observations. *Advances in Water Resources*, 83, 111–122. <https://doi.org/10.1016/j.advwatres.2015.05.017>
- Doucet A, Johansen AM. (2009). A tutorial on particle filtering and smoothing: fifteen years later. *Handbook Nonlinear Filter*.12, 656–704.
- Duan, Q., Schaake, J., Andréassian, V., Franks, S., Goteti, G., Gupta, H. V., ... Wood, E. F. (2006). Model Parameter Estimation Experiment (MOPEX): An overview of science strategy and major results from the second and third workshops. In *Journal of Hydrology* (Vol. 320, pp. 3–17). <https://doi.org/10.1016/j.jhydrol.2005.07.031>
- Efstratiadis, A., and Koutsoyiannis, D. (2010). Une décennie d'approches de calage multi-objectifs en modélisation hydrologique: Une revue. *Hydrological Sciences Journal*, 55(1), 58–78. <https://doi.org/10.1080/02626660903526292>
- Gao, F., & Han, L. (2012). Implementing the Nelder-Mead simplex algorithm with adaptive parameters. *Computational Optimization and Applications*, 51(1), 259–277. <https://doi.org/10.1007/s10589-010-9329-3>
- Gupta, H. V., Kling, H., Yilmaz, K. K., and Martinez, G. F. (2009). Decomposition of the mean squared error and NSE performance criteria: Implications for improving hydrological modelling. *Journal of Hydrology*, 377(1–2), 80–91. <https://doi.org/10.1016/j.jhydrol.2009.08.003>

- Han, H., Ding, Y. S., Hao, K. R., and Liang, X. (2011). An evolutionary particle filter with the immune genetic algorithm for intelligent video target tracking. *Computers and Mathematics with Applications*, 62(7), 2685–2695. <https://doi.org/10.1016/j.camwa.2011.06.050>
- Hernández, F., and Liang, X. (2017). Hybridizing Bayesian and variational data assimilation for robust high-resolution hydrologic forecasting. *Hydrology and Earth System Sciences Discussions*, (August), 1–33. <https://doi.org/10.5194/hess-2017-431>
- Jones, A. S., Vukićević, T., and Vonder Haar, T. H. (2004). A Microwave Satellite Observational Operator for Variational Data Assimilation of Soil Moisture. *Journal of Hydrometeorology*, 5(1), 213–229. [https://doi.org/10.1175/1525-7541\(2004\)005<0213:AMSOOF>2.0.CO;2](https://doi.org/10.1175/1525-7541(2004)005<0213:AMSOOF>2.0.CO;2)
- Kwok, N. M., Fang, G., and Zhou, W. (2005). Evolutionary particle filter: Re-sampling from the genetic algorithm perspective. *2005 IEEE/RSJ International Conference on Intelligent Robots and Systems, IROS*, 1053–1058. <https://doi.org/10.1109/IROS.2005.1545119>
- De Lannoy, G. J. M., Reichle, R. H., Houser, P. R., Pauwels, V. R. N., and Verhoest, N. E. C. (2007). Correcting for forecast bias in soil moisture assimilation with the ensemble Kalman filter. *Water Resources Research*, 43(9). <https://doi.org/10.1029/2006WR005449>
- Lee, H., Seo, D. J., and Koren, V. (2011). Assimilation of streamflow and in situ soil moisture data into operational distributed hydrologic models: Effects of uncertainties in the data and initial model soil moisture states. *Advances in Water Resources*, 34(12), 1597–1615. <https://doi.org/10.1016/j.advwatres.2011.08.012>
- Leisenring, M., and Moradkhani, H. (2012). Analyzing the uncertainty of suspended sedimentload prediction using sequential data assimilation. *Journal of Hydrology*. 468-469, 268–282. <http://dx.doi.org/10.1016/j.jhydrol.2012.08.049>.
- Liang, F., and Wong, W. H. (2001). Real-Parameter Evolutionary Monte Carlo with Applications to Bayesian Mixture Models. *Journal of the American Statistical Association*, 96(February 2001), 653–666. <https://doi.org/10.2307/2670304>
- Liu, Y., and Gupta, H. V. (2007). Uncertainty in hydrologic modeling: Toward an integrated data assimilation framework. *Water Resources Research*, 43(7), 1–18. <https://doi.org/10.1029/2006WR005756>
- Lorenc, A.C., Bowler, N.E., Clayton, A.M., Pring, S.R. (2015). Comparison of hybrid-4DVar and hybrid-4DVar data assimilation methods for global NWP. *Monthly Weather Review*, 143, 212–229.
- Lorenc, A. C. (2017). Improving ensemble covariances in hybrid variational data assimilation without increasing ensemble size. *Quarterly Journal of the Royal Meteorological Society*, 143, 1062–1072, <https://doi.org/10.1002/qj.2990>.
- Matgen, P., Montanari, M., Hostache, R., Pfister, L., Hoffmann, L., Plaza, D., ... Savenije, H. H. G. (2010). Towards the sequential assimilation of SAR-derived water stages into hydraulic

- models using the Particle Filter: Proof of concept. *Hydrology and Earth System Sciences*, 14(9), 1773–1785. <https://doi.org/10.5194/hess-14-1773-2010>
- Morzfeld, M., X. Tu, E. Atkins, and A.J. Chorin. (2012). A random map implementation of implicit filters. *Journal of Computational Physics*, 231(4), 2049-2066. <http://dx.doi.org/10.1016/j.jcp.2011.11.022>.
- Moradkhani, H., Sorooshian, S., Gupta, H. V., and Houser, P. R. (2005a). Dual state-parameter estimation of hydrological models using ensemble Kalman filter. *Advances in Water Resources*, 28(2), 135–147. <https://doi.org/10.1016/j.advwatres.2004.09.002>.
- Moradkhani, H., Hsu, K.-L., Gupta, H., and Sorooshian, S. (2005b). Uncertainty assessment of hydrologic model states and parameters: Sequential data assimilation using the particle filter. *Water Resources Research*, 41(5), 1–17. <https://doi.org/10.1029/2004WR003604>
- Moradkhani, H., DeChant, C. M., and Sorooshian, S. (2012). Evolution of ensemble data assimilation for uncertainty quantification using the particle filter-Markov chain Monte Carlo method. *Water Resources Research*, 48(12). <https://doi.org/10.1029/2012WR012144>
- Moradkhani, H., Hsu, K., Hong, Y., and Sorooshian, S. (2006). Investigating the impact of remotely sensed precipitation and hydrologic model uncertainties on the ensemble streamflow forecasting. *Geophysical Research Letters*, 33(12). <https://doi.org/10.1029/2006GL026855>.
- Moradkhani H., Nearing G., Abbaszadeh P., Pathiraja S. (2018) Fundamentals of Data Assimilation and Theoretical Advances. In: Duan et al. (eds), *Handbook of Hydrometeorological Ensemble Forecasting*. Springer, Berlin, Heidelberg, doi: https://doi.org/10.1007/978-3-642-40457-3_30-1.
- Nash, J. E., and Sutcliffe, J. V. (1970). River Flow Forecasting Through Conceptual Models Part I-a Discussion of Principles*. *Journal of Hydrology*, 10, 282–290. [https://doi.org/10.1016/0022-1694\(70\)90255-6](https://doi.org/10.1016/0022-1694(70)90255-6)
- Noh, S. J., Tachikawa, Y., Shiiba, M., and Kim, S. (2011). Applying sequential Monte Carlo methods into a distributed hydrologic model: Lagged particle filtering approach with regularization. *Hydrology and Earth System Sciences*, 15(10), 3237–3251. <https://doi.org/10.5194/hess-15-3237-2011>
- Parrish, M. A., Moradkhani, H., and Dechant, C. M. (2012). Toward reduction of model uncertainty: Integration of Bayesian model averaging and data assimilation. *Water Resources Research*, 48(3). <https://doi.org/10.1029/2011WR011116>
- Pathiraja, S., Marshall, L., Sharma, A., and Moradkhani, H. (2016). Detecting non-stationary hydrologic model parameters in a paired catchment system using data assimilation. *Advances in Water Resources*, 94, 103–119. <https://doi.org/10.1016/j.advwatres.2016.04.021>.
- Pathiraja, S., Moradkhani, H., Marshall, L., Sharma, A., and Geenens, G. (2018a). Data-Driven

Model Uncertainty Estimation in Hydrologic Data Assimilation. *Water Resources Research*. <https://doi.org/10.1002/2018WR022627>

- Pathiraja, S., Anghileri, D., Burlando, P., Sharma, A., Marshall, L., and Moradkhani, H. (2018b). Insights on the impact of systematic model errors on data assimilation performance in changing catchments. *Advances in Water Resources*, *113*, 202–222. <https://doi.org/10.1016/j.advwatres.2017.12.006>.
- Pathiraja, S., Anghileri, D., Burlando, P., Sharma, A., Marshall, L., and Moradkhani, H. (2018c): Time-varying parameter models for catchments with land use change: the importance of model structure, *Hydrol. Earth Syst. Sci.*, *22*, 2903-2919, <https://doi.org/10.5194/hess-22-2903-2018>.
- Plaza, D. A., De Keyser, R., De Lannoy, G. J. M., Giustarini, L., Matgen, P., and Pauwels, V. R. N. (2012). The importance of parameter resampling for soil moisture data assimilation into hydrologic models using the particle filter. *Hydrology and Earth System Sciences*, *16*(2), 375–390. <https://doi.org/10.5194/hess-16-375-2012>
- Reichle, R., McLaughlin, D. B., and Entekhabi, D. (2001). Variational data assimilation of microwave radiobrightness observations for land surface hydrologic applications. *IEEE Transactions on Geoscience and Remote Sensing*, *39*(8), 1708–1718.
- Reichle, R., McLaughlin, D. B., and Entekhabi, D. (2002). Hydrologic data assimilation with the ensemble Kalman filter. *Monthly Weather Review*, *130*(1), 103–114. [https://doi.org/10.1175/1520-0493\(2002\)130<0103:HDAWTE>2.0.CO;2](https://doi.org/10.1175/1520-0493(2002)130<0103:HDAWTE>2.0.CO;2)
- Renard, B., Kavetski, D., Kuczera, G., Thyer, M., and Franks, S. W. (2010). Understanding predictive uncertainty in hydrologic modeling: The challenge of identifying input and structural errors. *Water Resources Research*, *46*(5). <https://doi.org/10.1029/2009WR008328>
- Rios, L. M., & Sahinidis, N. V. (2013). Derivative-free optimization: a review of algorithms and comparison of software implementations. *Journal of Global Optimization*, *56*(3), 1247–1293. <https://doi.org/10.1007/s10898-012-9951-y>
- Salamon, P., and Feyen, L. (2009). Assessing parameter, precipitation, and predictive uncertainty in a distributed hydrological model using sequential data assimilation with the particle filter. *Journal of Hydrology*, *376*(3–4), 428–442. <https://doi.org/10.1016/j.jhydrol.2009.07.051>
- Seo, D. J., Cajina, L., Corby, R., and Howieson, T. (2009). Automatic state updating for operational streamflow forecasting via variational data assimilation. *Journal of Hydrology*, *367*(3–4), 255–275. <https://doi.org/10.1016/j.jhydrol.2009.01.019>
- Shaw, J. A., and Daescu, D. N. (2016). An ensemble approach to weak-constraint four-dimensional variational data assimilation. *Procedia Computer Science*, *80*, 496–506. <https://doi.org/10.1016/j.procs.2016.05.329>
- Shoab, S. A., Marshall, L., and Sharma, A. (2016). A metric for attributing variability in modelled streamflows. *Journal of Hydrology*, *541*, 1475–1487.

<https://doi.org/10.1016/j.jhydrol.2016.08.050>

- Slivinski, L., Spiller, E., Apte, A., and Sandstede, B. (2015). A hybrid particle–ensemble Kalman filter for Lagrangian data assimilation. *Monthly Weather Review*, 143(1), 195–211.
- Talagrand, O., and Courtier, P. (1987). Variational Assimilation of Meteorological Observations With the Adjoint Vorticity Equation. I: Theory. *Quarterly Journal of the Royal Meteorological Society*, 113(478), 1311–1328. <https://doi.org/10.1002/qj.49711347812>
- Taylor, K. E. (2001). Summarizing multiple aspects of model performance in a single diagram. *Journal of Geophysical Research: Atmospheres*, 106(D7), 7183–7192. <https://doi.org/10.1029/2000JD900719>
- Tian, X., Xie, Z., Dai, A., Shi, C., Jia, B., Chen, F., and Yang, K. (2009). A dual-pass variational data assimilation framework for estimating soil moisture profiles from AMSR-E microwave brightness temperature. *Journal of Geophysical Research Atmospheres*, 114(16), 1–12. <https://doi.org/10.1029/2008JD011600>
- Tremolet, Y. (2006). Accounting for an imperfect model in 4D-Var. *Quarterly Journal of the Royal Meteorological Society*, 132(621), 2483–2504. <https://doi.org/10.1256/qj.05.224>
- Van Leeuwen, P. J. (2015). Nonlinear data assimilation for high-dimensional systems. in *Nonlinear Data Assimilation*, P. J. van Leeuwen, C. Yuan, and S. Reich, Eds. Basel, Switzerland: Springer, ch. 1, pp. 1–73.
- Verkade, J. S., and Werner, M. G. F. (2011). Estimating the benefits of single value and probability forecasting for flood warning. *Hydrology and Earth System Sciences*, 15(12), 3751–3765. <https://doi.org/10.5194/hess-15-3751-2011>
- Vrugt, J. A., Gupta, H. V., Nualláin, B., and Bouten, W. (2006). Real-Time Data Assimilation for Operational Ensemble Streamflow Forecasting. *Journal of Hydrometeorology*, 7(3), 548–565. <https://doi.org/10.1175/JHM504.1>
- Wang, X., Barker, D.M., Snyder, C., Hamill, T.M. (2008). A hybrid ETKF–3DVAR data assimilation scheme for the WRF model. Part I: observing system simulation experiment. *Monthly Weather Review*, 136, 5116–5131.
- Wu, G., Zheng, X., Wang, L., Zhang, S., Liang, X., Li, Y. (2013). A new structure for error covariance matrices and their adaptive estimation in EnKF assimilation. *Quarterly Journal of the Royal Meteorological Society*, 139(672), 795–804.
- Yan, H., Moradkhani, H., and Zarekarizi, M. (2017). A probabilistic drought forecasting framework: A combined dynamical and statistical approach. *Journal of Hydrology*, 548, 291–304. <https://doi.org/10.1016/j.jhydrol.2017.03.004>
- Yin, S., Zhu, X., and Member, S. (2015). Intelligent Particle Filter and Its Application to Fault Detection of Nonlinear System. *IEEE Transactions on Industrial Electronics*, 62(6), 3852–3861. <https://doi.org/10.1109/TIE.2015.2399396>

- Zhu, M., van Leeuwen, P. J., Amezcu, J. (2016). Implicit equal-weights particle filter. *Quarterly Journal of the Royal Meteorological Society*, 142, 1904–1919. <https://doi.org/10.1002/qj.2784>.
- Zhu, M., van Leeuwen, P. J., and Zhang, W. (2017). Estimating model error covariances using particle filters. *Quarterly Journal of the Royal Meteorological Society*, doi:10.1002/qj.3132.
- Zhu, G., Li, X., Ma, J., Wang, Y., Liu, S., Huang, C., ... Hu, X. (2018). A New Moving Strategy for the Sequential Monte Carlo Approach in Optimizing the Hydrological Model Parameters. *Advances in Water Resources*. <https://doi.org/10.1016/j.advwatres.2018.02.007>
- Zhu, Y., Toth, Z., Wobus, R., Richardson, D., and Mylne, K. (2002). The economic value of ensemble-based weather forecasts. *Bulletin of the American Meteorological Society*, 83(1), 73–83. [https://doi.org/10.1175/1520-0477\(2002\)083<0073:TEVOEB>2.3.CO;2](https://doi.org/10.1175/1520-0477(2002)083<0073:TEVOEB>2.3.CO;2)
- Zupanski, D. (1997). A General Weak Constraint Applicable to Operational 4DVAR Data Assimilation Systems. *Monthly Weather Review*, 125(9), 2274–2292. [https://doi.org/10.1175/1520-0493\(1997\)125<2274:AGWCAT>2.0.CO;2](https://doi.org/10.1175/1520-0493(1997)125<2274:AGWCAT>2.0.CO;2)

CHAPTER 4 MULTIVARIATE REMOTELY SENSED AND IN-SITU DATA ASSIMILATION FOR ENHANCING COMMUNITY WRF-HYDRO MODEL FORECASTING⁴

Abstract

Floods are one of the most catastrophic natural disasters in the United States, particularly in the Southeast states where hurricanes and tropical storms are most prevalent, causing annually billions of dollars in damage and significant life and property losses. The Weather Research and Forecasting Hydrological model (WRF-Hydro) is a community-based hydrologic model designed to couple multi-scale and multi-physics models of the atmosphere and terrestrial hydrology. The model is used to improve the skill of hydrometeorological forecasts, such as river discharge, through simulating hydrologic prognostic (e.g., soil moisture) and diagnostic (e.g., energy fluxes) variables. These quantities are potentially biased or erroneous due to the uncertainties involved in all layers of hydrologic predictions. Therefore, the objective of this research is twofold: (1) evaluate the error in the WRF-Hydro model predictions by comparing the discharge values taken from the USGS stream gauges located in the Southeast region of Texas State for the year 2017, (2) use an ensemble based Data Assimilation (DA) approach to independently and jointly assimilate remotely sensed SMAP (Soil Moisture Active Passive) soil moisture and USGS streamflow observations into the WRF-Hydro model to improve the accuracy and reliability of model predictions while accounting for uncertainties. This study is

⁴ Abbaszadeh, P., Gavahi, K., Moradkhani, H. (2020). Multivariate Remotely Sensed and In-situ Data Assimilation for Enhancing Community WRF-Hydro Model Forecasting. *Advances in Water Resources*. Under review.

conducted over a large region near to Houston, Texas where heavy rainfall from hurricane Harvey caused flooding.

Keywords: Flood prediction, WRF-Hydro, Data Assimilation

Introduction

Tropical storms and hurricanes in the Southeast United States have become more frequent and intense over the past decades, mainly due to the effects of climate change and climate variability (Chen et al., 2015; Donnelly & Woodruff, 2007; Foltz et al., 2018; Kossin et al., 2013; Michener et al., 1997). They often produce torrential rains that may result in deadly and destructive floods depending on orographic (M. Liu & Smith, 2016; R. B. Smith et al., 2009), geomorphologic (Kourgialas & Karatzas, 2011; Naylor et al., 2017) and hydrologic (Eisenbies et al., 2007; Kundzewicz et al., 2014) characteristics of the region. In 2018, according to the annual Natural Hazard Report, severe rainfall- and hurricane-induced flooding throughout the nation were among the leading calamities that caused billions of dollars in damage and dozens of fatalities. In addition, urbanization and anthropogenic activities are expected to further increase flood vulnerability and risk in the coming decades (Doocy et al., 2013; Huong & Pathirana, 2013). Flood forecasting systems are widely used to mitigate the impacts of such hydrometeorological extremes by providing decision-makers and the public with early warning information. The most central part of a flood forecasting system is the hydrological model. One of the latest advances of hydrological models is the WRF-Hydro (Weather Research and Forecasting Model Hydrological modeling), an open-source community model developed by the National Center for Atmospheric Research (NCAR) for a range of studies including (flash) flood

prediction, regional hydroclimate impacts assessment, and water resources management (Gochis & Chen, 2003; Gochis et al., 2015).

Hydrological models, irrespective of their types, most often do not provide accurate and reliable estimates of prognostic variables (e.g., soil moisture and streamflow) as they are subject to large uncertainties stemming from different sources, including hydrometeorological forcing inputs, model parameters, boundary or initial condition and model structure (Abbaszadeh et al., 2019; Bi et al., 2015; Leach et al., 2018; Matgen et al., 2010; Pathiraja et al., 2016). These uncertainties can be accounted for when the hydrologic predictions are produced within a probabilistic framework (Kuczera & Parent, 1998; Marshall et al., 2004; Pathiraja et al., 2016; Smith & Marshall, 2008; Yan et al., 2015). Typically, this is performed through Bayesian inference. Over the last couple of decades, Data Assimilation (DA) has garnered increasing attention among researchers and practitioners as an effective and reliable method based on Bayesian theory to incorporate the hydrometeorological observations from in-situ and remotely sensed measurements into hydrological models for enhancing their forecasting skills while taking into account the associated uncertainties (Moradkhani, 2008; Liu et al., 2011; Moradkhani et al., 2018; Reichle et al., 2002, Seo et al., 2015). Particle Filter (PF) is a class of Bayesian data assimilation approach that has been widely used in hydrologic studies (DeChant & Moradkhani, 2012; Dong et al., 2015; Montzka et al., 2013; Moradkhani, DeChant, et al., 2012; Yan et al., 2017). Evolutionary Particle Filter and Markov Chain Monte Carlo (EPFM), recently developed by Abbaszadeh et al., (2018), is a successor version of PF-MCMC (Moradkhani et al., 2012) to improve both the state and parameter estimation of a high-dimensional system. In this study, we will use this data assimilation approach. For more information about data assimilation

techniques in hydrometeorological studies, we refer the interested readers to Moradkhani et al., (2018).

Soil moisture is a key hydrological variable that plays an imperative role in the terrestrial water cycle through controlling the water and energy fluxes in the land-atmosphere interface. Many studies have assimilated soil moisture data, collected from ground-based stations or retrieved from satellites, into hydrological models to improve their predictive skills. These include studies ranging from drought monitoring (Bolten et al., 2010; Yan et al., 2018), flood forecasting (Massari et al., 2018; Wanders et al., 2014) to irrigation and water resources management (Felfelani et al., 2018; El Sharif et al., 2015). Moreover, significant efforts have been made over the past few years to assimilate downscaled and disaggregated soil moisture products into land surface models, although their impact on hydrological model predictions has not yet been entirely explored (López López et al., 2017; Malbéteau et al., 2018; Sahoo et al., 2013). On the other hand, streamflow is the main component of the hydrologic cycle generated through a combination of land-surface and sub-surfaces processes that incorporate the information of hydrologic states and fluxes. Streamflow observations measured by in-situ sensors most often are assimilated into hydrological models to update the model states and/or parameters and hence to improve the estimation of predictive uncertainty (Abbaszadeh et al., 2018; Clark et al., 2008; Moradkhani et al., 2005; Moradkhani et al., 2012). While these prognostic variables (soil moisture and streamflow) are often independently assimilated into the hydrological models, many other studies have shown that their joint assimilation is a more effective approach in improving model predictions and quantifying associated uncertainties (Aubert et al., 2003; Lee et al., 2011; López López et al., 2017; Yan & Moradkhani, 2016). However, such experiments typically are based on lumped or semi-distributed hydrological

models due to their simplicity and low computational requirements. Multivariate (joint) data assimilation refers to the simultaneous assimilation of multiple observation data for different model state variables into a hydrological model.

With recent advances in satellite remote sensing technologies, soil moisture data have become available at a global scale with decent spatial and temporal resolutions. While these products are promoting a wide range of global and continental land-atmosphere studies, their coarse spatial resolutions impede their use in regional and local studies that require a finer resolution data, usually less than 1 km (Abbaszadeh et al., 2019; Entekhabi et al., 2010; Peng et al., 2017). For example, assimilating satellite soil moisture data into a high-resolution land surface model (e.g., WRF-Hydro) ideally requires soil moisture observation at the hydrological model resolution (from 250 m to 1 km); otherwise, the spatial discrepancy between the two would degrade the performance of the hydrologic data assimilation. On the other hand, particle filtering data assimilation in conjunction with fully distributed hydrologic models is still at infancy mostly due to its complexity and sophistication. It is therefore of particular interest to examine the benefit of independently and jointly assimilating high-resolution satellite soil moisture data and streamflow observations into a hyper-resolution hydrological model (here WRF-Hydro) and to understand the extent to which these observations can contribute to improving the model forecasts, particularly during the extreme events. Therefore, we conducted our study over a region in the Southeast Texas where heavy rainfall from hurricane Harvey caused flooding in 2017.

Model calibration and data assimilation play a complementary role in improving hydrological model simulations. Model calibration addresses the deficiencies in the model's representation of physical processes through tuning the model parameters and finding the best set

which maximizes the agreement between the model simulation and observation (Koster et al., 2018; Nikoo et al., 2019; Gavahi et al., 2019; Gavahi et al., 2018, Nikoo et al., 2019; Gavahi et al., 2020; Asadi et al., 2013; Abbaszadeh., 2016; Nourani et al., 2014; Hameed et al., 2019; Alipour et al., 2020, Alipour et al., 2020). However, data assimilation addresses such deficiencies by rectifying the model state variables depending on the availability of its corresponding observation data at a certain time and location (Moradkhani et al., 2018). Previous studies mostly relied on parsimonious hydrological models and results showed that using both approaches could lead to an acceptable accuracy of model estimates (Koster et al., 2018; Moradkhani & Sorooshian, 2008; Vrugt et al., 2005b; Xu et al., 2014; Yucel et al., 2015). In this study, we will examine this conjecture over a very large basin and using a high-resolution fully distributed hydrological model and advanced particle filter based data assimilation approach. The remainder of the paper is organized as follows. Section 2 and 3 describe the study area and the data, including the satellite soil moisture products, USGS observations, and NLDAS (North American Land Data Assimilation System) data. Section 4 and 5 briefly explain the WRF-Hydro hydrologic model and the data assimilation approach used in this study. Section 6 outlines the research framework and highlights the questions sought in this study. Section 7 provides a thorough explanation about the WRF-Hydro model setup and calibration. Section 8 discusses different data assimilation scenarios, including independent or joint assimilation of satellite soil moisture and streamflow observation into the WRF-Hydro model, and their contributions to improving the model simulations. Section 8 summarizes the findings of the paper and offers opportunities for future research.

Study Area

Following hurricane Rita in 2005 and Ike in 2008, hurricane Harvey with more than 50 inches of total rainfall in 2017 was the strongest (Category 4) with disastrous storm that struck the United States in more than a decade, resulting in catastrophic flooding, dozens of fatalities and more than \$200 million in crop losses. Hurricane Harvey with \$125 billion in damage was one of the costliest natural disasters in the history of the United States, comparable to hurricane Katrina in 2005. In this paper, we will address the research questions highlighted in the introduction section by conducting a study over a region with an area of 995.16 square miles located in the Southeast Texas (eastern part of San Jacinto basin). This area is one of the fastest population growing regions in the country. This population growth has led to increased urbanization within the basin. This along with the proximity to the Gulf of Mexico and tropical and hurricane storms has made this watershed more vulnerable to flooding from both intensified precipitation due to climate change and increased runoff because of acute urbanization.

Figure 4-1 demonstrates a detailed map of the study area, such as the watershed boundary, topography, lakes, stream networks, major rivers, and USGS streamflow gauges. San Jacinto is the main river in the region where flooding from hurricane Harvey damaged the protective barrier at the San Jacinto River Waste Pits site and polluted the river, costing \$115 million cleanup program. San Jacinto River flows across Montgomery County to the south and forms Lake Houston. San Jacinto basin has warm and humid climate. The annual average rain in this region is about 51 inches, while the snow is insignificant throughout the year. The topography of San Jacinto basin is slightly hilly except along the San Jacinto River where there are extensive areas of flood plains.

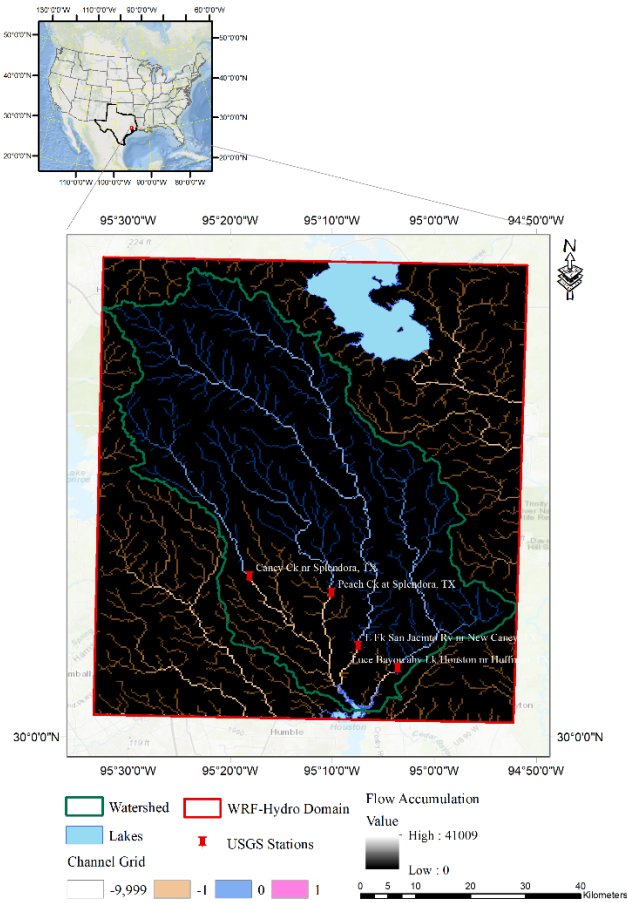


Figure 4-1 Study area located in Southeast Texas along with watershed boundary, WRF- Hydro geogrid domain, lakes, stream networks, major rivers, and USGS streamflow gauges.

Datasets

SMAP Soil Moisture Products

The Soil Moisture Active Passive (SMAP) satellite equipped with two instruments, a radar (active) and a radiometer (passive), was launched on January 2015 to provide high-resolution soil moisture and detect frozen and thawed soils on a global scale. The primary goal of this NASA (National Aeronautics and Space Administration) satellite mission is to understand the links between Earth's water, energy and carbon cycles, reduce the uncertainties in predicting

the weather and climate and improve monitoring and predicting natural disasters such as floods and droughts. The SMAP satellite was originally designed to measure topsoil layer moisture (0-5 cm) with a 9-km spatial resolution by combining L-band brightness temperatures at 36-km resolution and 3-km high-resolution L-band radar backscatter data. Unfortunately, on July 7 2015, SMAP's radar stopped transmitting due to the irrecoverable hardware failure of radar instrument, and since then SMAP's radiometer became the only operational instrument providing soil moisture at 36-km spatial resolution (Chan et al., 2016). Although this product has a decent spatial resolution for continental or global studies, it cannot be directly used for local or regional studies that require a finer resolution data (Entekhabi et al., 2010). To circumvent this problem, in January 2017, NASA announced a product named the enhanced SMAP radiometer. In this dataset, the standard SMAP data gridded at 36 km were interpolated into the global cylindrical EASE-Grid 2.0 projection with 9-km spacing using the Backus-Gilbert optimal interpolation algorithm (Xu et al., 2018). One year after, in 2018, NASA proclaimed a new soil moisture product with 3-km spatial resolution. In this dataset, SMAP L-band brightness temperatures and Copernicus Sentinel-1 C-band backscatter coefficients were used to generate soil moisture data, which is then resampled to an Earth-fixed, cylindrical 3 km Equal-Area Scalable Earth Grid, Version 2.0 (Das et al., 2018). It should be noted that these soil moisture products are available on both ascending and descending orbit.

Despite such advances, some land surface applications such as water management, agricultural production, drought monitoring and flood forecasting still require soil moisture at finer resolutions, from a kilometer to a sub-kilometer scale. For this purpose, few studies have rescaled the SMAP soil moisture data to a finer resolution (Abbaszadeh et al., 2019; Alemohammad et al., 2018; Zhao et al., 2018). In this paper, we evaluate the impact of

assimilating SMAP soil moisture observations at different spatial resolutions into the WRF-Hydro model. The descriptions of all SMAP soil moisture datasets used in this study are summarized in Figure 4-2. This figure, for example, illustrates SMAP soil moisture data at three different spatial resolutions across Southwest US on 25 April 2017.

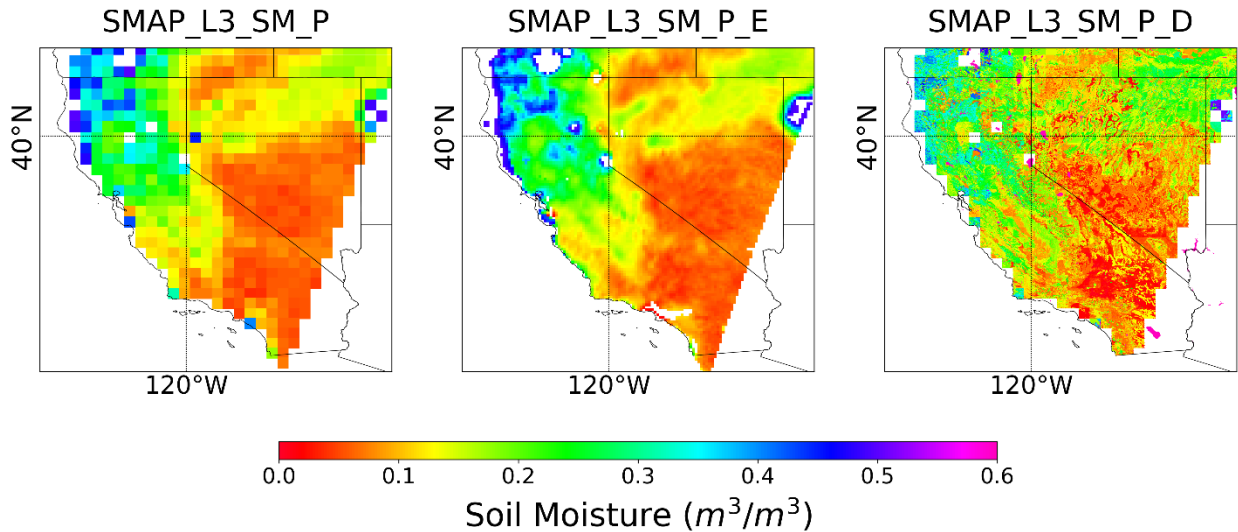


Figure 4-2. SMAP soil moisture data over the Southwest US. Right panel: SMAP_L3_SM_P (SMAP L3 Radiometer Global Daily 36 km EASE-Grid Soil Moisture, Version 5) at 36 km spatial resolution. Middle panel: SMAP_L3_SM_P_E (SMAP Enhanced L3 Radiometer Global Daily 9 km EASE-Grid Soil Moisture, Version 2) at 9 km spatial resolution. SMAP_L3_SM_P_D (SMAP Radiometer Downscaled Product (Abbaszadeh et al., 2019)) at 1 km spatial resolution.

NLDAS-2 Forcing Data

The North American Land Data Assimilation System (NLDAS-2) provides quality-controlled and spatiotemporally consistent datasets from best available observations to support modeling activities. In this paper, NLDAS-2 datasets including incoming shortwave radiation, incoming longwave radiation, specific humidity, air temperature, surface pressure, near-surface wind in the u-component, near-surface wind in the v-component and rain rate are used to force

WRF-Hydro model. NLDAS-2 has a 1/8th-degree spatial resolution, hourly timing and ranges from January 1979 to present. NLDAS-2 forcing data should be re-gridded to match the geogrid domain of WRF-Hydro model. This task is accomplished using the Earth System Modeling Framework (ESMF) Re-gridding Scripts. For more information, we refer readers to https://ral.ucar.edu/projects/wrf_hydro/regridding-scripts.

USGS Streamflow Gauges

In this study, we used four USGS gauges installed within the basin (Figure 1), to calibrate the WRF-Hydro model, assess the streamflow simulation results and perform data assimilation. The USGS discharge chart (not shown here) shows that the streamflow peak caused by hurricane Harvey in the river was well captured by all four gauges. Therefore, we seek to understand the efficacy of the WRF-Hydro model in simulating floods triggered by heavy rainfall from hurricane Harvey. USGS station 8070500 Caney Ck nr Splendora is located in the Caney Creek River in Caney Creek watershed. This perennial river is one of the tributaries of the San Jacinto River that flows 155 miles southeast and drains into the Gulf of Mexico. USGS station 8071000 Peach Ck at Splendora is installed in the Peach Creek River in Peach Creek watershed. This river is 27 miles long and is one of the tributaries of the San Bernard River. Caney Creek and Peach Creek are located about 40 miles north of Houston, Texas. The watersheds of these two rivers are similar, mostly dominated by pasture/hay and forest. The average annual rainfall in this area reaches to 46 inches with uneven distribution of rainfall throughout the year. USGS station 8070200 E Fk San Jacinto Rv nr New Caney is operated in San Jacinto River in San Jacinto watershed. This river flows southeast for about 28 miles and eventually drains into the Galveston Bay. USGS station 8071280 Luce Bayou abv Lk Houston nr Huffman is located in the Luce Bayou River in Luce Bayou watershed. This river with 35 miles length is a single primary stream

of this watershed that drains into the East Fork San Jacinto River. The prevailing climate in this watershed is humid subtropical, and cropland, rangeland, and pasture are the dominant land use.

WRF-Hydro Hydrological Model

WRF-Hydro model was initially designed to facilitate coupling between the WRF and different elements of terrestrial hydrological systems while accounting for the discrepancy between the resolutions of atmospheric and hydrological models (Gochis & Chen, 2003). Multiple Land Surface Models (LSMs) have been configured with the WRF-Hydro modeling system to simulate land surface processes. In this study, we compiled WRF-Hydro in the uncoupled mode (offline) with Noah-MP land surface model. In offline mode, there is no interaction between the LSM and WRF atmospheric model. Noah-MP is a land surface model enhanced from Noah LSM by adding improved physics and multi-parameterization options (Niu et al., 2011). WRF-Hydro model is a fully distributed system that integrates different hydrological and hydraulic modules to simulate the surface overland flow, subsurface saturated flow, channel routing and baseflow processes. Fully parallelized WRF-Hydro model enables us to run it on a cluster and High-Performance Computing (HPC) systems. WRF-Hydro consists of different water routing modules that enable diffusive wave surface routing and saturated subsurface flow routing on a 250 m grid, and Muskingum-Cunge channel routing down National Hydrography Dataset (NHDPlusV2) stream reaches. Noah-MP is available as a column LSM option in WRF-Hydro that accounts for soil infiltration and redistribution processes. In addition to this, WRF-Hydro with its routing module uses a high-resolution topography data to further help redistribute terrestrial moisture. One of the significant enhancements of WRF-Hydro model is its ability to route infiltration capacity excess and saturated subsurface water to simulate the

surface runoff. The routed infiltration capacity excess in the 1-D soil column along with additional exfiltration from saturated soil is allowed to remain on the land surface as ‘ponded water’, which is available for lateral redistribution if suitable conditions are met (Ryu et al., 2017; Senatore et al., 2015; Yucel & Onen, 2014). Although this model has recently been successfully applied in several regions throughout the world (Arnault et al., 2016; Lahmers et al., 2019; Lin et al., 2018; Silver et al., 2017; Wehbe et al., 2018), the integration of state-of-the-art data assimilation approaches, such as the particle filtering, with this model had not been implemented.

Data Assimilation Approaches

The data assimilation method in this study utilizes sequential Monte Carlo techniques to generate the replicates of model forcing and states and through a formal Bayesian approach obtains a full probability distribution of variables of interests and characterizes the predictive uncertainty. The sequential assimilation techniques have been used widely in hydrologic prediction studies (Moradkhani et al., 2018) and provide an effective means to assimilate ground-based and remotely sensed observations into an LSM. In this study, we use Particle Filter with Markov Chain Monte Carlo (PF-MCMC) and its successor version, Evolutionary PF-MCMC (hereafter EPFM), to improve the WRF-Hydro model predictions and quantify the associated uncertainties (Moradkhani et al., 2012; Abbaszadeh et al., 2018). Here we briefly explain these procedures.

Sequential Bayesian Theory

The equations 1 and 2 describe a generic state-space form of a nonlinear dynamic system (Moradkhani et al., 2018).

$$x_t = f(x_{t-1}, u_t, \theta) + \omega_t \quad (1)$$

$$y_t = h(x_t) + v_t \quad (2)$$

where $x_t \in \mathbb{R}^n$ and u_t are, respectively, the vector of the uncertain state variables and the uncertain forcing data at time step t . $\theta \in \mathbb{R}^d$ and $y_t \in \mathbb{R}^m$ denote the vector of model parameters and observation data. v_t and ω_t represent measurement error and model structural errors, which are mostly assumed to be independent and white noises with mean zero and covariance R_t and Q_t , respectively. Based on the Bayesian theory, the posterior distribution of the state variables at time t is approximated as:

$$p(x_t | y_{1:t}) = p(x_t | y_{1:t-1}, y_t) = \frac{p(y_t | x_t) p(x_t | y_{1:t-1})}{p(y_t | y_{1:t-1})} = \frac{p(y_t | x_t) p(x_t | y_{1:t-1})}{\int p(y_t | x_t) p(x_t | y_{1:t-1}) dx_t} \quad (3)$$

$$p(x_t | y_{1:t-1}) = \int p(x_t, x_{t-1} | y_{1:t-1}) dx_{t-1} = \int p(x_t | x_{t-1}) p(x_{t-1} | y_{1:t-1}) dx_{t-1} \quad (4)$$

Where $p(y_t | x_t)$ represents the likelihood at time step t and $p(x_t | y_{1:t-1})$ is the prior distribution. $p(y_t | y_{1:t-1})$ is the normalization factor and $p(y_{1:t})$ is the marginal likelihood function, which both can be calculated as follows:

$$p(y_{1:t}) = p(y_1) \prod_{t=1}^t p(y_t | y_{1:t-1}) \quad (5)$$

$$p(y_t | y_{1:t-1}) = \int p(y_t, x_t | y_{1:t-1}) dx_t = \int p(y_t | x_t) p(x_t | y_{1:t-1}) dx_t \quad (6)$$

The analytic solution for equation (3) is only available for special cases, such as the linear system with Gaussian assumption of noises in the system (i.e., the Kalman filter). Therefore, this equation is generally approximated using a set of random samples.

PF-MCMC

The PF-MCMC developed by Moradkhani et al. (2012) is a successor version of PF-SIR (Sampling Importance Resampling) (Moradkhani, et al., 2005). When MCMC is combined with the PF, it contributes to a more complete estimation of parameter posteriors, which therefore reduces the chance of parameter impoverishment that is the main concern in PF application.

Equation (3) is approximated as follows:

$$p(x_t|y_{1:t}) \approx \sum_{i=1}^N w^{i+} \delta(x_t - x_t^i) \quad (7)$$

where w^{i+} is the posterior weight of the i -th particle. δ and N are the Dirac delta function and the number of particles, respectively. The normalized weights are computed by:

$$w^{i+} = \frac{w^{i-} \cdot p(y_t|x_t^i, \theta_t^i)}{\sum_{i=1}^N w^{i-} \cdot p(y_t|x_t^i, \theta_t^i)} \quad (8)$$

In equation 8, w^{i-} is the prior weight of the i -th particle. $p(y_t|x_t^i, \theta_t^i)$ is computed using the likelihood $L(y_t|x_t^i, \theta_t^i)$ as follows:

$$L(y_t|x_t^i, \theta_t^i) = \frac{1}{\sqrt{(2\pi)^m |R_t|}} \exp \left[-\frac{1}{2} (y_t - h(x_t^i))^T R_t^{-1} (y_t - h(x_t^i)) \right] \quad (9)$$

According to the posterior weights, the SIR is used to resample the state variables and parameters. Afterward, the proposal parameter distribution is generated using equation 10:

$$\theta_t^{i,p} = \theta_t^{i+} + \varepsilon_t^i \quad \varepsilon_t^i \sim N[0, s_t \text{Var}(\theta_t^{i-})] \quad (10)$$

where θ_t^{i-} and θ_t^{i+} are the parameters before and after SIR implementation. s_t is a small tuning factor. To accept or reject the proposal parameter samples $\theta_t^{i,p}$, a metropolis acceptance ratio α is calculated:

$$\alpha = \min \left(1, \frac{p(x_t^{i,p}, \theta_t^{i,p} | y_{1:t})}{p(x_t^{i+}, \theta_t^{i+} | y_{1:t})} \right) \quad (11)$$

where $p(x_t^{i,p}, \theta_t^{i,p} | y_{1:t})$ is the proposed joint probability distribution:

$$p(x_t^{i,p}, \theta_t^{i,p} | y_{1:t}) \propto p(y_{1:t} | x_t^{i,p}, \theta_t^{i,p}) \cdot p(x_t^{i,p} | \theta_t^{i,p}, y_{1:t-1}) \cdot p(\theta_t^{i,p} | y_{1:t-1}) \quad (12)$$

$$x_t^{i,p} = f(x_{t-1}^{i+}, u_t^{i+}, \theta_t^{i,p}) \quad (13)$$

where $x_t^{i,p}$ is a sample from the state proposal distribution and u_t^{i+} is the resampled forcing data at time step t . The tuning factor s_t is a time-variant unknown variable that can be estimated using Variable Variance Multiplier (VVM) method (Leisenring & Moradkhani, 2011; Moradkhani, Dechant, et al., 2012).

EPFM

The EPFM developed by Abbaszadeh et al. (2018) is an extension of PF-MCMC (Moradkhani, DeChant, et al., 2012). This data assimilation approach utilizes the MCMC technique twice in a sequential framework, one before resampling, in order to crossover and mutate the particles and consequently produce a more informative prior distribution for state variables, and one after resampling to generate proposal parameter distribution as explained in the previous section. While improving data assimilation performance, EPFM significantly precludes the particle degeneracy and sample impoverishment problems that had been the main concerns in using the particle filter method. The four main steps of the EPFM approach are summarized below:

1. Particles are chosen for crossover operation from the original ensemble pool. To do this task, different options are available in Genetic Algorithm (GA); we used the roulette wheel selection method and then assigned a fitness value for each ensemble

member. The value of weights are representative of the quality of each particle, therefore, they can be directly used as the fitness value.

2. For crossover operation, we use the arithmetic crossover procedure to linearly combine the pair of selected particles. This process is shown by the following equations.

$$x_t^{i'} = \xi \cdot x_t^i + (1 - \xi) \cdot x_t^j \quad (14)$$

$$x_t^{j'} = (1 - \xi) \cdot x_t^i + \xi \cdot x_t^j \quad (15)$$

where x_t^i and x_t^j are the parent particles and $x_t^{i'}$ and $x_t^{j'}$ are the pair of newly generated offspring particles. ξ is a uniform random value ranging from 0 to 1.

3. To further intensify the diversity of the newly generated particles, we use GA mutation operator as follows:

$$x_t^{k'} = x_t^k + \eta \quad x_t^k \in \{x_t^{i'}, x_t^{j'}\} \quad \eta \sim N(0, \varphi \cdot \text{Var}(x_t^{k-})) \quad (16)$$

where η is a random sample from Gaussian distribution with mean zero and variance $\varphi \cdot \text{Var}(x_t^{k-})$. $\text{Var}(x_t^{k-})$ is the variance of the prior states at the time t , and φ is a small tuning parameter.

Finally, we implement the MCMC approach to accept or reject the new ensemble members generated by GA crossover and mutation operators. This process is similar to the one explained in the previous section for accepting or rejecting the parameter proposal distribution.

Research Framework

To improve the simulation of terrestrial hydrological processes at higher spatiotemporal resolutions, the WRF-Hydro model integrates a range of land surface

representations with the WRF model. In this study, we used the Noah-MP land surface model, which contains a set of canopy and surface energy fluxes to represent the exchanges of energy and water between the multiple-layer soil columns and atmosphere. When this land surface model is combined with the high-resolution routing module of WRF-Hydro (250 m grid), it enables producing soil moisture information to the Noah-MP 1 km grid. Figure 4-3 shows a schematic of the proposed research framework.

NLDAS meteorological forcing data are re-gridded to Noah-MP 1 km grid resolution that are required by the WRF-Hydro modeling system. Uncertainties that arise from this disaggregation process are accounted for in the data assimilation framework. In this research, the model is first set up over a geogrid domain covering the study region. The Dynamically Dimensioned Search (DDS) algorithm (Tolson & Shoemaker, 2007) is then used to calibrate the WRF-Hydro model parameters, and finally the calibrated model is used to simulate streamflow at four USGS gauges installed within the basin. We will provide a complete description of the WRF-Hydro model setup, calibration and simulation.

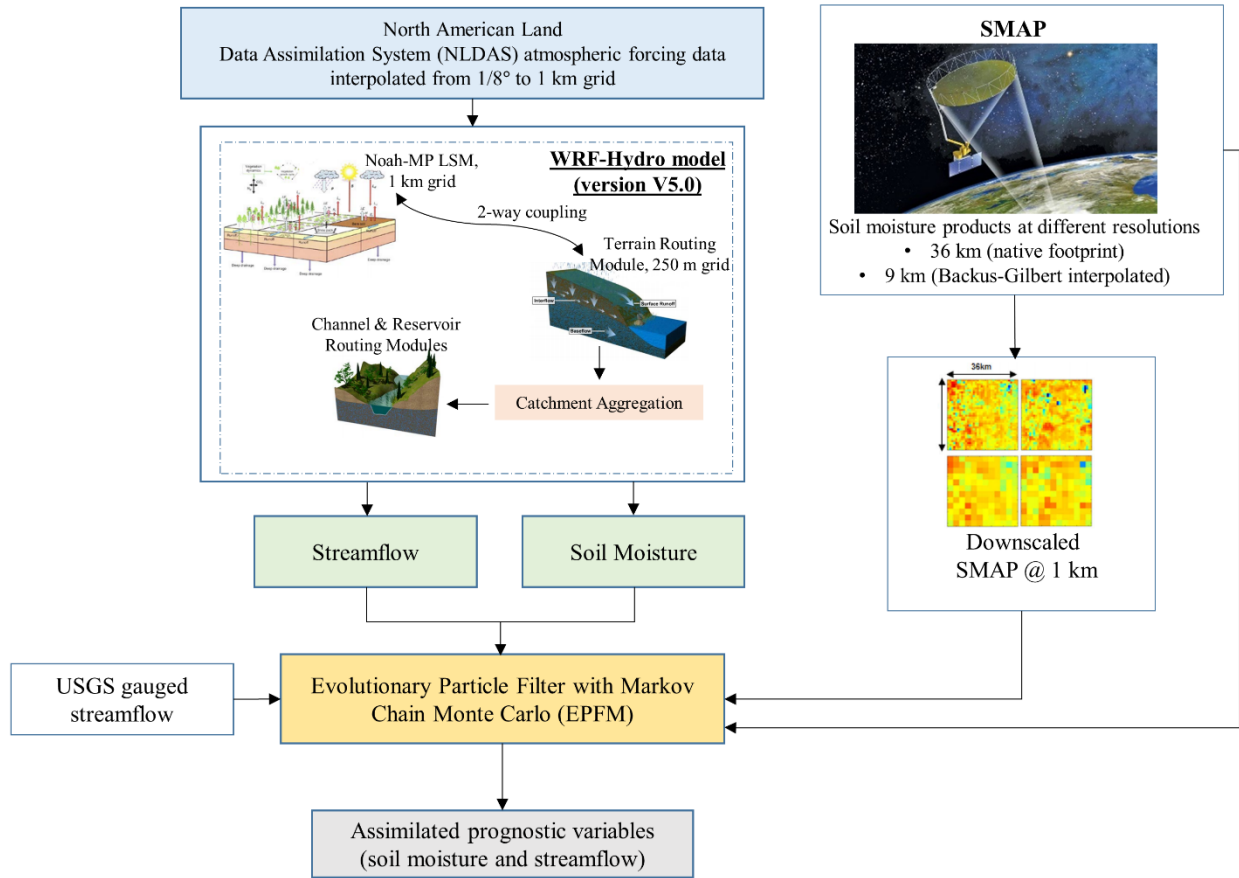


Figure 4-3 Schematic of the proposed framework.

In this study, we assimilate SMAP soil moisture observations (ascending and descending overpasses) at different resolutions (36 km- native footprint and 9 km- Backus-Gilbert interpolated) along with the recently downscaled SMAP product at 1 km (Abbaszadeh, et al., 2019) into the WRF-Hydro model with the aim to improve the accuracy and reliability of WRF-Hydro model predictions. In all four DA scenarios designed, we assimilate the soil moisture observation independently and in conjunction with the streamflow data to explore the best DA configuration leading to the most improved model estimates. The Noah-MP land surface model comprises a four-layer soil model (10, 30, 60 and 100 cm depth) to simulate the soil moisture by accounting for vertical soil infiltration and redistribution processes. Here, our target layer is the

first layer with 10 cm depth. Since this is in conflict with the shallow sensing depth of the SMAP satellite (0-5 cm), the assimilated soil moisture product may need to be bias-corrected. To do this, we use the Cumulative Distribution Function (CDF) matching approach (Reichle & Koster, 2004). In this research, the WRF-Hydro model is equipped with an enhanced ensemble DA approach, EPFM (Abbaszadeh et al., 2018), which is appropriate DA involving high-dimension of state variables and parameters.

WRF-Hydro Modeling

This section provides a progressive outline for the WRF-Hydro model setup and discusses in detail the model calibration process and assessment of the model.

WRF-Hydro Model Setup

The first step to setup the WRF-Hydro model is to define the geogrid domain file (*'geo_em.d01.nc'*) using the WRF Preprocessing System (WPS). The WPS consists of three programs namely *'ungrid.exe'*, *'metgrid.exe'* and *'geogrid.exe'* whose collective role is to prepare input for the WRF modeling system. For the WRF-hydro model setup, we only need to run the *'geogrid.exe'* program of this software to generate the WRF-hydro model domain and grid. It should be noted that in order to compile the WPS the WRF system should be first compiled and available in the system. For WRF and WPS compilation, we refer the readers to the instruction provided by UCAR (University Corporation for Atmospheric Research) at http://www2.mmm.ucar.edu/wrf/OnLineTutorial/compilation_tutorial.php. The only input file that *'geogrid.exe'* program requires to run is *'namelist.wps'*, in which *'e_we'* and *'e_sn'* should be equal to 67 and 84 so that the geogrid domain can cover the entire watershed boundary (see

Figure 4-1). The 'map_proj' is 'lambert' and the 'ref_lat' and 'ref_lon' were set to 30.403799 and -95.204175, respectively. The remainder of the namelist file is appropriate and should be maintained as it is. The next step is to use 'create_Wrfinput.R' script to prepare the initial condition file ('wrfinput_d01.nc'). Running this R script only requires 'geo_em.d01.nc' file, which was created in the previous step. 'wrfinput_d01.nc' consists of spatially uniform state variables, including soil moisture, soil temperature, and a few other variables required to initialize the cold-start model run. Using the geogrid file created earlier ('geo_em.d01.nc'), a high-resolution Digital Elevation Model (DEM) and other optional inputs (i.e., shapefiles of forecast points and lakes), the WRF-Hydro GIS Pre-processing Tool is used to create the geospatial and tabular data layers that define the terrestrial overland flow, subsurface flow and channel routing processes necessary for WRF-hydro modeling. In this study, we used the National Hydrography Dataset Plus, Version 2 (NHDPlusV2) to extract the DEM for the study area. The data is available at http://www.horizon-systems.com/NHDPlus/NHDPlusV2_home.php. The routing resolution was calculated as geogrid resolution (1000 m, dx and dy in namelist.wps) divided by re-gridding factor (4) and set to 250 m. The output of the tool is a high-resolution full domain file 'Fulldom_hires.nc' along with a few other netCDF files (i.e., 'GEOGRID_LDASOUT_Spatial_Metadata.nc', 'GWBASINS.nc', 'LAKEPARAM.nc' and 'GWBUCKPARAM.nc'), which will be used as inputs into WRF-Hydro. For more details about the contents of these files, we refer the readers to the WRF-Hydro GIS Pre-processing Toolkit v5.1 documentation available at https://ral.ucar.edu/projects/wrf_hydro/pre-processing-tools.

In this study, we considered the soil and vegetation parameters spatially distributed over the domain, therefore, we activated "SPATIAL_SOIL" option of the NOAH-MP module of the

WRF-Hydro model during the compilation process. The spatially distributed soil and vegetation parameter files can be created using ‘*create_SoilProperties.R*’ script. Running this R script requires a few tabular files including ‘*SOILPARAM.TBL*’, ‘*MPTABLE.TBL*’, ‘*GENPARAM.TBL*’, ‘*HYDRO.TBL*’, and a geogrid domain file (‘*geo_em.d01.nc*’). These .TBL parameter files can be retrieved from the directory where the WRF-Hydro model is compiled. The output files, including ‘*soil_properties.nc*’ and ‘*hydro2dtbl.nc*’, will be used as inputs into WRF-Hydro. There are still some additional input files, including ‘*VEGPARAM.TBL*’, ‘*URBPARAM.TBL*’, and ‘*CHANPARAM.TBL*’ necessary for running WRF-Hydro model. These files are automatically produced during the model compilation process, and therefore can be directly acquired. WRF-Hydro model has three routing configurations, National Water Model (NWM), Gridded and Reach. In this study, we used Gridded configuration of the WRF-Hydro model. Note that two additional netCDF files including ‘*spatialweights.nc*’ and ‘*Route Link.nc*’ should be provided if one is interested in operating the NWM configuration. The Earth System Modeling Framework (ESMF) script is used to re-grid the NLDAS meteorological forcing data to match the WRF-Hydro geogrid domain grid. This NCL (NCAR Command Language) script is available at https://ral.ucar.edu/projects/wrf_hydro/regridding-scripts. In order to run the WRF-Hydro executable (‘*wrf_hydro.exe*’), two namelist files, ‘*namelist.hrlas*’ (NOAH-MP land surface model namelist) and ‘*hydro.namelist*’ should be carefully configured. Up to this point, we concisely explained how the WRF-Hydro model was setup, for more detailed information on each of the aforementioned steps; we refer the readers to WRF-Hydro V5 Technical Description available at https://ral.ucar.edu/projects/wrf_hydro/technical-description-user-guide.

WRF-Hydro Model Calibration

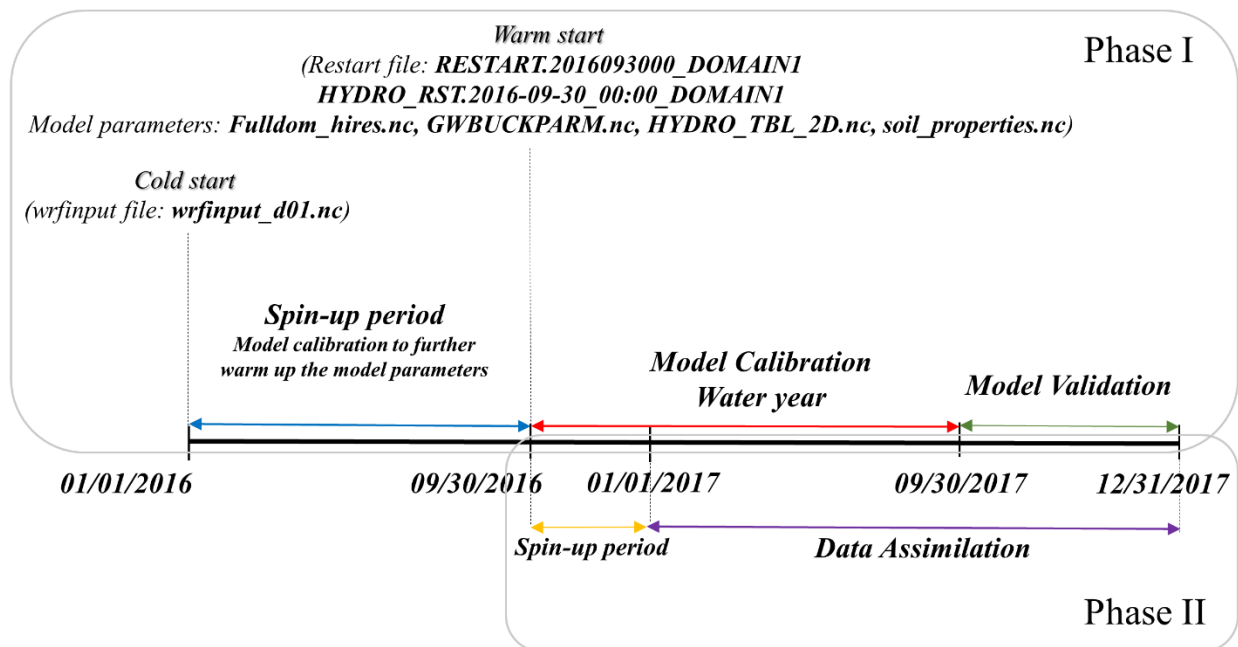
In this section, we will discuss how to calibrate the WRF-Hydro model parameters. For this purpose, all the parameters involved in WRF-Hydro modeling system should first be defined. WRF-Hydro model parameters are categorized into six groups including soil parameters, runoff parameters, groundwater parameters, vegetation parameters, snow parameter, and channel parameters. Table 4-1 provides a complete description of these model parameters along with their minimum and maximum values.

Table 4-1 WRF-Hydro model parameters/adjustment factors defined by NCAR

Parameter	Min, Max	Description	Units
bexp	0.4, 1.9	Pore size distribution index	dimensionless
smcmax	0.8, 1.2	Saturation soil moisture content (i.e., porosity)	volumetric fraction
dksat	0.2, 10	Saturated hydraulic conductivity	m/s
rsurfexp	1, 6	Exponent in the resistance equation for soil evaporation	dimensionless
refkdt	0.1, 4	Surface runoff parameter.	unit less
slope	0, 1	Linear scaling of "openness" of bottom drainage boundary	0-1
retdeprtfac	0.1, 10	Multiplier on retention depth limit	unit less
lksatfac	10, 10000	Multiplier on lateral hydraulic conductivity (controls anisotropy between vertical and lateral conductivity)	unit less
zmax	10, 250	Maximum groundwater bucket depth	mm
expon	1, 8	Exponent controlling rate of bucket drainage as a function of depth	dimensionless
cwpvt	0.5, 2	Canopy wind parameter for canopy wind profile formulation	1/m
vcmx25	0.6, 1.4	Maximum carboxylation at 25C	Umol/m ² /s
mp	0.6, 1.4	Slope of Ball-Berry conductance relationship	unit less
mfsno	0.5, 2	Melt factor for snow depletion curve; larger value yields a smaller snow cover fraction for the same snow height	dimensionless
Bw	0.1, 10	Parameterized width of the bottom of the stream network	m
HLINK	0.1, 10	initial channel depth	m
ChSSlp	0.1, 10	channel side slope	m/m
MannN	0.1, 10	Manning's roughness coefficient	s/m ^{1/3}

Figure 4-4 shows the procedure used to calibrate and validate the WRF-Hydro model (phase I) and implement the data assimilation approach (phase II). For model calibration, we split the entire period into three sub-periods, first nine months (from 01/01/2016 to 09/30/2016) is used as a spin-up period to provide a set of realistic initial conditions for model state variables, however the model parameters were kept at their default values. This type of model spin-up run is not sufficient as it only adjusts the model state variables and does not rectify the model parameters. Hence, in the model calibration period (from 09/31/2016 to 09/30/2017, 2016-2017 water year), although the model state variables reach the hydrological balance, they do not match with the model parameters. This inconsistency may lead to suboptimal performance of the model in the calibration phase, during the 2016-2017 water year. To circumvent this problem, we calibrated the WRF-Hydro model in the spin-up period to simultaneously warm up the model states and parameters. As shown in Figure 4-4, model calibration was performed using cold start initial condition (*wrfinput_d01.nc*) in the spin-up period (from 01/01/2016 to 09/30/2016), and state variables of the Noah-MP model (*RESTART.2016093000_DOMAIN*) and terrain routing module (*HYDRO_RST.2016-09-30_00:00_DOMAIN1*) of the WRF-Hydro system were obtained. These files will be used later to initialize the model calibration during the water year 2016-2017. Likewise, the model parameters including *Fulldom_hires.nc*, *GWBUCKPARAM.nc*, *HYDRO_TBL_2D.nc* and *soil_properties.nc* were updated. These filenames are briefly described in Figure 4-1. It is also important to note that WRF-Hydro model calibration was performed by optimizing hourly streamflow using Dynamically Dimension Search (DDS) algorithm (Tolson & Shoemaker, 2007). This optimization algorithm is able to converge to a near-optimal solution with approximately 100-500 iterations (Lespinas et al., 2018), which is much faster than the widely used Shuffled Complex Evolution (SCE) algorithm

that requires ~10,000 iterations to converge to an optimal solution (Duan et al., 1992). Therefore, DDS is better suited for calibration of the computationally intensive, fully distributed, physically based hydrological models, like WRF-Hydro (Lahmers et al., 2019). The cross-validation analysis showed that the USGS station 8071280 at Luce Bayou River, close to the watershed outlet, results in better model calibration performance compared to other streamflow gauges within the basin. Therefore, station 8071280 was selected for the model calibration in this study.



- Fulldom_hires.nc:** High-resolution routing terrain parameter file (e.g., topography, flow direction, channels).
- GWBUCKPARM.nc:** Groundwater/baseflow bucket model parameter file.
- HYDRO_TBL_2D.nc:** Spatial hydro parameters.
- soil_properties.nc:** Spatially varying soil and vegetation parameters.
- wrfinput_d01.nc:** Noah-MP LSM initialization file.
- RESTART...** : Noah-MP restart file.
- HYDRO_RST...** : Routing grid restart file.

Figure 4-4 Model calibration, validation and data assimilation configurations used in this study.

In the spin-up period (from 01/01/2016 to 09/30/2016), we first employed a manual calibration to identify the most relevant model parameters and roughly calibrate them. Therefore,

we excluded some of the parameters, including channel side slope (ChSSlp), initial channel depth (HLINK), melt factor for snow depletion curve (mfsno) and exponent in the resistance equation for soil evaporation (rsurfexp), from the parameter set due to their insignificant contribution to improving model calibration performance. Once the calibration process is completed, the model is run using the calibrated parameters and the model state variables at the end of the spin-up period are obtained, which later will be used as the initial “warm” state for calibration of the water year 2016-2017. This is consistent with the practices of the NCAR WRF-Hydro development team. Figure 4-5 shows the model calibration process using 100 iterations for the water year 2016-2017. Further investigations also revealed that increasing the number of DDS iterations beyond 100 does not improve the calibration efficiency and only adds to the computational burden. We used the Kling-Gupta Efficiency (KGE) (Gupta et al., 2009) as an objective function for all calibrations performed in this study. This metric along with other performance measures based on 100 calibration iterations was reported in Figure 4-S1 (in supporting information). These performance criteria are described in Appendix A.

It is worthy to mention that the calibration process in this study was set up and executed in the Cheyenne system at NCAR. Cheyenne is a 5.34-petaflops, high-performance computer developed for NCAR by SGI. The Cheyenne supercomputer features 145,152 Intel Xeon processor cores in 4,032 dual-socket nodes (36 cores/node) and 313 TB of total memory. For more information about this computing environment and access instruction, we refer the readers to Cheyenne webpage at <https://www2.cisl.ucar.edu/resources/computational-systems/cheyenne>. From Figure 4-5, we noticed that almost all the model simulations captured high flows caused by heavy rainfall from hurricane Harvey from August 17, 2017 to September 2, 2017. This indicates that the WRF-Hydro model is much more sensitive to torrential rain rather than the parameters’

variabilities. However, model parameters tend to be more determinant than the forcing data at low-to medium flows. For the model calibration, the Noah-MP time step was reduced from one hour, as the standard of the operational NWM, to 15 minutes in order to be consistent with the USGS streamflow data.

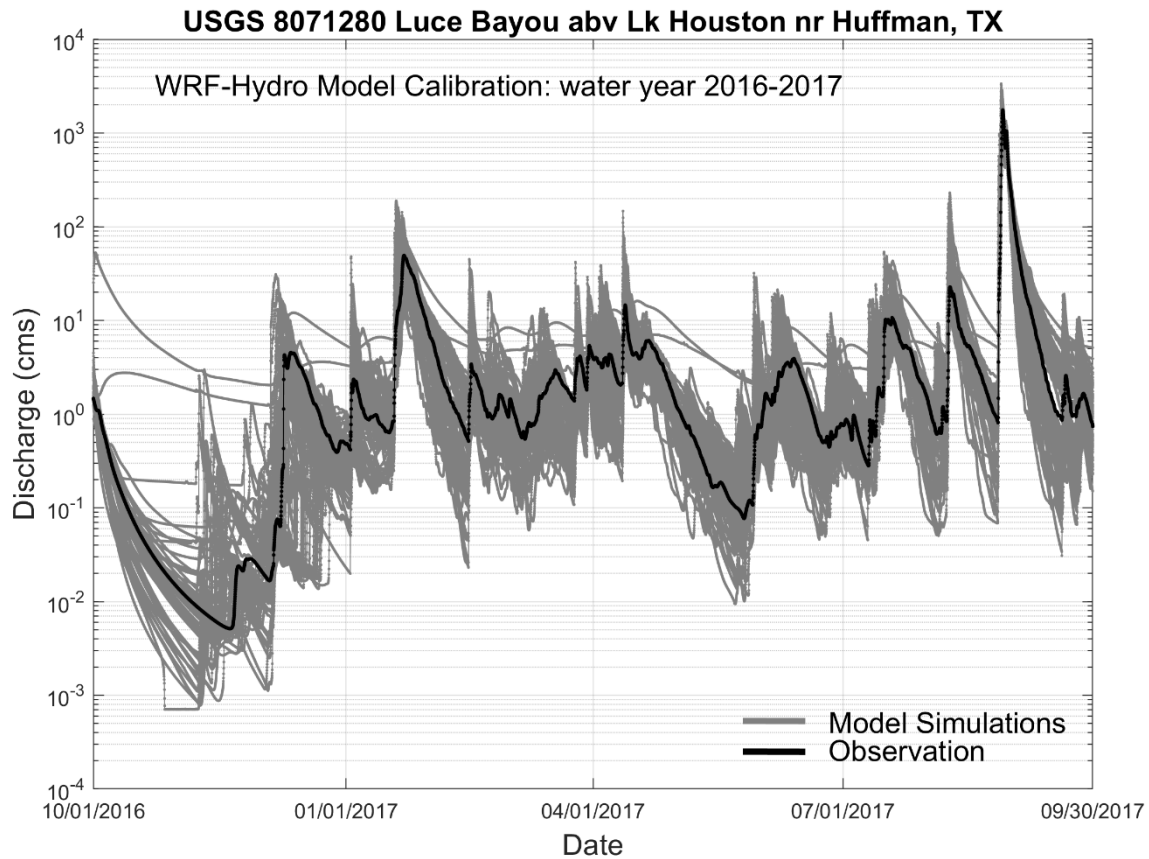


Figure 4-5 Model calibration at the USGS 8071280 gauge based on 100 DDS iterations.

Figure 4-6 illustrates the model parameters evolution over 100 DDS iterations during the calibration period, from 01/10/2016 to 09/30/2017. The first to fifth rows (from top) respectively show the runoff parameters, soil parameters, vegetation parameters, groundwater parameters and channel parameters. After the model calibration, we performed a simple one-at-a-time parameter sensitivity analysis on the model parameters shown in Figure 4-6 and the results revealed that

channel parameters (i.e., channel bottom width and Manning's roughness) and groundwater parameters (i.e., maximum groundwater bucket depth and bucket model exponent) along with surface runoff parameter ('refkdt') had the greatest impact on the WRF-Hydro model performance. 'refkdt' is a runoff parameter that significantly impacts surface infiltration and hence the partitioning of total runoff into surface and subsurface runoff. 'Zmax' is the maximum storage of the bucket to represent and conceptualize the groundwater process. WRF-Hydro uses an exponential function, which includes 'expon' parameter, to estimate the bucket discharge as a function of water depth in the bucket. 'Bw' and MannN are the channel bottom width and Manning's roughness coefficient that collectively shape the overland flow process. It is important to note that these parameters have no real physical meaning and are only used for model conceptualization. Our sensitivity analysis also indicated that in our case study the performance of the WRF-Hydro model is more sensitive to the runoff parameters compared to the vegetation and soil parameters. Therefore, in the next section, the most relevant model parameters (i.e., refkdt, zmax, expon, Bw and MannN) will be used in the development of the joint state-parameter data assimilation. However, the rest of the parameters will be used at their calibrated values.

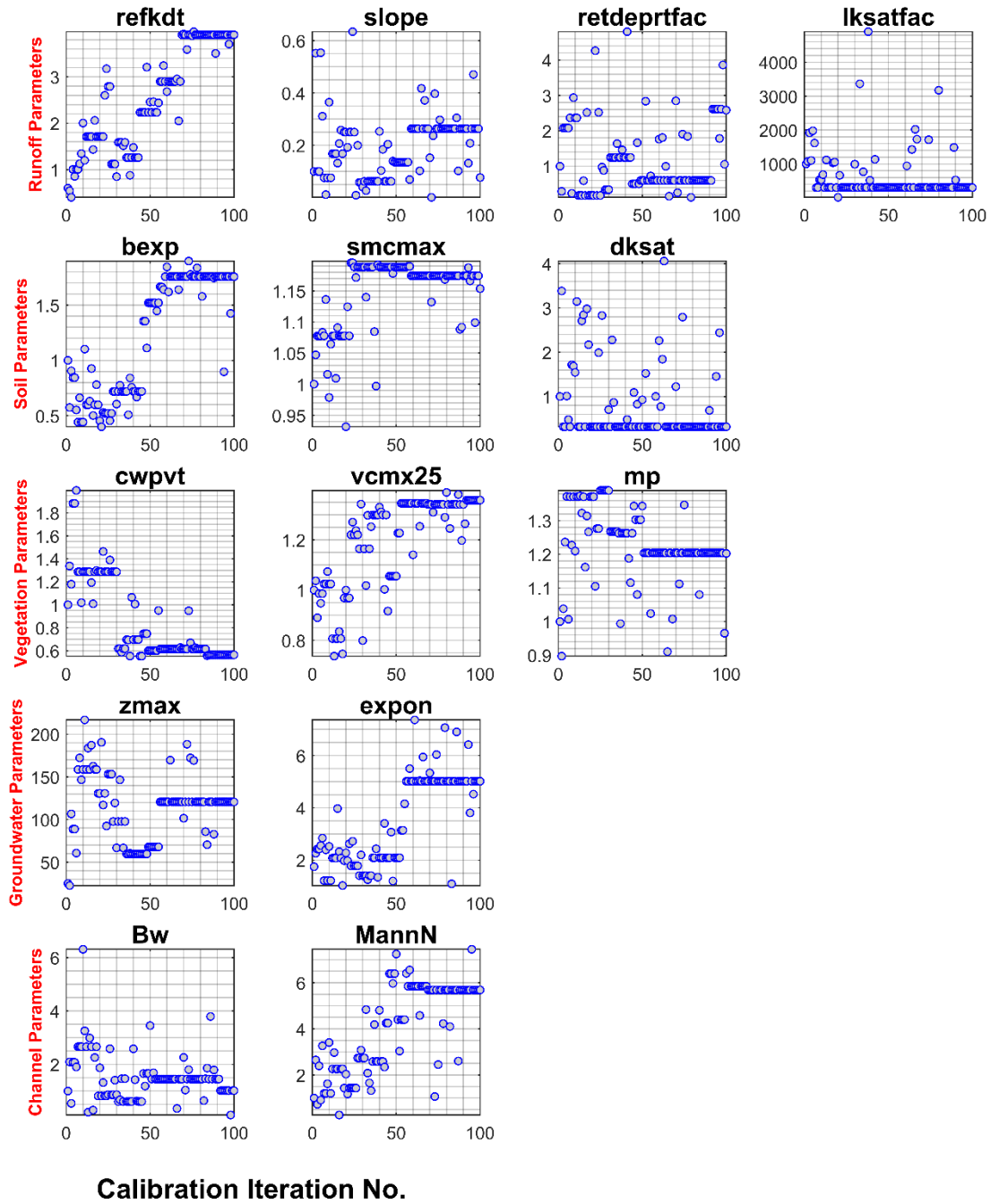


Figure 4-6 Evolution of model parameters during the model calibration process over 100 DDS iterations.

WRF-Hydro Model Simulation Analysis

Up to this point, the model parameters were calibrated. The next step is to evaluate the performance of the WRF-Hydro model at four USGS gauges located within the watershed. To this end, we run the model for the entire year 2017 using the ‘warm’ initial state variables obtained at the end of the spin-up period and the tuned parameters. Figure 4-7 shows the WRF-Hydro simulated streamflow versus observed streamflow at four USGS gauges. The Y-axis on the left hand side represents the streamflow value in CMS (cubic meter per second), while the Y-axis on the right hand side displays the precipitation amount in mm/day. To assess the effectiveness of the model, we computed four deterministic performance measures, including MAB (Mean Absolute Bias), KGE, RMSE (Root Mean Square Error) and PCC (Pearson Correlation Coefficient). The results indicate that the model has produced more accurate streamflow estimates at USGS gauges 8071280 (MAB= 6.422 cms, KGE=0.85, RMSE=44.70 cms and PCC=0.87) and 8070500 (MAB= 2.373 cms, KGE=0.75, RMSE=17.53 cms and PCC=0.90) compared to other two stations, 8071000 (MAB= 5.246 cms, KGE=0.45, RMSE=74.56 cms and PCC=0.91) and 8070200 (MAB= 19.17 cms, KGE=0.42, RMSE=175.53 cms and PCC=0.60). In all cases, the model exhibits either positive or negative bias in the simulations indicating overestimation and underestimation of the streamflows. This is most likely due to the model structure and parameterization errors in model calibration, which is expected to be accounted for later in the joint state-parameter data assimilation framework. It is also important to note that although the WRF-Hydro model estimated well the peak streamflow values, specifically those measured by USGS stations during the hurricane Harvey (from August 17, 2017 to September 2, 2017), it did not provide accurate estimates during recession periods and low flow conditions. ‘zmax’ and ‘expon’ are the two key groundwater parameters that affect

such flow regimes by controlling the baseflow and the groundwater storage. ‘refkdt’ is also an important parameter that influences the amount of water that flows into channel, which in turn affects the runoff process. The simultaneous adjustment of these model parameters together with model state variables through the dual state-parameter data assimilation approach introduced in section 5 may improve the effectiveness and usefulness of the WRF-Hydro model in estimating all possible streamflow regimes. This conjecture will be discussed in detail in next section.

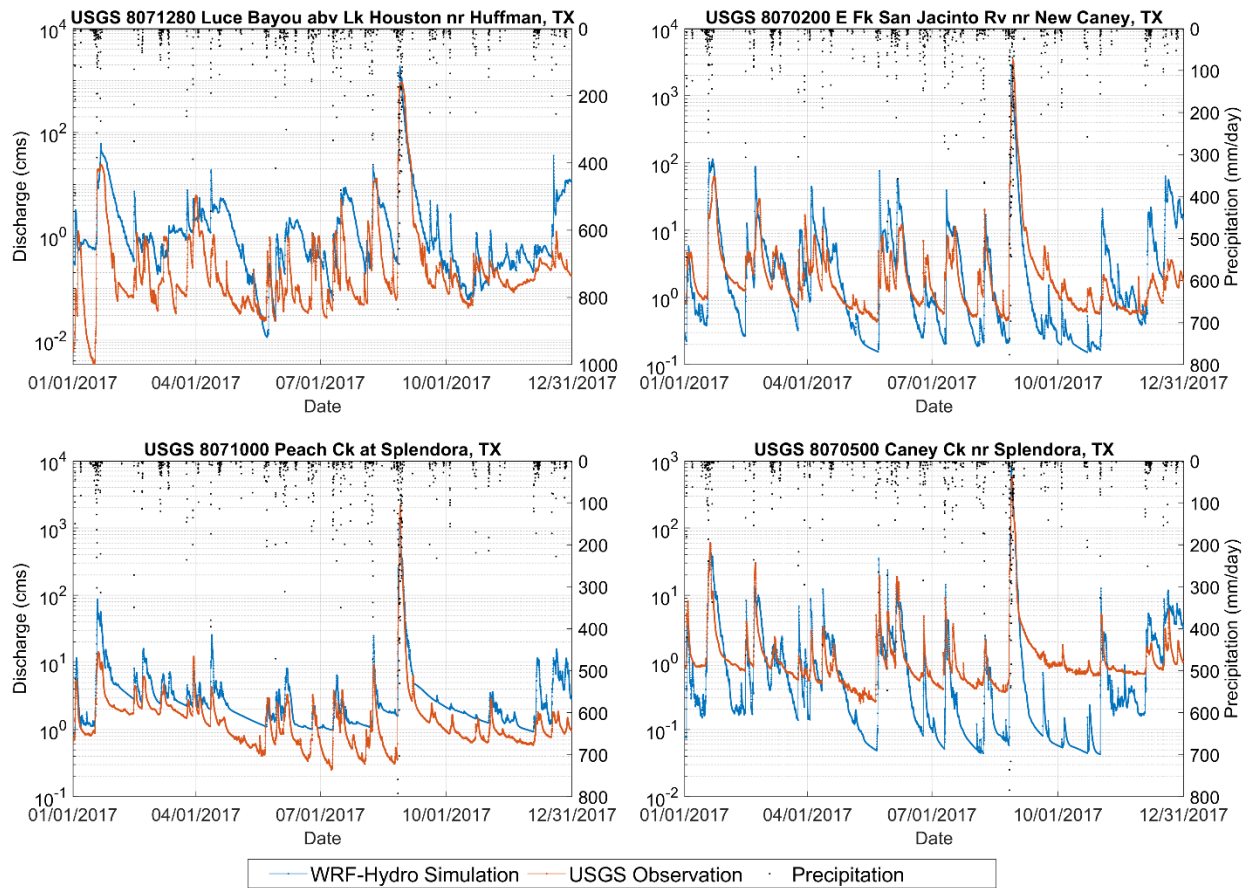


Figure 4-7 WRF-Hydro simulated streamflow versus USGS observed streamflow at four gauges within the watershed.

Assimilation of In-situ and Remotely Sensed Observations

In the following sections, we demonstrate an independent assimilation of USGS streamflow and SMAP soil moisture observations (at different spatial resolutions) into the WRF-Hydro model. Then, we conduct the multivariate assimilation of these two observations to show its usefulness in comparison to independent assimilation configuration. It is noted that all the assimilation experiments are based on joint state-parameter estimation. As discussed earlier, we only use the most sensitive model parameters (i.e., 'refkdt', 'zmax', 'expon', 'Bw' and 'MannN') in the joint sequential data assimilation framework. However, for other model parameters (please see Figure 4-6), their calibrated values are directly used.

Assimilation of Streamflow Observations into the WRF-Hydro Model

For data assimilation setting in this section, we considered lognormal and normal error distributions with a relative error of 25 percent for precipitation and temperature data respectively. However, uncertainty in other forcing data including incoming shortwave radiation, incoming longwave radiation, specific humidity, surface pressure, near-surface wind in the u-component and near-surface wind in the v-component was assumed insignificant. To characterize uncertainty in the initial condition, we assumed a normal error distribution with a relative error of 4 percent ($0.04 \text{ m}^3/\text{m}^3$) for the soil moisture at the topsoil layer. Note that WRF-hydro model has two restart files, 'RESTART' and 'HYDRO_RST' (please see Figure 4-4), that represent initial condition for the land surface model and routing module respectively. In this study, it is presumed that the uncertainty in the initial condition is associated more with the land surface model. Therefore, we only added white noise to the soil moisture at the top 10 cm soil layer in the 'RESTART' file. It is also assumed that the streamflow observation errors follow a

normal distribution with a relative error of 15 percent. In real case experiments, the other major part of the errors arises from the model structural uncertainty, which herein is represented by adding white noise with a relative error of 25 percent to the model outputs. In this study, all the errors were assumed uncorrelated and used with the same magnitude in all assimilation runs. To provide a comprehensive assessment of the effectiveness and usefulness of the EPFM data assimilation approach, we computed multiple deterministic (i.e., KGE and RMSE) and probabilistic (NRR and Reliability) performance measures. , The results show that the EPFM approach resulted in better streamflow simulations at stations 8071280 (KGE=0.92 RMSE=28.2 cms NRR=1.13 and Reliability=0.76) and 8070500 (KGE=0.81 RMSE=16.9 cms NRR=1.15 and Reliability=0.82) compared to other two stations, 8071000 (KGE=0.58 RMSE=60.5 cms NRR=1.30 and Reliability=0.86) and 8070200 (KGE=0.50 RMSE=165.9 cms NRR=1.37 and Reliability=0.85). When comparing the deterministic measures with those obtained earlier, it is concluded that assimilating streamflow into WRF-Hydro model is quite useful in improving its performance, although this improvement at two gauges (i.e., stations 8071000 and 8070200), where the WRF-Hydro model had produced poor results, remains limited. This is most likely due to sparse (point) observations that are assimilated into the gridded model, such that the spatial discrepancy between the model outputs and observations results in suboptimal model performance. This deficiency is expected to be alleviated by assimilating satellite soil moisture data into the WRF-Hydro model. This hypothesis will be examined in the next section. It is also important to mention that in this study all the assimilation runs are based on ensemble size of 90. The findings of this study also revealed that in ensemble data assimilation with WRF-Hydro model based on particle filtering, adjusting the model state variables in conjunction with model

parameters provides more accurate and reliable posterior distributions compared to state estimation only.

Figure 4-8.c illustrates the performance of the WRF-Hydro model with and without DA for the period of hurricane Harvey (August 17, 2017 to September 02, 2017). The results show that both DA and open loop (OL) model runs had similar performance in identifying the onset of flooding, however, DA showed better results for the recession period as compared to the OL.

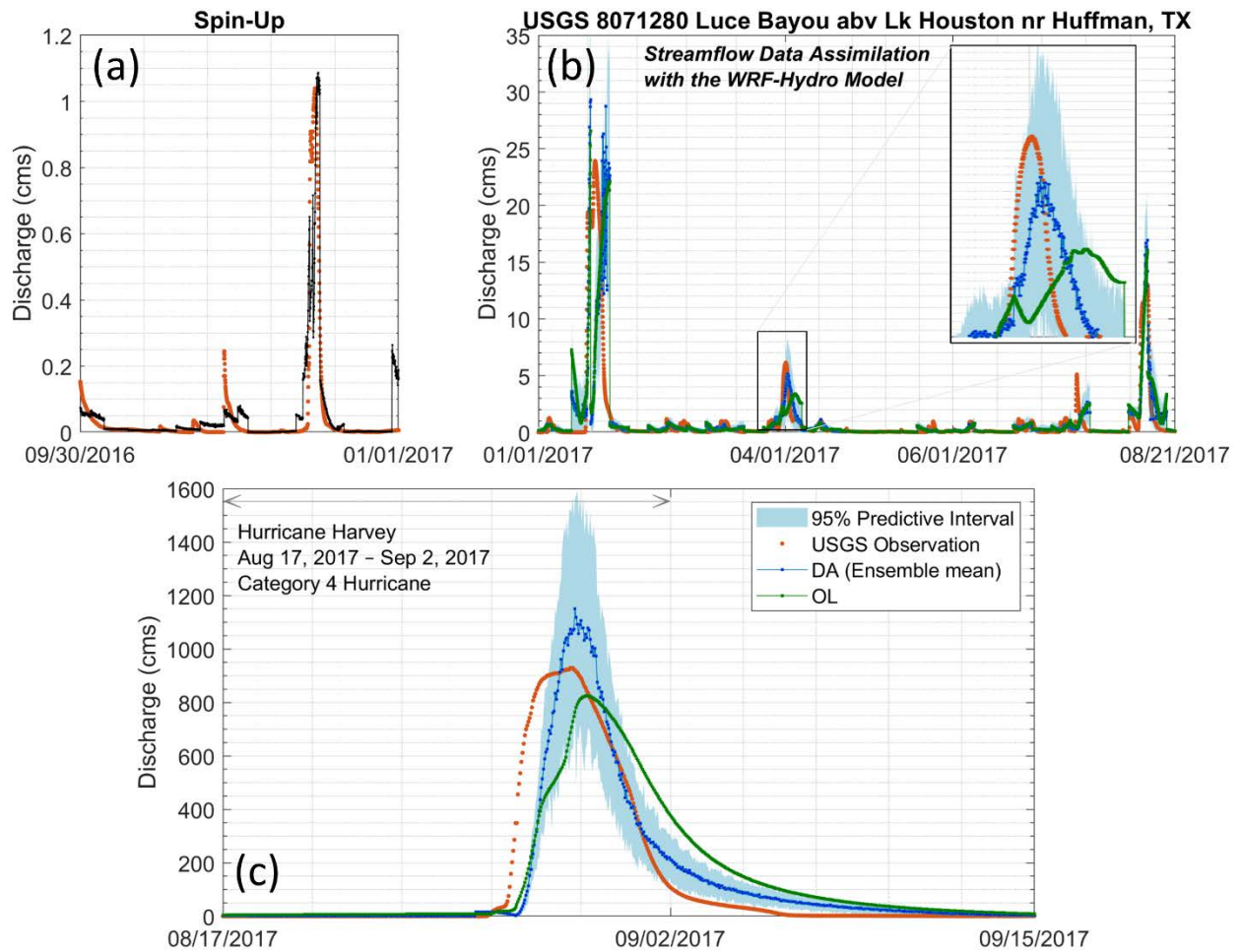


Figure 4-8 WRF-Hydro simulated streamflow with 95-percentile confidence interval versus USGS observed streamflow (01/01/2017 to 12/31/2017). The black line is the model spin-up run (a) (09/30/2016 to 01/01/2017), while the blue line and red points are the mean ensemble and observation, respectively. The green line also displays the open loop model run in subplots (b) and (c).

Assimilation of SMAP Soil Moisture Products into the WRF-Hydro Model

In this section, we examine the influence of assimilating SMAP soil moisture observations at different spatial scales on the WRF-Hydro model performance. Figure 4-9 is a Taylor diagram that simultaneously illustrates the deterministic (i.e., time series correlation, mean bias, and Normalized Root Mean Square Difference (RMSD)) and probabilistic (i.e., Normalized RMSE Ratio (NRR) (Moradkhani and Meskele, 2009) performance measures calculated at four USGS stations based on four assimilation configurations, including assimilation of all streamflow observations within the watershed and assimilation of SMAP soil moisture at three different spatial resolutions. NRR is calculated to measure the ensemble spread and assess how confidently the ensemble mean is statistically distinguishable from the ensemble spread. These performance measures are already described in previous chapters. The results revealed that assimilation of SMAP soil moisture at 1 km spatial resolution more than other SMAP products (36 and 9 km) contributes to the improvement of WRF-Hydro model prediction. The assimilation of SMAP soil moisture at 1 km scale and assimilation of streamflow observations have had an almost similar influence on the improvement of model prediction accuracy. However, assimilating streamflow data at the USGS locations resulted in better representation of posterior distribution compared to assimilating soil moisture data at even higher resolution. The results also show that the downscaled SMAP soil moisture data at 1 km spatial resolution yields more accurate predictive performance as compared to the soil moisture assimilation at coarser resolutions, i.e., the native and enhanced SMAP soil moisture products at 36 km and 9 km resolutions, respectively. It is important to note that the standard deviation ratios are always around the arc of one unit that indicates similar variability (bias in the variance) between the simulated streamflows and USGS observations regardless of the type of assimilation

configuration. Further analysis revealed that there is a complementary relationship between the NRR (probabilistic measure) and correlation coefficient/normalized RMSD (deterministic measures) almost in all assimilation runs, such that when the correlation coefficient/normalized RMSD improves, the NRR gets closer to 1 (which is an ideal value of NRR), and when the deterministic measures deteriorate, a suboptimal value for NRR is resulted. Please note that Reliability is not included in the Taylor diagram. Based on the aforementioned discussion, we will use the streamflow observations at all four USGS gauges and SMAP soil moisture at 1 km spatial resolution in the implementation of multivariate data assimilation. This will be discussed in the next section. The results also indicated that although assimilating the SMAP soil moisture into WRF-Hydro model would improve the streamflow estimates, assimilation of streamflow has insignificant impact on the improvement of soil moisture estimates.

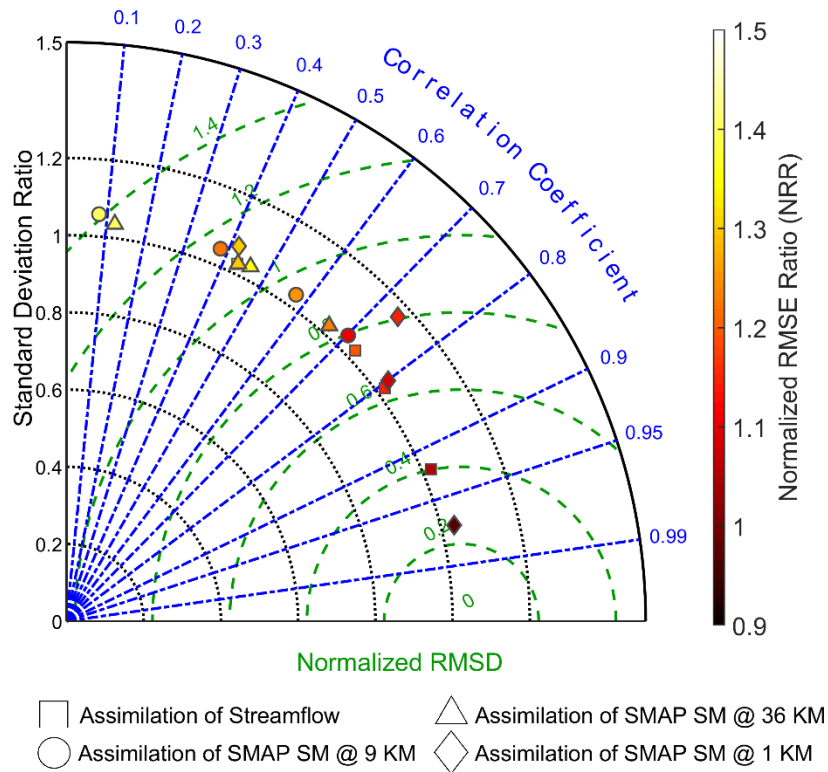


Figure 4-9. The deterministic and probabilistic performance measures of assimilation configurations at four USGS gauges. RMSD and correlation coefficient are represented by green

dashed line and blue dotted line, respectively. The black dashed line displays the standard deviation ratio. The color intensity of each symbol shows the value of Normalized RMSE Ratio (NRR).

Figure 4-10 demonstrates the spatial pattern of the updated soil moisture (posterior mean) versus the SMAP soil moisture data at 1 km spatial resolution. The upper panel shows the average SMAP and downscaled soil moisture over the study area. It is clear that, on average, the downscaled soil moisture at 1 km spatial resolution is dryer than the original SMAP soil moisture at 36 km grid cell. The lower panel shows an acceptable Pearson's correlation coefficient ($PCC > 0.6$) between the updated soil moisture and SMAP at 1 km spatial resolution across the entire domain except for the Northeast region where the Lake Livingston is located. This is because the footprint of original SMAP soil moisture at 36 km over this region is heavily affected by the lake that consequently leads to the overestimation of soil moisture. This wet bias in observational data when assimilated into the WRF-Hydro model results in inaccurate model predictions. On average, the RMSE between the updated and SMAP soil moisture data (at 1-km spatial resolution) is below $0.04 \text{ m}^3/\text{m}^3$ that corroborates with the accuracy requirement of SMAP soil moisture retrieval. It is worthy to mention that assimilation of SMAP soil moisture whether at 36 km or 9 km spatial resolution results in overestimation of peak flows, particularly during the hurricane Harvey (August 17, 2017 – September 2, 2017). However, assimilation of SMAP soil moisture at 1 km spatial resolution leads to more accurate estimation of peak flows. This could be attributed to a dryer SMAP soil moisture data at 1 km resolution as compared to coarser resolution soil moisture products. Both the PCC and RMSE confirm that the assimilation performance is degraded across the regions where 1 km grid cells are dominated by water bodies.

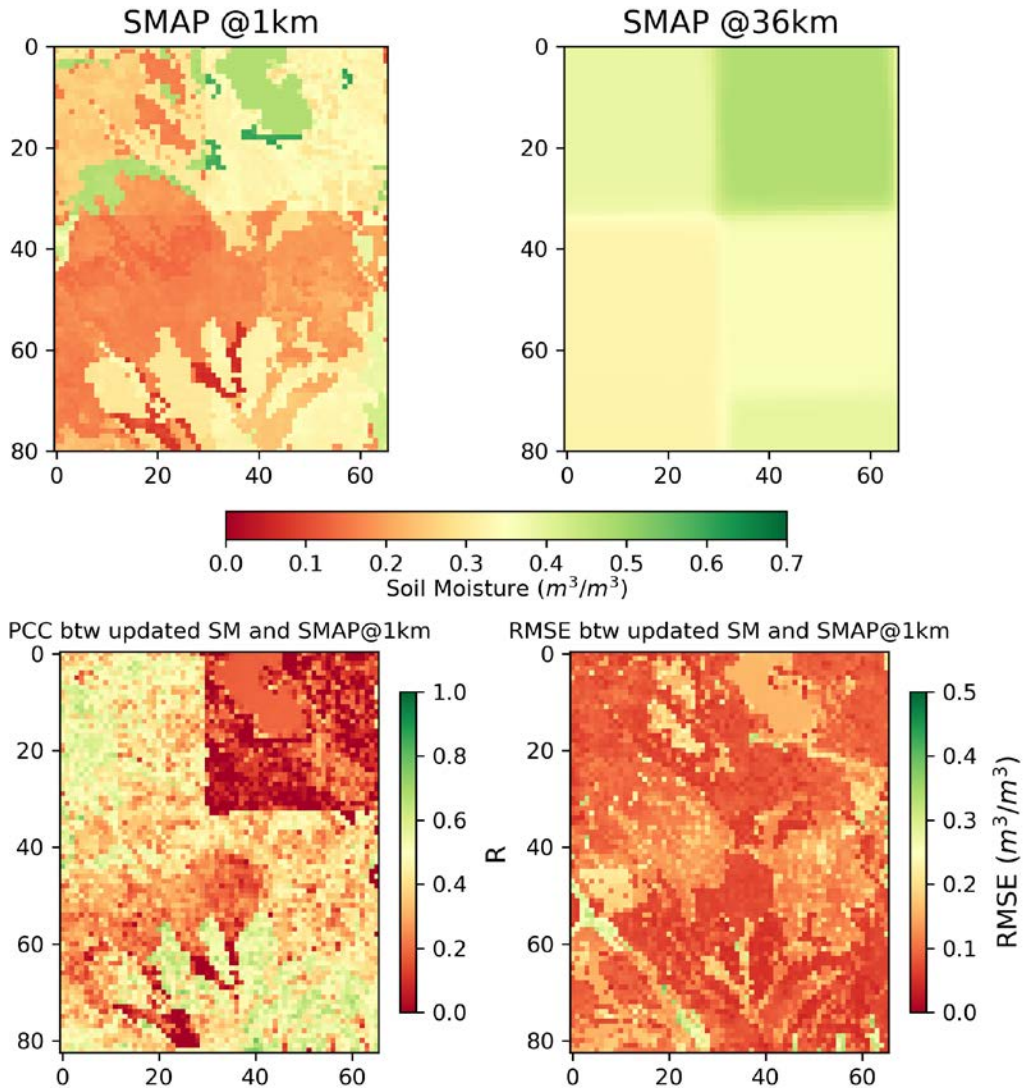


Figure 4-10. Upper panel: SMAP soil moisture at 36 km (right) and 1 km (left) spatial resolutions. Lower panel: correlation coefficient (left) and RMSE (right) between the updated soil moisture and SMAP soil moisture at 1 km spatial resolution.

Figure 4-11 shows the streamflow networks within the watershed for September 2, 2017 after the torrential rain due to hurricane Harvey. The river flows are represented by the mean ensemble values. We performed log transformation on river flow values for better visualization interpretation. The plots on the left and right side of the figure respectively show the univariate assimilation of SMAP soil moisture at 9 km and 36 km resolutions into the WRF-Hydro model.

As seen in the figure, assimilation of coarser resolution SMAP soil moisture data results in larger flood that may not be accurate. As explained earlier, the plausible reason behind this is that the coarser resolution SMAP data shows to be wetter than fine resolution due to existence of large water body in the region. According to the results discussed in Figure 4-9, the simulated streamflows at four USGS stations based on assimilation of 9-km SMAP soil moisture are more accurate than the results obtained by assimilation of original 36-km SMAP data. It is important to note that univariate assimilation of SMAP soil moisture products at different spatial resolutions or streamflow observations have had comparable impact on simulating the onset and termination of the high flows caused by the extreme rainfall.

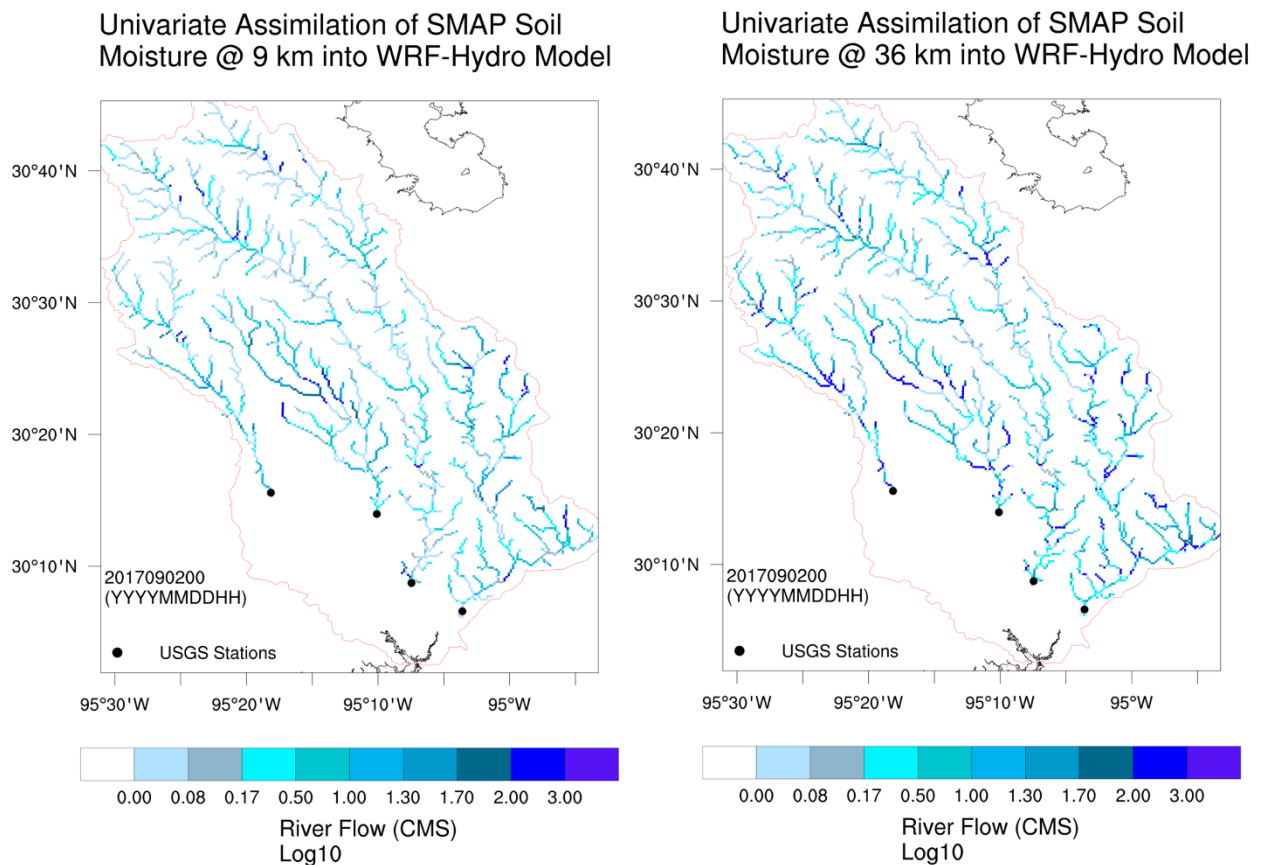


Figure 4-11. Univariate assimilation of SMAP soil moisture at 9 km (left) and 36 km (right) spatial resolutions into the WRF-Hydro model. This plot shows flows in the stream networks of the watershed for September 2, 2017 after termination of the heavy rainfall caused by the hurricane Harvey.

Multivariate Assimilation of SMAP Soil Moisture and Streamflow Observations

In this section, we will jointly assimilate the streamflow observations and 1-km SMAP soil moisture into the WRF-Hydro model with the aim of further improving the estimation of the topsoil layer moisture content and quality of ensemble streamflow prediction. We examined the results for the USGS gauge 8071280 and noticed that both the probabilistic (NRR=1.10, Reliability=0.90 and NRR=1.06) and deterministic (KGE=0.95 RMSE=20.12 cms) measures indicate the superior performance while conducting the joint assimilation as compared to a univariate assimilation configuration. Similar results were also observed for three other USGS gauges. Figure 4-S2-S5 (in supporting information) illustrate the benefit of multivariate assimilation of satellite soil moisture and streamflow observation in improving WRF-Hydro streamflow simulation during the period of hurricane Harvey. All performance measures are shown in Table 4-S1 (in supporting information). It is also important to note that the updated soil moisture at 1 km spatial resolution was in good agreement with the SMAP soil moisture observation at 1 km spatial resolution almost entire the domain except the region where the lake Livingston is located. This is similar to the results of the univariate assimilation of soil moisture data and streamflow observation discussed in Figure 4-10. The low performance of the model over this region is potentially due to the original SMAP soil moisture observation at 36 km spatial resolution that involves high retrieval error over this area. Comparing both univariate and multivariate assimilation configurations also revealed that in all scenarios, the data assimilation results in significant improvement of medium to high streamflow predictions. This may be attributed to the inherent of the WRF-Hydro model whose performance during the wet periods is higher than the dry periods.

Summary and Conclusion

Over the last decade, tropical storms and hurricanes have become more destructive and frequent in the Southeast US, mainly due to climate change and climate variability (Lim et al., 2018). They most often are accompanied by violent winds and torrential rains, which can lead to catastrophic flooding. Severe rainfall- and hurricane-induced flooding annually cause billions of dollars in damages, property losses and significant number of fatalities throughout the nation. Although hydrological models are widely used as an efficient means to estimate such floods, their predicted values most often are not accurate and reliable as the model prognostic variables, such as soil moisture and streamflow, are subject to large uncertainties stemming from hydrometeorological forcing, model parameters, boundary or initial condition and model structure. Data assimilation has been recognized as one of the effective methods to take into account these uncertainties and improve hydrologic prediction. With the recent advances in the satellite remote sensing technologies and ground-based observation, the observational data is becoming increasingly available, leading to widespread use of hydrologic data assimilation in various applications. Despite such developments, assimilation of remotely sensed soil moisture data at fine resolutions and streamflow observations into hyper-resolution hydrologic models (e.g., WRF-Hydro) has been rarely done. Therefore, as a prototype study we implemented hydrologic data assimilation using an evolutionary particle filter over a region in the Southeast Texas where heavy rainfall from hurricane Harvey caused fatal flooding.

The findings of this study showed that univariate assimilation of SMAP soil moisture at 1 km improves the streamflow simulation results more than the assimilation of coarse resolution products, including SMAP the native product of 36 km spatial resolution (SMAP_L3_SM_P)

and its interpolated version at 9 km spatial resolution (SMAP_L3_SM_P_E). Comparison between the univariate assimilation of 1-km SMAP soil moisture and streamflow observations at four USGS gauges within the watershed revealed that both had similar impact on the improvement of streamflow simulation results. The results also indicated that multivariate assimilation of soil moisture and streamflow observations results in more desirable posterior distribution than any independent assimilation configuration. We investigated the model performance during the hurricane Harvey and post-Harvey periods and realized that although DA, whether univariate or multivariate, and OL model runs have shown similar results in charactering the onset of flooding, the DA performed better in predicting the termination of flooding (streamflow recession period).

References

- Abbaszadeh, P., Alipour, A., & Asadi, S. (2018). Development of a coupled wavelet transform and evolutionary Levenberg-Marquardt neural networks for hydrological process modeling. *Computational Intelligence*, 34(1), 175–199. <https://doi.org/10.1111/coin.12124>
- Abbaszadeh, P., Moradkhani, H., & Daescu, D. N. (2019). The Quest for Model Uncertainty Quantification: A Hybrid Ensemble and Variational Data Assimilation Framework. *Water Resources Research*, 55(3), 2407–2431. <https://doi.org/10.1029/2018WR023629>
- Abbaszadeh, P., Moradkhani, H., & Yan, H. (2018a). Enhancing hydrologic data assimilation by evolutionary Particle Filter and Markov Chain Monte Carlo. *Advances in Water Resources*, 111, 192–204. <https://doi.org/10.1016/j.advwatres.2017.11.011>
- Abbaszadeh, P., Moradkhani, H., & Zhan, X. (2019). Downscaling SMAP Radiometer Soil Moisture Over the CONUS Using an Ensemble Learning Method. *Water Resources Research*, 55(1), 324–344. <https://doi.org/10.1029/2018WR023354>
- Abbaszadeh, P. (2016). Improving hydrological process modeling using optimized threshold-based wavelet Denoising technique. *Water Resources Management*. 30 (5), 1701-1721. <https://doi.org/10.1007/s11269-016-1246-5>
- Alemohammad, S. H., Kolassa, J., Prigent, C., Aires, F., & Gentine, P. (2018). Global downscaling of remotely sensed soil moisture using neural networks. *Hydrology and Earth System Sciences*, 22(10), 5341–5356. <https://doi.org/10.5194/hess-22-5341-2018>
- Asadi, S., Shahrabi, J., Abbaszadeh, P., Tabanmehr, S. (2013). A new hybrid artificial neural networks for rainfall– runoff process modeling. *Neurocomputing*. 121, 470–480. <https://doi.org/10.1016/j.neucom.2013.05.023>
- Alipour, A., Ahmadalipour, A., and Moradkhani, H. (2020). Assessing flash flood hazard and damages in southeast US (SEUS) J. Flood Risk Manage. (In press). DOI: 10.1111/JFR3.12605
- Alipour, A., Ahmadalipour, A., Abbaszadeh, P., and Moradkhani, H. (2020). Leveraging machine learning for predicting flash flood damage in the Southeast US. *Environmental Research Letters*, 15(2), 024011.
- Andreadis, K. M., & Lettenmaier, D. P. (2006). Assimilating remotely sensed snow observations into a macroscale hydrology model. *Advances in Water Resources*, 29(6), 872–886. <https://doi.org/10.1016/j.advwatres.2005.08.004>

- Arnault, J., Wagner, S., Rummeler, T., Fersch, B., Bliedernicht, J., Andresen, S., & Kunstmann, H. (2016). Role of Runoff–Infiltration Partitioning and Resolved Overland Flow on Land–Atmosphere Feedbacks: A Case Study with the WRF-Hydro Coupled Modeling System for West Africa. *Journal of Hydrometeorology*, *17*(5), 1489–1516. <https://doi.org/10.1175/JHM-D-15-0089.1>
- Aubert, D., Loumagne, C., & Oudin, L. (2003). Sequential assimilation of soil moisture and streamflow data in a conceptual rainfall–runoff model. *Journal of Hydrology*, *280*(1–4), 145–161. [https://doi.org/10.1016/S0022-1694\(03\)00229-4](https://doi.org/10.1016/S0022-1694(03)00229-4)
- Bi, H., Ma, J., & Wang, F. (2015). An Improved Particle Filter Algorithm Based on Ensemble Kalman Filter and Markov Chain Monte Carlo Method. *IEEE Journal of Selected Topics in Applied Earth Observations and Remote Sensing*, *8*(2), 447–459. <https://doi.org/10.1109/JSTARS.2014.2322096>
- Bolten, J. D., Crow, W. T., Zhan, X., Jackson, T. J., & Reynolds, C. A. (2010). Evaluating the Utility of Remotely Sensed Soil Moisture Retrievals for Operational Agricultural Drought Monitoring. *IEEE Journal of Selected Topics in Applied Earth Observations and Remote Sensing*, *3*(1), 57–66. <https://doi.org/10.1109/JSTARS.2009.2037163>
- Chan, S. K., Bindlish, R., O’Neill, P. E., Njoku, E., Jackson, T., Colliander, A., ... Kerr, Y. (2016). Assessment of the SMAP Passive Soil Moisture Product. *IEEE Transactions on Geoscience and Remote Sensing*, *54*(8), 4994–5007. <https://doi.org/10.1109/TGRS.2016.2561938>
- Chen, X., Kumar, M., & McGlynn, B. L. (2015). Variations in Streamflow Response to Large Hurricane-Season Storms in a Southeastern U.S. Watershed. *Journal of Hydrometeorology*, *16*(1), 55–69. <https://doi.org/10.1175/JHM-D-14-0044.1>
- Clark, M. P., Rupp, D. E., Woods, R. A., Zheng, X., Ibbitt, R. P., Slater, A. G., ... Uddstrom, M. J. (2008). Hydrological data assimilation with the ensemble Kalman filter: Use of streamflow observations to update states in a distributed hydrological model. *Advances in Water Resources*, *31*(10), 1309–1324. <https://doi.org/10.1016/j.advwatres.2008.06.005>
- Crow, W. T., & Wood, E. F. (2003). The assimilation of remotely sensed soil brightness temperature imagery into a land surface model using Ensemble Kalman filtering: a case study based on ESTAR measurements during SGP97. *Advances in Water Resources*, *26*(2), 137–149. [https://doi.org/10.1016/S0309-1708\(02\)00088-X](https://doi.org/10.1016/S0309-1708(02)00088-X)
- Das, N. N., Entekhabi, D., Dunbar, R. S., Colliander, A., Chen, F., Crow, W., ... Njoku, E. G. (2018). The SMAP mission combined active–passive soil moisture product at 9 km and 3 km spatial resolutions. *Remote Sensing of Environment*, *211*, 204–217. <https://doi.org/10.1016/j.rse.2018.04.011>
- DeChant, C. M., & Moradkhani, H. (2012). Examining the effectiveness and robustness of sequential data assimilation methods for quantification of uncertainty in hydrologic forecasting. *Water Resources Research*, *48*(4). <https://doi.org/10.1029/2011WR011011>

- Dong, J., Steele-Dunne, S. C., Judge, J., & van de Giesen, N. (2015). A particle batch smoother for soil moisture estimation using soil temperature observations. *Advances in Water Resources*, 83, 111–122. <https://doi.org/10.1016/j.advwatres.2015.05.017>
- Donnelly, J. P., & Woodruff, J. D. (2007). Intense hurricane activity over the past 5,000 years controlled by El Niño and the West African monsoon. *Nature*, 447(7143), 465–468. <https://doi.org/10.1038/nature05834>
- Doocy, S., Daniels, A., Murray, S., Hopkins, J. B., & Kirsch, T. D. (2013). The Human Impact of Floods: a Historical Review of Events 1980-2009 and Systematic Literature Review – PLOS Currents Disasters.
- Duan, Q., Sorooshian, S., & Gupta, V. (1992). Effective and efficient global optimization for conceptual rainfall-runoff models. *Water Resources Research*, 28(4), 1015–1031. <https://doi.org/10.1029/91WR02985>
- Eisenbies, M. H., Aust, W. M., Burger, J. A., & Adams, M. B. (2007). Forest operations, extreme flooding events, and considerations for hydrologic modeling in the Appalachians—A review. *Forest Ecology and Management*, 242(2–3), 77–98. <https://doi.org/10.1016/j.foreco.2007.01.051>
- Entekhabi, D., Njoku, E. G., O'Neill, P. E., Kellogg, K. H., Crow, W. T., Edelstein, W. N., ... Van Zyl, J. (2010). The Soil Moisture Active Passive (SMAP) Mission. *Proceedings of the IEEE*, 98(5), 704–716. <https://doi.org/10.1109/JPROC.2010.2043918>
- Evensen, G. (2003). The Ensemble Kalman Filter: Theoretical formulation and practical implementation. *Ocean Dynamics*. <https://doi.org/10.1007/s10236-003-0036-9>
- Felfelani, F., Pokhrel, Y., Guan, K., & Lawrence, D. M. (2018). Utilizing SMAP Soil Moisture Data to Constrain Irrigation in the Community Land Model. *Geophysical Research Letters*. <https://doi.org/10.1029/2018GL080870>
- Foltz, G. R., Balaguru, K., & Hagos, S. (2018). Interbasin Differences in the Relationship between SST and Tropical Cyclone Intensification. *Monthly Weather Review*, 146(3), 853–870. <https://doi.org/10.1175/MWR-D-17-0155.1>
- Gavahi, K., Mousavi, S. J., & Ponnambalam, K. (2019). Adaptive forecast-based real-time optimal reservoir operations: application to Lake Urmia. *Journal of Hydroinformatics*, 21(5), 908-924. <https://doi.org/10.2166/hydro.2019.005>
- Gavahi, K., Mousavi, S. J., & Ponnambalam, K. (2018). Comparison of Two Data-Driven Streamflow Forecast Approaches in an Adaptive Optimal Reservoir Operation Model. *EPiC Series in Engineering*, 3, 755-763.
- Gavahi, K., Abbaszadeh, P., Moradkhani, H. Zhan, W., Hains, C. (2020). Multivariate Assimilation of Remotely Sensed Soil Moisture and Evapotranspiration for Drought Monitoring. *Journal of Hydrometeorology* (in-press)

- Gochis, D., & Chen, F. (2003). Hydrological enhancements to the community Noah land surface model. *NCAR Scientific Technical Report*, 77. <https://doi.org/10.5065/D60P0X00>
- Gochis, D. J., Yu, W., & Yates, D. (2015). *The WRF-Hydro model technical description and user's guide, version 3.0. NCAR Technical Document*. Retrieved from http://www.mmm.ucar.edu/wrf/users/docs/arw_v3.pdf
- Gupta, H. V., Kling, H., Yilmaz, K. K., & Martinez, G. F. (2009). Decomposition of the mean squared error and NSE performance criteria: Implications for improving hydrological modelling. *Journal of Hydrology*, 377(1–2), 80–91. <https://doi.org/10.1016/j.jhydrol.2009.08.003>
- Hameed, M., Moradkhani, H., Ahmadalipour, A., Moftakhari, H., Abbaszadeh, P., Alipour, A., (2019). A review of the 21st century challenges in the food-energy-water security in the Middle East. *Water*. 11, 682. <https://doi.org/10.3390/w11040682>
- Houser, P. R., Shuttleworth, W. J., Famiglietti, J. S., Gupta, H. V., Syed, K. H., & Goodrich, D. C. (1998). Integration of soil moisture remote sensing and hydrologic modeling using data assimilation. *Water Resources Research*, 34(12), 3405–3420. <https://doi.org/10.1029/1998WR900001>
- Huong, H. T. L., & Pathirana, A. (2013). Urbanization and climate change impacts on future urban flooding in Can Tho city, Vietnam. *Hydrology and Earth System Sciences*, 17(1), 379–394. <https://doi.org/10.5194/hess-17-379-2013>
- Kossin, J. P., Olander, T. L., & Knapp, K. R. (2013). Trend Analysis with a New Global Record of Tropical Cyclone Intensity. *Journal of Climate*, 26(24), 9960–9976. <https://doi.org/10.1175/JCLI-D-13-00262.1>
- Koster, R. D., Liu, Q., Mahanama, S. P. P., & Reichle, R. H. (2018). Improved Hydrological Simulation Using SMAP Data: Relative Impacts of Model Calibration and Data Assimilation. *Journal of Hydrometeorology*, 19(4), 727–741. <https://doi.org/10.1175/JHM-D-17-0228.1>
- Kourgialas, N. N., & Karatzas, G. P. (2011). Flood management and a GIS modelling method to assess flood-hazard areas—a case study. *Hydrological Sciences Journal*, 56(2), 212–225. <https://doi.org/10.1080/02626667.2011.555836>
- Kuczera, G., & Parent, E. (1998). Monte Carlo assessment of parameter uncertainty in conceptual catchment models: the Metropolis algorithm. *Journal of Hydrology*, 211(1–4), 69–85. [https://doi.org/10.1016/S0022-1694\(98\)00198-X](https://doi.org/10.1016/S0022-1694(98)00198-X)
- Kundzewicz, Z. W., Kanae, S., Seneviratne, S. I., Handmer, J., Nicholls, N., Peduzzi, P., ... Sherstyukov, B. (2014). Flood risk and climate change: global and regional perspectives. *Hydrological Sciences Journal*, 59(1), 1–28. <https://doi.org/10.1080/02626667.2013.857411>
- Lahmers, T. M., Gupta, H., Castro, C. L., Gochis, D. J., Yates, D., Dugger, A., ... Hazenberg, P. (2019). Enhancing the Structure of the WRF-Hydro Hydrologic Model for Semiarid

- Environments. *Journal of Hydrometeorology*, 20(4), 691–714. <https://doi.org/10.1175/JHM-D-18-0064.1>
- De Lannoy, G. J. M., Reichle, R. H., Houser, P. R., Pauwels, V. R. N., & Verhoest, N. E. C. (2007). Correcting for forecast bias in soil moisture assimilation with the ensemble Kalman filter. *Water Resources Research*, 43(9). <https://doi.org/10.1029/2006WR005449>
- Leach, J. M., Kornelsen, K. C., & Coulibaly, P. (2018). Assimilation of near-real time data products into models of an urban basin. *Journal of Hydrology*, 563, 51–64. <https://doi.org/10.1016/j.jhydrol.2018.05.064>
- Lee, H., Seo, D.-J., & Koren, V. (2011). Assimilation of streamflow and in situ soil moisture data into operational distributed hydrologic models: Effects of uncertainties in the data and initial model soil moisture states. *Advances in Water Resources*, 34(12), 1597–1615. <https://doi.org/10.1016/j.advwatres.2011.08.012>
- Leisenring, M., & Moradkhani, H. (2011). Snow water equivalent prediction using Bayesian data assimilation methods. *Stochastic Environmental Research and Risk Assessment*. <https://doi.org/10.1007/s00477-010-0445-5>
- Lespinas, F., Dastoor, A., & Fortin, V. (2018). Performance of the dynamically dimensioned search algorithm: influence of parameter initialization strategy when calibrating a physically based hydrological model. *Hydrology Research*, 49(4), 971–988. <https://doi.org/10.2166/nh.2017.139>
- Lim, Y., Schubert, S.D., Kovach, R. et al. (2018). The Roles of Climate Change and Climate Variability in the 2017 Atlantic Hurricane Season. *Sci Rep* 8, 16172. doi:10.1038/s41598-018-34343-5
- Lin, P., Rajib, M. A., Yang, Z.-L., Somos-Valenzuela, M., Merwade, V., Maidment, D. R., ... Chen, L. (2018). Spatiotemporal Evaluation of Simulated Evapotranspiration and Streamflow over Texas Using the WRF-Hydro-RAPID Modeling Framework. *JAWRA Journal of the American Water Resources Association*, 54(1), 40–54. <https://doi.org/10.1111/1752-1688.12585>
- Liu, M., & Smith, J. A. (2016). Extreme Rainfall from Landfalling Tropical Cyclones in the Eastern United States: Hurricane Irene (2011). *Journal of Hydrometeorology*, 17(11), 2883–2904. <https://doi.org/10.1175/JHM-D-16-0072.1>
- Liu, Y., & Gupta, H. V. (2007). Uncertainty in hydrologic modeling: Toward an integrated data assimilation framework. *Water Resources Research*, 43(7), 1–18. <https://doi.org/10.1029/2006WR005756>
- López López, P., Sutanudjaja, E. H., Schellekens, J., Sterk, G., & Bierkens, M. F. P. (2017). Calibration of a large-scale hydrological model using satellite-based soil moisture and evapotranspiration products. *Hydrology and Earth System Sciences*, 21(6), 3125–3144. <https://doi.org/10.5194/hess-21-3125-2017>

- Malbêteau, Y., Merlin, O., Balsamo, G., Er-Raki, S., Khabba, S., Walker, J. P., & Jarlan, L. (2018). Toward a Surface Soil Moisture Product at High Spatiotemporal Resolution: Temporally Interpolated, Spatially Disaggregated SMOS Data. *Journal of Hydrometeorology*, *19*(1), 183–200. <https://doi.org/10.1175/JHM-D-16-0280.1>
- Marshall, L., Nott, D., & Sharma, A. (2004). A comparative study of Markov chain Monte Carlo methods for conceptual rainfall-runoff modeling. *Water Resources Research*, *40*(2). <https://doi.org/10.1029/2003WR002378>
- Massari, C., Camici, S., Ciabatta, L., & Brocca, L. (2018). Exploiting Satellite-Based Surface Soil Moisture for Flood Forecasting in the Mediterranean Area: State Update Versus Rainfall Correction. *Remote Sensing*, *10*(2), 292. <https://doi.org/10.3390/rs10020292>
- Matgen, P., Montanari, M., Hostache, R., Pfister, L., Hoffmann, L., Plaza, D., ... Savenije, H. H. G. (2010). Towards the sequential assimilation of SAR-derived water stages into hydraulic models using the Particle Filter: proof of concept. *Hydrology and Earth System Sciences*, *14*(9), 1773–1785. <https://doi.org/10.5194/hess-14-1773-2010>
- Michener, W. K., Blood, E. R., Bildstein, K. L., Brinson, M. M., & Gardner, L. R. (1997). Climate Change, Hurricanes and Tropical Storms, and Rising Sea Level in Coastal Wetlands. *Ecological Applications*, *7*(3), 770. <https://doi.org/10.2307/2269434>
- Montzka, C., Grant, J. P., Moradkhani, H., Franssen, H.-J. H., Weihermüller, L., Drusch, M., & Vereecken, H. (2013). Estimation of Radiative Transfer Parameters from L-Band Passive Microwave Brightness Temperatures Using Advanced Data Assimilation. *Vadose Zone Journal*, *12*(3). <https://doi.org/10.2136/vzj2012.0040>
- Moradkhani H., Meskele T.T. (2010) Probabilistic Assessment of the Satellite Rainfall Retrieval Error Translation to Hydrologic Response. In: Gebremichael M., Hossain F. (eds) *Satellite Rainfall Applications for Surface Hydrology*. Springer, Dordrecht
- Moradkhani, H. (2008). Hydrologic remote sensing and land surface data assimilation. *Sensors*, *8*(5), 2986–3004. <https://doi.org/10.3390/s8052986>
- Moradkhani, H., Sorooshian, S., Gupta, H. V., & Houser, P. R. (2005). Dual state–parameter estimation of hydrological models using ensemble Kalman filter. *Advances in Water Resources*, *28*(2), 135–147. <https://doi.org/10.1016/j.advwatres.2004.09.002>
- Moradkhani, H., Nearing, G., Abbaszadeh, P., & Pathiraja, S. (2018b). Fundamentals of Data Assimilation and Theoretical Advances. In *Handbook of Hydrometeorological Ensemble Forecasting* (pp. 1–26). Berlin, Heidelberg: Springer Berlin Heidelberg. https://doi.org/10.1007/978-3-642-40457-3_30-1
- Moradkhani, H., & Sorooshian, S. (2008). General Review of Rainfall-Runoff Modeling: Model Calibration, Data Assimilation, and Uncertainty Analysis. In *Hydrological Modelling and the Water Cycle*. https://doi.org/10.1007/978-3-540-77843-1_1
- Moradkhani, H., DeChant, C. M., & Sorooshian, S. (2012). Evolution of ensemble data

- assimilation for uncertainty quantification using the particle filter-Markov chain Monte Carlo method. *Water Resources Research*, 48(12). <https://doi.org/10.1029/2012WR012144>
- Moradkhani, H., Hsu, K.-L., Gupta, H., & Sorooshian, S. (2005). Uncertainty assessment of hydrologic model states and parameters: Sequential data assimilation using the particle filter. *Water Resources Research*, 41(5). <https://doi.org/10.1029/2004WR003604>
- Nourani, V., Tahershamsi, A., Abbaszadeh, P., Shahrabi, J., Hadavandi, E. (2014). A new hybrid algorithm for rainfall-runoff process modeling based on the wavelet transform and genetic fuzzy system. *Journal of Hydroinformatics*. 16 (5), 1004-1024. <https://doi.org/10.2166/hydro.2014.035>
- Naylor, L. A., Spencer, T., Lane, S. N., Darby, S. E., Magilligan, F. J., Macklin, M. G., & Möller, I. (2017). Stormy geomorphology: geomorphic contributions in an age of climate extremes. *Earth Surface Processes and Landforms*, 42(1), 166–190. <https://doi.org/10.1002/esp.4062>
- Niu, G.-Y., Yang, Z.-L., Mitchell, K. E., Chen, F., Ek, M. B., Barlage, M., ... Xia, Y. (2011). The community Noah land surface model with multiparameterization options (Noah-MP): 1. Model description and evaluation with local-scale measurements. *Journal of Geophysical Research*, 116(D12), D12109. <https://doi.org/10.1029/2010JD015139>
- Nikoo, M. R., Gavahi, K., & Khoramshokoh, N. (2019). A multi-objective simulation–optimization approach for Design of Cutoff Walls and Apron of diversion dams. *Iranian Journal of Science and Technology, Transactions of Civil Engineering*, 43(2), 241-252.
- Nikoo, M. R., Karimi, A., Kerachian, R., & Gavahi, K. (2019). Optimum Operation of Reservoirs in the Karkheh Basin in Iran Considering Impacts of Non-integrated Development and Climate Change. *Iranian Journal of Science and Technology, Transactions of Civil Engineering*, 43(1), 37-47.
- Noh, S. J., Tachikawa, Y., Shiiba, M., & Kim, S. (2011). Applying sequential Monte Carlo methods into a distributed hydrologic model: lagged particle filtering approach with regularization. *Hydrology and Earth System Sciences*, 15(10), 3237–3251. <https://doi.org/10.5194/hess-15-3237-2011>
- Panzeri, M., Riva, M., Guadagnini, A., & Neuman, S. P. (2014). Comparison of Ensemble Kalman Filter groundwater-data assimilation methods based on stochastic moment equations and Monte Carlo simulation. *Advances in Water Resources*, 66, 8–18. <https://doi.org/10.1016/j.advwatres.2014.01.007>
- Pathiraja, S., Marshall, L., Sharma, A., & Moradkhani, H. (2016). Hydrologic modeling in dynamic catchments: A data assimilation approach. *Water Resources Research*, 52(5), 3350–3372. <https://doi.org/10.1002/2015WR017192>
- Peng, J., Loew, A., Merlin, O., & Verhoest, N. E. C. (2017). A review of spatial downscaling of satellite remotely sensed soil moisture. *Reviews of Geophysics*, 55(2), 341–366. <https://doi.org/10.1002/2016RG000543>

- Plaza, D. A., De Keyser, R., De Lannoy, G. J. M., Giustarini, L., Matgen, P., & Pauwels, V. R. N. (2012). The importance of parameter resampling for soil moisture data assimilation into hydrologic models using the particle filter. *Hydrology and Earth System Sciences*, *16*(2), 375–390. <https://doi.org/10.5194/hess-16-375-2012>
- Reichle, R. H., & Koster, R. D. (2004). Bias reduction in short records of satellite soil moisture. *Geophysical Research Letters*, *31*(19), L19501. <https://doi.org/10.1029/2004GL020938>
- Reichle, Rolf H., McLaughlin, D. B., & Entekhabi, D. (2002). Hydrologic Data Assimilation with the Ensemble Kalman Filter. *Monthly Weather Review*, *130*(1), 103–114. [https://doi.org/10.1175/1520-0493\(2002\)130<0103:HDAWTE>2.0.CO;2](https://doi.org/10.1175/1520-0493(2002)130<0103:HDAWTE>2.0.CO;2)
- Ryu, Y., Lim, Y.-J., Ji, H.-S., Park, H.-H., Chang, E.-C., & Kim, B.-J. (2017). Applying a coupled hydrometeorological simulation system to flash flood forecasting over the Korean Peninsula. *Asia-Pacific Journal of Atmospheric Sciences*, *53*(4), 421–430. <https://doi.org/10.1007/s13143-017-0045-0>
- Sahoo, A. K., De Lannoy, G. J. M., Reichle, R. H., & Houser, P. R. (2013). Assimilation and downscaling of satellite observed soil moisture over the Little River Experimental Watershed in Georgia, USA. *Advances in Water Resources*, *52*, 19–33. <https://doi.org/10.1016/j.advwatres.2012.08.007>
- Senatore, A., Mendicino, G., Gochis, D. J., Yu, W., Yates, D. N., & Kunstmann, H. (2015). Fully coupled atmosphere-hydrology simulations for the central Mediterranean: Impact of enhanced hydrological parameterization for short and long time scales. *Journal of Advances in Modeling Earth Systems*, *7*(4), 1693–1715. <https://doi.org/10.1002/2015MS000510>
- Seo, DJ, Y Liu, H. Moradkhani, A. Weerts (2014), Ensemble prediction and data assimilation for operational hydrology, *Journal of Hydrology*, special issue, 519, 2661–2662, DOI:10.1016/j.jhydrol.2014.11.035.
- El Sharif, H., Wang, J., & Georgakakos, A. P. (2015). Modeling Regional Crop Yield and Irrigation Demand Using SMAP Type of Soil Moisture Data. *Journal of Hydrometeorology*, *16*(2), 904–916. <https://doi.org/10.1175/JHM-D-14-0034.1>
- Silver, M., Karnieli, A., Ginat, H., Meiri, E., & Fredj, E. (2017). An innovative method for determining hydrological calibration parameters for the WRF-Hydro model in arid regions. *Environmental Modelling & Software*, *91*, 47–69. <https://doi.org/10.1016/j.envsoft.2017.01.010>
- Slater, A. G., & Clark, M. P. (2006). Snow Data Assimilation via an Ensemble Kalman Filter. *Journal of Hydrometeorology*, *7*(3), 478–493. <https://doi.org/10.1175/JHM505.1>
- Smith, R. B., Schafer, P., Kirshbaum, D., & Regina, E. (2009). Orographic Enhancement of Precipitation inside Hurricane Dean. *Journal of Hydrometeorology*, *10*(3), 820–831. <https://doi.org/10.1175/2008JHM1057.1>
- Smith, T. J., & Marshall, L. A. (2008). Bayesian methods in hydrologic modeling: A study of

- recent advancements in Markov chain Monte Carlo techniques. *Water Resources Research*, 44(12). <https://doi.org/10.1029/2007WR006705>
- Tolson, B. A., & Shoemaker, C. A. (2007). Dynamically dimensioned search algorithm for computationally efficient watershed model calibration. *Water Resources Research*, 43(1). <https://doi.org/10.1029/2005WR004723>
- Vrugt, J. A., Gupta, H. V., Nualláin, B., & Bouten, W. (2006). Real-Time Data Assimilation for Operational Ensemble Streamflow Forecasting. *Journal of Hydrometeorology*, 7(3), 548–565. <https://doi.org/10.1175/JHM504.1>
- Vrugt, J. A., Diks, C. G. H., Gupta, H. V., Bouten, W., & Verstraten, J. M. (2005a). Improved treatment of uncertainty in hydrologic modeling: Combining the strengths of global optimization and data assimilation. *Water Resources Research*, 41(1), 1–17. <https://doi.org/10.1029/2004WR003059>
- Vrugt, J. A., Diks, C. G. H., Gupta, H. V., Bouten, W., & Verstraten, J. M. (2005b). Improved treatment of uncertainty in hydrologic modeling: Combining the strengths of global optimization and data assimilation. *Water Resources Research*, 41(1). <https://doi.org/10.1029/2004WR003059>
- Wanders, N., Karssenber, D., de Roo, A., de Jong, S. M., & Bierkens, M. F. P. (2014). The suitability of remotely sensed soil moisture for improving operational flood forecasting. *Hydrology and Earth System Sciences*, 18(6), 2343–2357. <https://doi.org/10.5194/hess-18-2343-2014>
- Wehbe, Y., Temimi, M., Weston, M., Chaouch, N., Branch, O., Schwitalla, T., ... Al Mandous, A. (2018). Analysis of an Extreme Weather Event in a Hyper Arid Region Using WRF-Hydro Coupling, Station, and Satellite data. *Natural Hazards and Earth System Sciences Discussions*, 1–34. <https://doi.org/10.5194/nhess-2018-226>
- Xu, X., Li, J., & Tolson, B. A. (2014). Progress in integrating remote sensing data and hydrologic modeling. *Progress in Physical Geography: Earth and Environment*, 38(4), 464–498. <https://doi.org/10.1177/0309133314536583>
- Yan, H., & Moradkhani, H. (2016). Combined assimilation of streamflow and satellite soil moisture with the particle filter and geostatistical modeling. *Advances in Water Resources*, 94, 364–378. <https://doi.org/10.1016/j.advwatres.2016.06.002>
- Yan, H., DeChant, C. M., & Moradkhani, H. (2015). Improving Soil Moisture Profile Prediction With the Particle Filter-Markov Chain Monte Carlo Method. *IEEE Transactions on Geoscience and Remote Sensing*, 53(11), 6134–6147. <https://doi.org/10.1109/TGRS.2015.2432067>
- Yan, H., Zarekarizi, M., & Moradkhani, H. (2018). Toward improving drought monitoring using the remotely sensed soil moisture assimilation: A parallel particle filtering framework. *Remote Sensing of Environment*, 216, 456–471. <https://doi.org/10.1016/j.rse.2018.07.017>

- Yan, H., Moradkhani, H., & Zarekarizi, M. (2017). A probabilistic drought forecasting framework: A combined dynamical and statistical approach. *Journal of Hydrology*, 548, 291–304. <https://doi.org/10.1016/j.jhydrol.2017.03.004>
- Yucel, I., Onen, A., Yilmaz, K. K., & Gochis, D. J. (2015). Calibration and evaluation of a flood forecasting system: Utility of numerical weather prediction model, data assimilation and satellite-based rainfall. *Journal of Hydrology*, 523, 49–66. <https://doi.org/10.1016/j.jhydrol.2015.01.042>
- Yucel, I., & Onen, A. (2014). Evaluating a mesoscale atmosphere model and a satellite-based algorithm in estimating extreme rainfall events in northwestern Turkey. *Natural Hazards and Earth System Sciences*, 14(3), 611–624. <https://doi.org/10.5194/nhess-14-611-2014>
- Zaitchik, B. F., Rodell, M., & Reichle, R. H. (2008). Assimilation of GRACE Terrestrial Water Storage Data into a Land Surface Model: Results for the Mississippi River Basin. *Journal of Hydrometeorology*, 9(3), 535–548. <https://doi.org/10.1175/2007JHM951.1>
- Zhao, W., Sánchez, N., Lu, H., & Li, A. (2018). A spatial downscaling approach for the SMAP passive surface soil moisture product using random forest regression. *Journal of Hydrology*, 563, 1009–1024. <https://doi.org/10.1016/j.jhydrol.2018.06.081>

CONCLUSION

This dissertation is an attempt to provide a unified approach toward hyper-resolution hydrologic data assimilation system for improved predictions of hydroclimate extremes, such as floods and droughts.

Tropical storms and hurricanes in the Southeast United States have become more frequent and intense over the past decades, mainly due to the effects of climate change and climate variability. They often produce torrential rains that may result in deadly and destructive floods depending on orographic, geomorphologic and hydrologic characteristics of the region. Hydrological models, irrespective of their types, most often do not provide accurate and reliable estimates of prognostic variables (e.g., soil moisture and streamflow) as they are subject to large uncertainties coming from different sources, including hydrometeorological forcing inputs, model parameters, boundary or initial condition and model structure. Data Assimilation (DA) has garnered increased attention among researchers and practitioners as an effective and reliable method based to incorporate the hydrometeorological observations from in-situ and remotely sensed measurements into hydrological models for enhancing their forecasting skills while taking into account the associated uncertainties. To account for these set of uncertainties involved in different layers of hydrologic predictions, this dissertation presented a state of the art data assimilation method. The Evolutionary Particle Filter with MCMC (EPFM) uses the Genetic Algorithm (GA) to effectively sample the particles to better represent the posterior distribution of model prognostic variables and parameters. This is followed by coupling EPFM and 4DVAR which results in a superior DA approach, the so-called Hybrid Ensemble and Variational Data Assimilation framework for Environmental systems (HEAVEN). The method explicitly characterizes the model structural uncertainty during the assimilation process. The application of

methods is presented for both flood and drought forecasting while utilizing the remotely sensed observations.

With recent advances in satellite remote sensing technologies, soil moisture data have become available at a global scale with decent spatial and temporal resolutions. While these products are promoting a wide range of global and continental land-atmosphere studies, their coarse spatial resolutions impede their use in regional and local studies that require a finer resolution data, usually less than 1 km. To circumvent this problem, many researchers have used Machine Learning (ML) techniques to rescale the coarse scale remotely sensed soil moisture products to finer resolutions. More investigation has shown that Random Forest (RF) algorithm in comparison with other ML approaches is more suitable for downscaling purposes. Therefore, in this dissertation, we developed a downscaling framework using this technique to rescale Soil Moisture Active Passive (SMAP) radiometer soil moisture from its native resolution (36 km) to a finer resolution (1 km) while using atmospheric and geophysical information acquired from high-resolution remote-sensing data and ground-based observations. The validation results based on in-situ soil moisture measurements collected from two core sites for SMAP validation and three hundred sparse soil moisture networks confirmed that the rescaled SMAP soil moistures adequately meet the SMAP soil moisture retrieval accuracy requirement ($ubRMSE=0.040\text{ m}^3/\text{m}^3$) and capture the spatial heterogeneity of soil parameters and dynamics of in-situ soil moisture observations.

Data assimilation in conjunction with fully distributed hydrologic models is still in its infancy mostly due to its complexity and sophistication. It is therefore of particular interest to examine the benefit of assimilating high-resolution satellite soil moisture products into a hyper-resolution hydrological model, here WRF-Hydro (Weather Research and Forecasting

Hydrological model) and to understand the extent to which they can contribute to improving the model predictions, particularly during an extreme event. To this end, in this dissertation, we conducted a prototype study over a region in Southeast Texas where heavy rainfall from Hurricane Harvey caused flooding.

Supplementary Information

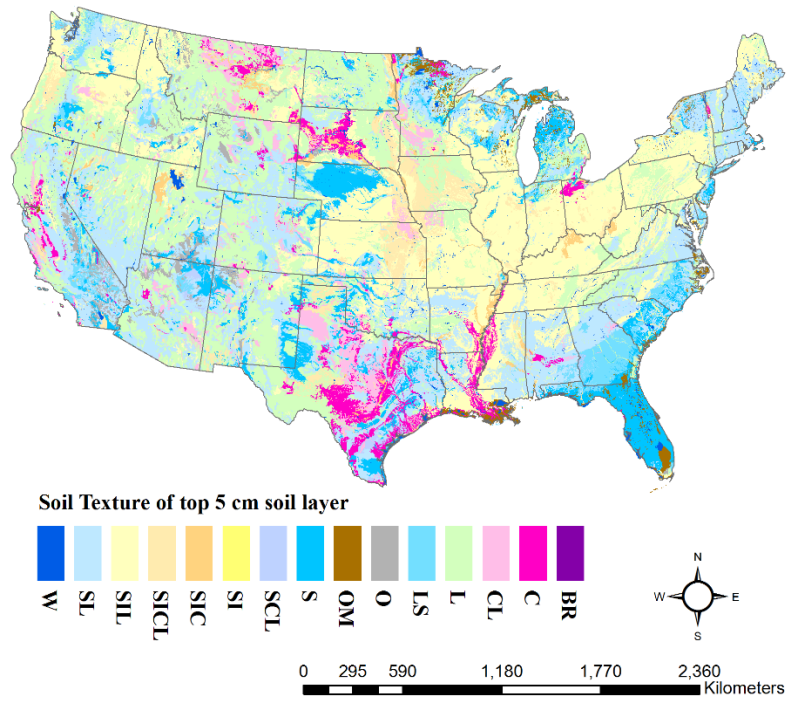


Figure 1-S1. Soil texture of top 5 cm soil layer over the CONUS

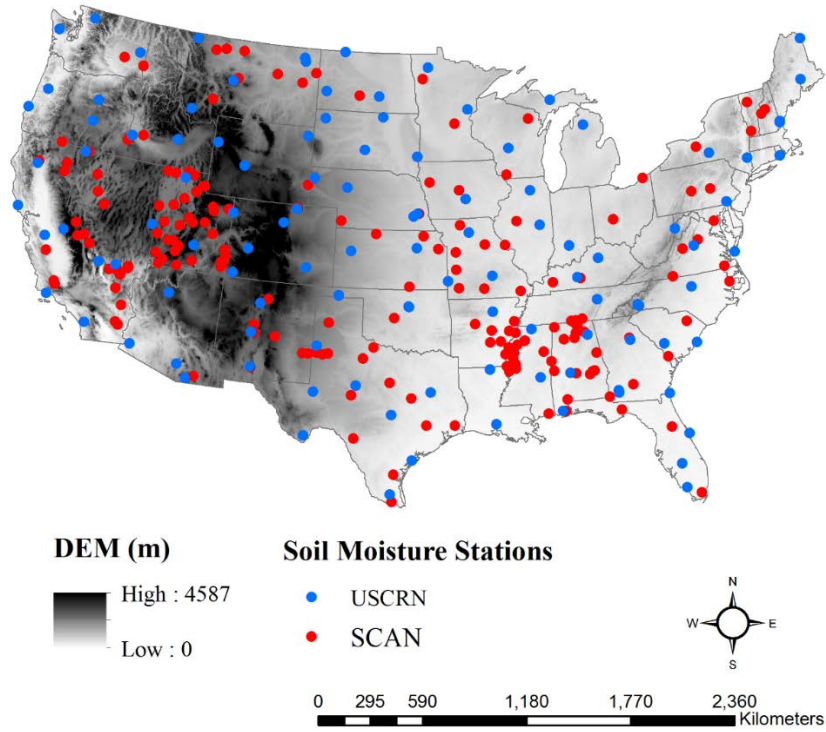


Figure 1-S2. The USCRN and SCAN soil moisture sensors throughout the CONUS and Digital Elevation Map (DEM) showing the variations of elevation.



Figure 1-S3. SCAN stations located at (a) Tift, Georgia (b) Whitman, Washington and (c) Fresno, California (<https://www.wcc.nrcs.usda.gov/scan/>).

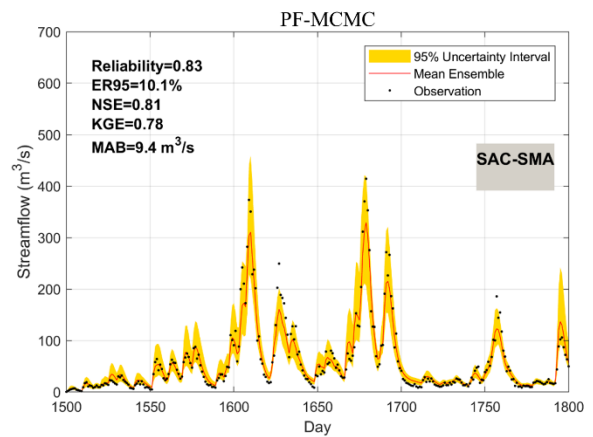
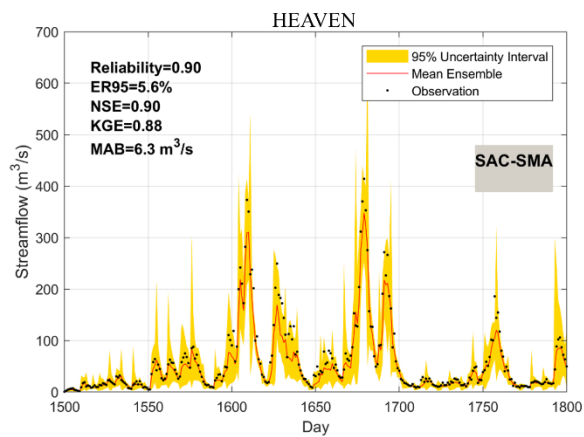
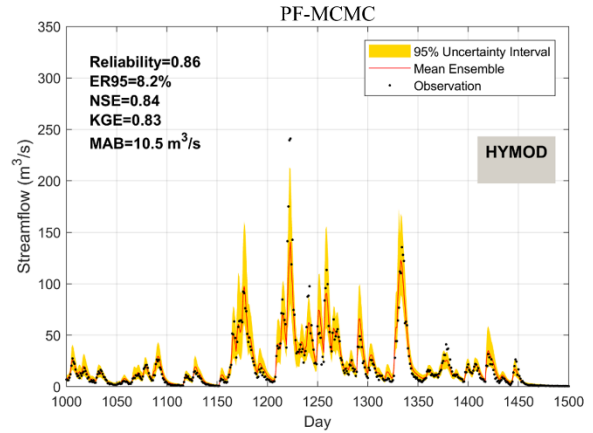
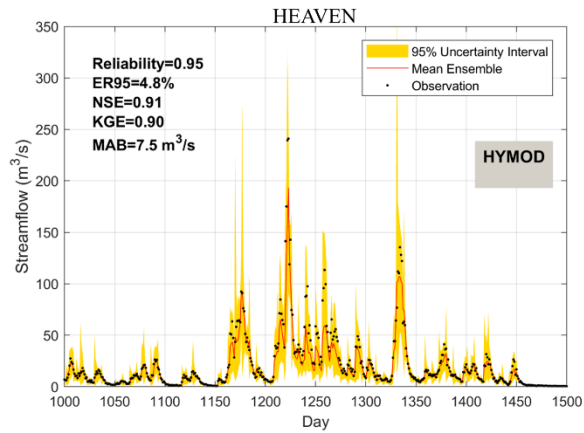


Figure 3-S1. The comparison of the PF-MCMC and HEAVEN skills for three-day streamflow forecast in the Leaf River Basin during the flood season.

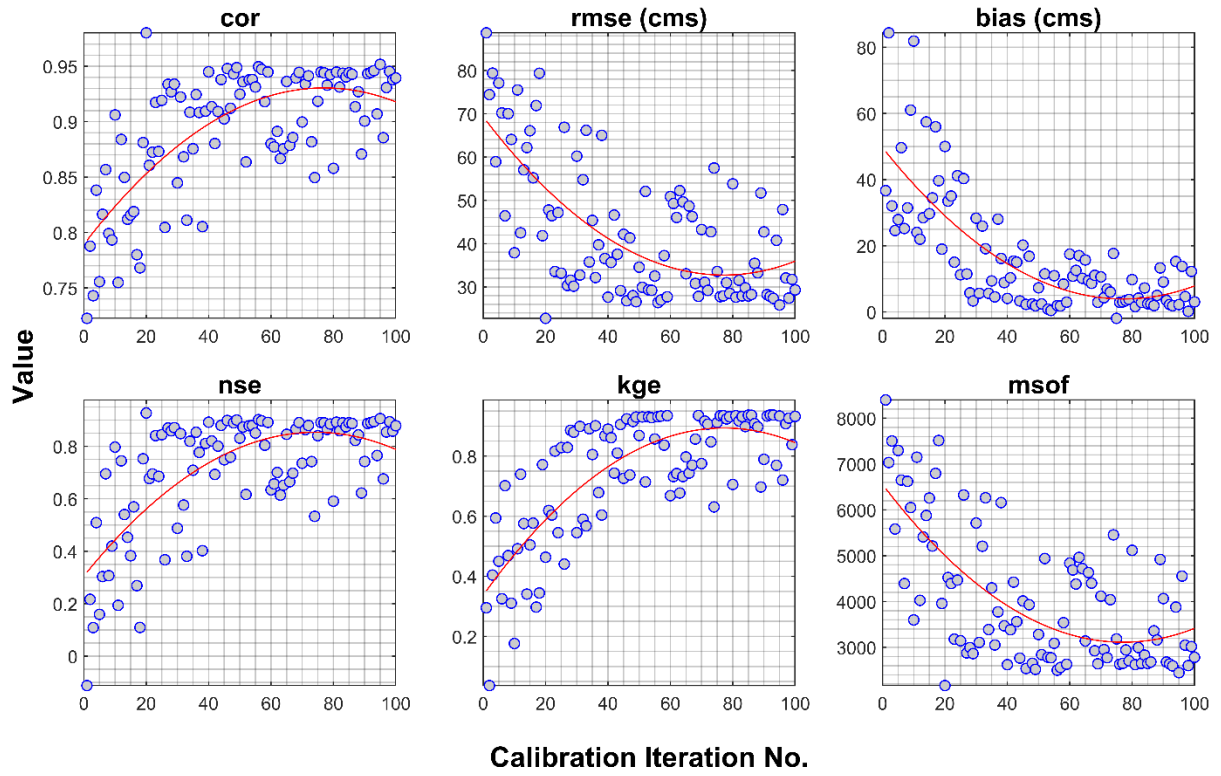


Figure 4-S1. Soil texture of top 5 cm soil layer over the CONUS

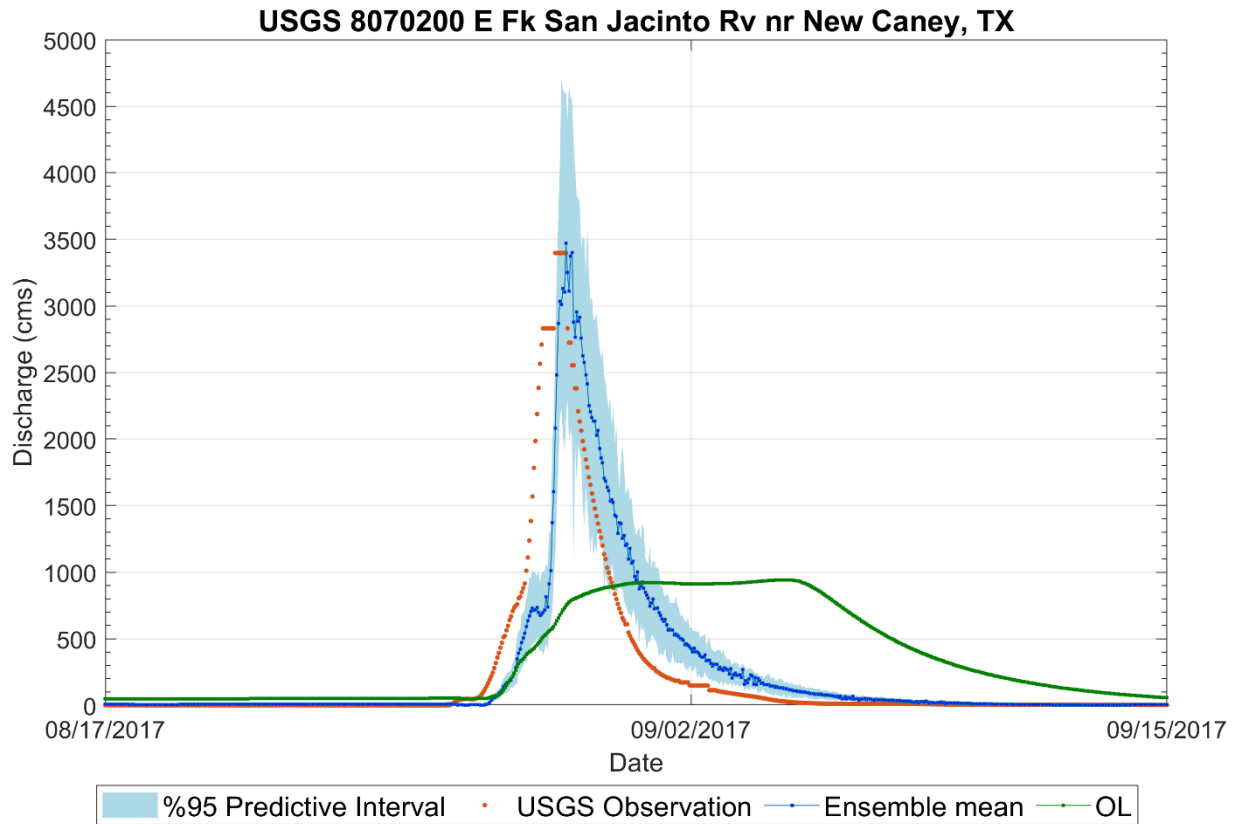


Figure 4-S2. WRF-Hydro simulated streamflow with 95-percentile confidence interval versus USGS observed streamflow for the period of Hurricane Harvey. The blue line and red points are the mean ensemble and observation, respectively. The green line displays the open loop model run.

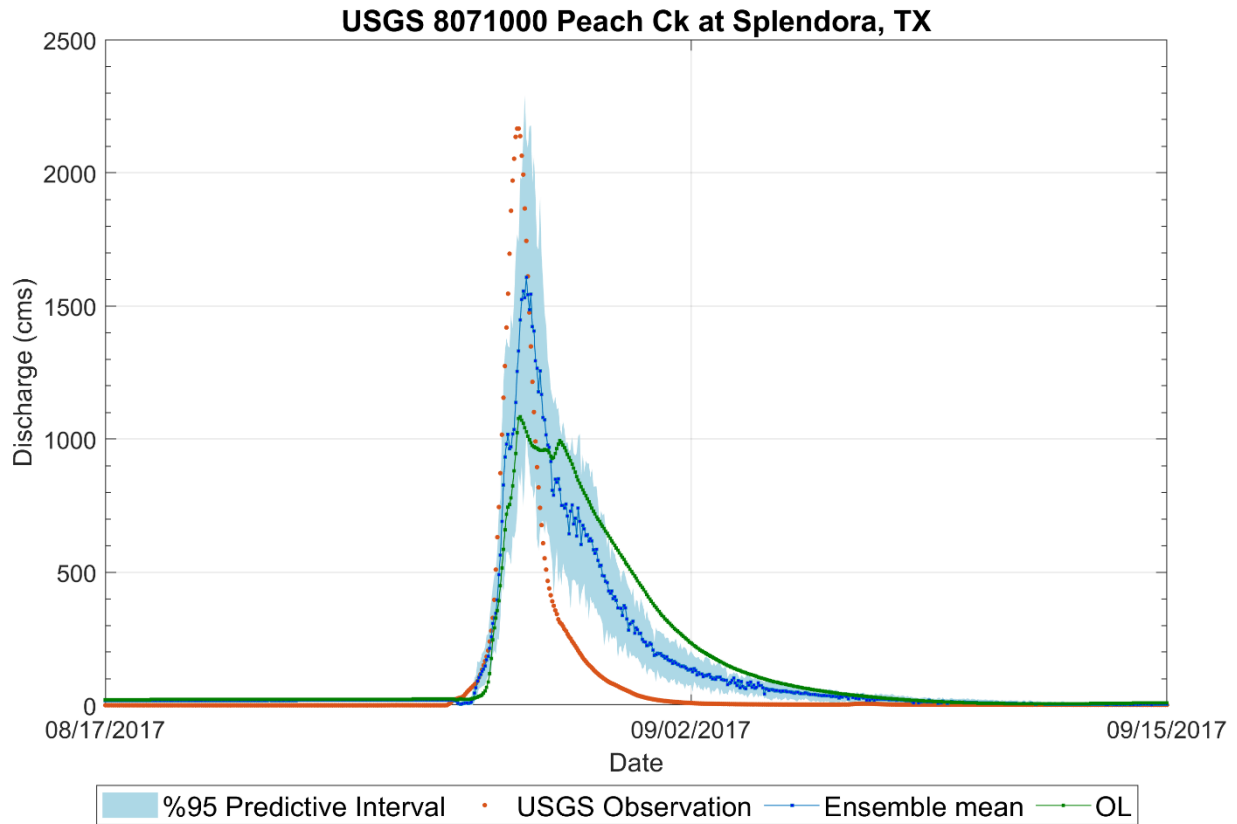


Figure 4-S3. WRF-Hydro simulated streamflow with 95-percentile confidence interval versus USGS observed streamflow for the period of Hurricane Harvey. The blue line and red points are the mean ensemble and observation, respectively. The green line displays the open loop model run.

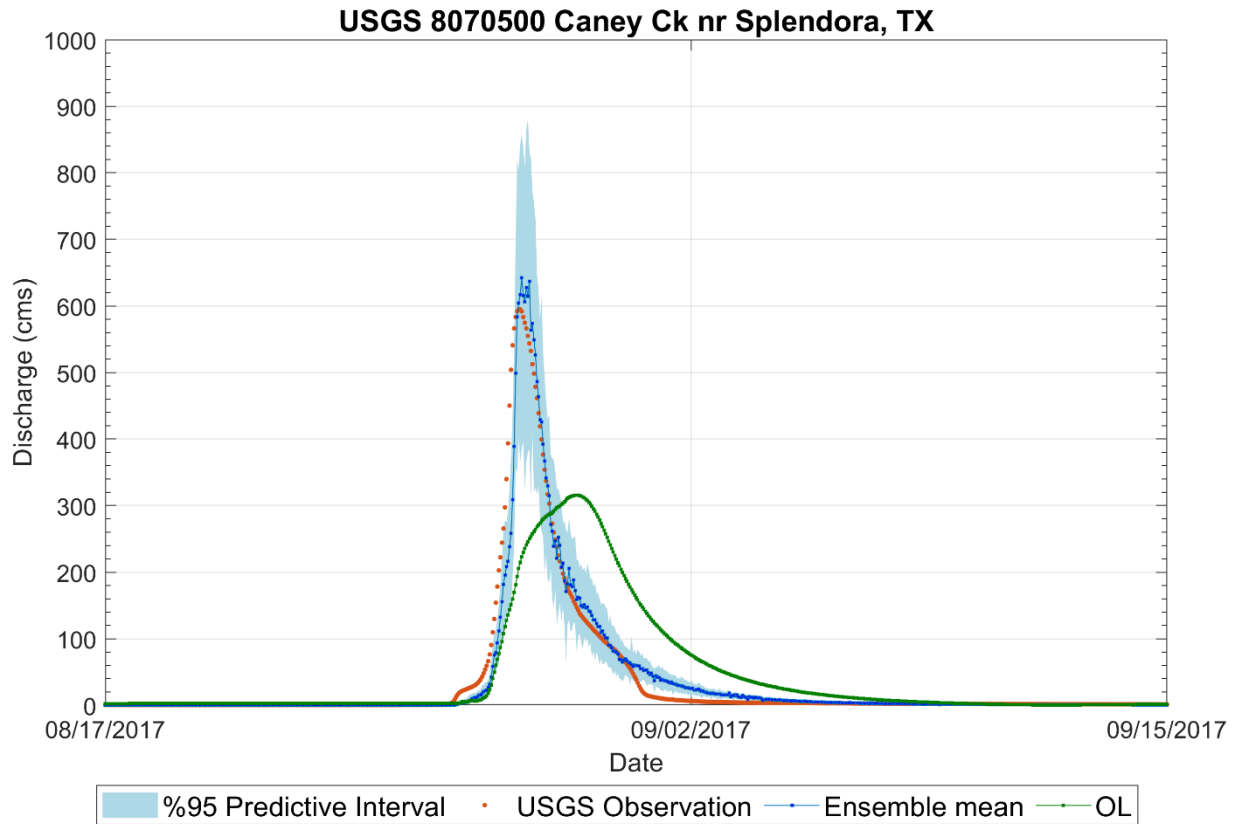


Figure 4-S4. WRF-Hydro simulated streamflow with 95-percentile confidence interval versus USGS observed streamflow for the period of Hurricane Harvey. The blue line and red points are the mean ensemble and observation, respectively. The green line displays the open loop model run.

Table 4-S1. Deterministic and probabilistic performance measures for the multivariate assimilation of satellite soil moisture and streamflow observations within the watershed.

USGS Station #	KGE	RMSE (cms)	Reliability	NRR
8070280	0.95	20.12	0.90	1.10
8070200	0.88	80.70	0.84	1.30
8071000	0.70	41.17	0.88	1.25
8070500	0.96	6.71	0.84	1.08

Appendix A

Summary of performance measures used in this study is tabulated in Table A1. These performances measures are fully described in (Abbaszadeh, Moradkhani, & Daescu, 2019; DeChant & Moradkhani, 2012).

Performance Measure	Mathematical Representation
Kling-Gupta Efficiency (KGE)	$1 - \sqrt{\left(\left(\frac{\text{Cov}_{y_t y'_t}}{\sigma \sigma'}\right) - 1\right)^2 + \left(\left(\frac{\sigma'}{\sigma}\right) - 1\right)^2 + \left(\left(\frac{\mu'}{\mu}\right) - 1\right)^2}$
Root Mean Square Error (RMSE)	$\sqrt{\frac{1}{T} \sum_{t=1}^T (y'_t - y_t)^2}$
centered Root Mean Square Difference (RMSD)	$\sqrt{\frac{1}{T} \sum_{t=1}^T ((y'_t - \bar{y}') - (y_t - \bar{y}_t))^2}$
Pearson Correlation Coefficient (PCC)	$\frac{1}{T-1} \sum_{t=1}^T \left(\frac{y'_t - \mu'}{\sigma'}\right) \left(\frac{y_t - \mu}{\sigma}\right)$
Mean Absolute Bias (MAB)	$\sum_{t=1}^T y_t - y'_t / T$
Normalized Root-Mean-Square Error Ratio (NRR)	$\sqrt{\frac{1}{T} \sum_{t=1}^T (y_t - \bar{y}'_{\bullet,t})^2} \times \left(\frac{1}{T} \left\{ \sum_{t=1}^T \sqrt{\frac{1}{T} \left[\sum_{t=1}^T (y_t - \bar{y}'_{\bullet,t})^2 \right]} \right\} \sqrt{\frac{N+1}{2N}}\right)^{-1}$
95% Exceedance Ratio (ER95)	$\frac{1}{T} \sum_{t=1}^T (y'_{97.5\%,t} < y_t \text{ or } y'_{2.5\%,t} > y_t) \times 100\%$
Reliability	$1 - \frac{2}{T} \sum_{t=1}^T \left \frac{Z_t}{T} - U_t \right $